June 26 -29, 2022 Struga, North Macedonia

8th Symposium on

APPLIED ELECTROMAGNETICS SAEM'2022

PROCEEDINGS OF SAEM'2022

Organised by

Ss. Cyril&Methodius University in Skopje
Faculty of Electrical Engineering & Information Technologies,
North Macedonia

University of Maribor
Faculty of Energy Technology, Slovenia

Czestochowa University of Technology
Faculty of Electrical Engineering, Poland

Polish Society of Applied Electromagnetics, Poland

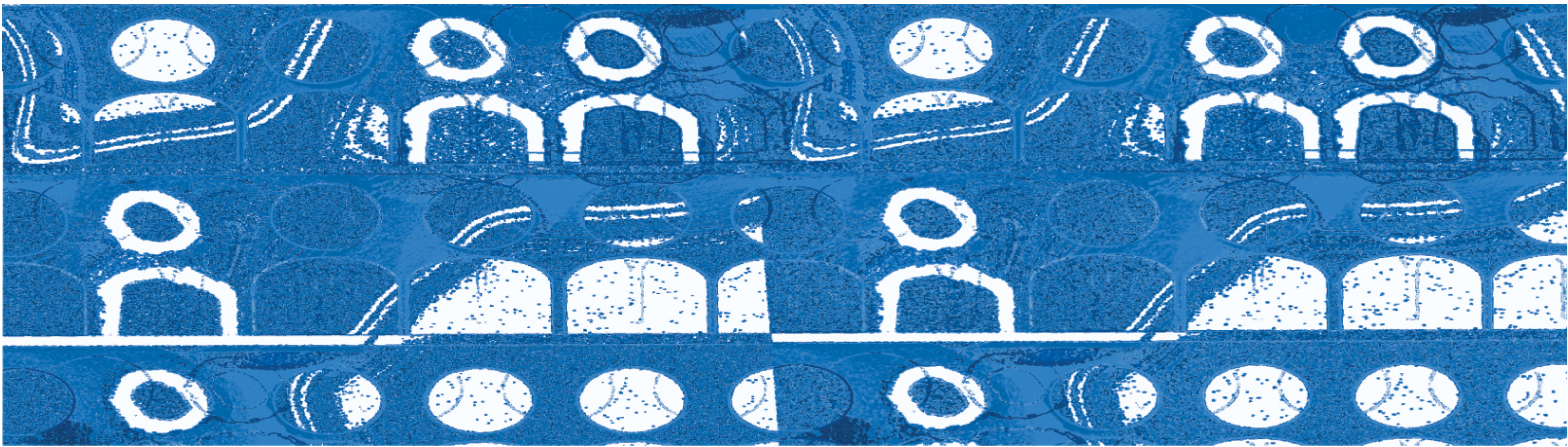

8th Symposium on Applied Electromagnetics
SAEM'2022
Struga, North Macedonia, 26-29 June, 2022

PROCEEDINGS OF SAEM'2022

Organised by:

Ss. Cyril and Methodius University in Skopje
Faculty of Electrical Engineering and Information Technologies, North Macedonia

Czestochowa University of Technology
Faculty of Electrical Engineering, Poland

University of Maribor
Faculty of Energy Technology, Slovenia

Polish Society of Applied Electromagnetics, Poland

December 2022, Skopje, North Macedonia

Title: PROCEEDINGS OF SAEM’2022

Editors: Prof. Lidija Petkovska
Prof. Goga Cvetkovski

Publisher: Ss. Cyril and Methodius University in Skopje, North Macedonia
Faculty of Electrical Engineering and Information Technologies

Cover graphic designed by: Wlodzinierz Mozerant

Cover graphic updated by: Goga Cvetkovski

Date: December 2022

ISBN 978-608-4999-01-0

CIP - Каталогизација во публикација
Национална и универзитетска библиотека "Св. Климент Охридски", Скопје

537(062)(048.3)
621.3(062)(048.3)

SYMPOSIUM on Applied Electromagnetics SAEM'2022 (8 ; 2022 ; Skopje)
Proceedings of SAEM’2022_ [електронски извор] / 8 th Symposium on Applied Electromagnetics, Struga, North Macedonia, 26-29 June, 2022 ; [editors Lidija Petkovska, Goga Cvetkovski]. - Skopje : Faculty of Electrical Engineering and Information Technologies =Скопје : Факултет за електротехника и информациски технологии, 2022

Начин на пристапување (URL):
https://saem2022.feit.ukim.edu.mk/assets/files/SAEM2022_PROCEEDINGSFINAL.pdf. - Текст во PDF формат, содржи 187 стр., илустр. - Фусноти кон текстот. - Наслов преземен од екранот. - Опис на изворот на ден 30.12.2022. - Библиографија кон трудовите. - Регистар

ISBN 978-608-4999-01-0

а) Електромагнетика -- Собири -- Апстракти

COBISS.MK-ID 59082245

International Scientific Committee

Chair	Lidija Petkovska	Ss. Cyril & Methodius University, Faculty of Electrical Engineering & Information Technologies, Skopje, North Macedonia
Co-chairs:	Andrzej Krawczyk	Polish Society of Applied Electromagnetics, Warsaw, Poland
	Bojan Štumberger	University of Maribor, Faculty of Energy Technology, Krško, Slovenia

Members:

Nenad Cvetković, SERBIA
Goga Cvetkovski, North MACEDONIA
Ivo Doležel, CZECH REPUBLIC
Dagmar Faktorova, SLOVAKIA
Rastko Fišer, SLOVENIA
Miralem Hadžiselimović, SLOVENIA
Željko Hederić, CROATIA
Masateru Ikehata, JAPAN
Ewa Korzeniewska, POLAND
Anna Koziorowska, POLAND
Roman Kubacki, POLAND
Marek Lis, POLAND
Damjan Miljavec, SLOVENIA
Maria Evelina Mognaschi, ITALY
Zdravko Praunseis, SLOVENIA
Tomasz Rymarczyk, POLAND
Vasilija Šarac, MACEDONIA
Sebastijan Seme, SLOVENIA
Gorazd Štumberger, SLOVENIA
Vesna Arnautovski-Toševa, N. MACEDONIA
Mladen Trlep, SLOVENIA
Jovica Vuletić, North MACEDONIA
Ivan Yatchev, BULGARIA
Mykhaylo Zagyrniak, UKRAINE
Damir Zarko, CROATIA

Local Organising Committee

Chair:	Goga Cvetkovski	Ss. Cyril & Methodius University, Faculty of Electrical Engineering & Information Technologies, North MACEDONIA

Members:

Vesna Arnautovski-Toševa, North MACEDONIA
Mihail Digalovski, North MACEDONIA
Jovica Vuletić, North MACEDONIA

Welcome address

Dear Participants to SAEM'2022, the 8th Symposium on Applied Electromagnetics

On behalf of the International Scientific Committee and the Organising Committee we are very pleased to welcome all participants of the 8th Symposium on Applied Electromagnetics – SAEM'2022 which will be held on June 26-29 2022, in Struga, North Macedonia. Struga, the second city on the shores of the Lake Ohrid, is the place where the River Black Drim leaves the Ohrid Lake and flows to the Adriatic Sea. It is famous for the poetry evenings every year at the end of August, when poets from all over the world come to Struga to read their poetry and share thoughts with other poets.

Paving the history of SAEM conferences, we would like to remind you on the previous successful editions: SAEM'2006, Ohrid (Macedonia), SAEM'2008, Zamosc (Poland), SAEM'2010, Ptuj (Slovenia) and SAEM'2012, Sopron (Hungary). Then SAEM'2014, Skopje (Macedonia), SAEM'2016, Wroclaw (Poland), SAEM'2018, Podčetrtek (Slovenia) and SAEM'2020, Beli Manastir (Croatia), unfortunately cancelled due to Covid-19 pandemic situation. With the development and growing of the symposium, the venue attracts more and more researchers. Indeed, our symposium has been always gathering people, not only from North Macedonia, Poland and Slovenia, but also from many other countries, for example Belgium, Bosnia and Herzegovina, Bulgaria, Croatia, Serbia, Finland, Hungary, Japan, Romania, Turkey, Ukraine, United Kingdom, etc.

SAEM'2022 is back where it started in 2006 on the banks of the Lake Ohrid, but now on its west side, in Struga.

SAEM'2022 is aimed at the presentation of research work results and/or the survey of works in various areas of applied electromagnetics. The Symposium is devoted to exchanging ideas, presenting achievements and results, providing the forum for researchers and academics. Open and friendly atmosphere, which our conferences are known for, encourages especially young researchers to present their achievements and ideas, even in an early stage of their research work. The venue also gives many opportunities for establishing professional links and to discuss collaboration areas for further international research projects and cooperation. We should like to ensure you that the Organizers will do their best to create and maintain friendly and warm atmosphere at the conference, both in scientific and social programme.

Thank you for your coming to Struga. We wish you a lot of fruitful scientific debates during the Symposium and a pleasant stay in this nice place.

Lidija Petkovska – Chair, North Macedonia
Andrzej Krawczyk – Co-chair, Poland
Bojan Stumberger – Co-chair, Slovenia

TABLE OF CONTENTS

Modelling of Temperature Distribution in Anatomically Correct Female Breast Cancer

Arkadiusz Miaskowski[1], **Piotr Gas**[2]

[1] University of Life Sciences in Lublin, Akademicka 13 Street, 20-950 Lublin, Poland, arek.miaskowski@up.lublin.pl,
[2] AGH University of Science and Technology, Mickiewicza 30 Avenue, 30-059 Krakow, Poland, piotr.gas@agh.edu.pl

***Abstract* – The paper aims at the temperature distribution modelling in anatomically correct female breast cancer model using modified Pennes bioheat equation. In our case a heat transfer in the tumor tissue was considered using different perfusion models i.e. constant, linear and non-linear temperature-dependent blood perfusion model. These temperature-dependent models have been applied in order to account for the strong temperature dependence due to bio-regulatory processes inside naturalistic irregular shaped breast tumor. It was found that the temperature patterns distributions do not strongly depend on the perfusion model but they have an impact on temperature rise and its value.**

1 Introduction

Electromagnetic (EM) field is increasingly used in the treatment of hyperthermia, due to the thermal effect in cancer tissue and proven efficacy in the treatment of tumors of various locations, including female breast tumors. Breast carcinoma is the most frequently diagnosed cancer in women [1,2]. One of the promising oncological therapies, still in the phase of intensive clinical trials, is the so-called magnetic fluid hyperthermia (MFH) [3]. MFH is based on feeding magnetic nanoparticles (MNPs) into cancer and then external EM field of hundreds of kilohertz is applied to induce the tumor temperature in the therapeutic range of 40–45^{o}C. In this way the MNPs dissipate heat and activate biochemical paths leading to necrosis or apoptosis of malignant cells [4]. The idea of MFH therapy is presented in Fig. 1.

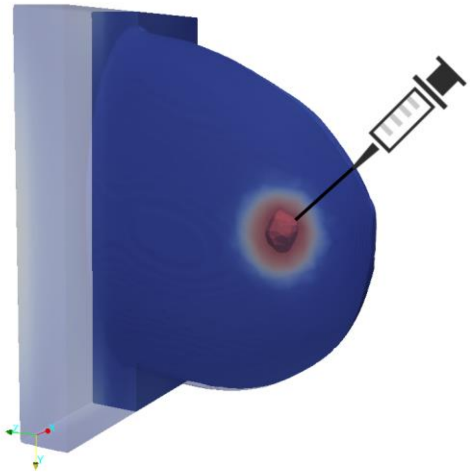

Fig. 1. Idea of magnetic fluid hyperthermia (MFH): magnetic nanoparticles (MNPs) are fed into tumor and then external EM field is applied.

On should realize, that when human tissues are exposed to an alternating EM field, the eddy currents effect is observed due to non-zero conductivity of the tissues [5,6]. That effect describes the process where the energy of an electric current is converted into heat as it flows through the tissues, which finally leads to their heating. In the case of MFH, apart from the eddy currents power losses, at the same time the single-domain nanoparticles magnetic power losses should be considered. The phenomenon of heat dissipation from MNPs is very sophisticated and depends on their concentration, the distribution and the relaxation mechanism in the tumor together with the magnetic field strength and its frequency [7]. However, when comparing both eddy currents and the single-domain nanoparticles magnetic power losses, the effect of the former can be neglected as it is about a hundred times lower [8].

The heat sources in EM-induced hyperthermia can be various types of applicators [9–11], coils [12] and antennas [3–15] operating on radio and microwave frequencies. Depending on the heating technique chosen, the temperature of the tumor may exceed 50°C, which is associated with the ablation of the cancerous tissue [16–18]. The efficacy of thermal therapy may be enhanced by associated targeted therapy, including radio-, chemo-, immune- or gene therapy [19,20], where nanocarriers might be magnetic particles of different physico-chemical structure [21–24].

During *in-silico* studies on hyperthermia and ablation treatments, cancerous tumors are most often modelled with spheres [2,25–27] or ellipsoids (prolate or oblate spheroids) [28]. However, a recent interest of naturalistic tumor shapes [29] asks about the possibility of taking into account irregular tumor models in thermal therapies procedures.

It should be emphasized that the presented paper ignores important aspects of alternating EM field generation, as they are irrelevant from the point of view of the analysis of various tumor perfusion models. The authors assumed a specific value of power dissipation of MNPs, which results from previous performed *in-silico* and *in-vitro* studies of magnetite nanoparticles immersed in an aqueous solution [30,31].

In the previous work [30], the authors have shown that the different perfusion tumor models effect significantly temperature rise taking into account the spherical tumor model. In the case of irregular shaped tumor such a situation is not straightforward as it is shown in the current work.

2 Modified Pennes Equation

A mathematical model dedicated to the numerical analysis of heat transfer in human tissues was proposed by Pennes in the middle of last century [32]. In this model, blood perfusion is assumed to be uniform throughout the tissue and all the heat leaving the artery is absorbed by the local tissue with no venous rewarming. However, the Pennes model is limited to the constant-rate blood perfusion i.e. the arterial temperature is assumed to be equal to the body core temperature. That means Pennes original model describes blood perfusion with acceptable accuracy if there are no large vessels nearby, like for example, liver [32].

Nevertheless, the vascularised tissue often experiences increased perfusion as temperature increases and it is necessary to consider a more general form of Pennes equation in which the blood perfusion is a function of temperature. The temperature dependent blood perfusion is especially desired when dealing with magnetic fluid hyperthermia and in the cases were high temperature gradients can occurred [8]. In spite of the fact that the temperature-dependent blood perfusion values are still open for discussion, the non-linear ones seem to be the most accurate and provide a faithful representation of the heat dissipation in human tissues [2,3,33,34].

In this work, the temperature distribution was calculated using the modified Pennes equation as [32]:

$$\rho c \frac{\partial T}{\partial t} = \nabla \cdot \left(k \nabla T\right) - \rho_\mathrm{b} c_\mathrm{b} \rho \omega\left(T\right)\left(T - T_\mathrm{b}\right) + \rho Q_\mathrm{m} + \rho Q_\mathrm{nano} \tag{1}$$

where ρ is the tissue density, c is the tissue specific heat capacity, k is the tissue thermal conductivity, c_b is the blood specific heat capacity, T_b is the arterial blood temperature, T is the local temperature, Q_m is the heat generation rate (HGR in W/kg) due to the metabolic heat, Q_nano is the external power losses due to the eddy current effect and other sources, and $\omega(T)$ is the blood perfusion. In practice, the temperature-dependent perfusion is often defined as so called heat transfer rate (HTR) and defined as $\mathrm{HTR}(T) = \rho_\mathrm{b} C_\mathrm{b} \rho\omega(T)$. In our case, the following perfusion models were considered [30]:

a) non-linear model:

$$\mathrm{HTR}(T) = 0.4 + 0.4\exp\left(-\frac{(T-37)^4}{880}\right)\left[\frac{\mathrm{mL}}{\mathrm{min\ kg\ K}}\right] \tag{2}$$

b) linear model:

$$\mathrm{HTR}(T) = -1.08 + 0.4T \tag{3}$$

c) constant model:

$$\mathrm{HTR}(T) = 0.6 \tag{4}$$

Beside the models (Eqs. 2–4) a completely free of no-blood-perfusion model, HTR(T) = 0, was investigated for comparative analysis.

In the case when dealing with MFH it was shown that the power losses generated by magnetic nanoparticles present in the tumor play a crucial role when comparing to the eddy currents [8]. That is why the external power losses can be expressed as [35]:

$$Q_{\mathrm{nano}} = \pi\mu_0\chi'' H_0^2 f \rho_{\mathrm{MNP}}^{-1}\ [\mathrm{W/kg}] \tag{5}$$

where χ'' is the average out-of-phase component of susceptibility from each magnetic nanoparticle and f is the frequency of applied electromagnetic field with magnetic field strength equal to H_0 and ρ_{MNP} is the density of core magnetic nanoparticles.

To specify the thermal conditions at the boundaries of the computational domain the mixed boundary conditions were set in order to describe convection effect as follows [36]:

$$k\frac{\partial T}{\partial n} + h(T - T_{\mathrm{ext}}) = F_{\mathrm{boundary}} \tag{6}$$

where $\partial T/\partial n$ means the directional derivative of temperature in normal direction, k is the thermal conductivity of skin, h is the heat transfer coefficient and T_{ext} is the external temperature. This boundary condition is appropriate for modeling effects like convection, e.g., the cooling effect of blood in major blood vessels or cooling effect of air around a body. Additionally, model includes exchange of radiative heat with the boundary term of the form [36]:

$$F_{\mathrm{radiation}} = \sigma_{\mathrm{SB}}\left(T^4 - T_{\mathrm{ext}}^4\right) \tag{7}$$

where $\sigma_{\mathrm{SB}} = 5.67\cdot10^{-8}\ \mathrm{W/m^2/K^4}$ is the Stefan-Boltzmann constant.

Above equation can be also expressed as:

$$F_{\mathrm{radiation}} = \sigma_{\mathrm{SB}}\left(T - T_{\mathrm{ext}}\right)\left(T + T_{\mathrm{ext}}\right)\left(T^2 + T_{\mathrm{ext}}^2\right) \tag{8}$$

or for small temperature differences, it can be approximated by:

$$F_{\mathrm{radiation}} = 4\sigma_{\mathrm{SB}}\left(T - T_{\mathrm{ext}}\right)T_{\mathrm{ext}}^3 \tag{9}$$

Finally, taking the above into account, the mixed boundary condition (6) used in the simulation with coefficient $h = 4\sigma_{\mathrm{SB}}T^3_{\mathrm{ext}}$ can be written as:

$$k\frac{\partial T}{\partial n} + 4\sigma_{\mathrm{SB}}\left(T - T_{\mathrm{ext}}\right)T_{\mathrm{ext}}^3 = F_{\mathrm{boundary}} \tag{10}$$

3 Anatomically Correct Female Breast Phantom

In order to get as close as possible to the real disease case, the authors performed calculations using the anatomically correct model of the female breast with irregular shaped cancer as presented in Fig.2. The breast screening of tumor was provided by Dalian University of Technology, China. In Fig. 2-left the screening mammography image can be seen together with the tumor marked by red circle. On the right in Fig. 2, it can be seen the tumor model with regard to sphere of radius r = 10 mm in order to better visualise tumor's irregular shape.

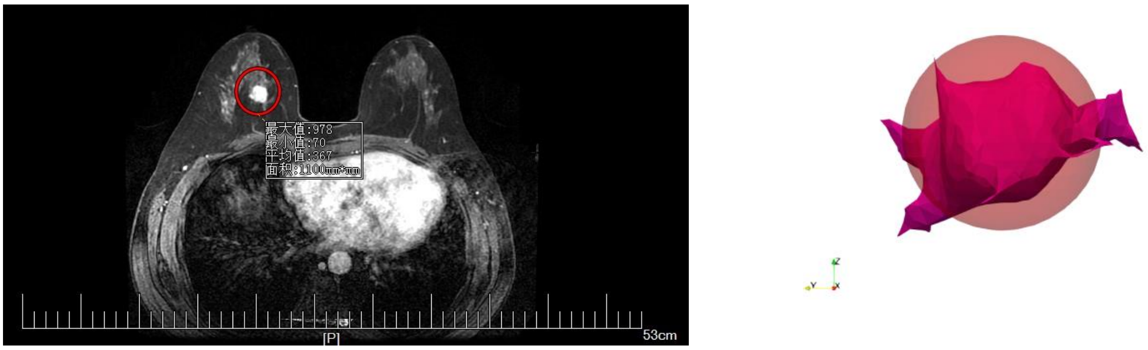

Fig. 2. Screening mammography of the tumor (left) and the tumor model (right) with regard to sphere of radius r = 10 mm.

As for the female breast phantom used in this work, it was taken from UWCEM Numerical Breast Phantom Repository (see Fig. 3-left) and the following tissues were extracted and coloured: skin – red, muscle – orange, breast fat – yellow, fat – green, breast gland – blue. Besides, in order to mirror the screening mammogram from Fig. 2, the tumor model was included in the breast as it is shown in Fig. 3. Similar breast phantoms one can find in [3,15,25,27,29,37] however, the proposed models were simplified to the semi-ellipsoidal block, the semi-sphere or to the anatomically correct shape without naturalistic breast tissues. In this work the anatomically correct female breast model was used together with naturalistic tumour model. Tissue parameters were taken from freely available databases [38] and their physical parameters are gathered in Table 1 for frequency 100 kHz. Importantly, the HTR coefficient for tumor, given in Table 1, is variable due to used blood perfusion model (see Eqs. 2–4).

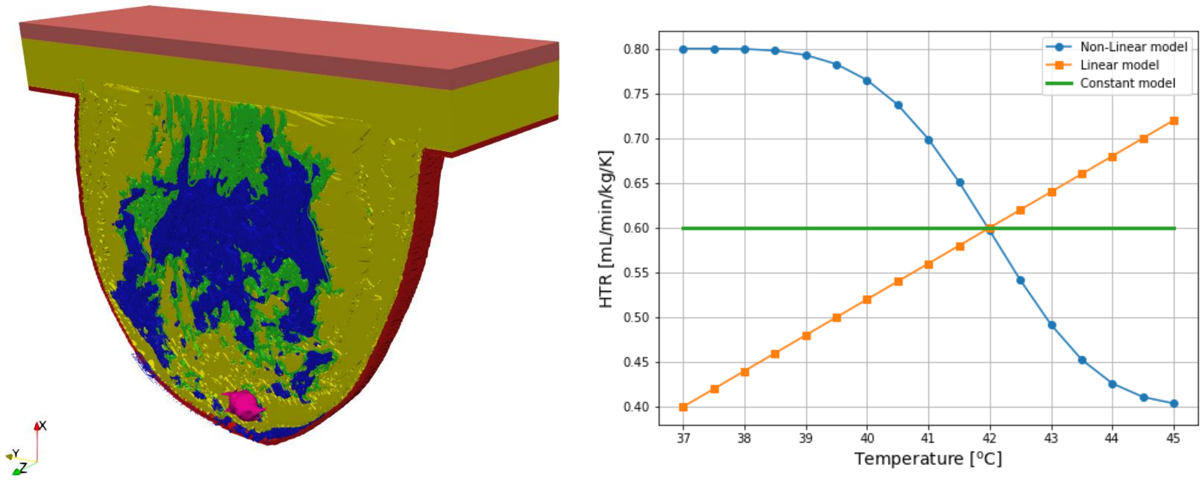

Fig. 3. Female breast phantom *xy*-cross section including irregular shaped tumor (left), the different perfusion models as presented in Eqs. 2–4 [30] (right).

Table 1. Physical parameters of the breast phantom for frequency f = 100 kHz [38].

Tissue	Density ρ [kg/m^3]	Heat capacity c [J/kg/K]	Thermal conductivity k [W/m/K]	Heat Transfer Rate HTR [mL/min/kg]	Heat Generation Rate HGR [W/kg]
Skin	1109	3391	0.37	106	1.65
Muscle	1090	3421	0.49	37	0.91
Fat	911	2348	0.21	33	0.51
Breast fat	911	2348	0.21	47	0.73
Breast gland	1041	2960	0.33	150	2.32
Blood	1050	3617	0.52	10000	0.00
Tumor	1090	3437	0.57	*var*	12

4 Numerical analysis

In order to numerically investigate the described problem as presented in Sections 2 and 3 a commercially available Sim4Life software [36] was employed. In our case the Thermal Solver integrated into Sim4Life platform was used to simulate the thermal effects in the particular setup as presented above. From mathematical point of view, the thermal solver is based on the extended form of diffusion differential equation with specific boundary conditions.

In our case the initial conditions, T_0, understood as temperature for each individual breast tissue at the start of the simulation was set to 37°C, the overall (background) temperature was set to 25°C and the heat transfer coefficient h was set to 5 W/m^2/K. In addition, it was assumed that the power density generated by MNPs (placed inside the tumor) is homogenous and it is at the level of Q_{nano} = 100 W/kg. This value is already recognized as a minimum one, which is desired to reach the therapeutic temperature 42°C [30]. In this way, it was assumed that magnetic nanoparticles are uniformly distributed in the tumor volume as found in many similar papers [31]. However, heterogeneous nanofluid spatial distribution inside tumor tissue is also the subject of intensive hyperthermia studies [39]. One should also realise that the coefficients of the blood perfusion models have been chosen so that their common point falls to 42°C i.e. at therapeutic temperature, which seems to be relevant assumption.

In Fig. 4 can be seen the cross-section temperature distributions in the breast model in the steady-state after 1800 seconds due to heat source from magnetic nanoparticles Q_{nano}. One can notice that temperature about 42°C inside the tumor and its vicinity has been reached for every perfusion model under consideration. However, it can also be seen that the temperature patterns distributions have changed a little from case to case. It is clear that heterogeneous temperature distribution in the tumor vicinity can be observed because of irregular tumor shape as well as due to different properties of the tissues surrounding the tumor. To better visualise these heterogeneous patters the circle of radius r = 10 mm has been added to the drawings.

Fig. 5 indicates that the therapeutic temperature profiles in the middle of the tumor was reached in all cases except the one where there is no perfusion – in this case the temperature was the highest, as expected, and it was about 43°C. Moreover, for the constant and linear perfusion models the temperature over time is almost the same. From computational point of view such a situation is very important as every nonlinear model is very time-consuming. Therefore, it is advisable to use simplification models with linear or constant tumor blood perfusion rates.

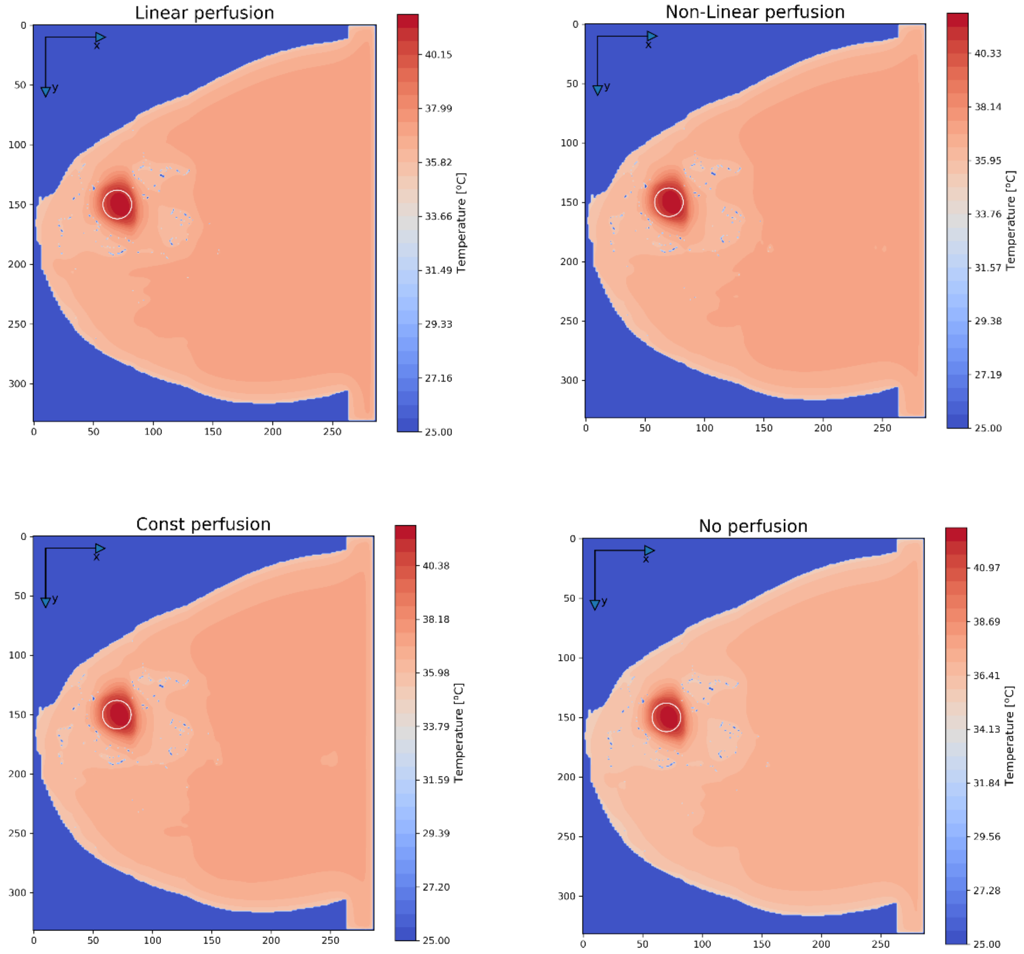

Fig. 4. The *xy*-cross section of temperature distributions passing through the middle of the tumor in the steady-state for different perfusion models.

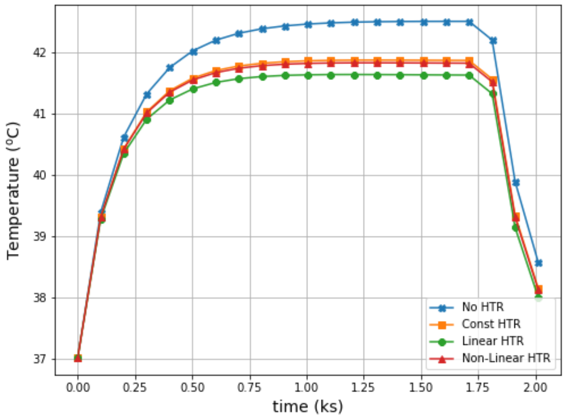

Fig. 5. Temperature over time in the tumor centre for different blood perfusion models.

5 Conclusions

In present paper, the temperature distribution modelling in anatomically correct female breast cancer using the modified Pennes bio-heat equation has been presented. Three different perfusion models i.e. constant-, linear- and non-linear temperature-dependent blood perfusion models in the tumor tissue were considered. In addition the perfusion-free model was investigated for comparative analysis. These dependences have been applied in order to account for the strong temperature dependence due to bio-regulatory processes inside naturalistic irregular shaped female breast tumor. It was found that the temperature patterns distributions do not strongly depend on the perfusion model but the application of the particular model has an impact on temperature rise ratio and its value.

Regardless of the irregular shaped tumor and the anatomically correct female breast tissues distribution, the differences in blood perfusion models do not influence the temperature patterns distributions. However, it was shown that temperature rise ratio depends on the applied perfusion model. Moreover, it is worth noticing that the application of the non-linear model and the constant one in the modified Pennes bio-heat equation, gave the same temperature rise in the function of time. This result can be very useful from computational point of view i.e. non-linear models are often time- and memory-consuming models. Therefore, the authors recommend the use of simplified models with linear or constant perfusion rates during the hyperthermia treatment planning.

All in all, the results presented above indicate that uniform MNPs distribution in the tumor volume leads to non-uniform temperature distribution in its volume and vicinity. It was shown that the application of different perfusion models has an impact on the temperature rise in the tumor’s centre. The considered and investigated mathematical model did not include the eddy currents power losses but one should realize that they can lead to undesired energy dissipations limiting the amount of energy that can be deposited in an individual patient. In order to correlate the hyperthermia treatment with the clinical results, it is mandatory to know what temperatures are reached in the target tissue. This study may represent a step forward in the planning procedures for each patient individually. The authors showed that taking into account the temperature dependence of blood perfusion in the treated tissue might play an important role in the complex process of a treatment planning.

References

[1] R.L. Siegel, K. D. Miller, H. E. Fuchs, A. Jemal, (2021), "Cancer statistics, 2021", *CA: A Cancer Journal for Clinicians*, **Vol. 71**, No. 1, pp. 7–33.

[2] P. Gas, A. Miaskowski. M. Subramanian, (2020), "In silico study on tumor-size-dependent thermal profiles inside an anthropomorphic female breast phantom subjected to multi-dipole antenna array", *International Journal of Molecular Sciences*, **Vol. 21**, No. 22, 8597.

[3] B. Sawicki, A. Miaskowski, (2014), "Nonlinear higher-order transient solver for magnetic fluid hyperthermia", *Journal of Computational and Applied Mathematics*, **Vol. 270**, pp. 143–151.

[4] C. A. Minnaar, A. Szasz, (2022), "Forcing the Antitumor Effects of HSPs Using a Modulated Electric Field", *Cells*, **Vol. 11**, 1838.

[5] P. Gas, (2010), "Temperature inside tumor as time function in RF hyperthermia", *Przegląd Elektrotechniczny*, Vol. 86, No. 12, 42–45.

[6] P. Syrek, C. Barz, M. Skowron, A. Ciesla, (2019), "Eddy Currents Distribution in Upper Extremities During Magnetotherapy", *2019 11th International Symposium on Advanced Topics in Electrical Engineering (ATEE)*, pp. 1–4.

[7] J. Carrey, B. Mehdaoui, and M. Respaud, (2011), "Simple models for dynamic hysteresis loop calculations of magnetic single-domain nanoparticles: Application to magnetic hyperthermia optimization", *Journal of Applied Physics*, **Vol. 109**, No. 8, 083921.

[8] A. Miaskowski, M. Subramanian, (2019), "Numerical Model for Magnetic Fluid Hyperthermia in a Realistic Breast Phantom: Calorimetric Calibration and Treatment Planning", *International Journal of Molecular Sciences*, **Vol. 20**, No. 18, 4644.

[9] M. D. Geyikoglu, B. Cavusoglu, (2022), "Microwave hyperthermia with X band flexible hyperthermia applicator for bone and joint cancer treatment", *Journal of Electromagnetic Waves and Applications*, **Vol. 36**, No. 9, pp. 1285–1297.

[10] A. Kalogeropoulos, N. Tsitsas, (2021), "Excitation of a layered medium by *N* sources: Scattering relations, interaction cross sections and physical bounds", *Quarterly of Applied Mathematics*, **Vol. 79**, pp. 335–356.

[11] V. Portosi, A. M. Loconsole, M. Valori, V. Marrocco, F. Bonelli, G. Pascazio, V. Lampignano, A. Fasano, R. Lorusso, F. Prudenzano, (2021), "Feasibility investigation of low-cost microwave needle applicator for thermal ablation cancer therapy", *2020 IEEE International Symposium on Medical Measurements and Applications (MeMeA),* pp. 1–6.

[12] J. I. Lopez Perez, R. D. Serna Maldonado, L. A. Bermeo Varon, J. F. Castillo Garcia, (2020), "Estimation of Electrical Conductivity from Radiofrequency Hyperthermia Therapy for Cancer Treatment by Levenberg Marquardt Method", Communications in Computer and Information Science, **Vol. 1195**, pp.142–154.

[13] N. Nizam-Uddin, W. M. Abdulkawi, I. Elshafiey, A. F. A. Sheta, (2022), "Towards an efficient system for hyperthermia treatment of breast tumors", *Biomedical Signal Processing and Control*, **Vol. 71**, 103084.

[14] S. Suseela, P. Wahid, (2020), "Breast cancer hyperthermia using a grid array applicator", *2020 SoutheastCon*, pp. 1–4.

[15] W. V. Ling, K. Lias, N. Buniyamin, H. M. Basri, M. Z. A. Narihan, (2021), "SAR distribution of non-invasive hyperthermia with microstrip applicators on different breast cancer stages", Indonesian Journal of Electrical Engineering and Computer Science, **Vol. 22**, pp. 232–240.

[16] A. S. Ashour, M. Asran, D. I. Fotiadis, (2020), "Optimal power for microwave slotted probes in ablating different hepatocellular carcinoma sizes", *Computers in Biology and Medicine*, **Vol. 127**, 104101.

[17] M. Radmilovic-Radjenovic, D. Radjenovic, B. Radjenovic, (2021) Finite element analysis of the effect of microwave ablation on the liver, lung, kidney, and bone malignant tissues, *EPL*, **Vol. 136**, 28001.

[18] C. J. Trujillo-Romero, L. Leija-Salas, A. Vera-Hernandez, G. Rico-Martinez, J. Gutierrez-Martinez, (2021), "Double Slot Antenna for Microwave Thermal Ablation to Treat Bone Tumors: Modeling and Experimental Evaluation", *Electronics*, **Vol. 10**, 761.

[19] O. A. A. Aziz, K. Arafa, A. S. A. Dena, I. M. El-Sherbiny, (2020), "Superparamagnetic iron oxide nanoparticles (SPIONs): preparation and recent applications", *Journal of Nanotechnology Advanced Material*, **Vol. 8,** No. 1, pp. 21–29.

[20] A. Orrico, L. Bianchi, S. Korganbayev, M. De Landro, P. Saccomandi, (2021), "Controlled photothermal therapy based on temperature monitoring: theoretical and experimental analysis", *2021 IEEE International Symposium on Medical Measurements and Applications (MeMeA)*, pp. 1–6.

[21] O. Oehlsen, S. I. Cervantes-Ramírez, P., Cervantes-Avilés, I. A. Medina-Velo, (2022), "Approaches on Ferrofluid Synthesis and Applications: Current Status and Future Perspectives", *ACS Omega*, **Vol. 7**, No. 4, pp. 3134–3150.

[22] M. Theodosiou, E. Sakellis, N. Boukos, V. Kusigerski, B. Kalska-Szostko, E. Efthimiadou, (2022), "Iron oxide nanoflowers encapsulated in thermosensitive fluorescent liposomes for hyperthermia treatment of lung adenocarcinoma", *Scientific Reports*, **Vol. 12**, No. 1, pp. 1–15.

[23] M. Szczęch, (2020), "Experimental studies of magnetic fluid seals and their influence on rolling bearings", *Journal of Magnetics*, **Vol. 25**, No. 1, pp. 48–55.

[24] X. Yu, R. Yang, C. Wu, W Zhang, (2020), "Effect of chromium ion substitution of ZnCo ferrites on magnetic induction heating", *Journal of Alloys and Compounds*, **Vol. 830**, 154724.

[25] M. Paruch, (2020), "Mathematical Modeling of Breast Tumor Destruction using Fast Heating during Radiofrequency Ablation", *Materials*, **Vol. 13**, No. 1, 136.

[26] J. Michałowska-Samonek, A. Miaskowski, A. Wac-Włodarczyk, (2012), "Numerical analysis of high frequency electromagnetic field distribution and specific absorption rate in realistic breast models", *Przeglad Elektrotechniczny*, **Vol. 88**, No. 12b, 97–99.

[27] C. D. Neto, Y. P. Buabssi, J. V. C. Vargas, W. Balmant, A. B. Mariano, (2021), "A simplified mathematical model to predict the human breast thermal response", 26th International Congress of Mechanical Engineering (COBEM 2021), 1070.

[28] N. D. Polychronopoulos, A. A. Gkountas, I. E. Sarris, L. A. Spyrou, (2021), "A Computational Study on Magnetic Nanoparticles Hyperthermia of Ellipsoidal Tumors", *Applied Sciences*, **Vol. 11**, 9526.

[29] B. K. Byrd, V. Krishnaswamy, J. Gui, T. Rooney, R. Zuurbier, K. Rosenkranz, K. Paulsen, R. J. Barth, (2020), "The shape of breast cancer", *Breast Cancer Research and Treatment*, **Vol. 183**, pp. 403–410.

[30] P. Gas, A. Miaskowski, D. Dobrowolski, (2020), "Modelling the tumor temperature distribution in anatomically correct female breast phantom", *Przeglad Elektrotechniczny*, **Vol. 96**, No. 2, pp. 146–149.

[31] I. Raouf, P. Gas, H. S. Kim, (2021), "Numerical Investigation of Ferrofluid Preparation during In-Vitro Culture of Cancer Therapy for Magnetic Nanoparticle Hyperthermia", Sensors, **Vol. 21**, 5545.

[32] H. H. Pennes, (1948), Analysis of tissue and arterial blood temperature in the resting human forearm. *Journal of Applied Physiology*, **Vol. 1**, No. 2, pp. 93–122.

[33] E. Kengne, I. Mellal, A. Lakhssassi, (2014), "A mathematical model to solve bio-heat transfer problems through a bio-heat transfer equation with quadratic temperature-dependent blood perfusion under a constant spatial heating on skin surface", *Journal of Biomedical Science and Engineering*, **Vol. 7**, No. 9, pp. 721–730.

[34] J. Lang, B. Erdmann, and M. Seebass, (1999), "Impact of nonlinear heat transfer on temperature control in regional hyperthermia", *IEEE Transactions on Biomedical Engineering*, **Vol. 46**, No. 9, pp. 1129–1138.

[35] R. E. Rosensweig, (2002), "Heating magnetic fluid with alternating magnetic field", *Journal of magnetism and magnetic materials*, **Vol. 252**, 370–374.

[36] Sim4Life Manual (2021), Realise 6.2.

[37] L. M. Neira, R. O. Mays, S. C. Hagness, (2017), "Human breast phantoms: Test beds for the development of microwave diagnostic and therapeutic technologies", *IEEE Pulse*, **Vol. 8**, No. 4, pp. 66–70.

[38] Hasgall PA, Di Gennaro F, Baumgartner C, Neufeld E, Lloyd B, Gosselin MC, Payne D, Klingenböck A, Kuster N, "IT'IS Database for thermal and electromagnetic parameters of biological tissues", Version 4.1, Feb 22, 2022.

[39] Y. D. Tang, J. Zou, R. C. Flesch, T. Jin, (2022), "Effect of injection strategy for nanofluid transport on thermal damage behavior inside biological tissue during magnetic hyperthermia", *International Communications in Heat and Mass Transfer*, **Vol. 133**, 105979.

The 8th International Symposium on Applied Electromagnetics – SAEM'2022

Struga, North Macedonia, 26-29 June 2022

Comparison of Multilayer Perceptron and Convolutional Neural Networks in 3D Process Electrical Tomography

Tomasz Rymarczyk[1], **Grzegorz Kłosowski**[2], **Konrad Niderla**[1]
[1] Research & Development Center Netrix S.A., University of Economics and Innovation in Lublin, Institute of Computer Science and Innovative Technologies, Lublin, Poland, tomasz@rymarczyk.com, [2] Lublin University of Technology, Faculty of Management, Lublin, Poland, g.klosowski@pollub.pl

***Abstract* – The aim of this article is to optimize the structure of the artificial neural network (ANN) in order to obtain the best imaging results. During the research, many variants of prediction models were trained, differing in the number of neurons, the number of hidden layers, the learning algorithm, transfer functions, overfitting prevention method, etc. As a result of comparing the results of the obtained reconstructive images with the reference images, the optimal network structure was selected. Noteworthy is the original approach, which consists in training separate ANNs for each voxel of an image separately. As a result, the model consists of many separately trained, single-output ANNs, creating a complex system of models that constitute multiple neural network (MNN).**

1 Introduction

Electrical process tomography is a dynamically developing field that enables non-invasive diagnosis of the interior of various industrial devices [1]. In particular, thanks to the use of tomography, it is possible to effectively visualize flat and spatial cross-sections of objects such as pipelines, tanks and chemical reactors [1–3]. In order to guarantee the proper course of the industrial process, its parameters should be constantly monitored [4]. In the case of industrial reactors, such a parameter may be the degree of crystallization [5]. This applies to tank reactors filled with a liquid substance, in which, as a result of the changes taking place, crystals may precipitate or form gas bubbles [6]. The level of liquid crystallization determined by the number and size of crystals, as well as the level of liquid gassing determined by the number and location of gas bubbles, testify to the quality of the process [7]. Therefore, knowing the current state of the process, you can influence its parameters by, for example, changing the mixing speed, adjusting the temperature, pressure, chemical composition of the substrates or the flow intensity. Figure 1 shows the interior of a gas-fired industrial chemical reactor containing all 3 phases of a substance undergoing physical and chemical changes - liquid, solid and gas. Under certain conditions, crystals, solid particles, or gas bubbles may appear in the liquid [8]. Figure 2 shows an example installation with a tank reactor as the major component of an industrial system.

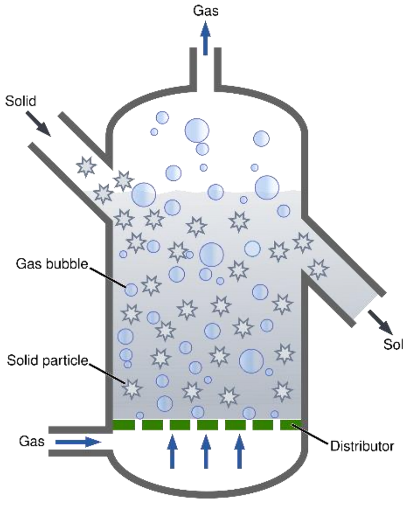

Fig. 1 Gas-fired industrial chemical reactor

Fig. 2 Plant with a tank reactor as the main element of the industrial system

The aim of the research is to develop an optimal machine learning model based on artificial neural networks, thanks to which the obtained spatial tomographic reconstructions will be characterized by the highest quality of mapping real states.

2 Materials and methods

The study looked at the optimal use of the artificial neural network (ANN) and/or the convolutional neural network (CNN) to solve the inverse problem in industrial electrical impedance tomography (EIT) [9–11]. The first considered model took into account many neural networks (MANN), each of which had measurements at the input and a real number at the output reflecting the value of a single voxel [12]. The second model considers training of CNN based on the input data vector (1D). The tomograph uses 32 electrodes placed around the tested reactor. The number of voltage measurements between the individual electrode pairs was 448 for each tested case. The resolution of the 3D image was 14100, which means that the structure of the MANN includes 14100 separately trained ANNs with a single output. The structure of an MNN can be specified as MNN = $(448 \rightarrow 20 \rightarrow 1) \times 14100$. According to the mentioned model, all the networks included in the MANN have 20 neurons in the hidden layer. Figure 3 shows the flow chart of MANN. As you can see, the key is to dedicate a separate neural network to each voxel of the output image. Thanks to this original approach, the computational complexity of the neural network that directly generates the value of each of the 14100 voxels is reduced. Figure 4 shows the general model of how CNN works [13]. It is a homogeneous neural network that processes 448 inputs into 14,100 outputs in one pass.

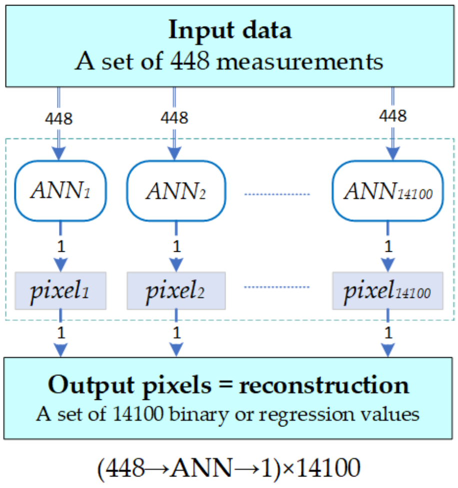

Fig. 3 Workflow of multiple artificial neural network (MANN)

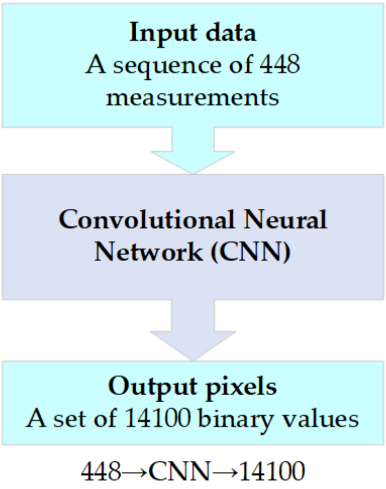

Fig. 4 Workflow of a convolutional neural network (CNN)

The set of all observations consisted of 30,000 cases. The results of training the multilayer perceptron network for a randomly selected voxel are presented in Table 1. The main criterion for assessing the quality of the MANN neural network used during its training was MSE. Mean squared error (MSE) is the mean squared difference between patterns and reconstruction images and it is satisfied by formula (1)

$$\mathrm{MSE} = \frac{\sum_{i=1}^{n}(y_i - \hat{y}_i)^2}{n} \tag{1}$$

where n – the number of voxels in the image and, at the same time, the number of finite elements in the image mesh, y_i – the reference value of i-th pixel, $\hat{y}_i$—the reconstruction value of i-th pixel. R is regression R-value. It depicts the correlation between patterns and reconstructions. The set of observations was divided into three subsets - training, validation, and test, in the proportions 70:30:30.

Table 1 Parametric ANN learning results for a selected voxel

Sets	Observations	MSE	R

Training	21000	0.0011	0.9361
Validation	4500	0.0018	0.8914
Test	4500	0.0011	0.9304

Figure 5 shows the test stand used to verify the tomographic measurements. On the left side you can see the reservoir surrounded by a set of electrodes for EIT measurements. On the right, we see a tomograph which supplies electric current to the appropriate pairs of electrodes, in a fixed sequence and with appropriately selected current parameters, both voltage and amperage.

Fig. 5 View of the test stand. On the left side is the reactor model with electrodes, and on the right side there is a tomograph

Table 2 shows the 7 layers of CNN used. The first layer is sequential (1D) and contains 448 measurement values. The second layer is a convolutional layer containing seven 160-element filters. The next layer is the ReLu layer, which is designed to zero negative values. The fourth layer is the global max pooling layer. It accomplishes downsampling by producing an output that is maximal in all of the spatial dimensions of the input, so in this network the layer pools over the spatial dimension. Fully connected layers sum the products of inputs and weights and adds bias to each input. The fifth layer contains 5000 neurons and the sixth layer 14100 neurons. The regression input layer is designed to compute the MSE after each iteration.

Table 2 Layers of the CNN network

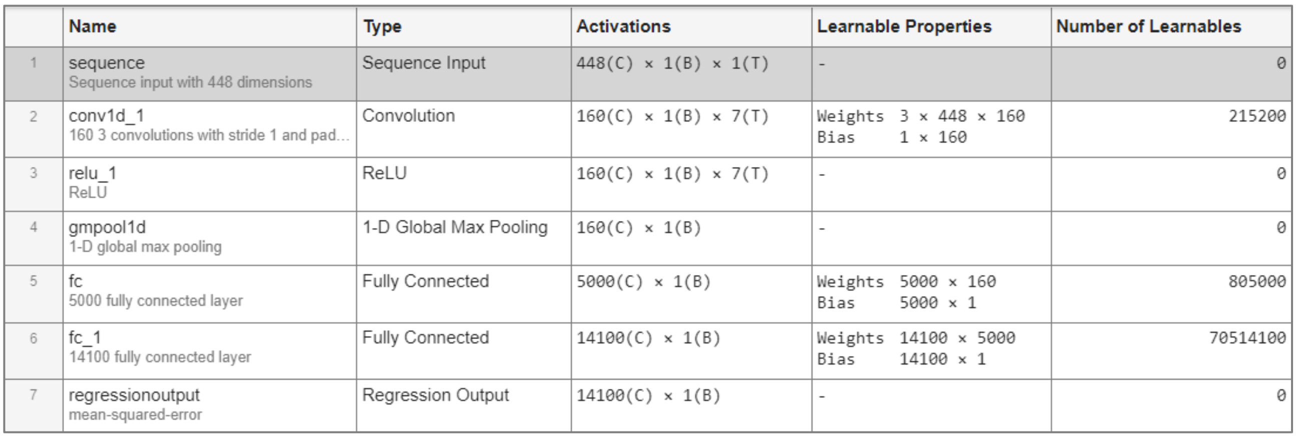

	Name	Type	Activations	Learnable Properties	Number of Learnables
1	sequence Sequence input with 448 dimensions	Sequence Input	448(C) × 1(B) × 1(T)	-	0
2	conv1d_1 160 3 convolutions with stride 1 and pad…	Convolution	160(C) × 1(B) × 7(T)	Weights 3 × 448 × 160 Bias 1 × 160	215200
3	relu_1 ReLU	ReLU	160(C) × 1(B) × 7(T)	-	0
4	gmpool1d 1-D global max pooling	1-D Global Max Pooling	160(C) × 1(B)	-	0
5	fc 5000 fully connected layer	Fully Connected	5000(C) × 1(B)	Weights 5000 × 160 Bias 5000 × 1	805000
6	fc_1 14100 fully connected layer	Fully Connected	14100(C) × 1(B)	Weights 14100 × 5000 Bias 14100 × 1	70514100
7	regressionoutput mean-squared-error	Regression Output	14100(C) × 1(B)	-	0

Figure 6 shows the CNN learning process. The quality evaluation criterion is root mean square error (RMSE). Figure 7 shows a graph of the learning process using MSE as a quality criterion. All three lines showing the errors of the training validation and test sets are highly concurrent, which proves the correct course of the training process. The best validation performance of 0.0017883 was obtained at epoch 12. Both during CNN and MANN training, the course of the error line is hyperboidal, which proves the lack of overfitting and gives hope for high efficiency of the trained predictive model.

In order to protect the neural network against overfitting, the early stopping method was used. The method is based on the application of a validation set to automatically complete the training process. The training process is stopped if the learning error does not decrease for the next six iterations. Small, cyclical fluctuations in the

CNN training performance chart are the result of the necessity to set up a relatively small minibatch. This in turn is due to the memory limitations of the GPU used.

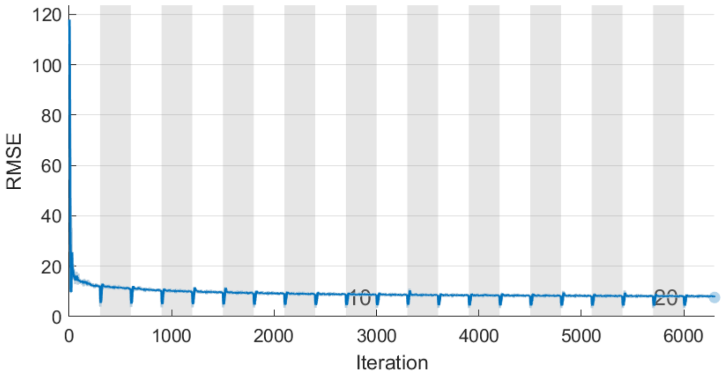

Fig. 6 CNN training performance (RMSE) for a randomly selected voxel

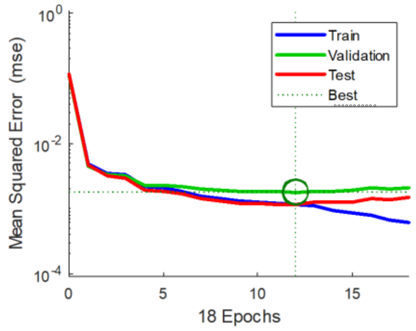

Fig. 7 ANN training performance (MSE) for a randomly selected voxel

3 Results

Figure 8 shows a comparison of the reconstruction of the MANN and CNN methods. The first column contains reference images. The second column contains the reconstructions generated with the use of the MANN model, and the third column contains the tomographic images resulting from the use of CNN. The comparison includes three cases, differing in the number, shape, dimensions, and location of the inclusions. What immediately catches the eye are the non-obvious differences between the MANN and CNN reconstructions. Upon closer examination of the images, it can be seen that the MANN method generates inclusions larger than CNN, and since CNN produces inclusions larger than patterns, it can be estimated that CNN is more accurate than MANN.

#	Pattern	Reconstruction MANN	Reconstruction CNN
1.	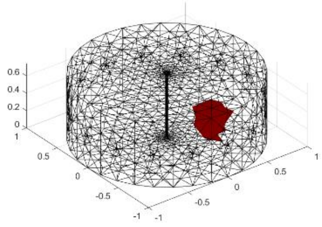	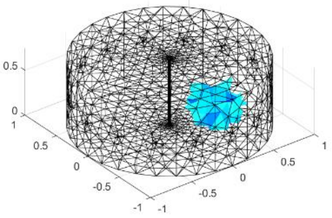	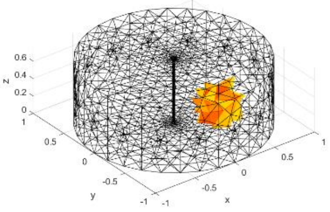
2.	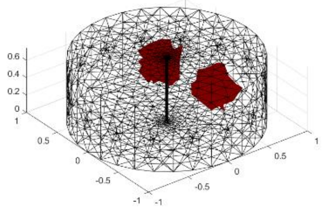	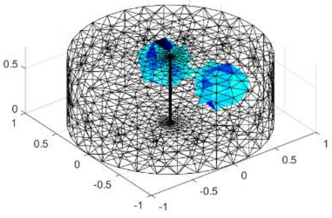	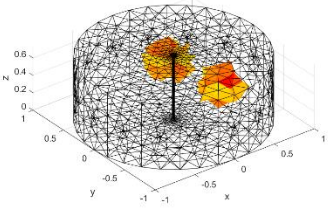
3.	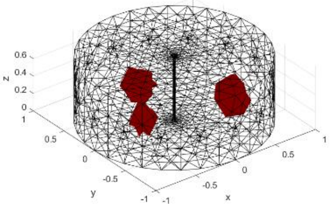	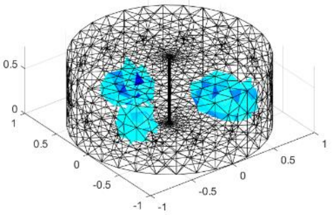	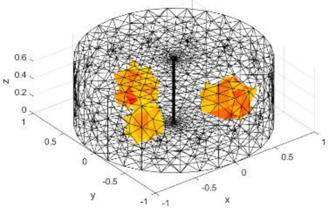

Fig. 8 Comparison of the reconstructive tomographic image with the template

In order to enable an objective comparative assessment, it was decided to use four indicators: mean square error (MSE), normalized mean square error (NMSE), relative image error (RIE), and image correlation coefficient (ICC) [14]. The MSE metric was already described in the previous section by equation (1). Normalized mean squared error (NMSE) is the Euclidean norm of MSE and it is calculated as NMSE = ||MSE||. Formula (2) describes the RIE indicator.

$$\mathrm{RIE} = \frac{\|\hat{y} - y\|}{\|y\|} \tag{2}$$

The MSE, NMSE and RIE indicators are error indicators, therefore the lower their value, the better the assessed model. The last indicator used is the ICC. It is a correlation index, so the closer its value is to 1, the better for the model. The ICC calculation method is presented in formula (3)

$$\mathrm{ICC} = \frac{\sum_{i=1}^{N}(y_i - \bar{y})\left(\hat{y}_i - \bar{\hat{y}}\right)}{\sqrt{\sum_{i=1}^{N}(y_i - \bar{y})^2 \sum_{i=1}^{N}\left(\hat{y}_i - \bar{\hat{y}}\right)^2}} \tag{3}$$

where: $\bar{\hat{y}}$ is the mean voxel values of the reconstructed image and $\bar{y}$ is the mean ground-truth voxel values of the reference image.

Table 3 presents a comparative comparison of both methods (MANN and CNN) based on the 4 above-mentioned indicators.

Table 3 Comparison of the values of qualitative indicators for both compared models – MANN and CNN

Method	Indicator	Observation #1	Observation #2	Observation #3	Average
MANN	MSE	0.00173	0.00479	0.00613	0.00422
	NMSE	0.00478	0.00388	0.00581	0.00482
	RIE	0.70622	0.61952	0.75966	0.69514
	ICC	0.70886	0.78215	0.66800	0.71967
CNN	MSE	0.00124	0.00358	0.00475	0.00319
	NMSE	0.00343	0.00290	0.00450	0.00361
	RIE	0.59876	0.53559	0.66849	0.60095
	ICC	0.80100	0.84868	0.74919	0.79963

Table 3 presents a comparative comparison of both methods (MANN and CNN) based on the 4 above-mentioned indicators. Table 3 corresponds to Figure 8 because it assesses the same three observations. Observation # 1 contains a single inclusion. All three types of errors, MSE, NMSE, and RIE, are greater for MANN than for CNN. On the other hand, the ICC for CNN is as much as 10% higher than the ICC obtained by the MANN method. The same is true for the other two observations. In none of the tested cases, none of the four indicators promoted the MANN method. The last column of Table 3 presents the average results of the ratio analysis. Again, it turned out that all indicators show the superiority of CNN. In other words, the quantitative assessment carried out with the use of indicators showed a clear and decisive dominance of the CNN method over MANN.

4 Conclusions

Industrial tomography is a field that provides solutions that enable technological progress [15]. Modern industrial processes are often characterized by high dynamics and precision. These are basically two divergent goals which, however, must be met if the enterprise wants to be competitive. Speed and precision in the field of industrial process control is a guarantee of obtaining a good product delivered to the market in a short time. The only method to achieve both goals simultaneously is to automate industrial processes. Automation, in turn, requires constant monitoring using appropriate measuring sensors and software that is able to analyze the measurements and draw conclusions as to the corrective actions taken. Tomography is the only known method that enables imaging the interior of the examined object without damaging its structure or disturbing the processes taking place in it [9,16].

This study was aimed at assessing the suitability of the MANN and CNN methods in industrial electrical tomography. For this purpose, two models were trained, with the help of which a number of reconstructions were made. The reconstructions were compared both subjectively and using four indicators - MSE, NMSE, RIE and ICC. The conclusions that arise are that both methods are suitable for solving the tomographic inverse problem because they generate quite good reconstructions. A more detailed analysis, especially the index ones, indicates the superiority of the CNN method over MANN.

References

[1] Kłosowski, G.; Rymarczyk, T.; Cieplak, T.; Niderla, K.; Skowron, Ł. Quality Assessment of the Neural Algorithms on the Example of EIT-UST Hybrid Tomography. *Sensors (Switzerland)* **2020**, *20*, doi:10.3390/s20113324.

[2] Rymarczyk, T.; Kłosowski, G. Innovative Methods of Neural Reconstruction for Tomographic Images in Maintenance of Tank Industrial Reactors. *Eksploatacja i Niezawodnosc -- Maintenance and Reliability* **2019**, *21*, 261–267.

[3] Nordin, N.; Idroas, M.; Zakaria, Z.; Ibrahim, M.N. Tomographic Image Reconstruction of Monitoring Flaws on Gas Pipeline Based on Reverse Ultrasonic Tomography. In Proceedings of the 2014 5th International Conference on Intelligent and Advanced Systems (ICIAS); IEEE, June 2014; pp. 1–6.

[4] Soleimani, M. Super-Sensing through Industrial Process Tomography. *Philosophical Transactions: Mathematical, Physical and Engineering Sciences* **2016**, *374*, 1–5.

[5] Kłosowski, G.; Rymarczyk, T.; Kania, K.; Świć, A.; Cieplak, T. Maintenance of Industrial Reactors Supported by Deep Learning Driven Ultrasound Tomography. *Eksploatacja i Niezawodnosc - Maintenance and Reliability* **2020**, *22*, 138–147, doi:10.17531/ein.2020.1.16.

[6] Xin, L.P.; Yu, B.; Yu, J. A Novel Control for a Continuous Stirred Tank Reactor. In Proceedings of the Chinese Control Conference, CCC; 2021; Vol. 2021-July.

[7] Wang, M. *Industrial Tomography: Systems and Applications*; Elsevier Ltd., Ed.; Woodhead Publishing, 2015; ISBN 9781782421184.

[8] Tian, G.; Yang, B.; Dong, M.; Zhu, R.; Yin, F.; Zhao, X.; Wang, Y.; Xiao, W.; Wang, Q.; Zhang, W.; et al. The Effect of Temperature on the Microbial Communities of Peak Biogas Production in Batch Biogas Reactors. *Renew Energy* **2018**, *123*, 15–25, doi:10.1016/J.RENENE.2018.01.119.

[9] Kozlowski, E.; Rymarczyk, T.; Cieplak, T.; Klosowski, G.; Tchorzewski, P. Application of Logistic Regression to Image Reconstruction in EIT. In Proceedings of the 2019 International Interdisciplinary PhD Workshop (IIPhDW 2019); 2019; pp. 80–83.

[10] Korzeniewska, E.; Sekulska-Nalewajko, J.; Gocławski, J.; Dróżdż, T.; Kiełbasa, P. Analysis of Changes in Fruit Tissue after the Pulsed Electric Field Treatment Using Optical Coherence Tomography. *The European Physical Journal Applied Physics* **2020**, *91*, 30902, doi:10.1051/EPJAP/2020200021.

[11] Rymarczyk, T.; Kozłowski, E.; Kłosowski, G. Electrical Impedance Tomography in 3D Flood Embankments Testing – Elastic Net Approach. *Transactions of the Institute of Measurement and Control* **2019**, *42*, 680–690, doi:10.1177/0142331219857374.

[12] Rymarczyk, T.; Kłosowski, G.; Hoła, A.; Sikora, J.; Wołowiec, T.; Tchórzewski, P.; Skowron, S. Comparison of Machine Learning Methods in Electrical Tomography for Detecting Moisture in Building Walls. *Energies (Basel)* **2021**, *14*, 2777, doi:10.3390/en14102777.

[13] Yuen, B.; Dong, X.; Lu, T. Inter-Patient CNN-LSTM for QRS Complex Detection in Noisy ECG Signals. *IEEE Access* **2019**, *7*, 169359–169370, doi:10.1109/ACCESS.2019.2955738.

[14] Kłosowski, G.; Rymarczyk, T.; Niderla, K.; Rzemieniak, M.; Dmowski, A.; Maj, M. Comparison of Machine Learning Methods for Image Reconstruction Using the LSTM Classifier in Industrial Electrical Tomography. *Energies (Basel)* **2021**, *14*, doi:10.3390/en14217269.

[15] Wajman, R.; Banasiak, R.; Babout, L. On the Use of a Rotatable ECT Sensor to Investigate Dense Phase Flow: A Feasibility Study. *Sensors 2020, Vol. 20, Page 4854* **2020**, *20*, 4854, doi:10.3390/S20174854.

[16] Fabijańska, A.; Banasiak, R. Graph Convolutional Networks for Enhanced Resolution 3D Electrical Capacitance Tomography Image Reconstruction. *Appl Soft Comput* **2021**, *110*, 107608, doi:10.1016/J.ASOC.2021.107608.

Assumptions of the Electrical Drive Unit for Commercial Vehicles

Bartłomiej Będkowski[1], Piotr Dukalski[2], Łukasz Cyganik[3], Tomasz Jarek[4]
Łukasiewicz Research Network – Institute of Electrical Drives and Machines - KOMEL, Al. Roździeńskiego 188,
40-203 Katowice, Poland, E-mail: [1]bartlomiej.bedkowski@komel.lukasiewicz.gov.pl,
[2]piotr.dukalski@komel.lukasiewicz.gov.pl, [3]lukasz.cyganik@komel.lukasiewicz.gov.pl,
[4]tomasz.jarek@komel.lukasiewicz.gov.pl

Abstract* – The article presents the concept of an electric drive for installation in the wheels of commercial vehicles, which will be developed as part of the project "Innovative electric drive unit for commercial vehicles", financed by the National Center for Research and Development under the LIDER XI program, in accordance with the agreement no. LIDER/15/0060/L-11/19/NCBR/2020. In the article, the authors presented the advantages and disadvantages of this type of drive and its possible applications. The paper presents the results of design calculations for the electromagnetic circuit along with thermal calculations and the mechanical structure of the drive.

1 Introduction

Along with the growing interest and ever newer concepts of electric vehicles, various solutions of electric drives are being developed, influencing the broadly understood electromobility [1-22]. Research and implementation in the field of electric vehicle drives concern, inter alia, power sources, control systems, battery power systems, energy transmission techniques and the drive motors themselves [3-14]. In recent years, one of the developed solutions in the field of electric traction drives are motors installed in the wheel hub [15-22]. This solution was first used at the beginning of the 20th century by Ferdinand Porsche to create the world's first hybrid car [11]. At that time, achievable parameters of such powertrain systems did not allow them to compete with internal combustion engines. Currently, with the development of electric motors with high power density, this concept is being developed again [15-22]. Motors of this type can be widely used in the electric vehicle industry for various applications: from small city cars, through vans, buses to demanding commercial vehicles. It should be noted that electric drives installed in wheel hubs can also serve other types of drive support, including diesel, e.g. when starting, when the highest torque values are required from the drive or during maneuvers, increasing the driving dynamics. Taking into account the numerous inquiries from entrepreneurs and the results of observation of the electric vehicle market, it can be noted that the direct drive concept is not limited only to applications in typical road vehicles. The advantages of this type of solution also qualify them for use in many other applications, such as: industrial transport vehicles, service vehicles used in large factories, warehouses, mines or airports, recreational vehicles such as golf carts, quads, ground drones, military vehicles, off-road, police or fire services that require high torque. The Łukasiewicz Research Network - Institute of Electric Drives and Machines KOMEL has undertaken research and design work aimed at developing technical and technological solutions, which resulted in the development of a prototype of the motor for installation in the wheels of the vehicle. These works were carried out under the LIDER VII program financed by the National Center for Research and Development. Currently, under the LIDER XI program, this subject will be further developed, it is planned to develop an electric drive integrated with a mechanical transmission and a brake for commercial vehicles with high torque requirements.

2 Advantages and disadvantages of direct drives in electric vehicles

Most of the drive systems of internal combustion vehicles that can be found on the market today have been constructed on the basis of the same concept for approx. 100 years. The torque from the engine is transferred to the wheels via the clutch, gear ratios, differential and driveshafts. A similar structure is found in most electric and hybrid vehicles proposed on the market or presented in various review materials. The presented drive systems replace the "central" internal combustion engine with an electric motor [8], and in these solutions the clutch is often omitted, because in the case of an electric motor, it is not needed. With the development of technology and technologies related to drives and the electric motors themselves, manufacturers are able to achieve better and better operating parameters of drives while maintaining their high energy efficiency [3, 4, 12-14]. One of the main directions of the development of drives is to obtain the highest ratio of torque (maximum and possible to achieve in long-term operation) to volume / mass (the so-called power / torque density ratio). This trend fits very well with the direct drive concept, which offers a number of advantages, including:

- elimination of the multi-ratio mechanical transmission, which in addition to reducing the efficiency of the system is an element that requires maintenance and may be damaged,
- providing additional space in the car, which can be used to install power batteries or increase its ground clearance,
- no need for indirect power transmission through drive shafts, differentials and other complex mechanisms,
- the possibility of a relatively simple implementation of a drive for 2, 4 or more wheels,
- more effective recuperative braking (omitting the decrease in the efficiency of the drive system due to the gear ratios),
- relatively easy disassembly of the drive during service,
- better steering of the vehicle due to the possibility of direct torque setting separately on each of the wheels.

In addition to a number of the advantages mentioned, this solution also has some disadvantages and limitations:

- limited space in which the motor must fit,
- impeded motor cooling,
- additional unsprung mass resulting from the mass of the motors installed in the wheels, [16-20]
- structure in some applications more complicated in terms of sealing / maintaining high IP,
- the necessity to cooperate with the braking system.

During the implementation of many e-mobility projects in the Łukasiewicz - KOMEL institute, a lot of inquiries were made about the possibility of developing an electric direct drive for heavy commercial vehicles, requiring off-road or agricultural vehicles, which would have even greater torque, a structure resistant to harsh operating conditions and additionally integrated with the brake. On the basis of the knowledge acquired during the implementation of the e-mobility project and the analysis of various electric vehicle powertrains structures, in order to meet the above-mentioned expectations, it is necessary to develop a drive integrated with a mechanical transmission, which will fit in the wheel of a commercial vehicle.

3 Assumptions of the drive structure

During the implementation of the electric powertrain project for commercial vehicles, co-financed by the National Center for Research and Development under the LIDER XI program, it was planned to develop an innovative drive for installation in the wheel, characterized by a compact structure, integrated electromagnetic circuit, brake system and transmission, with the possibility of mounting in a wheel with a diameter of 17", and a maximum torque of 2000Nm (ultimately over 3000Nm). The developed drive will also be characterized by innovative design solutions, such as an efficient cooling system, low weight, the possibility of two operating modes ("low" utility and "high" normal). A drive with such functionalities is currently not available on the market. Functionally similar competitive solutions that can be found offer only some of the functions mentioned. They (which are usually not protected against external factors), moreover, they do not offer such maximum moments. The offered solutions of the gears for installation in the wheel for commercial vehicles do not have the possibility of switching the operating modes (only the possibility of disconnecting the drive) and after connecting to the motor they are much larger in size, and they do not have a brake. Summarizing, the final effect of the project will be a developed, manufactured and tested prototype of a drive system for wheel assembly with the following features:

- design that allows installation in a 17" rim with a maximum torque of 2000Nm (ultimately over 3000Nm), consisting of a gear and motor part, and a brake built inside, integrated into one functional unit,
- possibility of obtaining two modes of operation of the drive system: the so-called utility mode. "low" (obtained maximum torque at the level of 2000Nm), and the so-called "high" mode (ratio 1: 1 between the

drive output and the electric motor part, the faster travel of the commercial vehicle at a speed of at least 80kmh),
- optimized structure in terms of strength, stiffness, dimensions and technology.

Figures 1 present the analyzed different solutions of the planetary gear located in the wheel hub

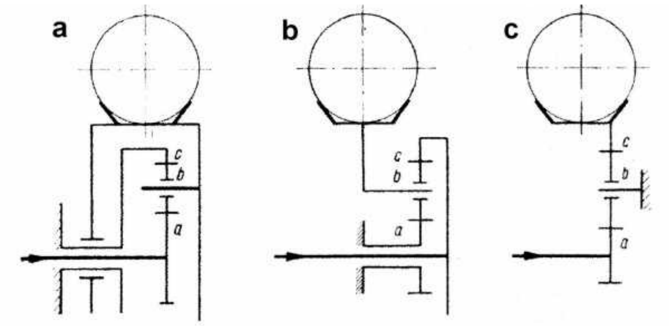

Fig. 1 Different solutions of the planetary gear located in the wheel hub

At the current stage of the project, preliminary design calculations of the transmission part and the electromagnetic circuit of the drive were carried out. The MitCalc software was used to calculate the transmission, while the Ansoft Motor-CAD program was used to calculate the electromagnetic circuit, which allows for the implementation of simulations of operation based on coupled models of the electromagnetic circuit, using FEM 2D and a thermal model based on thermal diagrams. Taking into account the conditions of the drive installation in a 17 "rim and the limitations of the drive width, it was decided to use a solution based on a planetary gear in the drive. The 3D Model of developed powertrain is presented on the figure 2.

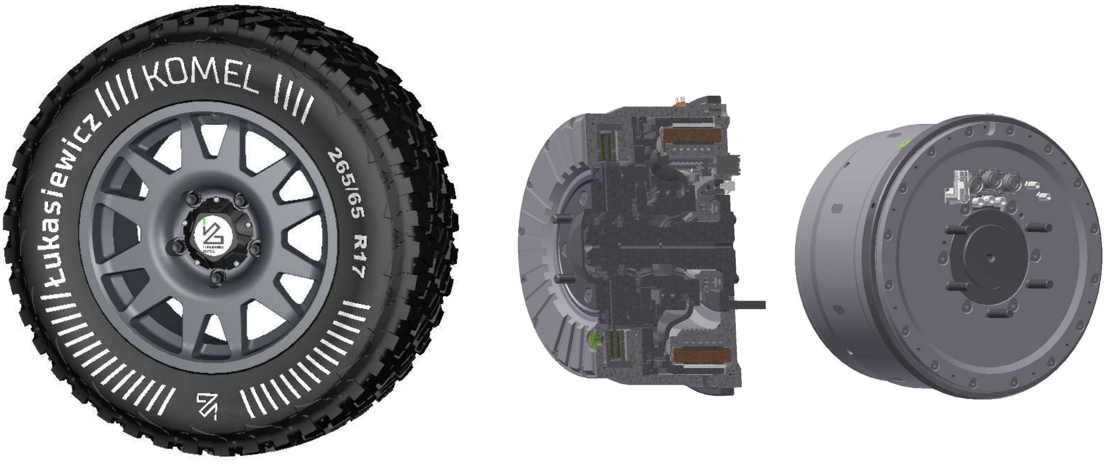

Fig. 2 3D model prototype drive

Various solutions of the epicyclic gear located in the wheel hub were analyzed, based on various kinematic schemes presented in Figure 1. Each of the presented solutions obtains a different kinematic ratio. In the solution based on the kinematic diagram 1a, the yoke of the planetary gear is rigidly connected to the road wheel hub, so it transmits the torque to it. The ring wheel is fixedly connected to the housing. The torque to the gearbox is introduced by the sun gear. In this solution, the gear ratio i> 3 can be obtained. In the solution based on the kinematic diagram 1b, the gear yoke is rigidly connected to the wheel hub and transmits the torque to it. The torque for the gearbox is supplied to the ring gear. The sun gear is fixedly connected to the housing. This solution allows for moderate gear ratios i = 1.0 - 2.0. In the solution based on the kinematic diagram 1c, the gear yoke is rigidly connected to the housing, and the driving sun gear drives the ring gear associated with the road wheel hub by rotating the satellites. We are dealing here with a change in the direction of the rotational speed, and the size of the ratios obtained is approximately i = 2.5 - 2.8. Due to the possibility of obtaining high gear ratios and integration with the electromagnetic circuit, the solution 4a was used in the drive structure. Preliminary analyzes allowed to estimate that in the given dimensions it is possible to obtain even a gear ratio i = 3-3.5. Then, the analysis of an electromagnetic circuit possible to be made in the assumed dimensions was started. A motor with 48 magnetic poles and 54 slots was adopted for the calculations, this assumption results from the rotor angle sensors available on the market and possible to use in the analyzed structure and the inverters that support them. Initially, as a solution for the motor winding, concentrated coils were adopted, which guarantees a shorter structure of the fronts, lower winding losses and better winding cooling possibilities. Table 1 shows the motor/drive power supply parameters. Design calculations were carried out in the Ansoft Motor-CAD program. It uses a combination of advance analytical equations and calculations based on 2D FEM. The temperature can be determined in steady and transient conditions. The program uses advanced models in the form of thermal networks.

Table 1 Input data and calculation results for the square configuration with filling of the slot with the impregnating varnish

Parameter	value	unit
Number of slots Q	54	-
Number of poles 2p	48	-
Number of slots per pole and phase q	0,375	-
Drive supply voltage V_{DC}	375	V
Maximum current $I_{max.}$	400	A

The supply voltage result from the adopted voltage of the battery supplying the vehicle drive. The currents supplying the motor (rated and maximum) result from the operation of the parameters of the intended inverter. Figure 3 shows a longitudinal section of the motor model. Figure 4 shows the model of the electromagnetic core with the calculated saturation distribution of the magnetic induction from permanent magnets using the FEM 2D method.

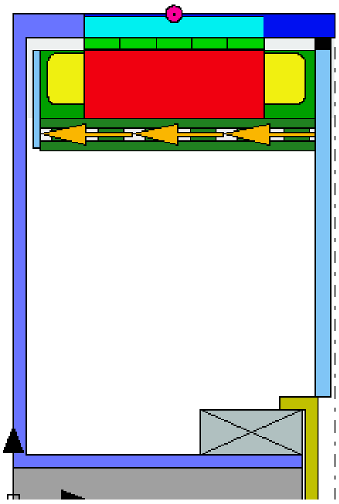

Fig. 3 Model of the motor section in the Ansoft Motor-CAD program - longitudinal section

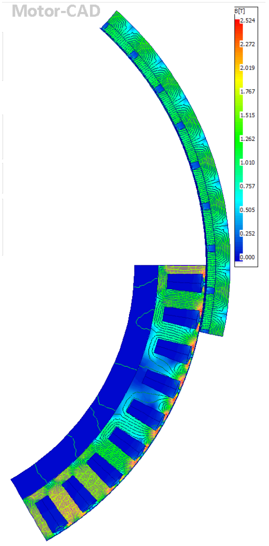

Fig. 4 Calculated magnetic induction distribution from permanent magnets in the magnetic core of the motor

The performed calculations are based on the coupling of the electromagnetic circuit model with the thermal model. The calculations were based on water cooling with flow Q=10l/min, ambient temperature t_{ot}=45°C, coolant temperature (EGW 50/50) t_{ch} = 60°C. Figure 5 presents the results of thermal calculations for the motor operating point: T_m = 450Nm and n = 800 rpm, I_{RMS} = 123A (approx. 13 A/ mm^2). The operating point has been selected so that the winding temperature at the warmest point does not exceed the value of t_{Cu} = 150°C. Under these cooling conditions, this operating point can be designated as the rated operating point for the motor.

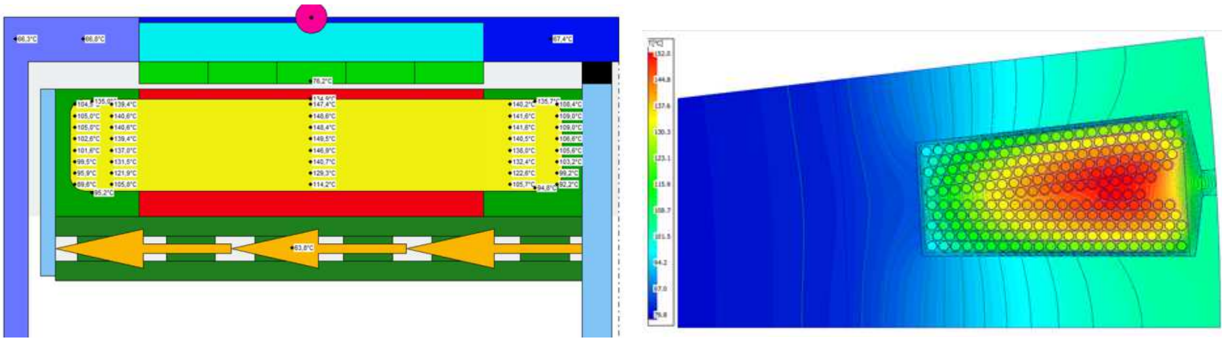

Fig. 5 Calculated motor temperatures for work at the base point Tm = 450Nm, n = 800 rpm at slot cross-section and in the slot in the FEM models of the Motor CAD program

The thermal calculations were verified with the module embedded in the Motor-CAD program, using the finite element method. The method allows to calibrate the schematic model with the FEM model. Table 2 shows the maximum temperatures that have been calculated in the individual elements of the electric motor.

Table 2 Calculated maximum temperatures established for the motor operating point Tm = 450Nm n = 800 rpm

Element of the motor	Thermal diagram
Winding endD	140,6
Winding end ND	141,6
Winding in a slot	149,5
Stator tooth	104,6
Stator side radiatorD	77,4
Stator side radiatorND	80
Magnets	75,8
Air	45
Coolant EGW 50/50	60

The results presented in Figure 5 and in Table 2 refer to the steady state, assuming the S1 work regime. These are illustrative results, because in fact, the electric motor in the drive of the car works with dynamically changing operating parameters. Figure 6 shows the torque characteristics as a function of rotational speed.

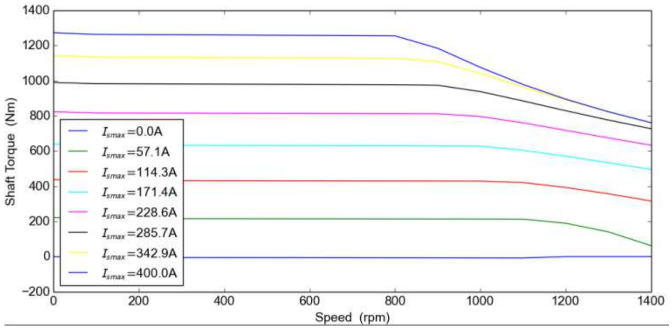

Fig.6. Torque characteristics as a function of rotational speed for supply of various currents

The torque increases with the current intensity, the motor operates in two control zones, in the zone with constant torque and in the zone with weakening of the magnetic flux from permanent magnets. The maximum torque that the motor will achieve with the permissible maximum current of the inverter is T_{max}=1200Nm. Maximum torque is available over a wide speed range from 0 to 600rpm. Fig. 7 shows analogous characteristics of mechanical power as a function of rotational speed.

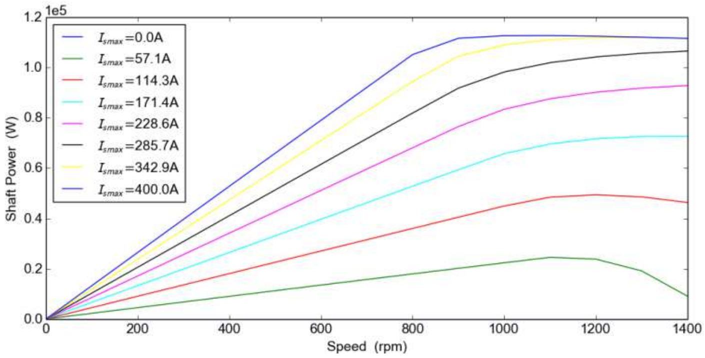

Fig. 7 Characteristics of mechanical power as a function of rotational speed for supply with different currents

The characteristics of the losses in the magnetic core of the stator show the deflection of the characteristics, which is characteristic for the zone with magnetic field weakening.

Figures 8 and the calculated operating temperatures, assuming that the maximum temperature of the winding will not exceed $T_{Cu} \leq 150°C$. Figure 9 shows the calculated map of the efficiency for this work area.

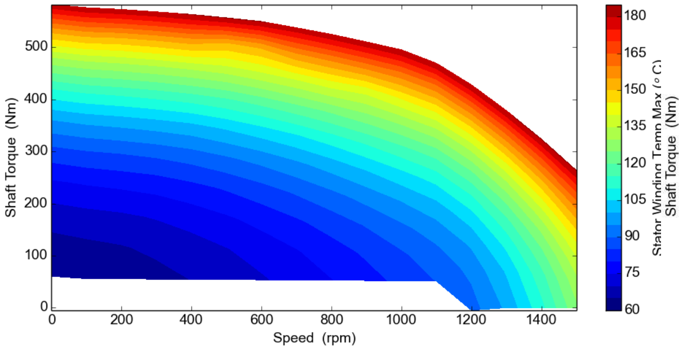

Fig. 8 Calculated maximum temperatures in the motor winding for the operating area with temperature limitation: $T_{Cu} \leq 150°C$, $T_{mag} \leq 100°C$

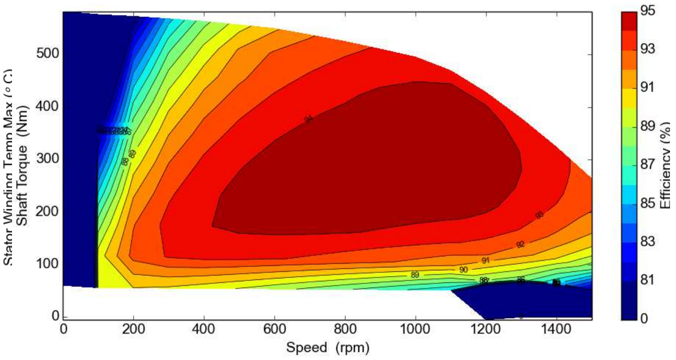

Fig. 9 Calculated efficiency map for the working area with temperature limitation: $T_{Cu} \leq 150°C$, $T_{mag} \leq 100°C$

4 Conclusion

The drive for installation in the wheels of commercial vehicles with increased demand for torque, due to the place of application, should be characterized by:

- relatively high ratio of torque (rated and maximum) to weight,
- high energy efficiency, having a direct impact on the range and working time of the vehicle,
- structure ensuring adequate tightness and strength,
- appropriate dynamics of work, high maximum torque, ensuring proper driving parameters of the vehicle,
- built-in brake system, resistant to difficult working conditions.

The calculations presented in the article allowed to simulate the operation of an electric motor with a built-in planetary gear in any commercial vehicle consisting of two or four drive motors.

Presented simulations allow to predict of the maximum operating temperatures of the sensitive points of the motor like winding or magnets.

All the features of the discussed drive and the limitation of the given volume intended for the drive assembly require the design team to look for compromise solutions. The design concept should include design and research activities covering the following issues:

- Design of the electromagnetic circuit,
- Selection and design of the gear construction solution,
- Selection and design of the brake,
- Technological tests,
- Thermal and strength calculations.

The presented results obtained on the basis of the developed models and calculations confirm the correctness of the adopted design concept.

The next stage of work in the project will be a series of technological tests in terms of the feasibility of individual elements of the drive structure. Multivariate work simulations will also be carried out for various designs of the cooling system, and then the possible operating parameters of the drive will be determined for them.

Acknowledgements

The work was created as part of the project " Innovative electric drive unit for commercial vehicles", financed by the National Center for Research and Development under the LIDER XI program, in accordance with the agreement no. LIDER/15/0060/L-11/19/NCBR/2020.

References

[1] Global EV Outlook 2016 Beyond one million electric cars IEA(International Energy Agency), May 2016

[2] Mobility Model, April 2016 version (database and simulation model), www.iea.org/etp/etpmodel/transport

[3] E. Król: Silniki Elektryczne w Napędach Pojazdów Sportowo-Rekreacyjnych, Zeszyty Problemowe – Maszyny Elektryczne Nr 2/2014 (102)

[4] E. Król, R. Rossa: Silnik synchroniczny z magnesami trwałymi jako napęd pojazdu hybrydowego. Zeszyty Problemowe -Maszyny Elektryczne, nr 4/2012 (97)

[5] W. Radwański, B. Będkowski, A. Białas, R. Rossa; Koncepcja napędu elektrycznego „E-Kit" dla miejskich samochodów osobowych. Zeszyty Problemowe -Maszyny Elektryczne, nr 4/2012 (97)

[6] www.komel.katowice.pl/elektromobilnosc.html

[7] https://solarisbus.com

[8] J. Bernatt, S. Gawron, E. Król: Zastosowania trakcyjne nowoczesnych silników z magnesami trwałymi., Przegląd Elektrotechniczny" 12/2009

[9] J. Thorton: Circular Precision Electric& Hybrid Vehicle Technology International, lipiec 2013

[10] E. Król: Hamowanie odzyskowe, jako efektywny sposób zwiększenia zasięgu pojazdu hybrydowego. Śląskie Wiadomości Elektryczne 2013

[11] http://www.electricvehiclenews.com/2014/08/the-global-market-for-ev-traction.html

[12] Dukalski, P.; Krok, R. Selected Aspects of Decreasing Weight of Motor Dedicated to Wheel Hub Assembly by Increasing Number of Magnetic Poles. Energies 2021, 14(4), 917.

[13] J. Bernatt: Obwody elektryczne i magnetyczne maszyn elektrycznych wzbudzanych magnesami trwałymi, ISBN 978-83-910585-9-6

[14] R. Rossa, E. Król: Dwustrefowa regulacja prędkości obrotowej w nowoczesnych napędach elektrycznych opartych na silnikach synchronicznych z magnesami trwałymi, Zeszyty Problemowe – Maszyny Elektryczne, nr 81/2009, str. 125-129

[15] A. Fraser: In-Wheel Electric Motors. The Packaging and Integration Challenges. http://www.proteanelectric.com

[16] G. Ślaski, A. Gudra, A. Borowicz: Analysis of the influence of additional unsprung mass of in-wheel motors on the comfort and safety of a passenger car. Arch. Autom. Eng. Arch. Motoryz. 2014, 65, 51–64

[17] K. Parczewski, R. Romaniszyn, H. Wnęk: Influence of electric motors assembly in hubs of vehicle wheels on the dynamics of movement, especially on surfaces with different adhesion coefficient. Combust. Eng. 2019, doi:10.19206/CE-2019-XXX

[18] P. Dukalski, B. Będkowski, K. Par-czewski, H. Wnęk, A. Urbaś, K. Au-gustynek: Analysis of the influence of assembly electric motors in wheels on behaviour of vehicle rear suspension system. Mater. Sci. Eng. 2018, 421, doi:10.1088/1757-899X/421/2/0220

[19] P. Dukalski, B. Będkowski, K. Parczewski, H. Wnęk, A. Urbaś, K. Au-gustynek: Dynamics of the vehicle rear suspension system with electric motors mounted in wheels. Maint. Reliab. 2019, 21, 125–136, doi:10.17531/ein.2019.1.14.

[20] M. Frajnkovic, S. Omerovic, U. Rozic, J. Kern, R. Connes, M. Biček: Structural Integrity of In-Wheel Motors. SAE Tech. Paper 2018

[21] M. Biček, R. Connes, S. Omerović, A. Gündüz, R. Kunc, S. Zupan: The Bearing Stiffness Effect on In-Wheel Motors. Sustainability 2020, 12

[22] K. Parczewski, H. Wnek: Comparison of overcoming inequalities of the road by a vehicle with a conventional drive system and electric motors placed in the wheels. In Proceedings of the Conference Transport Means 2020, Palanga, Lithuania, 2 October 2020

Increase of Energy Efficiency in Pump Electric Drive

Mihail Digalovski and Goga Cvetkovski

Ss. Cyril & Methodius University, Faculty of Electrical Engineering & Information Technologies,
RugjerBošković 18,P.O.Box 574, 1000 Skopje, North Macedonia
E-mail: mihaild@feit.ukim.edu.mk, gogacvet@feit.ukim.edu.mk

Abstract*–Typical low efficiency drives are pumps, fans and blowers that have a centrifugal torque characteristic $T=f(n^2)$. In these electric drives there is great technical and economic potential for significant energy savings. Pumps are the most numerous working machines, therefore the electric drives with pump will be considered in this paper. First a brief introduction to pump systems will be given and then the ways in which the operating point of the pump can be regulated will be also presented. For the purpose of this investigation, a program was developed in the MATLAB software package for the calculation of energy savings and with its helpa comparison between conventional ways of regulating the operating point of the pump and regulation of the operating point through variable electric drive speed was realized. Using this program, the electricity consumption of low, medium and high power pumps driven by induction motors that have the ability to regulate the rotation speed through an inverter with U/f regulation will be analyzed.

1 Introduction

The industry is a large consumer of electricity which in 2014 participated with approximately 42.5% in the total electricity consumption in the world.As much as 65% -70% of the total electricity consumption in industry is accounted for by electric drives [1].Due to their wide application, electric drives as a major consumer of electricity are becoming quite attractive for finding ways to improve their energy efficiency and its implementation.

This paper highlights the importance of energy efficiency in electric drives and what it represents in general. In electric drives, there are two possible ways to increase energy efficiency.One of them is the application of high efficient induction motors [2]. The second way that is considered and contributes to the improvement of energy efficiency at electric drives involves the application of power converters. For this purpose, scalar U/f regulation is explained as one of the ways to regulate it. Then an example is presented for improving the energy efficiency of the electric drives with pumps in which the regulation of the operating point is needed. In addition a brief introduction to pumping systems and their characteristics is given. Furthermore, a program has been developed in the MATLAB software package that calculates energy savings in operating point regulation by applying inverters with U/f regulation compared to operating point regulation with mechanical control. With the help of the program, an analysis was made of seventeen types of centrifugal pumps with low, medium and high power driven by induction motors. At the end, the results are presented, conclusions are drawn and the benefits of the implementation of energy converters are listed.

2 Pump system

At the beginning of this work a brief presentation of a pump system is going be presented. A pump is an energy machine or device in which energy is exchanged between the working fluid flowing through the pump and the moving parts of the pump, thereby increasing the mechanical energy of the fluid flowing from the inlet to the outlet of the pump.Pump height or pump effortH_T(m), is a measure of the pressure required to transport liquid from one tank (sucked) to another tank (suppressed) at a given flow.There is a difference between static effort and dynamic effort.Static effort H_S(m) is a measure of the pressure required to transport fluid from one tank to another in order to perform useful work.

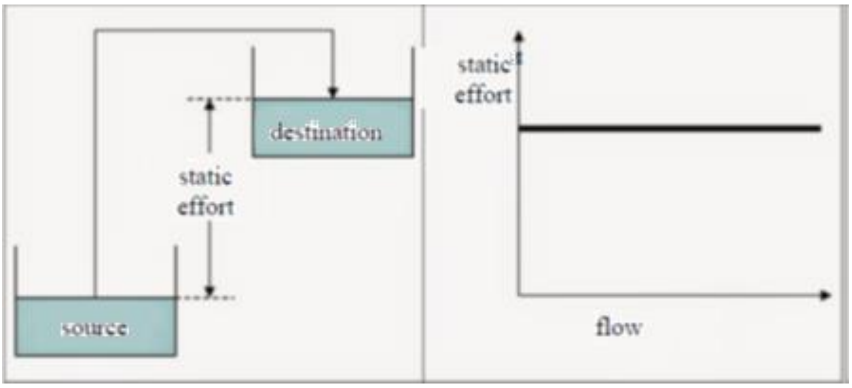

Fig.1 Static effort and its dependence on flow

Friction effort or dynamic effortH_d(m), is a measure of the components resistance that make up the system, of the energy losses that occur and is a result of the size and diameter of the pipes, the materials from which they are madeetc. and in the first approximation is proportional to the square of the flow.

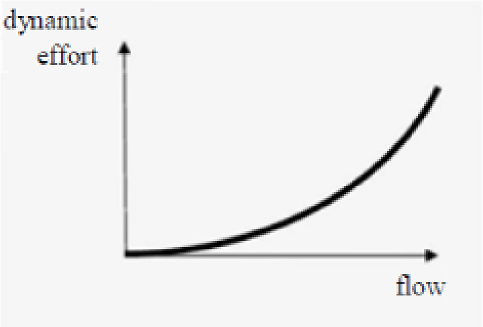

Fig.2 Dynamic effort and its dependence on flow

The sum of the static and the dynamic effort is the total effort that the pump must achieve to transfer the fluid to the required level (total head of the pump).

$$H_T=H_s+H_d \tag{1}$$

When the static effort and the dynamic effort are taken into account, is obtained the plant characteristic or the system characteristic.Two of these are shown in Fig. 3. a) and 3. b).

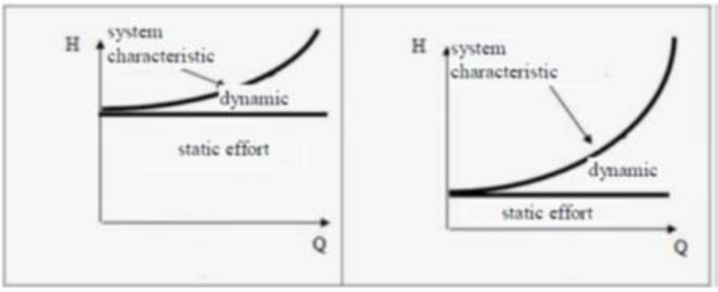

a) b)

Fig. 3 System characteristic at a) high static and low dynamic effort b) low static and high dynamic effort

The system characteristic is the one that is significant for the possibility of saving electricity and improving the efficiency of the system.If the static effort is relatively large compared to the dynamic one as in the case of Fig. 3a then there are smaller possibilities for energy savings.If this is not the case as shown in Fig. 3b then there is a greater potential for energy savings.

There are two types of pump systems: open and closed. Closed pump systems are circulating systems such as heating and cooling systems such as condensate cooling systems in an industry where the pump has to overcome only losses in the elements that make up the system such as friction through pipes, valves and other equipment. In other words, the pump spends all its effort on overcoming the hydraulic resistances in the piping system. Fig.4 gives an example of a closed pump system, followed by Fig.5 for the corresponding system characteristic.

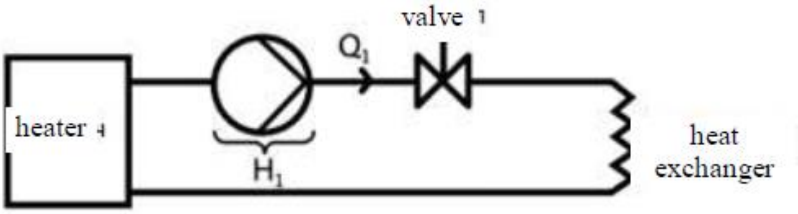

Fig. 4 Schematic representation of a closed pump system [3]

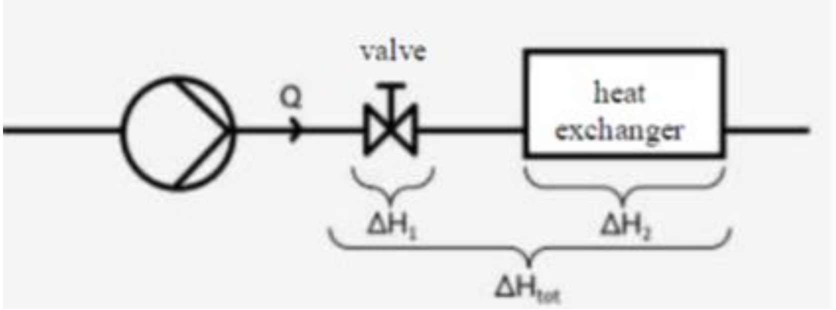

Fig. 5 Resistance of system components and losses [3]

The total hydraulic losses in the system are represented by $\Delta H_{tot} = \Delta H_1 + \Delta H_2$.By adding resistance in series increases the hydraulic losses and thus increases the effort that the pump ΔH_{tot} has to overcome (m).

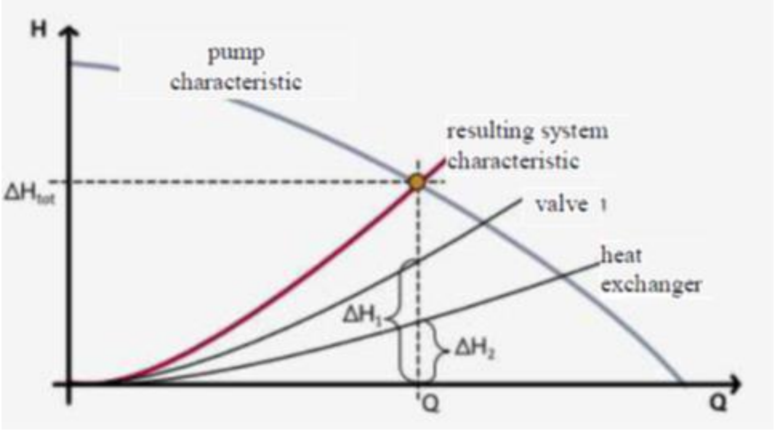

Fig. 6 Reduction of flow-Q by increasing resistance in a closed pump system [3]

As shown in Fig. 6 the effort to be overcome by the pump increases, the resulting system characteristic becomes steeper and at the intersection of the system characteristic and the pump characteristic is the new operating point of the pump with higher H and lower Q.

In open systems, the role of the pump is to generate sufficient pressure or sufficient effort H (m) to overcome the static and dynamic effort of the system (losses in pipelines and other components) to transfer the fluid to the appropriate level.

An example of an open system can be the water supply system, when the water is drained from a river and it is stored in one tank and then transferred to the required locations to be distributed. Open systems also include irrigation systems, etc. Fig.7 shows a schematic representation of an open system and Fig. 8 shows the corresponding system characteristic.

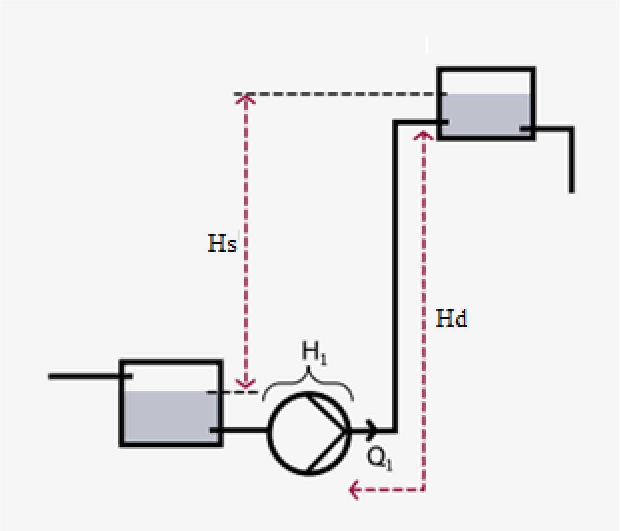

Fig. 7 Schematic representation of an open pump system [3]

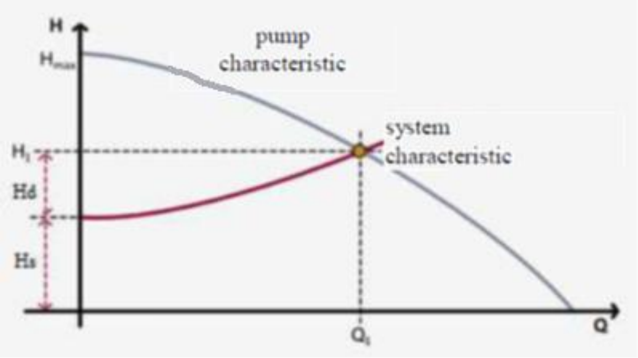

Fig. 8 System characteristic of an open pump system [3]

If the system characteristics of open and closed systems are compared, a difference will be noticed in the starting point of the parabola. In closed systems it starts from the coordinate origin, and in open systems from the value of static effort. This is because as it was previously stated in closed systems it is necessary to overcome only the hydraulic losses in the system and in open systems to those losses is added the static effort that needs to be overcome.

The characteristic of the pump is the interdependence of H and Q also known as the effort characteristic $H = f(Q)$, it is different for each pump and is given in a catalog by each manufacturer. The intersection of the system characteristic and the characteristic of the pump determines the operating point of the pump, Fig. 8.

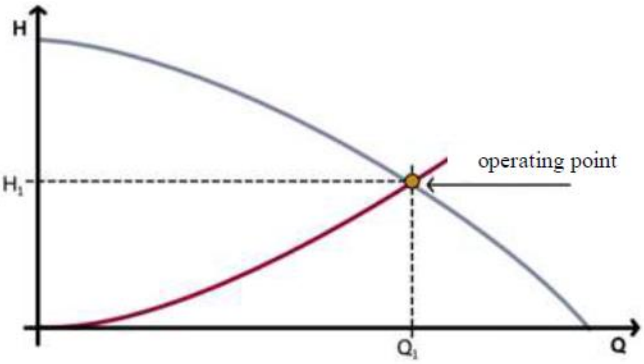

Fig. 9 Pump operating point (Q_1, H_1), intersection of system characteristic with pump characteristic

Regardless of the type of pump, the plant and the pump are two coupled parts of one system, and each of them has its own characteristic as stated above in the text. The operating point defines such operating regime of the pump in which the required effort is equal to the effort generated by the pump. The partial operating characteristics of the pump, given in the catalog by each manufacturer, provide information on the pump operating properties under variable operating conditions. The effort characteristic of the pump, as well as the characteristic of the plant can't separately provide information in which operating regime the pump will operate. In order to obtain information in which operating regime the pump will operate, it is necessary to make a joint analysis of the pumping plant characteristic with the effort characteristic of the pump.

Pump manufacturers also include several other important characteristics of the pump: the dependence of the pump efficiency on the flow, the dependence of the power on the flow and others.These characteristicsare shown in Fig.10 and 11.

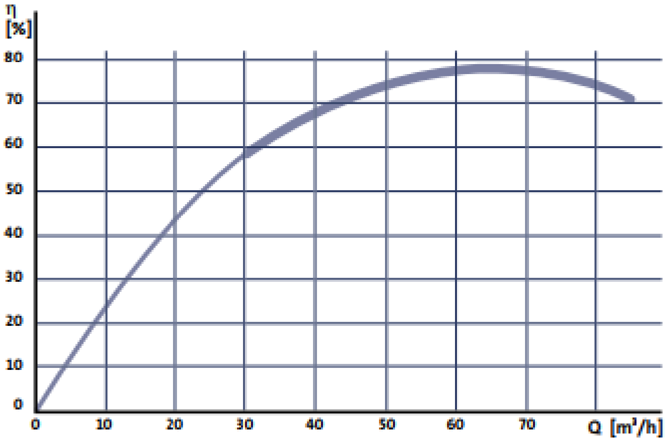

Fig. 10 Efficiency characteristic of a typical centrifugal pump [3]

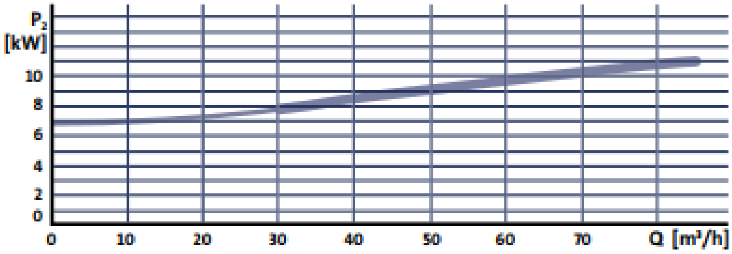

Fig. 11 Power characteristic of a typical centrifugal pump [3]

3 Changing of pump operating point

Pump regulation means intentional change of pump parameters such as flow and pressure.This can be done in two ways: by changing the pump characteristics or by changing the plant characteristics.

The operating point of the pump, flow and pressure, as needed, can be changed in one of the following ways: mechanically by applying regulating valves, by changing the blades angle of the impeller, bypass control or regulation with bypass line, useof multiple pumping system, speed regulation etc.

By installing regulating valves, usually just behind the pump, it is possible to change the hydraulic losses in the piping to be overcome by controlling its openness. Namely, by opening the regulating valve, the losses are reduced, and by closing the valve, i.e. by closing it, they increase, thus changing the resistance coefficient of the pipeline and thus changing the position of the operating point of the pump along the curve $H = f(Q)$. This method of regulation is the cheapest and simplest to apply. Fig. 12 shows how the system characteristic changes at different valve openings. Characteristic R4 shows the largest valve opening and characteristic R1 the smallest opening.

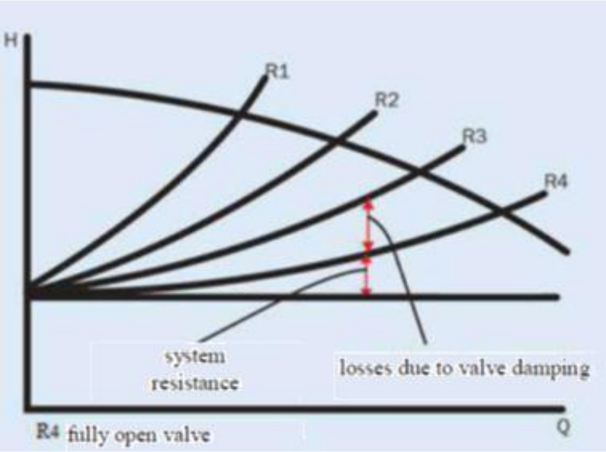

Fig. 12 Change the operating point by closing the valve in a several position

The pump is usually driven by an electric motor, more recently by an induction motor, and since one of the ways to regulate the flow of the pump is by changing the rotation speed it follows that the regulation of the flow of the pump can be donebymotor speed control.For pump systems, it is sufficient for the motor speed regulation to be scalar by applying a voltage and frequency – *U/f* converter.

For variable speed pumps, instead of the standard *H = f (Q)* characteristic, the operating range corresponds to a set of characteristics corresponding to different rotational speeds of the electric motor.One such characteristic is shown in Fig.13.

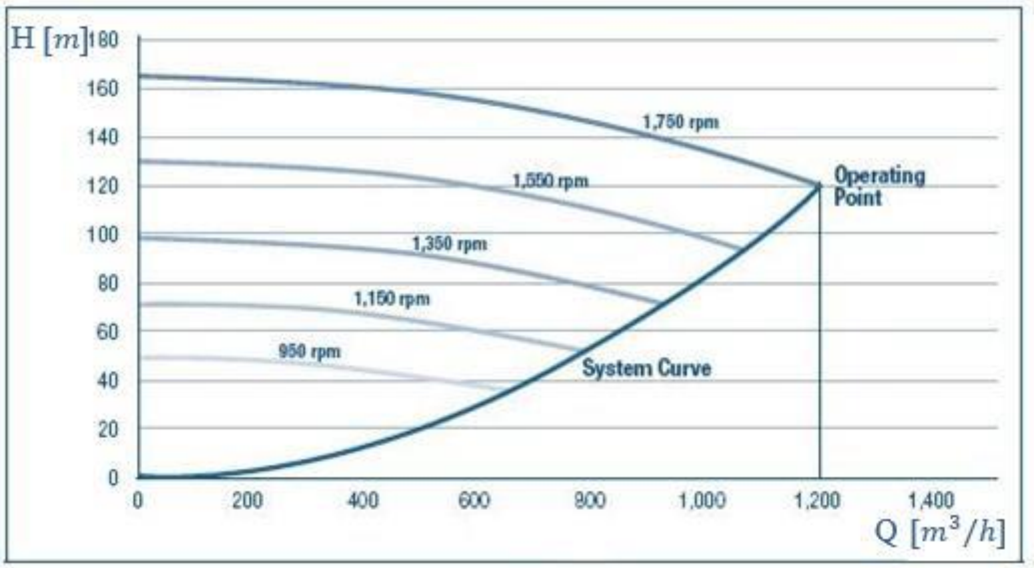

Fig. 13 Q-H characteristics at different speeds

4 Regulation of water flow in the pump system

Fig. 14 shows a diagram for the regulation of water flow through a pump in two ways.The aim is to change the water flow from Q_1 to Q_2.The first is the conventional way, with mechanical control, i.e. with the use of a control valve where the motor speed does not change.The second way is by regulating the motor speed by using an inverter.

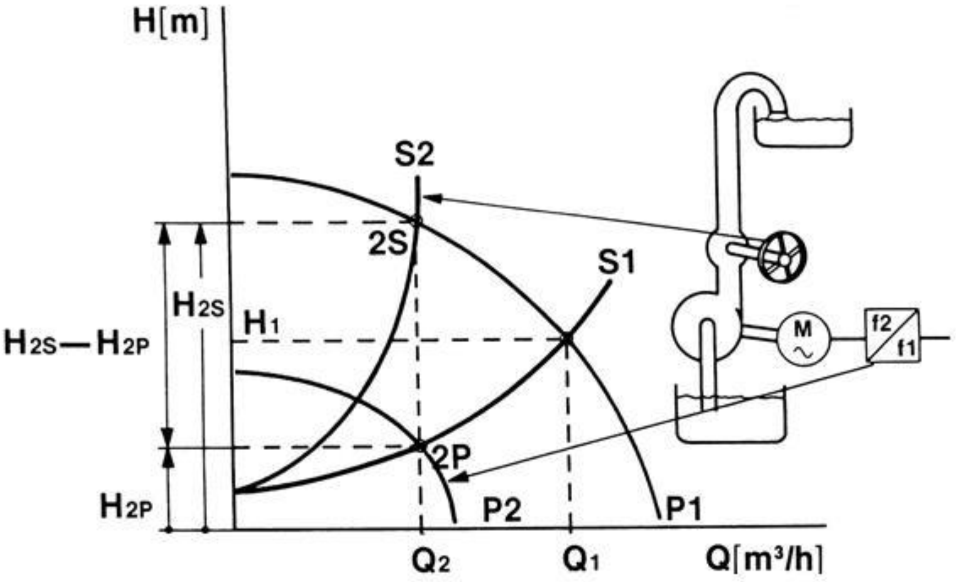

Fig. 14Centrifugal pump diagram with flow regulation

P_1– pump characteristic at rated speed n_1(min^{-1})
P_2– pump characteristic at reduced speed n_2(min^{-1})
S_1– system characteristic
S_2– system characteristic
Q_1, Q_2– pump flow (m^3/h)
H_{2S}– pump effort expressed in (m) at flow Q_2 during valve control
H_{2P} – pump effort expressed in (m)at flow Q_2 during motor speed control

In the text that follows a brief presentation of the two types of flow regulations is presented.

- **Valve control**

To reduce the flow from Q_1 to Q_2 it is necessary to close properly the regulating valve. The operating point of the pump is moved along the characteristic $H=f(Q)$ marked in Fig.14 as P_1, and passes from the system characteristic S_1 to the system characteristic S_2. The system characteristic changes from S_1 to S_2 because resistance is added to the system (damping) i.e. the hydraulic losses increase. Increasing the hydraulic losses by closing the valve, increases the effort that the pump has to make to overcome those losses during flow Q_2. In fact, damping changes the coefficient of resistance of the pipeline and thus changes the position of the operating point of the pump along the curve $P_1=H=f(Q)$. The pump effort increases from H_1 to H_{2S}.

- **Motor speed control**

To reduce the flow from Q_1 to Q_2, the operating point of the pump is shifted from characteristic P_1 with a rotational speed n_1 of the P_2 curve with a reduced motor speed n_2.By reducing the motor speed at flow Q_2, the effort required for the pump to overcome system losses and the required pressure is reduced from H_1 to H_{2P}.

The equations for the calculation of the required mechanical power of the pump generated on the shaft in both regimes of regulation is presented in the text below.

The required pump power for valve control(P_v) can be calculated using the following equation:

$$P_v = \frac{\mathrm{Q_m}[m^3/h] \times \mathrm{H_{2S}}[m] \times \rho[kg/dm^3] \times g[m/s^2]}{3600 \times \eta_1} \quad [kW] \tag{2}$$

Where the required pump power for motor speed control(P_e) can be determined using equation (3).

$$P_e = \frac{\mathrm{Q_m}[m^3/h] \times \mathrm{H_{2P}}[m] \times \rho[kg/dm^3] \times g[m/s^2]}{3600 \times \eta_2} \quad [kW] \tag{3}$$

The equations for the required input electrical power for both regimes of regulation is presented with the following equations.

The required input electrical power for valve control (P_{1m}), can be determined with equation (4), where the required input electrical power for motor speed control (P_{2m})can be determined with equation (5).

$$P_{1m} = \frac{P_v}{\eta_m} \quad [kW] \tag{4}$$

$$P_{2m} = \frac{P_e}{\eta_m \times \eta_{vfd}} \quad [kW] \tag{5}$$

The energy saving (E_s) if the valve control system is replaced with a power converter control can be determined using equation (5):

$$E_s=(P_{1m}-P_{2m}) \text{ x } t_a\text{(kWh/year)} \tag{6}$$

This energy converted into saved money per year (K_s) can be determined using equation (7):

$$K_s\text{(saving many per year) =}E_s \text{ (kWh/year) x k (price/kWh)} \tag{7}$$

where:

$\rho(\mathrm{kg/dm^3})$– liquid density
$g(\mathrm{m/s^2})$–ground acceleration
η_1– pump efficiency at operating point 2S, Fig.1
η_2– pump efficiency at operating point 2P, Fig.1
η_m–motor efficiency
η_{vfd}– efficiency of the inverter
t_a– number of working hours per year

5 Computer Program for calculation of energy efficiency and electricity savings

Significant energy savings can only be achieved if a wider range of control is required. If the process does not require any regulation and is constant and not dynamic, then there can be no question of saving energy by changing the working point. However, a small percentage of processes do not need regulation. In many activities related to human life such as water supply systems, heating, air conditioning, condensate cooling in industrial processes, etc. due to different activities and needs during different parts of the day, different seasons, different processes, etc. regulated processes are necessary.

To calculate the energy savings if the pump flow is regulated by changing the motor speed by means of a *U/f* converter compared to the use of regulating valves, a short computer program has been developed in MATLAB software package.

- **Program description**

The aim of the program is to enable a comparison of the two regimes of flow regulation at an arbitrarily selected pump and to give an overview of the saved electricity if the flow is regulated by changing the rotation speed compared to the conventional mode of regulation using regulating valves.The program works for any pumpentry data.

At the beginning, a function has been defined in order the user to be able to select whether the input data needed for the program should be entered from the keyboard, read from an Excel document or the user wants to close the program. In addition, a function for entering data from the keyboard is made and it is called if the user selects that option. Input variables are the flow with which the pump should operate, the pump effort corresponding to the inlet flow during valve control and the effort at the appropriate speed change, the efficiency of the pump in both regimes of regulation, motor efficiency, number of working hours per year and electricity price per kWh. It works with global variables which are then called and written to. The function for reading the above mentioned input parameters from an Excel file is made in a similar way.

The energy saving function is then activated and it invokes the previously entered variables as input data from the keyboard and reading from an Excel file. The energy saving calculation function calculates: the required power of the pump when regulating the flow with a regulating valve and when regulating the flow by changing the rotation speed, the required electric power in both modes of regulation, the consumed electricity annually the same for both regimes.It then compares them and gives how much power has been reduced in percentages if the flow is regulated by changing the rotational speed, not mechanically.Finally, it shows the annual energy savings in kWh and money saving for the predefined price.The equations used in the program are given in the text earlier.

6 Results

In order to evaluate the efficiency of the two solutions that can regulate the water flow through the pump, it is necessary to make an analysis for a specific pump.For this purpose, a comparison and analysis of the two regulation modes on 17 types of centrifugal single-stage pumps was made, selected from the catalogue of the pump manufacturer Grundfos [4].The pumps are from the same family and are powered by high efficient induction motors with low, medium and high power.The power range of the motors that will be considered is from 1.5kW to 426kW.

The parameters used in the calculations are taken from the characteristics of each of the pumps from the appropriate catalogues.Table1 provides data on the pumps used in the analysis, such as the type and serial number of the pump, the rated power of the pump and the induction motor in the drive, nominal flow and effort, efficiency, efficiency class and number of poles.

Table2 shows the data for the operating point of each of the pumps and the corresponding efficiencies depending on it in both regulation modes, then shows the efficiency of the motor that drives each of the pumps, the number of working hours per year andthe price per consumed kWh electric energy.

The analysis goes in the direction of changing the operating point of the pump.A flow reduction of 20% of the nominal was made.

Table 1Pumps data [4]

Serial number of the pump	P_n (kW)	P_2 (HP)	Q_n (m^3/h)	H_n (m)	η_{pn} (%)	η_{mn} (%)	IE	Number of poles
NKE 32-125.1/121 A1-F-A-E-BAQE	1.5	2	19.7	15.7	63.0	88.9	IE4	2
NKE 32-125.1/140 A1-F-A-E-BAQE	2.2	3	23.4	22.6	67.4	90.1	IE4	2
NKE 32-160/151 A2-F-L-E-BQQE	3	4	24.8	24.9	61.1	87.1	IE3	2
NKE 32-160/177 A2-F-K-E-BQQE	5.5	7.5	32.5	36.1	65.4	89.2	IE3	2
NKE 40-160/172 A1-F-A-E-BAQE	7.5	10	43.7	38.6	75.3	90.1	IE3	2
NKE 40-160/177 A2-F-A-E-BAQE	11	15	46.0	41.5	75.3	89.4	IE2	2
NKE 40-200/219 A2-F-L-E-BQQE	15	20	60.2	51.9	69.3	90.3	IE2	2
NKGE 150-125-250/249 A1-F-A-E-BAQE	18.5	25	254	17.4	79.8	91.2	IE2	4
NB 65-250/238 AS-F2-B-E-BAQE	37	50	134	68.1	72.7	92.6	IE2	2
NB 65-250/251 A-F2-A-E-BAQE	45	60	145	77.0	73.6	93.7	IE3	2
NB 65-250/270 AS-F-B-E-BAQE	75	100	161	89.5	75.0	94.6	IE3	2
NK 80-315/295 A1-F-A-E-BAQE	110	150	244	113.8	75.5	94.3	IE2	2
NKG 125-80-315/310 A1-F-L-E-BQQE	132	180	263	126.8	75.5	94.6	IE2	2
NK 80-315/328 A1-F-I-E-BQQE	160	210	289	143.7	76.8	95.6	IE3	2
NKG 125-80-400/398 A1-F-R-E-DAQF	250	340	289	196.9	70.2	95.4	IE2	2
NKG 200-150-315.1/335 G1-F-A-E-BAQE	355	480	965	148.9	83.0	95.5	IE2	2
TP 400-540/4 A-F-A-DBUE	450	540	2890	35.0	83.1	94.0	IE2	4

When the flow is realized by **regulating the valve opening**, to reduce the flow by 20% from Q_1=Q_n to Q_2 = Q_m (Fig. 14), it is necessary to close it properly.The operating point of the pump moves along the characteristic $P_1=H=f(Q)$ and passes from the system characteristic S_1 to the system characteristic S_2.The speed at which the motor runs is 100% of the nominal.The pump effort increases from H_1 to H_{2S}.

When the flow is realized by **regulating the motor speed** to reduce the flow by 20% from Q_1 to Q_2=Q_m, the operating point of the pump is shifted from characteristic P_1 with a rotational speed n_1 of the P_2 curve with a reduced engine speed n_2. By reducing the rotational speed of the motor at flow Q_2, the effort required for the pump to overcome system losses and the required pressure is reduced from H_1 to H_{2P}. The percentage for which the rotation speed should be reduced in order to achieve the required flow depends on the characteristics of the system, i.e. the system characteristic. In other words, the percentage of speed reduction cannot be arbitrary but depends on how much effort the pump has to withstand at reduced flow. For the purposes of this analysis the speed of all analyzed pumps is reduced by 25% of the nominal, which means the motor is running at 75% of the nominal speed and it is assumed that the total effort that the pump has to overcome is not greater than the value H_{min} of Table2.

Table 2Pumps working point data

P (kW)	Q_m (m^3/h)	H_{2s} (m)	H_{2p} (m)	η_1 (%)	η_2 (%)	η_m (%)	t_a(h)	(€/kWh)	H_{min}
1.5	15.8	17.37	8.702	60.4	62.8	88.9	3000	0.15	8
2.2	18.7	24.67	12.77	65.6	67.0	90.1	3000	0.12	12
3	18.4	27.6	14.43	57.8	61.1	87.1	3000	0.12	14
5.5	26	39.6	19.57	64.0	64.8	89.2	3000	0.12	19
7.5	35	41.46	21.83	71.0	75.0	90.1	3000	0.12	21
11	36.8	44.42	23.56	71.0	76.1	89.4	3000	0.12	23
15	48.2	58.4	29.24	68.4	69.1	90.3	3000	0.12	29
18.5	203	19.58	9.938	77.0	80.1	91.2	3000	0.12	9
37	107	75.1	38.22	71.0	72.6	92.6	3000	0.12	38
45	116	85	42.34	72.6	73.3	93.7	3000	0.12	42
75	130	98.66	48.78	74.2	74.4	94.6	3000	0.12	48
110	195	121.5	51.5	73.8	75.0	94.3	5000	0.12	61
132	210	134.8	71.03	73.3	75.4	94.6	5000	0.12	71
160	231	152.7	79.37	74.8	76.5	95.6	5000	0.12	79
250	231	213.7	107	69.1	70.1	95.4	5000	0.12	107
355	773	131.2	69.53	81.6	85.0	95.5	5000	0.12	69
450	2310	41.27	18.69	79.5	82.6	94.0	5000	0.12	18

The pump data shown in Table2, as previously stated, is the data required to perform the calculations. The definition of the variables presented in Table 2 is given below:

Q_m– flow through the pump (m^3/h)
H_{2S}– pump effort expressed in (m) at Q_m flow with valve regulation and rated motor speed
H_{2P}– pump effort expressed in (m) at Q_m flow with motor speed regulation with inverter at 75% of nominal speed
η_1– pump efficiency at operating point (Q_m, H_{2S})
η_2 - pump efficiency at operating point (Q_m, H_{2P})
η_m– motor efficiency
t_a– number of working hours per year.

In Table3a presentation of the calculated data for each of the pumps defined in Table1 and Table2 is presented. The definition of the variables presented in Table 3 is stated as:

P_v (kW) – required pump power for valve regulation
P_e (kW) – required pump power for motor speed regulation at 75% of rated speed
P_s (%) – percentage of power required less when the flow is regulated by motor speed to 75% of the nominal compared to the valve regulation, where:

$$P_s = (P_e/P_v) \times 100 \tag{8}$$

E_s (kWh) – saving electricity by applying an energy converter with U/f regulation at a reduced speed of 25%
K_s (€) – saving money from the saved electricity.

As can be seen from the results of the table, the regulation of the motor speed by using energy converters as a way to change the operating point of the pump is a much more efficient solution compared to the valve control and brings great savings in electricity if it is the same implements. This is especially true for drives that have variable operating regimes.

Table 3Result analysis

P (kW)	P_v (kW)	P_e (kW)	P_s (%)	E_s(kWh)	K_s(€)
1.5	1.238	0.597	48.183	2165.100	259.810
2.2	1.916	0.971	50.682	3146.900	377.620
3	2.394	1.184	49.459	4167.900	500.140
5.5	4.384	2.140	48.809	7547.500	905.700
7.5	5.569	2.776	49.845	9300.700	1116.100
11	6.274	3.105	49.845	10635.000	1276.200
15	11.214	5.558	49.561	18792.000	2255.000
18.5	14.066	6.863	48.792	23695.000	2843.400
37	30.841	15.350	49.771	50188.000	6022.600
45	37.009	18.259	49.336	60033.000	7203.900
75	47.103	23.226	49.310	75719.000	9086.200
110	87.482	43.573	49.807	232819.297	27983.315
132	105.237	53.908	51.225	271297.099	32555.651
160	128.503	65.309	50.822	330516.350	39661.962
250	194.672	96.082	49.355	516719.967	62006.396
355	338.680	172.305	50.875	871070.850	104528.502
450	326.773	142.432	43.588	980535.586	117664.270

As can be seen from the results of the table, the regulation of the motor speed by using energy converters as a way to change the operating point of the pump is a much more efficient solution compared to the valve control and brings great savings in electricity if it is the same implements. This is especially true for drives that have variable operating regimes.

7 Conclusion

The world industry and economy are facing a major energy challenge. Global electricity demand is growing, and pressures to reduce electricity consumption and reduce the impact on the environment and climate change are growing. If we take into account, the fact that as much as 65% -70% of the total electricity consumption in industry is accounted for by electric motors then it is clear that the potential for saving electricity is huge and their role in reducing environmental pollution is crucial.

The control strategy of the working mechanisms depends on its mechanical characteristic. With mechanical control of the working mechanisms is consumes unnecessarily much electricity. Reducing the flow of a pump with a valve control is as inefficient as regulating the car speed only with brake. At a reduced motor speed of 25% of the rated power of converter, the power required by the pump is 50% lower than the power required for valve control. This means a reduction of the required electricity by 50%. Given the fact that pumps make up 33% of all working mechanisms, it is again concluded that by increasing the energy efficiency of pump systems there is a great potential for energy savings and improvement of their work.

The concept of energy efficiency is a very effective way to reduce the emission of carbon dioxide and other harmful substances into the air that contribute to global warming, air pollution and climate change. Global programs aimed at helping industrial companies improve the energy efficiency of their electric drives are needed and are of great importance for raising awareness and assisting in the implementation of energy efficiency.

References

[1] IEA, “www.iea.org,” 2016. Available: https://www.iea.org/publications/freepublications/publication/KeyWorld2016.pdf.

[2] E. Commission, “Motor Challenge Program,” 2009.

[3] GRUNDFOS,“http://www.grundfos.com/,”Available:http://net.grundfos.com/doc/webnet/mining/_downloads/pump-handbook.pdf.

[4] GRUNDFOS, “Products,” GRUNDFOS, 2017. Available: http://www.grundfos.com/products.html.

[5] ABB, “www.abb.com,”. Available: http://new.abb.com/.

[6] ABB, “Variable speed control form demand to decision”.

[7] F. C. Systems, “Massive savings with industrial process energy saving solutions,” Finesse Control Systems Ltd. Available: http://www.finessecs.com/industrial-energy-saving-solutions.html.

Cutting-Edge Technology for Innovative Electric Motors

Lidija Petkovska, Goga Cvetkovski
Ss. Cyril and Methodius University, Faculty of Electrical Engineering and Information Technologies
Skopje, North Macedonia, E-mail: lidijap@feit.ukim.edu.mk ; gogacvet@feit.ukim.edu.mk

Abstract ***– With the growing interest in electrification from clean energy technologies, such as wind power, as well as the use of electric mobility in various applications, the demand for the next-generation high-performance electric motors has risen significantly. Electrical machine designers for these applications are facing challenges in terms of meeting very demanding metrics for power density and conversion efficiency. Thereby, it is a substantial motivation of researchers for exploration of not only the novel topologies and advanced new materials, but also for exploitation of the innovative manufacturing processes for the new generation of compact, high-efficient and light-weight electric motors. Nowadays, thanks to cutting-edge technologies and new materials, a hi-tech 3D printed motor became a reality.***

1 Introduction

The electric motor is one of the few inventions that shaped overall electric technology the most. The very beginning of it is found exactly two hundred and one more year ago, in 1821. However, over the time many significant changes in the technology have been moving forward, opening new frontiers for innovative electric motors. In particular, new trends in e-mobility as the developments of EV (Electric Vehicles) and HEV (Hybrid Electric Vehicles), forced new requirements related to size/weight of the drive and resulted in awesome innovations for in-wheel electric motors, thus creating substantial solutions. Consequently, the rise of mobile applications has created a need for more efficient, space constrained and smaller drives. At the same time the electric motor design topology drifted mostly from radial to axial flux motor configurations. What are new trends and challenges? It is first to explore novel electric motor topologies, then to use advanced optimisation methods for their shape design and synthesis – to encompass the new materials – and finally, to exploit the *cutting-edge technology* for manufacturing electric motors. At this stage the most inspiring, for a wide range of products, is the use of *additive manufacturing* (AM), widely known as direct 3D printing. The possibilities of exploiting AM in this state-of-the-art production technology for innovative electric motors are open [1]. The expected outcome of the feasible applications is to obtain an electric motor with compact and lightweight multi-material components with higher magnetic flux density, meaning higher power density and/or efficiency, at easier manufacturing and with innovative cooling; also, without deteriorating the noise and vibration level. Hence, to provide the best problem solution, the process is always carried out with participation of experts in motor design, material sciences, electromagnetics, electromechanics, cooling, bearings, etc.

2 Trends in Electric Motor Technology

With the development of new technologies, the electrical industry and in particular the manufacturing of electro-magneto-mechanical devices has been moving forward. Over the time many significant changes have taken the place in the electric motor technology. Among them, several more important present trends in the production of electric motors, without giving any priority, are depicted in Fig. 1.

Fig. 1 Trends in electric motor technology advancements

2.1 Design & Manufacture and Cost

Important aspect of motor innovations is the production process. The most recent 3D printing technology developments, have added a huge value to the designing, prototyping as well as manufacturing process of electric motors. The broad spectrum of production applications has been unlocked. The laser technology is growing, becoming more workable and affordable, such that additive manufacturing (AM) from 3D printing of only parts of an electric motor has been moved to the printing even of the whole motor structure [2]. The significant reduction of time and money consumption, required for the stage of prototyping an electric motor, led to cost-effective massive motor production. Thus, for less money the same quality can be reached, as well as for the same money more quality motor is obtained.

2.2 Efficiency

For many years, the energy efficiency of electric motors was subject of a voluntary commitment by the manufacturers and the agreement with the customers. However, the globally increasing demand for energy savings, gave rise to a range of regulations for determining motor efficiency. Intending to harmonize the standards describing the motors' energy efficiency worldwide, the International Electrotechnical Commission (IEC) has developed the completely *new classification* and established globally regulated requirements placed upon the efficiency of electric motors. The highest class is reserved for super *premium efficiency* of electric motors. The comparison of the earlier (EFF) and actual (IE) efficiency classes is presented in Fig. 2. As both the electric motor designers and producers are receptive to the great importance for efficiency increase of electric motors, further innovative advancements have been already undertaken by stakeholders.

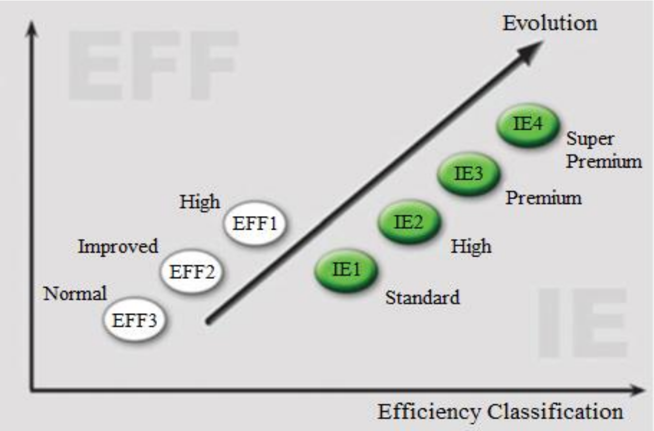

Fig. 2 Electric motor efficiency classes comparison

2.3 Control

One concept of the substantial importance for an electric motor performance is speed control. The classical speed control of AC motors, performed by gear reducers or by the number of poles variations, grace to the fast advancements of variable frequency drives (VDF) with pulse width modulation (PWM), has been sent away. The recent drastic cost reduction and reliability increase of variable frequency drives has driven changes in electric motor designs and the adoption of VFD's to new levels. That fact has brought about to become a standard addition of the inverter as an integral part of the motor structure inside the common housing. As a result of semiconductor technology and microprocessor advances, the VFD has become smarter, more efficient, and more accurate. Current motor innovations, such as in the permanent magnet AC motor technology, are being refined to bring higher efficiency, cooler running temperatures, and incredible speed and torque control accuracy. On the other hand, the rediscovery of synchronous permanent magnet and reluctance motors, together with recently added PM assisted reluctance motors, is becoming evident [3].

2.4 Space

Finally, new trends in e-mobility, the developments of EV (Electric Vehicles) and HEV (Hybrid Electric Vehicles), forced new requirements related to the size and the weight of the drive, resulting in innovations for the embedded electric motors. Consequently, the rise of mobile applications has created a need for more efficient space constrained by smaller drives. At the same time the electric motor topology drifted from radial to axial flux motor configurations.

3 What is an Innovative Motor?

The first question to be answered is: *"What makes an electric motor innovative?"* As an offered answer, firstly it would be an innovative design topology and the use of novel materials, then an innovative production technology and, the most recently, the new State-of-the-Art manufacturing processes. Taking into consideration all aspects of the motor performance (electro-magneto-thermal-mechanical coupling), a design engineer of electric motors will be seeking for answers to the following questions:

- What are novelties in the electric motor design?
- How to extend the limits of the motor's performance reached today?
- What are structural/shape choices that define novel motor topology and make the motor better-performing?
- What are the most effective new materials to obtain the best of each component/shape in the design layout?

An example of an innovative motor structure, in expanded view, where its main innovative design components are outlined, is presented in Fig. 3.

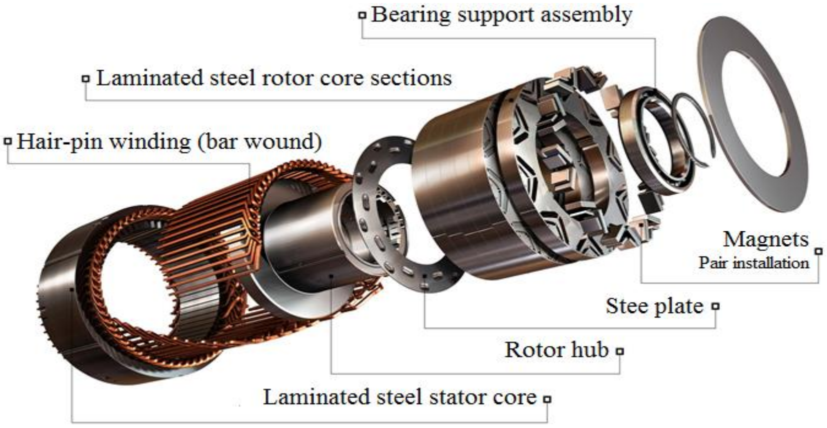

Fig. 3 Expanded view of an innovative PM assisted reluctance motor produced by cutting-edge technology

3.1 Novel Design Topologies

When seeking for a well synthesized electric motor for the selected topology, the designer should encompass the most of used materials – iron and copper – and to optimize electromagnetic, thermal and mechanical design, combined with some aspects of noise and vibration. To lower electrical energy consumption, while keeping functionality of appliances, it is required to design devices with increased efficiency level. On the other hand, the new concept of *e-mobility* attracted electric machine designers towards innovative topologies and shape designs, to meet the new requirements.

These meaningful themes have challenged researchers and scientist worldwide to innovation of electric motors design, by means of their topology. Commercialization of innovative motor topologies that have been around for a long time, but have not been broadly found in practice, triggered the growth and penetration of brushless permanent magnet motors. Some fifty years ago, the major motor sale was for induction and DC brushed motors. Today induction motors are still important, but brushless PM (BLPM) have grown dramatically, relegating DC commutator ones. Thus, along with other topologies such as synchronous reluctance – with or without PM assistance – and switched reluctance have grown application and can be found even in a higher volume motors. Recently, permanent magnet motors (PMMs) have been rediscovered and their application in various devices, from small house appliances to large aircrafts, has been visibly extended.

3.2 New Materials

Regarding the materials, used for designing and manufacturing of an electric motor, yet fundamental role is played by the core lamination and permanent magnet materials. Apart from the windings' copper loss, another significant loss component that affects the overall motor performance and efficiency is iron loss in the motor core lamination. Hence, proper selection of the electric steel material for cores is an important matter of exploration. New developments in electric steel properties to ongoing applications contribute to better motor performance. Acknowledging the trends in PMMs production, developments of the PM materials are also worth to be considered. Another novel material found in the innovative motor designs are Soft Magnetic Composite (SMC) materials, which are becoming interesting at frequency values >500 Hz.

A. Core Lamination Materials

Speaking about AC motors, induction and permanent magnet, usually the rotor core loss is with negligible value, and only the stator core loss is considered. In this regard, it is not enough to have a state-of-the-art designed stator, but also to have state-of-the-art materials for manufacturing. Stator and rotor cores of an electric motor, depending on the topology, have a variety of shapes and are manufactured from a variety of materials. Lamination examples are presented in Fig. 4.

Fig. 4 Lamination examples for stator and rotor cores

Electrical steel is a soft magnetic material, comprising silicon-iron, nickel-iron, and cobalt-iron alloys, where iron is the main component. The *silicon-iron* (SiFe) alloys with 0.5% to 4.0% Si, referred to as silicon steel, are found in a broad use across the applications in variety of electromagnetic devices. Silicon steel can be oriented or non-oriented in dependence of magnetic properties, while depending on the thermal treatment it can be fully processed or semi-processed. Non-oriented fully processed silicon iron is found in the widest use. It has uniform magnetic properties in all directions and is available in a range of grades and thicknesses so that may be well tailored for various applications. Silicon electric steel is generally specified and selected on the basis of allowable specific iron loss in watts/kg.

Today the *cobalt-iron* (CoFe) electric steel for building stator/rotor core of an innovative motor is more and more often in use. This novel material is characterized by better electromagnetic behaviour, broader use range before saturation and low loss figures, at the same values for magnetic flux densities and frequencies, compared to materials of the silicon-iron (SiFe) class. Thanks to quite high value of magnetic saturation, the cobalt-iron electric steel is generally suitable for applications where high flux density is required, allowing to lower the iron mass, which in return gives decreased iron loss and weight reduction of the cores. To illustrate the advantages of the high performance CoFe electric steel, the comparative characteristics of VACOFLUX® and VACODUR®, with reference to 3% SiFe alloy are presented in Fig. 5 [4].

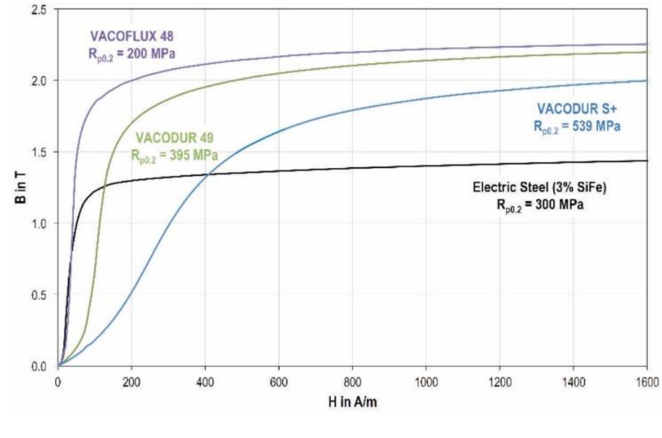

Fig. 5 Normal DC magnetization curves of CoFe alloys in comparison with a reference SiFe core material

Other important features of CoFe alloy are high magnetic saturation up to 2.4 T, and small specific iron loss 1.5-1.6 W/kg. Although the mass density is a bit higher, due to improved magnetic properties, the iron consumption is lowered and, in turn, motor dimensions and weight will be reduced. Further expansion of innovations in electric motor technology with new lamination materials is foreseen.

B. Permanent Magnet Materials

The use of permanent magnets in favour of the mankind is long lasting. But their application for building electric motors started somehow less than a century ago. In the past, the most expensive part for building a PM motor, was production of rotor/stator with permanent magnets. It was a serious obstacle to their wider use, besides very good performance characteristics. However, throughout the recent years, started an intensive research and innovative discoveries in permanent magnet manufacture resulted in highly effective and commercially viable PM materials. This research is extended up to todays, and is still in the course. Nowadays, the permanent magnets available on the market, are with higher values of remanence B_r, intrinsic coercivity H_c and energy product, known as maximum energy density $(BH)_{max}$. The benefit of these advancement is that demagnetization problems became minor, while the higher motor performance with the same magnet volumes, or the same motor performance with reduced magnet volumes, is enabled.

The historical development of PM materials by decades is depicted in Fig. 6, where the ranges for maximum energy density as per time of their discovery for four distinctive PM materials are shown. As seen in the figure, the frontiers are open. Series of various permanent magnet materials, with remarkably improved features, have been invented. Typical demagnetisation curves for PMs, which are in the most frequent use, are presented in Fig. 7 [5]. Owing to rare-earth Samarium-Cobalt (SmCo) permanent magnet class, the innovative motor topologies recorded rapid development. Thus, brushless PM motor, became a combo set with its power supply and control device, dominating in innovative and modern AC electric drives. The only disadvantage was the high cost of PMs production, the fact that challenged future research for PM with features like SmCo and prices as ferrite. The solution is found in the last generation of permanent magnets – based on Neodymium-Iron-Boron (NdFeB) composition – that is the best suitable for mounting in an electric motor topology.

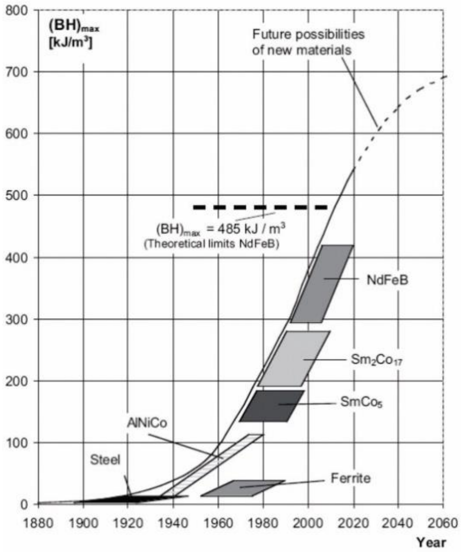

Fig. 6 Development of permanent magnets through years by name and energy density

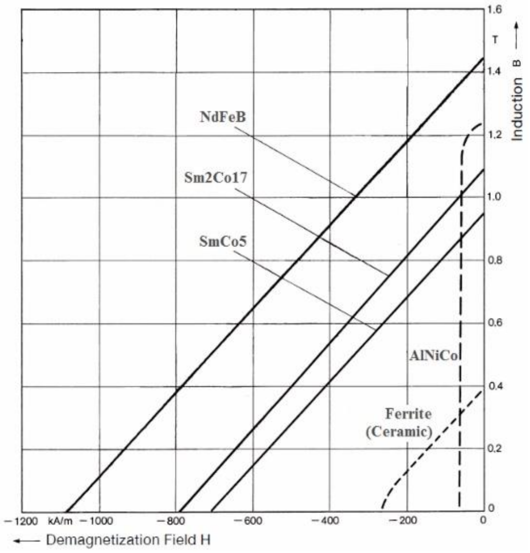

Fig. 7 Typical demagnetization characteristics for permanent magnet material

Electric motors that use permanent magnets are generally more expensive. Consequently, the motor designer should be able to efficiently select the most suitable permanent magnet material, depending on the particular purpose and the specific motor topology, in order to provide best quality/price. Permanent magnet motors, either radial or axial flux, provide a good compromise of high specific torque and low losses; at the same time the motor is lighter, safer, quieter and more energy efficient than any other top drive motor on the market, which justifies its choice for the most automotive applications. Today, PM motors for direct EV/HEV drive are in the forefront of all competitive motors.

C. Soft Magnetic Composite Materials

The fast developments of e-traction and renewable power generation, that are characterised with electrical machines of high compactness, higher efficiency and high power/torque density, have driven the research towards not only developing the novel topologies of electrical machines to meet special requirements, but also to inventing new materials that will enable their easier manufacturing. Continual advances in the area of e-mobility and high power density electric motors have brought new challenges to the motor constructions. The traditional laminated motor construction is limited to 2D radial magnetic flux to minimize losses in the direction perpendicular to the steel lamination. On the contrary, the topologies of the axial flux motors require very complex 3D magnetizing directions where the use of electrical steels is often not practical. In addition, the use of conventional electrical steels is limited to medium frequency values, up to 1000 Hz. What to do?

The solution is found in application of soft magnetic composites (SMCs) to manufacture some parts of an electromagnetic device, or even in the whole. By means of the powder metallurgy and advanced additive manufacturing (AM), SMCs can be formed into complex shapes, allowing three-dimensional magnetic circuits to be designed and easy manufactured. With their help it is possible to produce more compact innovative and cost-efficient electric motors. The SMCs have many unique characteristics, which can be utilized to improve the performance of traditional electrical machines and to develop innovative designs and topologies with more complex magnetic circuits and increased power density. Sometimes, the geometrical size of the available parts is limited, mainly due to specific compacting processes. But, there is a number of disadvantages of SMCs that should be also taken into account during the design and construction of electro-magneto-mechanical devices.

Advantages of the soft magnetic composites are: • higher power density due to existence of 3D magnetic flux in the device; • complex shapes are possible, to enable a broad range for the product design; • lower loss at high frequencies, compared with lamination steel; • isotropic physical properties (thermal conductivity and relative magnetic permeability); • the lower eddy current losses due to higher electrical resistance of SMCs.

Disadvantages of the soft magnetic composites are: • high values of magnetic field strength required to reach magnetic saturation; • low magnetic saturation ≈1.5T@10000A/m; • low magnetic permeability, on average $\mu_r \approx 600$; • higher hysteresis losses; • inferior mechanical properties.

D. State-of-the-Art Applications

The benefits of SMCs solutions for both the motor topology design and production processes enabled wide spectrum of state-of-the-art products, which are released by several big world-wide known companies. Soft magnetic powder composites coupled with PM production processes open new possibilities in the design and manufacture of parts for electrical device applications or the whole structures. With increasing values of operating frequency for electric motors, the use of SMCs can contribute to a substantial decrease of specific core losses of the machine, increasing at the same time the total efficiency. In contrast to laminated cores, the manufacturing process of soft magnetic composites does not influence their final homogenous magnetic properties, which do not change after assembly of the motor.

Somaloy® is a trademark of Höganäs AB from Sweden, the world-known producer of soft magnetic composite materials [6]. They have developed a variety of electromagnetic applications. Capabilities of the Somaloy® materials have opened up new opportunities to design innovative motors, produced by novel technology, as elaborated in [7]. They are designed for efficient modular production at low cost, by exploiting state-of-the-art technology for 3D magnetic properties and the net volume shaping. Taking as an example the axial-flux electric motor for e-mobility, both single- and double- sided, the proposed solution is pictured in Fig. 8.

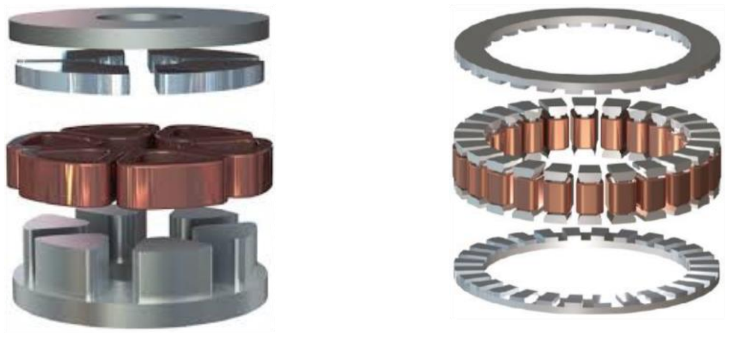

(a) Single-sided (b) Double-sided

Fig. 8 SOMALOY® Innovative axial flux PM motor solutions

Through application of advanced production technologies and 3D shape-making capabilities, invented motor topologies are manufactured with reduced size and weight, meeting the high performance requirements, with less need for machining, i.e. with reduced need for subsequent operations, all that in a cost-effective manner.

4 Cutting-Edge Production Technologies

Another aspect of motor innovations is the production process. The questions to be asked here are:

- How is an innovative motor manufactured?
- What are the novelties in electric motor production technologies?

What are challenges? After exploring the new electric motor topologies, to use advanced optimisation methods for their shape design and synthesis, and finally to exploit the state-of-the-art manufacturing technologies for electrical machines. The broad spectrum of modern production applications have been recently unlocked. The expected outcome of the feasible applications is to obtain an electric motor that is with compact and lightweight multi-material components, with higher magnetic flux, meaning the higher power density and/or efficiency, easier manufactured and with innovative cooling but, without deteriorating the noise and vibration level [8]. The significant reduction of time and money consumption, required for the stage of prototyping an electric motor, led to cost-effective massive motor production. Thus, for less money the same quality can be reached, or for the same money better quality motor is obtained.

While the innovative electric motors are used in numerous innovative areas, their production has been limited to traditional techniques which, in turn, result in unreliable and not enough efficient products. It is common that electrical machines are usually produced by using traditional manufacturing processes, as laminate punching with packing or powder based alloy pressing, procedures that often require expensive tooling for extensive machining, or other techniques to remove surplus material. When prototyping a new product, design changes are required, and with conventional manufacturing techniques, an extensive and expensive work should be done. Needless to say that in every step, the motor must be carefully designed while the used material must be thoroughly selected, to meet the fabrication requirements.

Thereby, it is a substantial motivation of researchers for exploration of not only advanced novel materials, but also innovative production processes for the next novel generations of compact, high-efficient and light-weight electric motors. Accordingly, it is needed a shift in how these innovative motors are manufactured, and with respect to this, how are designed. At this stage it seems the most inspiring is the use of direct 3D printing, widely known as *additive manufacturing* (AM). Thus, it is additive manufacturing that actually can provide this shift. Using 3D computer aided design (CAD), and having in hand 3D scanners, additive manufacturing allows the creation of objects with precise geometric shapes, built layer by layer by adding material, opposite to classical manufacturing processes when the excess of material is subtracting. Nowadays, thanks to new technologies and new materials, 3D printed motors became a reality.

To present days this promising technology, due to complexity of motor topology is difficult to be applied on the whole motor structure, although several pioneering research centres throughout the world have reported successful applications. Hence, the AM is used only for particular parts of the motor, e.g. copper windings, or the electric motor is assembled by modular elements fabricated by AM. However, some simple electromagnetic devices, like an inductor, can be performed in whole by 3D printing, and that would result in full multi-material processing and production. In Fig. 9 is presented expanded view of an axial flux PM motor for e-drive, to identify parts of the motor topology with respective materials, for viable production by AM.

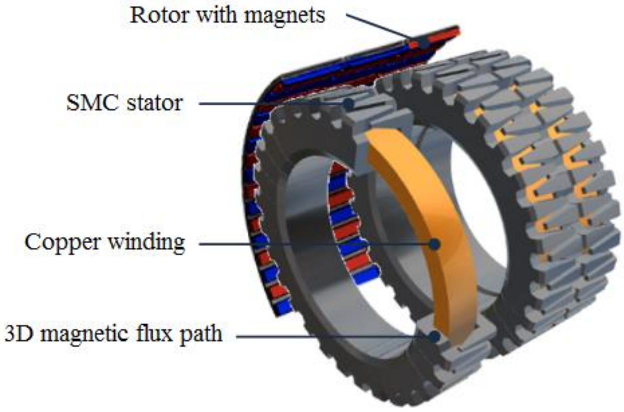

Fig. 9 Expanded view AFPM motor

4.1 Electric Motors from 3D Printer

The earliest practical implementation of the 3D printing in modern electric motor technology was for the purpose of e-mobility, where only some parts of the motor topology (Fig. 3) have been manufactured, e.g. windings or modular stator core, being used in the stage of prototyping. The 3D printed functional prototypes can help eliminate expensive early tooling costs, giving engineers ability to make design changes, to iterate quickly and to reduce development time for new products. However, the real challenge for motor designers is producing the whole motor by using AM, the task rather complicated. Another important issue to consider is which materials are feasible for AM? With respect to this, SMCs and SiFe alloys are excellent candidates, while CoFe alloys although with high saturation flux density are still in investigations [9].

The first fully 3D-printed stator for a reluctance electric motor was developed by an enthusiastic group of electrical engineers from Chemnitz University, Germany [10]. The stator of the reluctance machine was printed in the Chemnitz University Laboratory using iron for magnetic core, copper for electrical conductors of the winding and ceramics as insulating material, to insulate conductors from each other and from the iron components. This pioneering work was premiered quite recently, at 'Hannover Messe' – the trade fair, in 2018.

The 3D-printed stator of the motor – that was created, produced and displayed – is a real breakthrough in the innovative cutting-edge technology for additive manufacturing of electric motors, proving the applied technical principles and demonstrating the feasibility of the processes. The production phases for this part of the motor are shown in Fig. 10. Left in the figure is presented the 3D-CAD model of the stator, in the middle is the production phase of sintered stator, while the rightmost is fully 3D-printed part before a heat treatment.

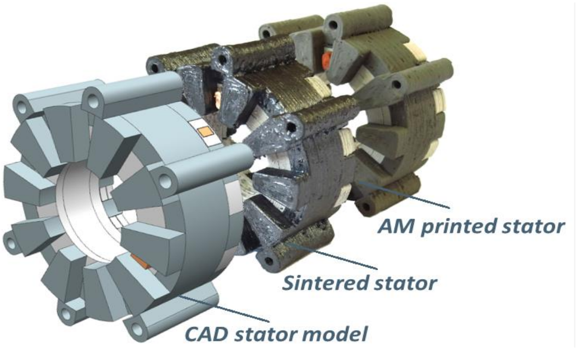

Fig. 10 3D-printed stator of a reluctance machine without winding head

4.2 Power Supply and Control Trends

The drastic reduction of cost and increase in reliability of variable frequency drives (VFD) has driven their adoption for electric motors to all new levels. Thus, the further innovations in electric motor technology provide the full integration of a motor with power electronics and mechanical transmission system. This perfect mix of components for the best possible motor performance is presented in Fig. 11. The whole motor enclosure is devised for its connection with the electronic converter for power supply and motor control, and also with the gearbox, when required [11].

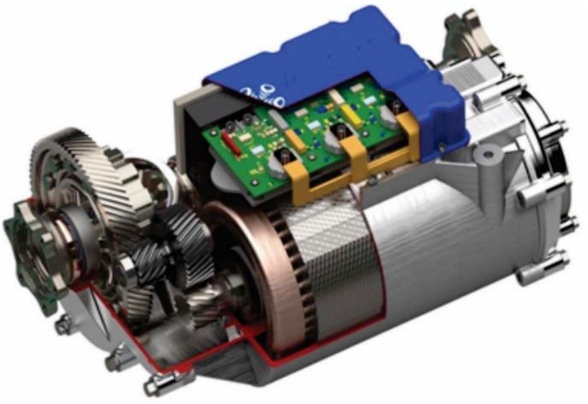

Fig. 11 An example of innovative fully integrated electric motor

5 Concluding Remarks

The innovative electric motors find applications across multiple industry branches including energy production, e-mobility, manufacturing plants, industrial automation and variety of consumer appliances. To conclude the paper, there are few outlines about the new trends, expected future of the innovative motors' developments and the novelties in cutting-edge production technologies.

- In general, electric motors and drives will continue to get smaller with higher power densities. The used materials and topologies will be improved and changed to meet the need for increased efficiency and controllability.
- Induction motors, with significant increase of their efficiency certainly will not go away, and will be still remaining in the widest application.
- Continued growth in variable speed drives, with integrated solutions and other electric motor technologies, will be gaining larger scale of use.
- Brushless permanent magnet motors, synchronous reluctance motors without/with permanent magnet assistance, and even switched reluctance motors, all they based on higher efficiencies and lower cost for power electronic devices, will continue to expand and enlarge their use.
- High speed applications will demand new special motor designs, with embedded VFD, to improve the whole system efficiency and replace traditional mechanical geared drives.
- Due to the increased production of electric vehicles the new topologies required for automotive industry is expected to drastically drive the demand for innovative electric motors.
- Additive manufacturing with 3D-printing will enable designing, prototyping and manufacturing of an electric motor to become easier, faster and more reliable.

References

[1] L. Petkovska, G. Cvetkovski, *Chapter 4: "Innovative motors and shape optimisation"*, pp. 139-188, in the book ISBN-13: 978-1-83953-351-8, by Group of Authors: "Optimal Design Exploiting 3D Printing and Metamaterials", Edited by: P. Di Barba and S. Wiak, IET – The Institution of Engineering and Technology, London, UK (2021), Book DOI: 10.1049/PBME023E, Chapter DOI: 10.1049/PBME023E_ch4, (2021).

[2] F. Wu, A. M. El-Refaie, (2019) "Towards Fully Additively-Manufactured Permanent Magnet Synchronous Machines: Opportunities and Challenges", *Proceedings of the 2019 IEEE International Electric Machines & Drives Conference – IEMDC'2019*, https://doi.org/10.1109/IEMDC.2019.8785210, San Diego, CA, USA, pp. 2225-2232.

[3] G. Pellegrino *et al.*, "The Rediscovery of Synchronous Reluctance and Ferrite Permanent Magnet Motors", SpringerBriefs in Electrical and Computer Engineering, DOI 10.1007/978-3-319-32202-5_1, (2016).

[4] "Soft Magnetic Cobalt-Iron Alloys Vacoflux & Vacodur", Catalogue Edition 2016, VACUUMSCHMELZE® GmbH&Co. KG, Hanau, Germany, pp. 1-20, https://www.vacuumschmelze.com/Assets/Cobalt-Iron%20Alloys.pdf.

[5] "Rare Earth Permanent Magnets VACODYM&VACOMAX" Catalogue, VACUUMSCHMELZE® GmbH & Co. KG (VAC), VACODYM-VACOMAX-PD002_2015_en.pdf, pp. 1-72, Hanau, Germany, (2015).

[6] "Soft Magnetic Composite SOMALOY®", Höganäs AB Products Catalogues and material data on-line Somaloy 1P, 3P, 5P, https://www.hoganas.com/.

[7] "Somaloy® Axial Flux Machine solutions", Somaloy Axial Flux Solutions_Aug_2016_1701HOG.indd, Brochure by Höganäs AB, pp. 1-4, (2016).

[8] M. C. Halbig, "Compact Additively Manufactured Innovative Electric Motor – CAMIEM". (2017), Proceedings of *Energy Tech2017 Conference,* Track_6, https://www.energytech.org/wp-content/uploads/ET2017Presentations/, Track_6/HALBIG_Energy-Tech-2017.pdf, pp. 1-19.

[9] M. Garibaldi, C. Gerada, I. Ashcroft, R. Hague, H. Morvan, (2015), "The Impact of Additive Manufacturing on the Development of Electrical Machines for MEA Applications: A Feasibility Study". *Proceedings of the European Conference on More Electric Aircraft – MEA2015*, Toulouse, France, hal-01178353.

[10] J. Rudolph, F. Lorenz, (2018), "Fully 3D-Printed Electric Motors", https://www.tu-chemnitz.de/tu/pressestelle/aktuell/8718/en#.

[11] "Electric Motor: What is the Real Innovation?", https://www.electricmotorengineering.com/electric-motor-what-is-the-real-innovation/.

The 8th International Symposium on Applied Electromagnetics – SAEM'2022

Struga, North Macedonia, 26-29 June 2022

Design of Interior Permanent Magnet Synchronous Motor for Energy-Efficient Electric Propulsion System

Bojan Ġtumberger [1,2], Iztok Brinovar[1], Klemen Sredenġek[1], Miralem Hadǵiselimoviĺ [1,2], Sebastijan Seme[1,2], Amor Chowdhury[1]and Gregor Srpļiļ [1]

[1] University of Maribor, Faculty of Energy Technology, Hočevarjev trg 1, 8270 Krško, Slovenia,
bojan.stumberger@um.si, iztok.brinovar1@um.si, klemen.sredensek@um.si, miralem.h@um.si,
sebastijan.seme@um.si, amor.chowdhury@um.si, grega.srpcic@um.si

[2] University of Maribor, Faculty of Electrical Engineering and Computer Science, Koroška cesta 46, 2000 Maribor, Slovenia

***Abstract* ï The paper presents the design of interior permanent magnet synchronous motor (IPMSM) for energy-efficient electric propulsion system with 70 kW peak power motor power rating. Efficiency and power capability performance of IPMSM with distributed winding over a wide-speed range is presented on the basis of the finite element analysis (FEA) within the IEC 112 frame size.**

1 Introduction

IPMSMs dominate in the electric propulsion systems for electric vehicles (EVs) [1], [2]. In general, electric motors for EVs require a certain speed range with continuous torque, a certain speed range with maximal overload torque at given maximal inverter current limitation and good overall efficiency over the operating torque and speed area. With increasing the maximum DC link voltage from 310-350 V up to 650-800 V in recent years, the maximal motor speeds and used gear ratios in EVs are increasing as well in order to decrease the material usage. At present, maximal speed of electric motors in EVs is normally limited to maximal speed of 15.000 – 16.000 rpm with gear ration around 10:1. It would therefore be convenient to increase the maximal electrical motor speed above 20.000 rpm in combination with a gear ratio around 14:1 in order to minimize total weight of EV drivetrain. The paper presents the design of interior permanent magnet synchronous motor (IPMSM) for energy-efficient electric propulsion system with 70 kW peak power motor power rating and maximal motor speed around 22.000 - 24.000 rpm, which has to be appropriate for a mid-sized C segment electric vehicle. Efficiency and power capability performance of IPMSM with distributed winding over a wide-speed range is presented on the basis of the finite element analysis (FEA) within the IEC 112 frame size. Cross-section of IPMSM with 36 stator slots and 8 poles is presented in Fig. 1, while the main geometry and used material data are presented in Table I.

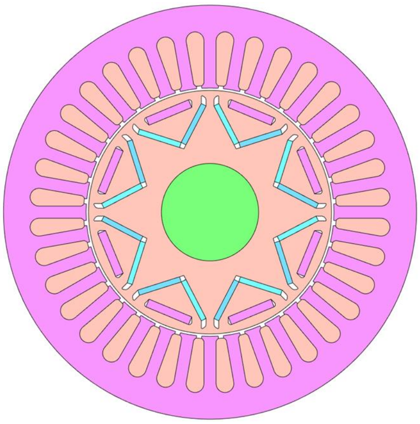

Fig. 1 Cross-section of IPMSM (36 stator slots and 8 rotor poles, D-type rotor configuration).

---

[1] University of Maribor, Faculty of Energy Technology, Hočevarjev trg 1, 8270 Krško, Slovenia, e-mail: bojan.stumberger@um.si

[2] University of Maribor, Faculty of Electrical Engineering and Computer Science, Koroška cesta 46, 2000 Maribor, Slovenia

Table I..Main geometry and used material data of IPMSM

Number of stator slots	36
Number of poles	2p=8
Outer stator diameter	170 mm
Stator bore diameter	102 mm
One-side air-gap	1 mm
Rotor outside diameter	100 mm
Stator and rotor height	140 mm
Shaft diameter	40 mm
Depth of stator slot	23.3 mm
Stator slot opening	2.1 mm
Width of stator tooth	5 mm
Upper magnet thickness	3.4 mm
Upper magnet width	19 mm
Lower magnet thickness	2.2 mm
Lower magnet width	18 mm
Magnet material	N28AH (Nd-Fe-B)
Stator and rotor electrical steel	M270-35A
Stator winding type	distributed, star connection, double layer
Number of turns	3 turns per coil
Number of strands	18 per turn

2 Results

Torque capability, power capability, efficiency performance and different loss components over the whole speed-range for IPMSM with 70 kW peak power motor power rating are presented in Fig. 2 to Fig. 8.

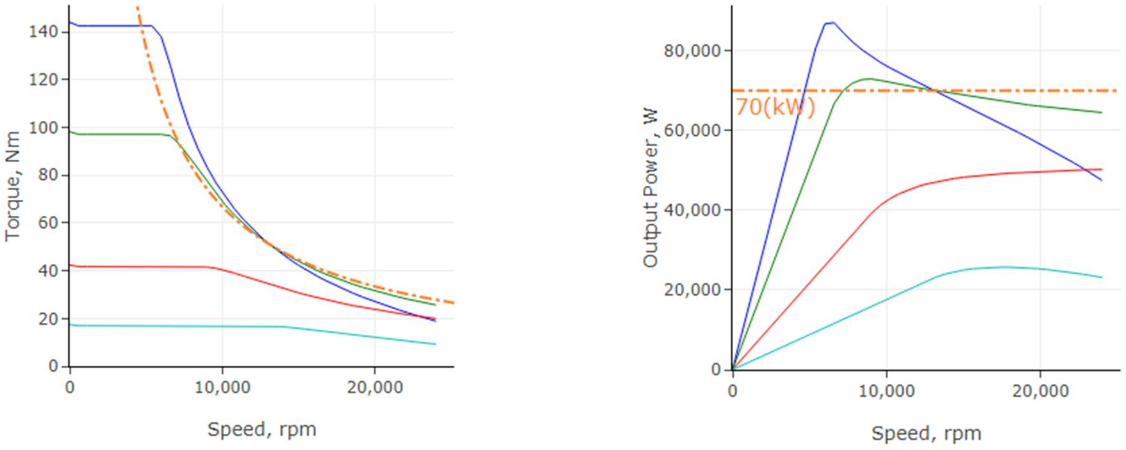

a.) b.)

Fig. 2 Motor torque and power characteristics for different maximal peak values of phase current: a.) motor shaft torque versus speed; b.) motor output power versus speed. 311 Apk (blue color line), 200 Apk (green color line), 100 Apk (red color line) and 50 Apk (cian color line).

In Fig. 2a (torque versus speed characteristics) and in Fig. 2b (output power versus speed characteristics) results for different current levels are presented. Current level of phase current 311 Apk (220 A RMS) corresponds to current density of 30.86 A/mm^2, current level of phase current 200 Apk (141 A RMS) corresponds to current density of 19.84 A/mm^2, current level of phase current 100 Apk (70.71 A RMS) corresponds to current density of 9.92 A/mm2 and current level of phase current 50 Apk (35.36 A RMS) corresponds to current density of 4.96 A/mm^2. During the FEM analysis the average absolute temperature of 130 degree Celsius was taken into account for stator winding, while the average absolute temperature of 120 degree Celsius was taken into account for permanent magnet material. From the presented results in Fig. 2 (results are presented for battery voltage level of 700 V) it can be seen that the presented motor design with 36 slot/8 rotor poles exhibits excellent torque versus speed and output power versus speed characteristics.

Efficiency characteristics, copper and iron loss characteristics in dependency on speed and torque are presented for different current levels in Figs. 3 – 8.

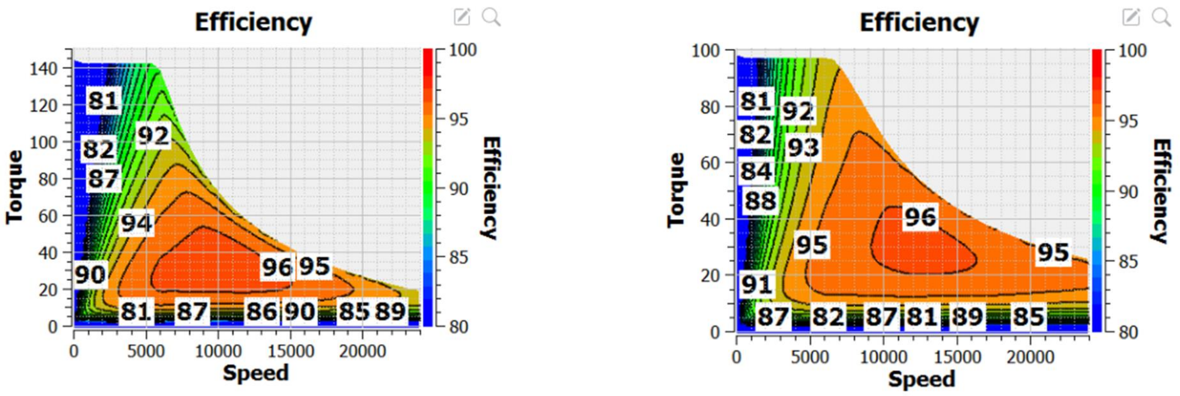

a.)

b.)

Fig. 3 Efficiency characteristics in dependency on speed and torque: a.) efficiency for current limit 311 Apk; b.) efficiency for current limit 200 Apk.

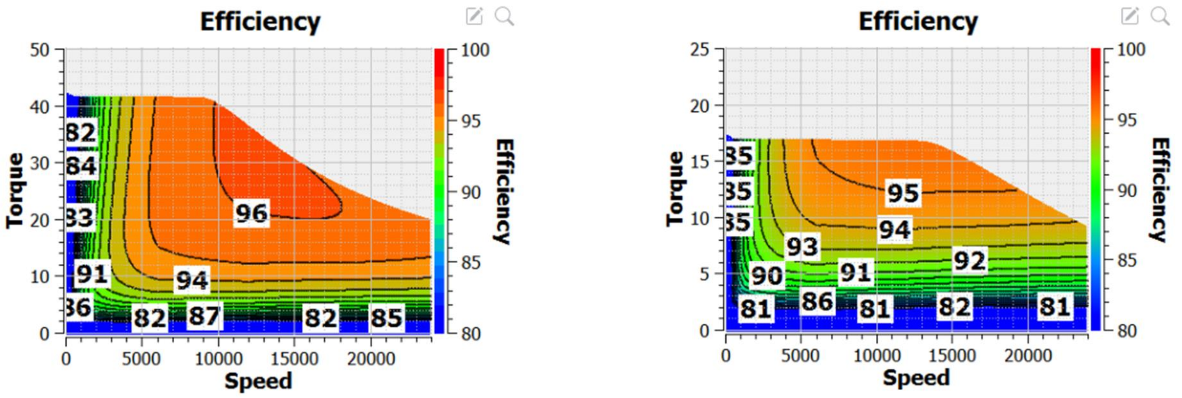

a.)

b.)

Fig. 4 Efficiency characteristics in dependency on speed and torque: a.) efficiency for current limit 100 Apk; b.) efficiency for current limit 50 Apk.

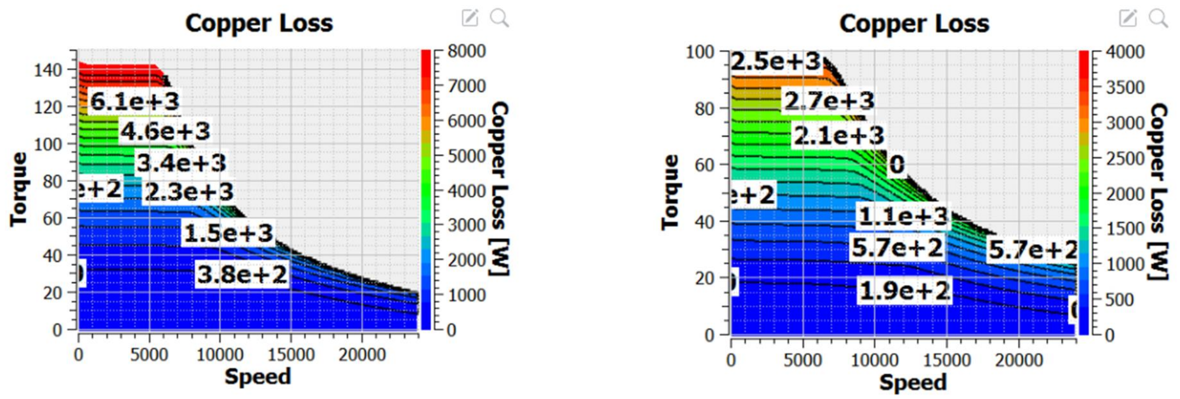

a.)

b.)

Fig. 5 Copper loss characteristics in dependency on speed and torque: a.) copper loss for current limit 311 Apk; b.) copper loss for current limit 200 Apk.

Results of loss characteristics were used for design of motor cooling system. The water cooling system with housing spiral water jacket with maximal fluid volume flow rate of 10 l/min and maximal inlet temperature of 65 degree Celsius was taken into account. Presented motor design in combination with water cooling system enables motor operation with continuous output power which exceeds 45 kW. In operation with continuous output power load the maximal absolute temperature in the motor hot spot does not exceed absolute temperature of 126 degree Celsius.

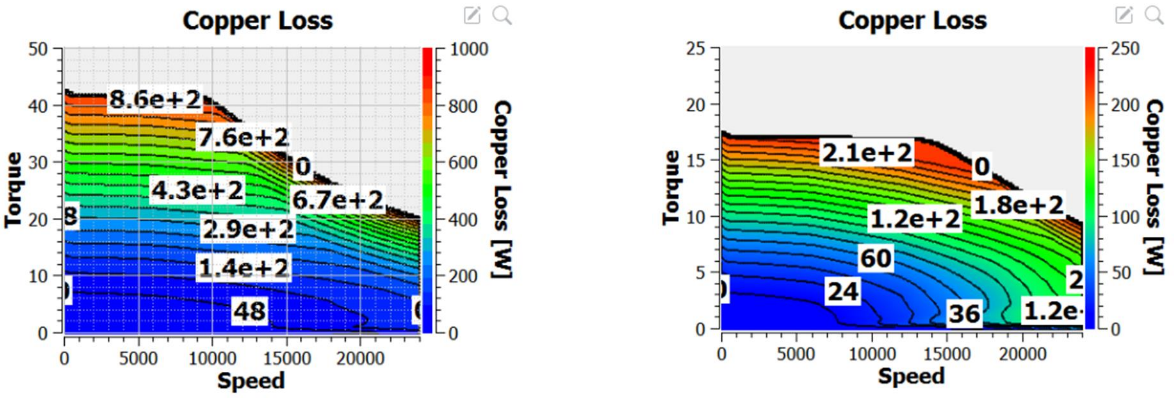

a.) b.)

Fig. 6 Copper loss characteristics in dependency on speed and torque: a.) copper loss for current limit 100 Apk; b.) copper loss for current limit 50 Apk.

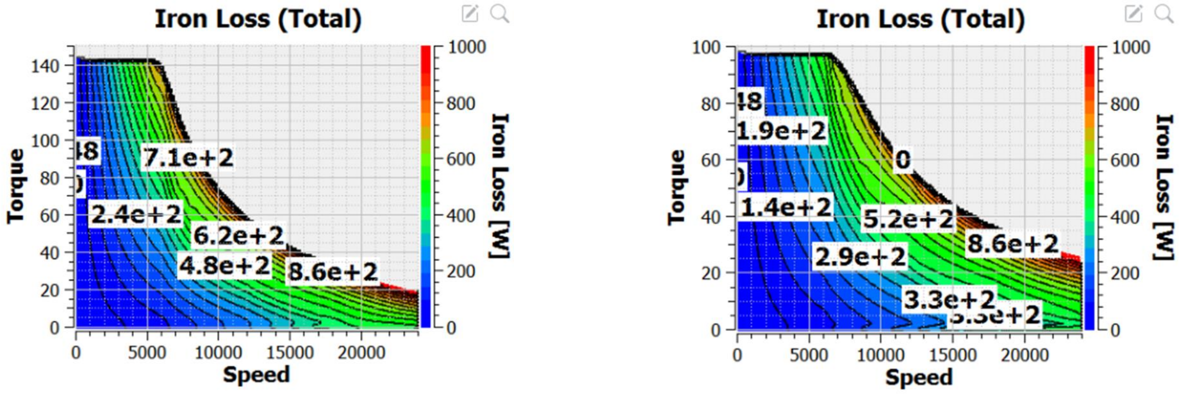

a.) b.)

Fig. 7 Iron loss characteristics in dependency on speed and torque: a.) iron loss for current limit 311 Apk; b.) iron loss for current limit 200 Apk.

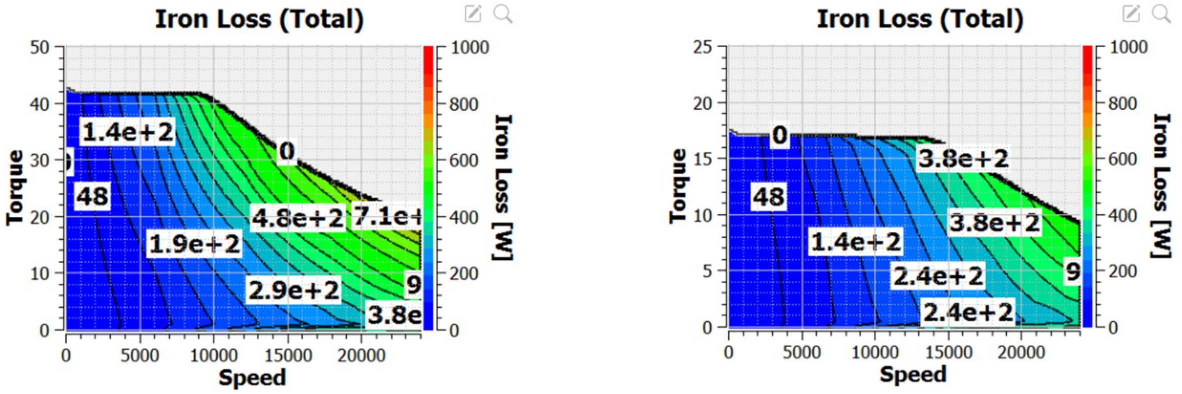

a.) b.)

Fig. 8 Iron loss characteristics in dependency on speed and torque: a.) iron loss for current limit 100 Apk; b.) iron loss for current limit 50 Apk.

3 Conclusion

According to the presented results it can be concluded that the presented IPMSM design can be a serious candidate for high-speed operation for energy-efficient electric propulsion system with 70 kW peak power motor power-rating. Designed water cooling system enables motor operation with continuous output power load which exceeds 45 kW.

Acknowledgement

This work was supported in part by the Slovenian Research Agency (ARRS) under the research grant for research programme Applied Electromagnetics P2-0114.

References

[1] Z. Wang, T. W. Ching, S. Huang, H. Wang, T. Xu, (2020), "Challenges Faced by Electric Vehicle Motors and Their Solutions", IEEE Access, DOI 10.1109/ACCESS.2020.3045716.
[2] L. Shao, A. E. H. Karci, D. Tavernini, A. Sorniotti, M. Cheng (2020), "Design Approaches and Control Strategies for Energy-Efficient Electric Machines for Electric Vehicles a Review", IEEE Access, DOI 10.1109/ACCESS.2020.2993235.

Optimising Stator Design of a Single Phase PM BLDC Motor for Improved Cogging Torque Profile

Lidija Petkovska, Goga Cvetkovski
Ss. Cyril and Methodius University in Skopje, Faculty of Electrical Engineering and Information Technologies
Skopje, North Macedonia, E-mail: lidijap@feit.ukim.edu.mk ; gogacvet@feit.ukim.edu.mk

***Abstract* – In the paper is presented a step-by-step development of the topology for a novel single phase permanent magnet (PM) brushless DC (BLDC) motor, aiming to improve its performance at more efficient utilisation of the active materials. The studied motor is based on a generic design, where asymmetrical, particularly shaped stator poles and respective shaping of the permanent magnets is applied. Accurate 2D finite element simulations were employed for numerical prototyping of the motor design, until the expected results were obtained. Based on FEA, cogging and static torque waveforms, along with other relevant performance characteristics are examined. The results show that the novel motor design and, in particular, the specific shape of the stator poles have the most important impact on the smooth operation of the studied single phase BLDC permanent magnet motor.**

1 Introduction

Single phase Permanent Magnet Brushless DC (PM BLDC) motors are widely used in low power applications. The most attractive features of this type of motor are the design simplicity and a low production cost. However, the torque ripple, as an important drawback of these PM motors, is a challenging matter for study and analysis. Hence, one of the intensively researched issues for single phase PM motors is the reduction of torque pulsations, caused by the variations in the reluctance of the magnetic circuit during rotation. The torque ripple at no-load caused by the motor topology, is referred to as cogging torque, and is one of the reference characteristics for assessing the motor performance. The general problems with cogging torque of PM motors have been intensively studied [1-3]. The measures for its mitigation have been proposed [4,5] and have been widely accepted. Although these techniques work quite well in multi-phase permanent magnet motors, they are not always valid in their single-phase counterparts.

In this paper are presented the results of our research work where, by optimising the stator topology, a remarkable performance improvement for a single phase permanent magnet brushless DC motor is achieved. For this purpose, after a series of FEM based numerical experiments have been performed, the best motor design is proposed and a comprehensive performance analysis of the novel motor is carried out.

2 Single Phase PM BLDC Generic Motor

The research starts with investigations of a typical widely used four-pole topology of a single phase PM BLDC motor, presented in Fig. 1, which is taken as *generic motor*.

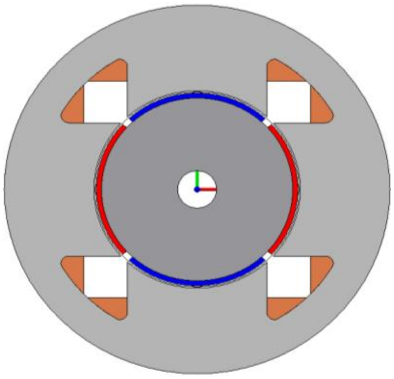

Fig. 1 Generic PM BLDC motor topology

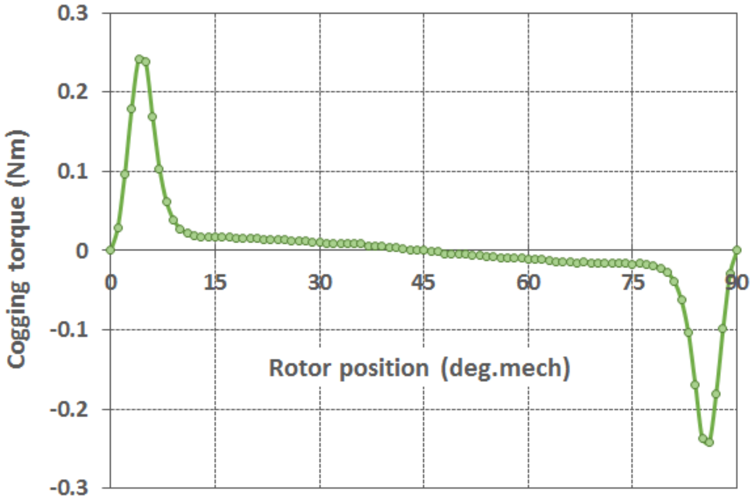

Fig. 2 Cogging torque profile of the generic motor

The research interest is focussed on the profile of cogging torque characteristic, presented in Fig. 2. Evidently, the generic PM BLDC motor exhibits good features of the both peak-value and the cogging torque profile.

From the first glance on Fig. 1, it is evident that inside the motor volume is built a large amount of the material for permanent magnets, as well as the iron for the stator core. This way the utilisation of active materials is certainly inefficient. In addition, the large mass of permanent magnet poles will significantly influence the motor production cost. Because of that, we propose to redesign the rotor poles and accordingly the stator core lamination. Our target is to transform this generic motor topology into a practical model with more efficient material utilization for stator core and for rotor permanent magnets, but without deteriorating the good profile of the cogging torque and low peak-value, while keeping a good motor performance as well.

3 Development of PM BLDC Motor Prototype

In the first step, taking the same shape of stator poles as in the generic PM BLDC motor from Fig. 1, the arc of the permanent magnets is reduced, and a *motor A* is derived; it is shown in Fig. 3 (a). Afterwards, with this redesigned PM shape, a *motor B* is developed, as shown in Fig. 3 (b), where the stator poles are with an arc corresponding to the pole arc of the new designed PMs.

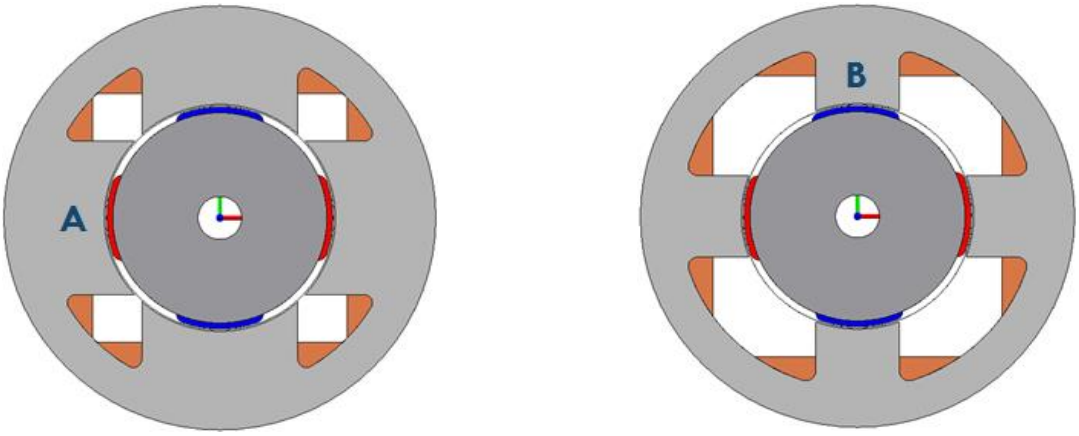

(a) Motor A

(b) Motor B

Fig. 3 Topology developments for PM BLDC motors

These new designed topologies for Motor A and Motor B have been intensively investigated by using FEA as a tool [6]. The focus was put on the cogging torque characteristics, presented in Fig. 4. Obviously, both the profile of cogging torque and especially the peak-value are in favour of Motor A; hence, with respect of torque ripples, Motor A will be better performing, than Motor B. However, the problem with iron usage for stator poles A is still existing and hence, further investigations for improved designs have to be carried out.

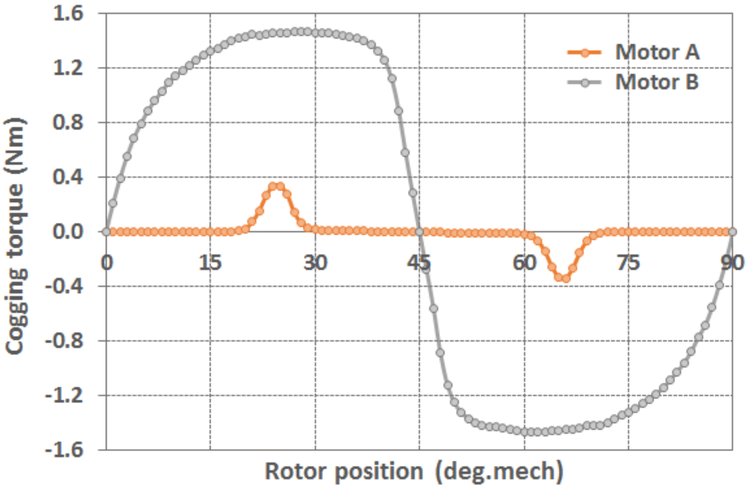

Fig. 4 Characteristics of cogging torque for Motor A and motor B

The original idea was to design a new motor with an asymmetric stator, where the neighbouring pairs of stator poles have different pole arc lengths. Hereafter, one stator poles pair is taken from the generic motor and is referred to as large pole A, while the other pair of poles, placed in between, is small pole B. For to simplify the motor manufacturing, despite different lengths of stator pole arcs, the built-in PMs are with the same arc lengths that coincide with the small stator pole arc. Consequently, an original combination of stator poles taken from the two motor models A and B is proposed, and a new Motor A–B is developed. In the further study, this motor model, which is presented in Fig. 5, is adopted as a *prototype* PM BLDC motor.

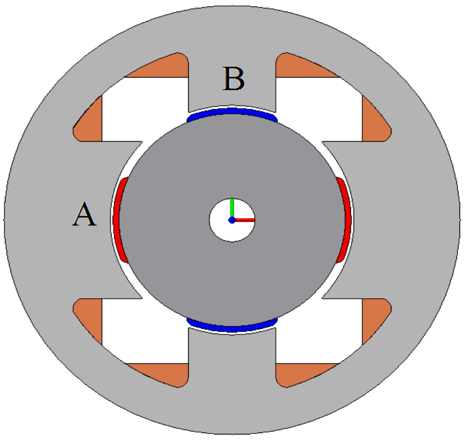

Fig. 5 Motor A-B: a prototype of PM BLDC motor

4 Designing and Shaping Stator Poles

To optimise the stator poles design and to improve performance characteristics of the studied motor, thorough investigations of this A–B topology, have been carried out. As might be seen in Fig. 5, the gap between two adjacent stator poles A and B is rather big, which will certainly worsen the cogging torque profile and the respective peak-value. Consequently, there is a need to reduce the inter-pole gap, through an extension of the large stator pole arc A.

In order to select the best ratio of the both stator pole arcs A and B, an investigative study of the prototype motor, based on extensive FEM calculations, is carried out and the small stator pole B arc of 42^0 is determined. Also, it has been found the large stator pole arcs (A) to be 3 times the width of the small stator pole arcs (B), defining the large stator pole A arc of 126^0. The PM arc, as was defined before, is same as for pole B, i.e. 42^0. The result of this designing procedure for the stator poles is that the gap between two adjacent poles A and B will be kept the same (6^0), as in the generic motor shown in Fig. 1. The air-gap length along the stator bore is constant. The sketch of the modified stator topology is presented in Fig. 6.

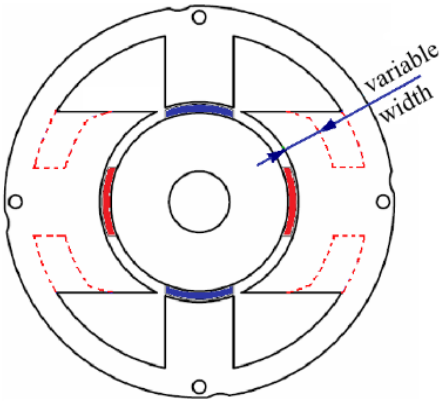

Fig. 6 Designing and shaping the stator poles of PM BLDC motor

As might be expected, the result of this operation is a larger cross-section of the stator pole A and again an inefficient utilisation of iron. Also, due to the bigger cross section, the stator pole A will be unsaturated to a greater extent than before. In order to achieve material saving and to create more winding space, a part of the iron from the large stator poles is removed to implement a classical *pole shoe design* [7], as depicted with the dotted line in Fig. 6. This shape modification of the stator pole A will certainly influence the level of pole body saturation, as well as the cogging and static torque waveforms and hence, the motor operation characteristics.

To investigate and to understand the effect of the proposed shape change, different pole shoe widths of the large stator pole A were investigated in the FE motor model. Starting with an unmodified stator pole without a pole shoe, full line in Fig. 6, a series of FEM simulations were performed, changing the radial pole shoe width from 1.5 mm to 12 mm. The width of 9 mm exhibits the best results [8]. It is worth emphasizing that the saturation of the pole neck and shoes, as well as the stator yoke have been avoided.

On the stator poles there are placed four concentrated windings. In the generic motor the total number of turns was 648 turns, got by 162 turns/pole, and is accepted to be kept the same in the novel motor design. Obviously, the different poles' cross sections will require different coils' design. For that reason, another issue to investigate is the number of turns per coil for pole A and for pole B, respectively. To obtain the smooth magnetic field distribution in the motor with new topology, and also the similar flux density values in the both poles A and B, the coils with different number of turns for A and B pole are proposed. To properly define their values, a significant research work has been involved. Implementing FEM based numerical experiment, the coil A was determined with W_A = 190 turns/pole, while the coil B with W_B = 134 turns/pole.

The proposed *novel motor* design with modified stator poles will affect the PM BLDC motor performance and operating characteristics, and in particular:

- the level and distribution of the flux in the stator core, leading to higher level of saturation;
- the winding linkage flux and hence, the back EMF value and shape;
- the cogging and static torque waveforms and hence, the motor operating characteristics.

As a final result of the research a *novel* PM BLDC *motor*, which has the reduced cogging torque and good performance characteristics, has been designed. The 3D view of the *novel motor topology* is shown in Fig. 7.

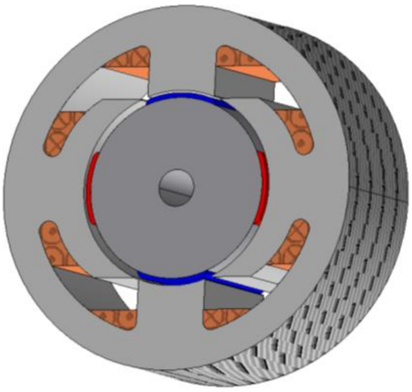

Fig. 7 The novel PM BLDC motor topology

5 Performance Analysis of the Novel PM BLDC Motor

The proposed *novel motor* design, derived from the *prototype motor* by modifying and shaping the large stator poles, will certainly have different performance and characteristics. Using FEA as well established numerical tool, a bulk of performance characteristics for the novel designed motor compared to the prototype motor, are determined [9]. The initial rotor position is defined when the stator poles axes are aligned with permanent magnet axes. The no-load and rated load operating regimes are considered and investigated. Magnetic field and the respective torque characteristics are computed, comparatively presented on charts and analysed.

5.1 No-Load Operation and Cogging Torque

Magnetic flux distribution at no-load is obtained when the magnetic field of the motor is energised by the permanent magnets only. Flux lines at the selected initial position, for the prototype and the novel motor are presented in Fig. 8 (a) and (b), respectively. It is evident that the saturation of the stator poles is avoided, although a huge amount of iron mass of the large pole body in the novel motor has been removed.

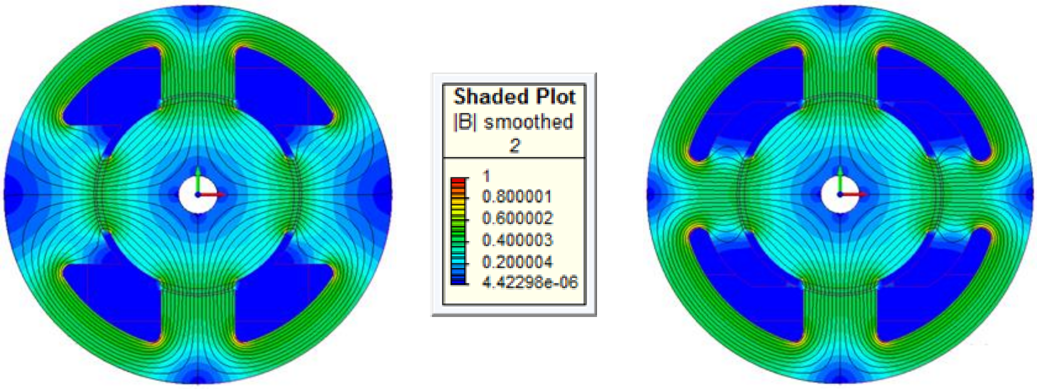

(a) Prototype motor

(b) Novel motor

Fig. 8 Magnetic flux distribution at no-load

The no-load operating regime, when the rotor is freely changing the position, enables calculation of the cogging torque characteristic, spanned over a rotor poles pitch [10]. Comparative cogging torque characteristics for the novel PM BLDC motor and for the prototype motor are presented on the chart in Fig. 9.

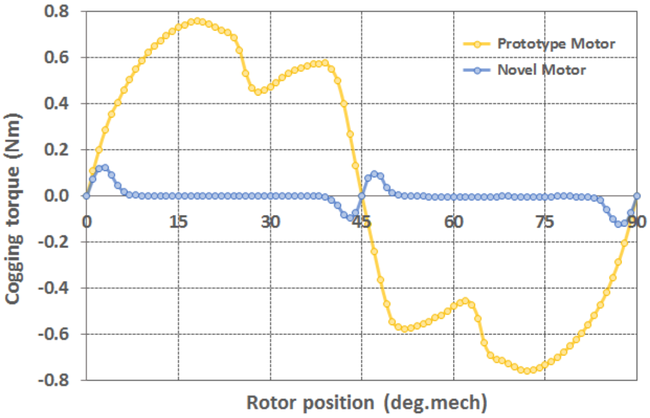

Fig. 9 Cogging torque comparative characteristics

Obviously, the PM BLDC motor with the novel topology produces a significantly lower peak cogging torque. In the novel motor it is 0.124 Nm, apart from the prototype with 0.758 Nm. i.e. the peak cogging torque is with more than six times lower value; even more it is with halved value compared to the generic motor (Fig. 2).

In addition, the profile of the novel motor, due to reduced gap between the stator poles and asymmetrical stator pole arcs, is smoother and with no significant oscillations along one pole pitch. Comparative characteristics for the novel PM BLDC motor and prototype motor, presented in the chart, evidently show that the novel motor produces a notably more favourable cogging torque profile.

5.2 Rated Load Operation and Static Torque

To evaluate the novel motor full performance, FEA analyses at load conditions have been accomplished. The computations start for rated current $I_n = 3.3$A, at the initial rotor position when the armature field and PM field are aligned. Magnetic field distribution for the both motor models, as presented in the Fig. 10, show more effective utilisation of iron in the novel motor, one of the targets in this study; at the same time, the maximum allowed flux density of 1.7 T in the stator yoke cross-section is not surpassed.

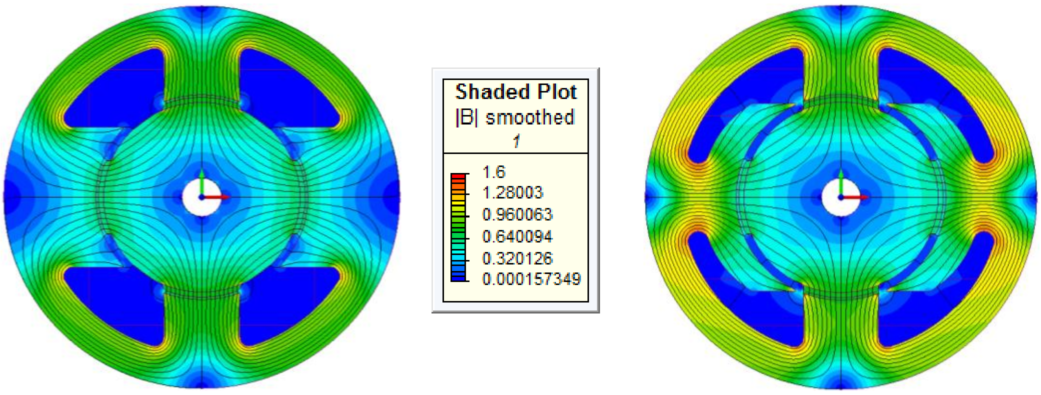

(a) Prototype motor

(b) Novel motor

Fig. 10 Magnetic flux distribution at rated current I_n and for aligned stator and rotor field axes

The load operating regime enables calculation of the static torque characteristics, for different armature currents and different rotor positions, along one pole pitch. The armature current is changed from zero up-to the rated value in several predefined steps, while the rotor position is changed quasi-statically for 1^0 along one pole pitch of 0–90^0 mechanical. Series of numerical calculations have been accomplished. The static torque characteristics at rated curent I_n for the both studied topologies are shown in Fig. 11.

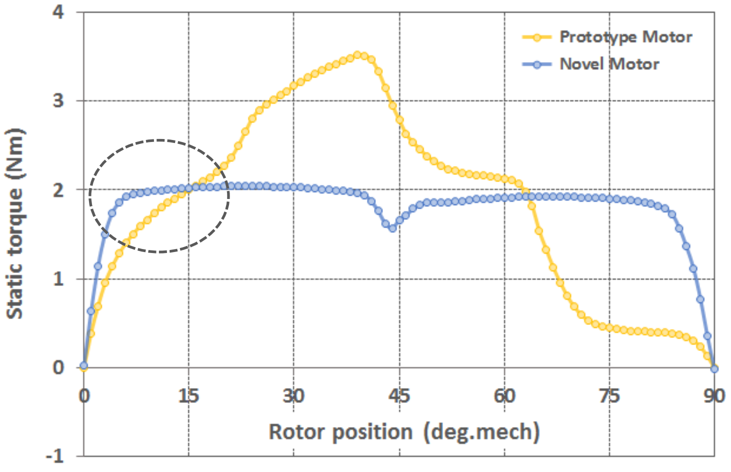

Fig. 11 Static torque comparative characteristics at rated current I_n

The novel motor exhibits maximum static torque of 2.042 Nm, which is only 0.58 of the pull-out toque of 3.524 Nm in the prototype motor. However, it is worth emphasising, that PM BLDC motors are not allowed to ever reach this working point. On the other hand, the average value of the static torque is higher in the novel motor and the profile is smoother, enabling operation with (almost) constant torque in a wide range for rotor positions. The first part of the curves, is more favourable in the novel motor: the torque increase is steeper, which will result in more stable motor starting.

In analysis conclusion, the *novel motor* evidently produces more favourable profile of the static torque characteristic. This fact proves that the target of this research work and corresponding tasks have been successfully accomplished.

6 Concluding Remarks

In the paper is presented step-by-step development of the topology for a novel single phase permanent magnet brushless DC motor, aiming to improve its performance with more effective utilisation of iron and PMs material. Accurate 2D finite element simulations have been employed for numerical prototyping of the motor design, until the expected results were obtained.

Afterwards, a comprehensive FEA was performed, and the cogging and the static torque waveforms were calculated, presented on charts and examined. The results showed that the novel motor topology with the specific shape of stator poles has an important impact on obtaining the smoother and better operation characteristics of the novel motor.

At the end, to answer in brief, why the proposed PM BLDC motor is considered to be novel? It is *novel* because the presented topology consists of:

- two stator pole pairs – with one small and one large pole, and with different arc lengths;
- the number of turns per pole is also different;
- the rotor magnets have the same arc length as the small stator pole arc of 42^0;
- the large stator pole arc is 3 times the length of the small arc, i.e. 126^0;
- the large stator pole is shaped with a pole shoe, with thickness 9 mm, creating more winding space and contributing to less iron utilisation, at no higher level of saturation;
- inter-pole gap of 6^0, kept the same as in the generic motor model, is sufficient for easy inserting the stator coils during the motor manufacturing.

All these unique features when combined together significantly reduce the peak-cogging torque and improve performance characteristics of the novel motor design.

The next foreseen challenge will be to investigate the techniques for reducing the peak-cogging torque and improving the novel motor performance characteristics, where the static electromagnetic toque will be of the highest interest.

References

[1] L. Ferraris, F. Franchini, E. Poskovic, (2015), "Design optimization of bonded PM BLDC motors with reference to the cogging torque amplitude", *Proceedings of the 41st Annual Conference of the IEEE Industrial Electronics Society*, Yokohama, Japan, pp. 001264-001269.

[2] M. Rezal, D. Ishak, (2019), "Performance enhancement of underwater propulsion motor using differential evolution optimization", *Indian Journal of Geo Marine Sciences*, **Vol. 48**, No. 7, pp. 1113-1119.

[3] Wrobel, R., Mellor, P. H., (2008), "Design Considerations of a Direct Drive Brushless Machine with Concentrated Windings", *IEEE Transactions on Energy Conversion*, **Vol. 23**, No. 1, pp. 1-8.

[4] C. Ocak, A. Dalcalı, E. Celik and D. Uygun, (2017), "FEA-Based Design Improvement of Small Scale BLDCMs Considering Magnet Thickness and Pole Embrace", *Int'l Journal of Computing, Communications & Instrumentation Engg.* (IJCCIE), **Vol. 4**, Issue 1, pp. 31-35.

[5] P. Ling, D. Ishak, T. L. Tiang, (2016), "Influence of magnet pole arc variation on the performance of external rotor permanent magnet synchronous machine based on finite element analysis", *Proceedings of IEEE International Conference on Power and Energy* (PECon), Melaka, Malaysia, pp. 552-557.

[6] https://www.plm.automation.siemens.com/global/en/products/simcenter/magnet.html

[7] S. Ahmed and P. Lefley, (2009), "Development of a Single Phase PM BLDC Motor from a Novel Generic Model", *Proceedings of the 11CHLIE*, published on CD, Zaragoza, Spain, pp. 1-5.

[8] P. Lefley, L. Petkovska and G. Cvetkovski, (2011), "Optimisation of the Design Parameters of an Asymmetric Brushless DC Motor for Cogging Torque Minimisation", *Proceedings of 14th International European Conference on Power Electronics and Applications* – EPE'2011, Birmingham, United Kingdom, published on CD, pp. 1-8.

[9] L. Petkovska, P. Lefley, G. Cvetkovski, (2011), "Static Characteristics of a Novel Low Cost Brushless DC Permanent Magnet Motor", *Proceedings of the 12th Portuguese-Spanish Conference on Electrical Engineering –* XIICLEEE'2011, Paper ID #1803, Ponta Delgada (Azores), Portugal, published on CD, pp. 1-6.

[10] P. Lefley, L. Petkovska and G. Cvetkovski, (2013), "In-Depth Cogging Torque Analysis of a Single Phase PMBLDC Motor", *Proceedings USB of the 16th ISEF*, Ohrid, Macedonia, pp. 1-8.

Efficiency Improvement of Permanent Magnet Motor Using Swarm Intelligence Algorithms

Goga Cvetkovski and Lidija Petkovska
Ss. Cyril and Methodius University, Faculty of Electrical Engineering and Information Technologies
Rugjer Bošković 18, P.O.Box 574, 1000 Skopje, North Macedonia
E-mail: gogacvet@feit.ukim.edu.mk, lidijap@feit.ukim.edu.mk

Abstract* – This paper presents a novel approach to the efficiency improvement of permanent magnet synchronous motor using several swarm intelligence algorithms as an optimisation tool. In this research work the following algorithms are used: particle swarm optimisation, cuckoo search, grey wolf algorithm and dragonfly optimisation algorithm. They all belong to the so called meta-heuristic optimisation group of algorithms, which so far have proven to be quite suitable for optimisation of standard mathematical functions. The idea is to implement those novel optimisation algorithms for the efficiency improvement of permanent magnet synchronous motor, where the objective function in the optimisation process is the efficiency of the investigated motor. Comparative analysis of the initial and the optimal solutions gained from the optimisations using different swarm intelligence algorithms is performed.

1 Introduction

The electric motor is the mechanism that transforms electrical energy into mechanical energy. Nowadays, electric motors are the cause of a considerable share of the use of electricity and therefore of the energy consumptions (70% in the industrial sector and 25-30% in the tertiary sector). Faced with ever-increasing energy demand and the overall strategy to reduce energy consumption in all the involved sectors, the use of efficiency enhanced electric motors is required. Generally, the efficiency of an electric motor depends on the type of motor, the size of the motor, the utilization factor, but also on the quality and quantity of the materials employed. In order all of this to be integrated into one energy efficient solution a good and reliable optimal design procedure is needed. To achieve this goal in the past three or four decades a variety of optimization methods have been used as tools for optimal design of power devices. Following this trend, a variety of optimization methods are used today for optimal design of electrical machines.

In general, the optimization methods can be divided into two groups: deterministic and stochastic methods. The term stochastic methods generally refer to the use of randomness in the objective function or in the optimization algorithm performance. They are challenging optimization algorithms that can be very successfully applied in high-dimensional nonlinear objective problems, problems that contain multiple local optima in which deterministic optimization algorithms may get stuck. Stochastic optimization algorithms provide an alternative approach that permits less optimal local decisions to be made within the search procedure that may increase the probability of the procedure locating the global optima of the objective function. They can be also divided in two general groups of methods such as: direct search methods and nature inspired algorithms. The nature inspired method are divided in the following groups: evolutionary algorithms, swarm intelligence algorithms, human based algorithms and physics-chemistry based algorithms, as presented in Fig. 1.

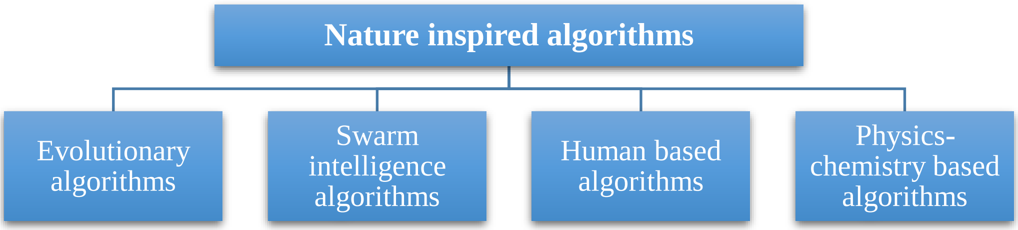

Fig. 1. Nature inspired algorithms

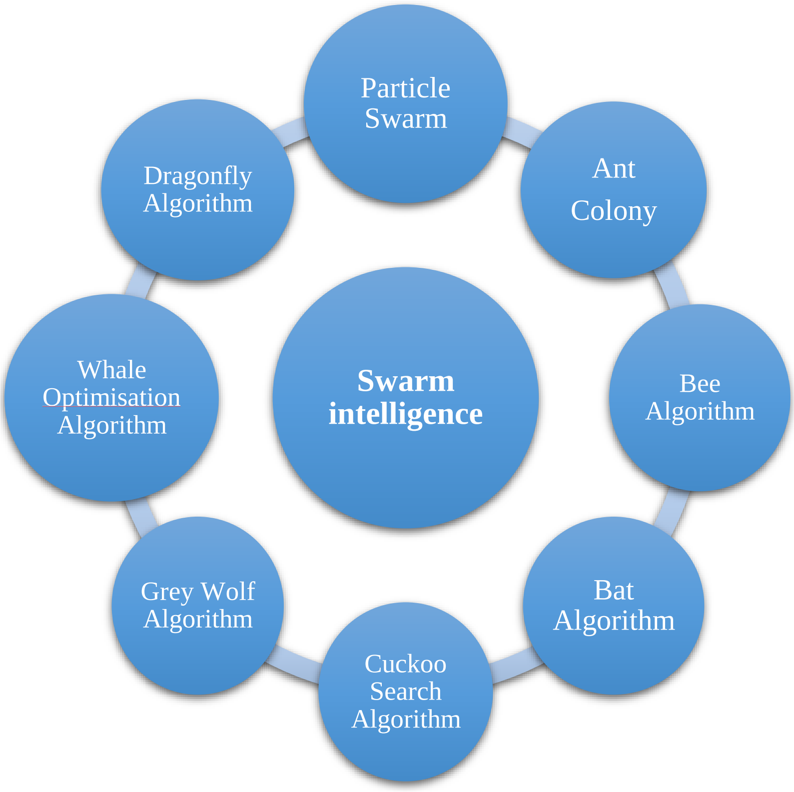

Fig. 2. Swarm intelligence algorithms

In this paper the application of swarm intelligence algorithms in the optimal design of a permanent magnet synchronous motor is presented and analyzed. A graphical presentation of some of those methods is shown in Fig. 2. From the presented swarm intelligence algorithms, the following methods have been selected for the research work in this paper: Particle Swarm Optimization Algorithm (PSOA), Cuckoo Search Algorithm (CSA), Grey Wolf Algorithm (GWA) and Dragonfly Algorithm (DFA). In the following text a brief introduction to the above mentioned algorithms is presented.

2 Swarm Intelligence Algorithms

In the past two or three decades the stochastic optimisation methods have been successfully used in optimisation and optimal design of various power devices.

The use of randomness in the algorithms often means that the techniques are referred to as "heuristic search" as they use a rough rule-of-thumb procedure that may or may not work to find the optima instead of a precise procedure. Many stochastic algorithms are inspired by a biological or natural process and may be referred to as "metaheuristics" as a higher-order procedure providing the conditions for a specific search of the objective function. They are also referred to as "black box" optimization algorithms. There are many stochastic optimization algorithms and their number has reached over 150 and is rising day by day.

The stochastic nature of the procedure means that any single run of an algorithm will be different, given a different source of randomness used by the algorithm and, in turn, different starting points for the search and decisions made during the search. The pseudorandom number generator used as the source of randomness can be seeded to ensure the same sequence of random numbers is provided each run of the algorithm. This is good for small demonstrations and tutorials, although it is fragile as it is working against the inherent randomness of the algorithm. Instead, a given algorithm can be executed many times to control for the randomness of the procedure. This idea of multiple runs of the algorithm can be used in two key situations: comparing algorithms and evaluating final result. Algorithms may be compared based on the relative quality of the result found, the number of function evaluations performed, or some combination or derivation of these considerations. The result of any one run will depend upon the randomness used by the algorithm and alone cannot meaningfully represent the capability of the algorithm. Instead, a strategy of repeated evaluation should be used.

Here are some examples of stochastic optimization algorithms [1,2]: Iterated Local Search, Stochastic Hill Climbing, Stochastic Gradient Descent, Tabu Search, Greedy Randomized Adaptive Search Procedure. In the following text some examples of stochastic optimization algorithms that are inspired by biological or physical processes include: Simulated Annealing, Evolution Strategies, Genetic Algorithm, Differential Evolution, Particle Swarm Optimization etc. As mentioned previously those methods can be grouped in four groups:

- Evolutionary algorithms, (Genetic algorithms, Evolutionary strategies, Differential evolution, etc.)
- Swarm intelligence algorithms, (Particle swarm, Cuckoo search, Grey wolf, Dragonfly, Ant colony, etc.)
- Human based algorithms (Harmony search, Cooperative search, Cultural evolution, etc.)
- Physics-chemistry based algorithms (Simulated annealing, Gravitational search, Artificial chemical process, etc.).

The aim of this research work is to implement several particle swarm optimisation algorithms in the optimal design process of permanent magnet synchronous motor. Therefore, a brief presentation of the investigated algorithms (Particle swarm optimisation, Cuckoo search, Grey wolf and Dragonfly) is presented in the following text.

2.1 Particle Swarm Optimisation Algorithm

Particle Swarm Optimization algorithm (PSOA) is a swarm intelligence algorithm that is based on the analogy of swarm of bird and school of fish [3]. PSOA mimics the behaviour of individuals in a swarm to maximize the survival of the species. In PSO, each individual makes his decision using his own experience together with other individuals' experiences. The algorithm, which is based on metaphor of social interaction, searches a space by adjusting the trajectories of moving points in a multi-dimensional space. The individual particles are drawn stochastically toward the position of present velocity of each individual, their own previous best performance, and the best previous performance of their neighbours.

2.2 Cuckoo Search Algorithm

Cuckoo search algorithm (CSA) is inspired by the egg-laying and parasitic behaviour of the Cuckoo bird [4]. The adult birds lay their eggs in other birds' nests. They choose nests where the host bird just laid its eggs. The optimization algorithm follows three main hypotheses. The first is that each adult bird lays only one egg each time. The second is that the adult Cuckoo bird puts its eggs in randomly chosen nest and the best found nest is saved for the next generation. The last hypothesis is that the host bird can discover the strange egg with a probability $p_d \in [0, 1]$. It is known that animals search for food follows a random or at least a quasi-random pattern in nature. The foraging path can be seen as a random walk as it is affected by the current location and the transition probabilities to neighbouring locations. For Cuckoo, and many birds and insects, this random walk has characteristics of a Levy flight where the step sizes are evaluated according to a heavy-tailed probability distribution.

2.3 Grey Wolf Algorithm

Grey wolf algorithm (GWA) is a relatively new metaheuristic algorithm developed in 2014 [5]. It is a population-based stochastic algorithm for finding the optimal result from the solution set (population). GWO algorithm is inspired from grey wolves that belong to Canidae family which simulates the behaviour of leadership quality and the social hunting mechanism of grey wolves in three steps as tracking, encircling and attacking. There are particularly four types of grey wolves namely alpha (α), beta (β), delta (δ) and omega (ω) having a strict social dominant hierarchy.

2.4 Dragonfly Algorithm

The main inspiration of the Dragonfly algorithm (DFA) [6] originates from the dragonflies that are considered as small predators that hunt almost all other small insects in nature. The interesting fact about dragonflies is their unique and rare swarming behaviour. Dragonflies swarm for only two purposes: hunting and migration. The former is called static (feeding) swarm, and the latter is called dynamic (migratory) swarm. The two essential phases of optimization, exploration and exploitation, are designed by modelling the social interaction of dragonflies in navigating, searching for foods, and avoiding enemies when swarming both ways.

In this work all the presented optimization algorithms are implemented in the procedure for efficiency improvement of a permanent magnet synchronous motor and the optimization results are compared.

3 Optimisation Results

The efficiency of the motor is selected as an objective function in the efficiency improvement of the permanent magnet motor. The investigated object in this work is a brushless three-phase permanent magnet synchronous motor (PMSM) that has a laminated stator with 36 slots and a rotor with 6-skewed $SmCo_5$ surface-mounted permanent magnets with $B_r = 0.95$ T. The rated data of the motor are: I=18 A, T=10 Nm and n=1,000 rpm at frequency of 50 Hz.

The following motor parameters have been selected as optimisation parameters in the optimization procedure realised with the different swarm intelligence algorithms: outside radius of the rotor iron core R_{ro}, permanent magnet fraction f_m, permanent magnet radial height h_m, air-gap g, and axial active length of the motor L. The presentation of the optimized motor and the optimization parameters are presented in Fig. 3.

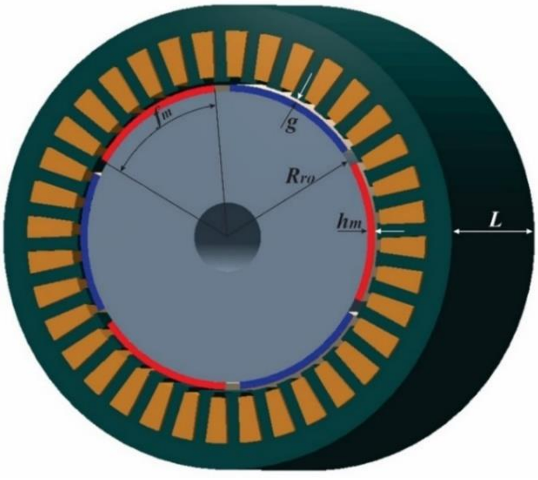

Fig. 3. Presentation of the permanent magnet synchronous motor and its optimization parameters

The efficiency of the motor used for the optimisation in general can be defined with the following equation:

$$Efficiency(R_{ro}, f_m, h_m, g, L) = \frac{T \cdot \omega_m}{T \cdot \omega_m + P_{Cu} + P_{Fe} + P_{wf}} \tag{1}$$

where: T–rated torque, ω_m –rated speed, P_{Cu} – ohmic power loss, P_{Fe} – iron core loss and P_{wf} – windage and friction power losses. In the mathematical model [7] of the motor for the efficiency improvement each of the power losses are properly defined in relation to the optimization parameters. The same mathematical model and objective function is applied in all the swarm optimization algorithms. In the case of the PSOA efficiency improvement the objective function is defined with the efficiency, where in the case of CSA, GWA and DFA the objective function is defined as an inverse value of the efficiency, because those three optimization methods are defined as minimization methods. In such case the minimization of the objective function maximizes the efficiency of the motor.

In order the search to be feasible each optimization parameter is defined in its upper and lower bounds. There values as well as the values for the initial solution are presented in Table 1.

Table 1 Optimization parameters and their boundaries

Variables	Lower boundary	Upper Boundary	Initial model
R_{ro} (m)	0.03798	0.4642	0.042
g (m)	0.00072	0.00088	0.0008
f_m (/)	0.81	0.99	0.90
h_m (m)	0.0018	0.0022	0.002
L (m)	0.081	0.099	0.09
Efficiency	-	-	0.8489

The optimisation process is realised for a large number of runs for all algorithms. A presentation of the objective function value change during the iterations for the best search for the analysed algorithms is presented in Fig. 4.

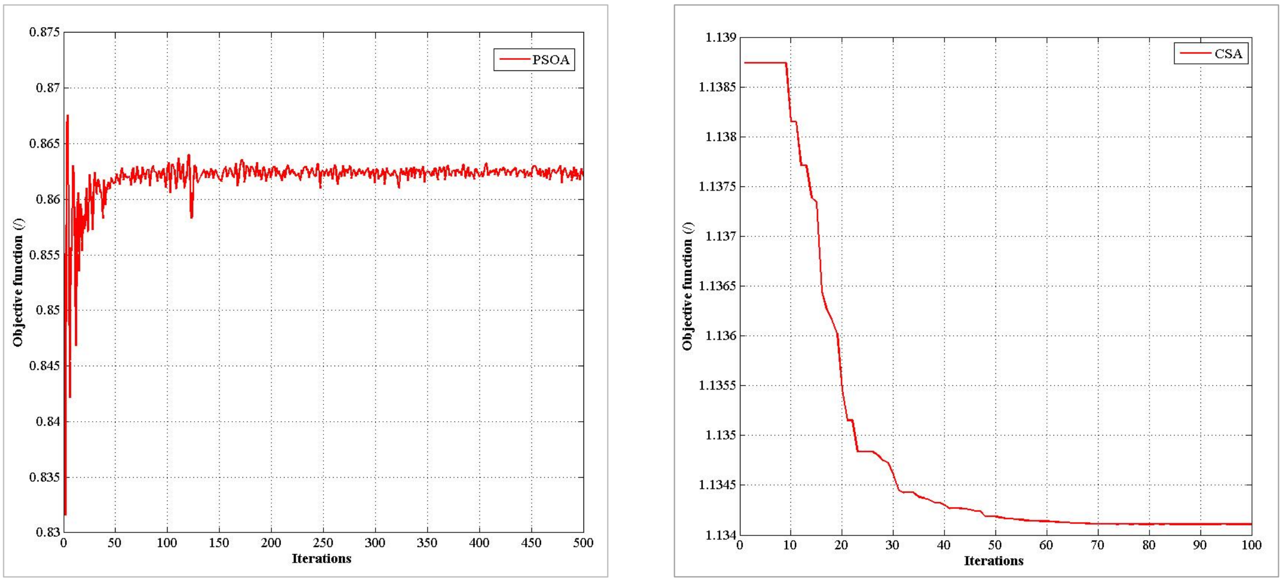

a) Particle swarm optimization algorithm

b) Cuckoo search algorithm

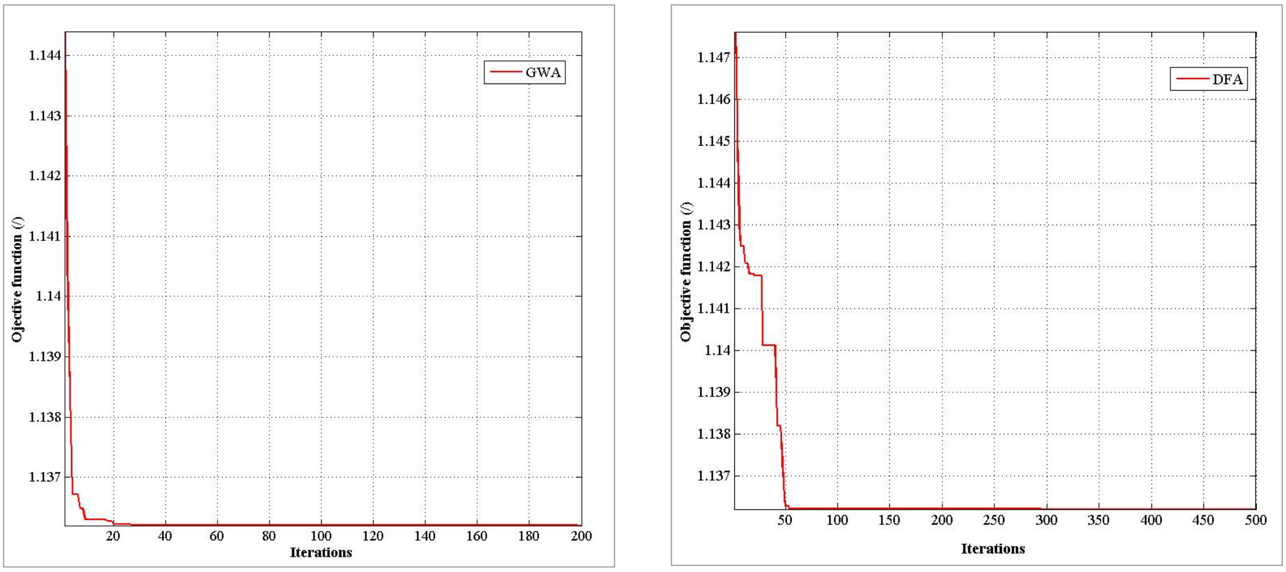

c) Grey wolf algorithm

d) Dragonfly algorithm

Fig. 4. Objective function value change during iterations

The results of the optimisation procedure realised with the investigated optimisation algorithms are presented in Table 2. In Table 2, due to the stochastic nature of the investigated algorithms, only the best solution for each algorithm is presented. The presented data includes the values for each optimization parameter, the value of the objective function as well as the value of the efficiency of the motor.

Table 2 Optimization results

Optimization parameters	Initial motor	PSOA	CSA	GWA	DFA
R_{ro} (m)	0.042	0.0412	0.0378	0.03798	0.03798
f_m (/)	0.9	0.82	0.9143	0.90705	0.90701
h_m (m)	0.002	0.00195	0.0022	0.0021	0.0021
g (m)	0.0008	0.00072	0.00072	0.00076	0.00076
L (m)	0.09	0.09813	0.099	0.0945	0.0945
Objective function (/)	-	0.8676	1.136235	1.136196	1.136196
Efficiency	0.8489	0.8676	0.8801	0.88013	0.88013

For further solution analysis additional motor parameters and quantities are presented in Table 3. The presented parameters and their values are: N – number of turns per phase of the stator winding, B_g – air gap flux density, R_{ph} – stator winding phase resistance, P_{Cu} – stator winding copper power losses, P_{Fest} – stator core iron power losses, m_{Cu} – total mass of the stator winding, m_{FeS} – total mass of stator iron core, m_{FeR} – total mass of rotor iron core, m_{PM} – total mass of permanent magnets and *Efficiency* – efficiency of the motor

Table 3 Comparative presentation of motor parameters

Parameters	Prototype	PSOA solution	CSA solution	GWA solution	DFA solution
N (turns)	9	9	8	8	8
B_g (T)	0.5868	0.572	0.61964	06012	0.61622
R_{ph} (Ω)	0.1564	0.1207	0.0921	0.0888	0.0943
P_{Cu} (W)	147.091	135.849	99.8397	111.3839	112.7449
P_{Fest} (W)	17.357	17.4099	20.3934	19.18865	19.870
m_{Cu} (kg)	1.5979	2.0422	2.3292	2.3117	2.1757
m_{FeS} (kg)	3.5878	3.5248	4.1309	3.888	4.0273
m_{FeR} (kg)	3.243	2.795	2.7599	2.6646	2.6646
m_{PM} (kg)	0.36497	0.3522	0.4041	0.36639	0.39185
Efficiency (/)	0.8489	0.8676	0.8801	0.88013	0.88013

Based on the presented data in Table 2 and Table 3 it can be noticed that the GWA and DFA in their optimization process have reached the highest values of the objective function (0.88013), and CSA reached a value (0.8801) very close to the values of the previously mentioned algorithms. In this analysis the PSOA unfortunately reached the smallest value of the objective function (0.8676). Generally speaking, all investigated methods have reached a higher value of the motor efficiency in relation to the efficiency of the initial solution (0.8489). In relation the efficiency improvement of the presented solutions the other motor parameters also face certain improvement as well.

For further detailed analysis of the four optimal solution in relation to the initial motor modes of the permanent magnet synchronous motor, a calculation of the magnetic field will be performed for all models. This approach will be used to calculate main electromagnetic and electromechanical characteristics [8, 9] of the motor models that will be used for their more detailed analysis.

4 Conclusion

In this paper the authors are giving a brief presentation, as well as implementation of different swarm based optimization algorithms. Particle swarm optimization algorithm, cuckoo search algorithm, Frey wolf algorithm and Dragonfly algorithm are the investigated and implemented algorithms in the efficiency improvement of the permanent magnet synchronous motor. Selected results from the application of the four different optimization methods and a comparative analysis are presented. Finally, the several motor solutions in relation to the initial solution have been analysed based on the presented values and few solutions have been proposed. Additionally, for a more detailed investigation a traditional finite element method analysis for the initial solution and a selected number of optimized solutions will be performed in other near future works.

References

[1] J. C. Spall, (2003), "Introduction to Stochastic Search and Optimization: Estimation, Simulation, and Control", *John Wiley & Sons, Inc.*, New Jersey, pp. 1-617.

[2] S. Uryasev, P. M. Pardalos, (2001), "Stochastic Optimization: Algorithms and Applications", *Applied Optimization,* **Vol. 54**, Springer, New York, pp. 1-438.

[3] J. Kennedy, (1997), "The Particle Swarm: Social Adaptation of Knowledge", *Proceedings of the IEEE International Conference on Evolutionary Computation*, pp. 303-308.

[4] X-S. Yang, S. Deb, (2010), "Engineering Optimization by Cuckoo Search", *International Journal of Mathematical Modelling and Numerical Optimization*, **Vol. 1 (4)**, pp. 330–343.

[5] S. Mirjalili, S, M. Mirjalili, A. Lewis, (2014), "Grey Wolf Optimizer", *Advances in Eng. Soft.*, **Vol. 69**, pp. 46– 61.

[6] S. Mirjalili, (2016), "Dragonfly Algorithm: A New Meta-Heuristic Optimization Technique for Solving Single-Objective, Discrete, and Multi-Objective Problems", *Neural Computer & Application*, **Vol. 27**, pp. 1053–1073.

[7] L. Petkovska, G. Cvetkovski, (2021), Innovative Motors and Shape Optimisation, Chapter 4 of the Book Optimal Design Exploiting 3D Printing and Metamaterials, *IET*, pp.139-188. (Editors: Paolo Di Barba, Sławomir Wiak)

[8] Infolytica, "User's Manual", 2016.

[9] Motor Solve, Infolytica Co. "User's Manual", 2016.

Efficiency and Power Capability Maximization of Interior Permanent Magnet Synchronous Motors with Ferrite Permanent Magnets

Bojan Ġtumberger [1,2], Iztok Brinovar[1], Klemen Sredenġek[1], Miralem Hadģiselimovií [1,2], Sebastijan Seme[1,2], Amor Chowdhury[1]and Gregor Srpļiļ [1]

[1] University of Maribor, Faculty of Energy Technology, Hočevarjev trg 1, 8270 Krško, Slovenia,
bojan.stumberger@um.si, iztok.brinovar1@um.si, klemen.sredensek@um.si, miralem.h@um.si,
sebastijan.seme@um.si, amor.chowdhury@um.si, grega.srpcic@um.si

[2] University of Maribor, Faculty of Electrical Engineering and Computer Science, Koroška cesta 46, 2000 Maribor, Slovenia

<u>Abstract</u> ï The paper presents efficiency and power capability performance comparison of interior permanent magnet synchronous motors (IPMSMs) with fractional slot concentrated windings (FSCWs) and ferrite permanent magnets. Performances of four basic rotor configurations with radial and/or tangential permanent magnets were compared on the basis of the finite element analysis (FEA).

1 Introduction

Interior permanent magnet (IPM) synchronous motors (SMs) with fractional slot concentrated windings (FSCWs) without heavy rare earth (HRE) PM material in the rotor structure have been the object of intense investigations in recent years [1], [2]. Although some important guidelines for selection of several design factors have been reported, general recommendations for rotor type selection (radial or tangential PM configuration, the most appropriate stator slot-rotor pole number combination) for different applications are still not available in the literature. This work is an attempt to fill the gap in this field.

2 Results of the FEA

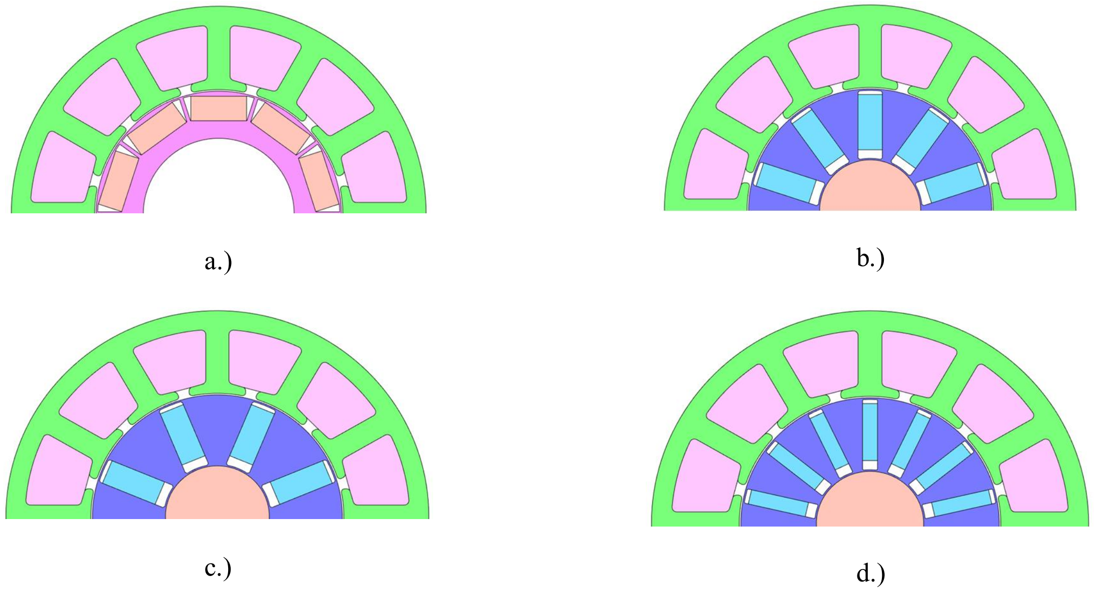

a.) b.) c.) d.)

Fig. 1 Motor cross-section: a.) 12 slot/10 pole FSCW IPM motor with radial PM configuration; b.) 12 slot/10 pole FSCW IPM motor with tangential PM configuration; c.) 12 slot/8 pole FSCW IPM motor with tangential PM configuration; d.) 12 slot/14 pole FSCW IPM motor with tangential PM configuration.

---

[1] University of Maribor, Faculty of Energy Technology, Hočevarjev trg 1, 8270 Krško, Slovenia, e-mail: bojan.stumberger@um.si

[2] University of Maribor, Faculty of Electrical Engineering and Computer Science, Koroška cesta 46, 2000 Maribor, Slovenia

Results of the FEA for four basic rotor configurations with the most promising slot-pole combination were accounted for in the presented comparison. Results for the following slot-pole combinations of IPM motors with FSCWs are presented: 12 slot/10 pole motor with radial PM placement, 12 slot/10 pole motor with tangential PM placement, 12 slot/8 pole motor with tangential PM placement and 12 slot/14 pole motor with tangential PM placement. Cross-sections of FSCW IPM motors with ferrite PM material taken into comparison are presented in Fig. 1 (the same quality of electrical steel material and the same quality of PM material has been used in all motors included in the comparison of the results). All motors' dimensions are limited to the outside stator diameter equal to 110 mm and stack length equal to 50 mm. Efficiency maps for 12 slot/10 pole motors taken into comparison are presented in Fig. 2. and Fig. 3. Efficiency map for 12 slot/8 pole motor and efficiency map for 12 slot/14 pole motor are presented in Fig. 4. and Fig. 5.

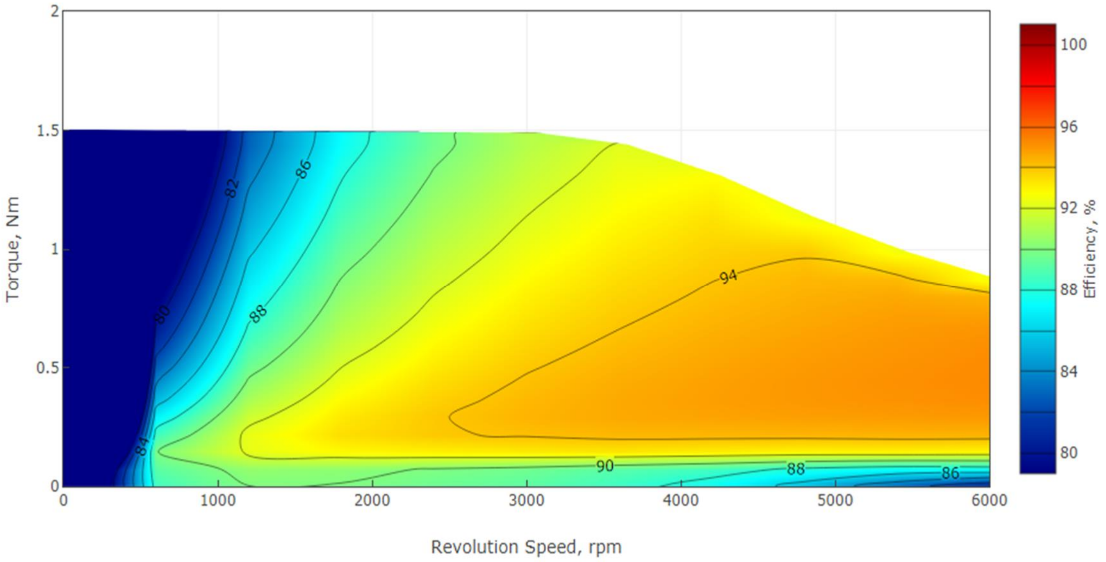

Fig. 2 Efficiency map of 12 slot/10 pole FSCW IPM motor with radial PM configuration, phase current limit of 2.3 A (RMS value).

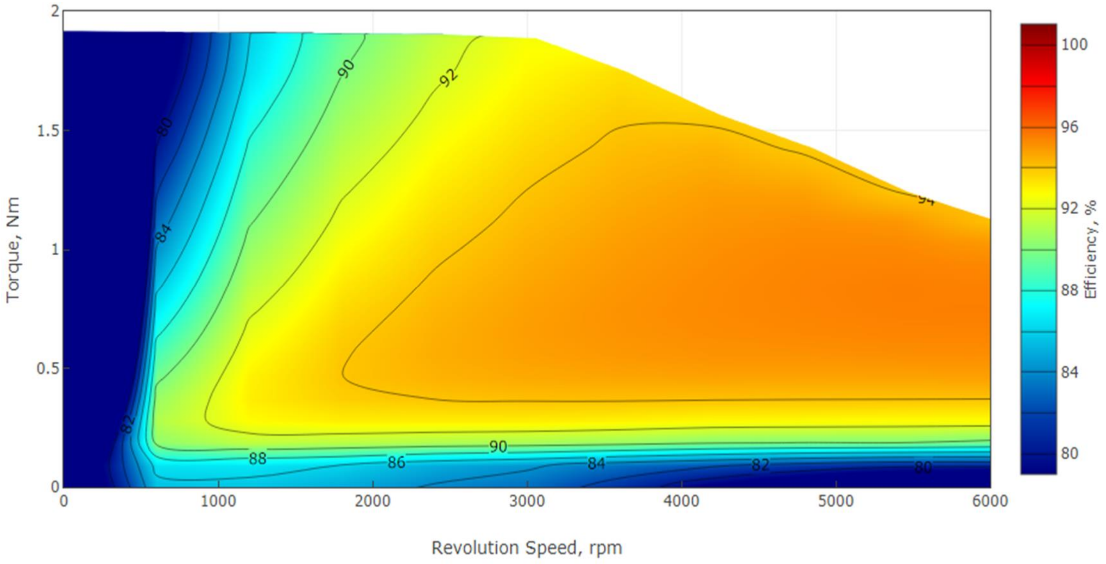

Fig. 3 Efficiency map of 12 slot/10 pole FSCW IPM motor with tangential PM configuration, phase current limit of 2.3 A (RMS value).

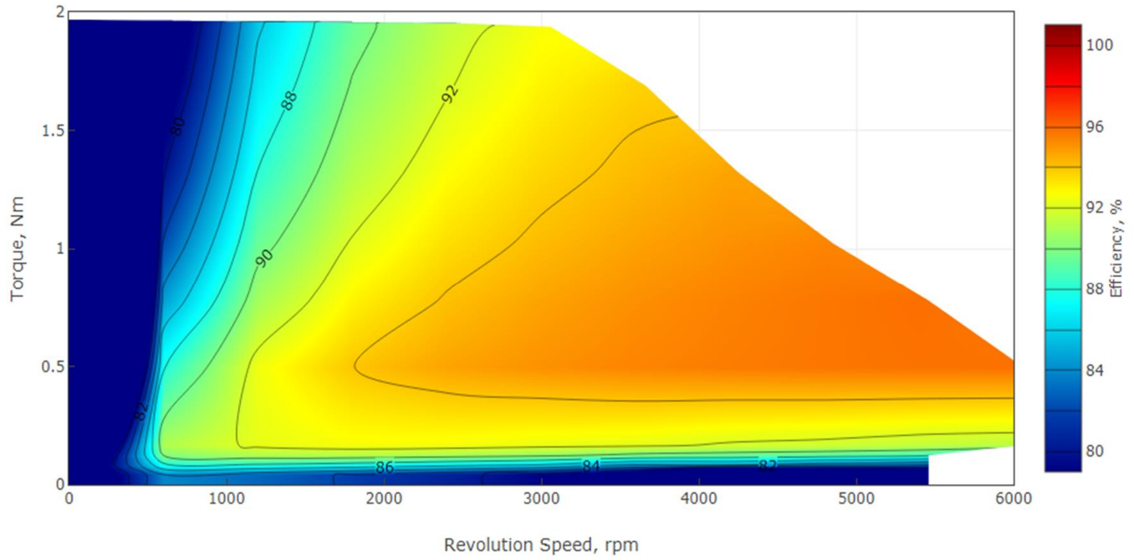

Fig. 4 Efficiency map of 12 slot/8 pole FSCW IPM motor with tangential PM configuration, phase current limit of 2.3 A (RMS value).

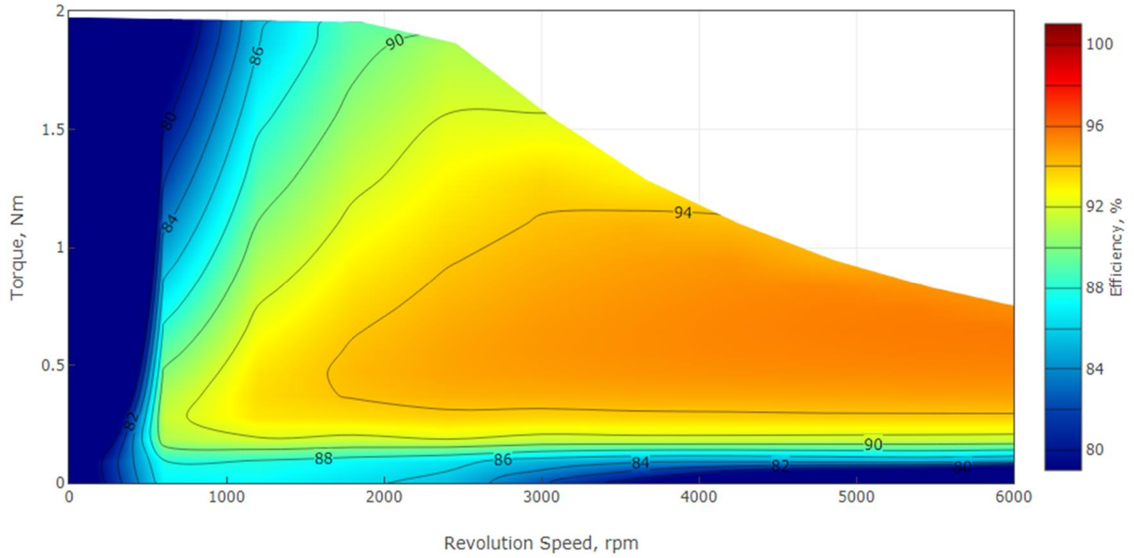

Fig. 5 Efficiency map of 12 slot/14 pole FSCW IPM motor with tangential PM configuration, phase current limit of 2.3 A (RMS value).

Comparison of efficiency maps for IPM motors with different rotor configuration reveals that the lowest maximal torque capability at low speed exhibits 12 slot/10 pole FSCW IPM motor with radial PM configuration. FSCW IPM motors with tangential PM configurations exhibit comparable torque capability at low speed. Situation at higher speed level, however, is changed. While both 12 slot/10 rotor pole configurations (with radial and tangential PM placement) exhibit good torque capability at higher speed level, the torque capability of 12 slot/8 pole motor and 12 slot/14 pole motor were decreased significantly.

3 Experimental results

In order to check the correctness of the presented results, the experimental prototype of 12 slot/10 pole FSCW IPM motor with tangential PM configuration in rotor structure has been built and tested. The experimental prototype test results for 35 mm stack height are presented in Fig. 6 at speed 4300 rpm for different line-to-line voltage levels. From the presented results in Fig. 10 it can be concluded that the high efficiency level can be obtained by using 12 slot/10 pole FSCW IPM motor with tangential PM configuration.

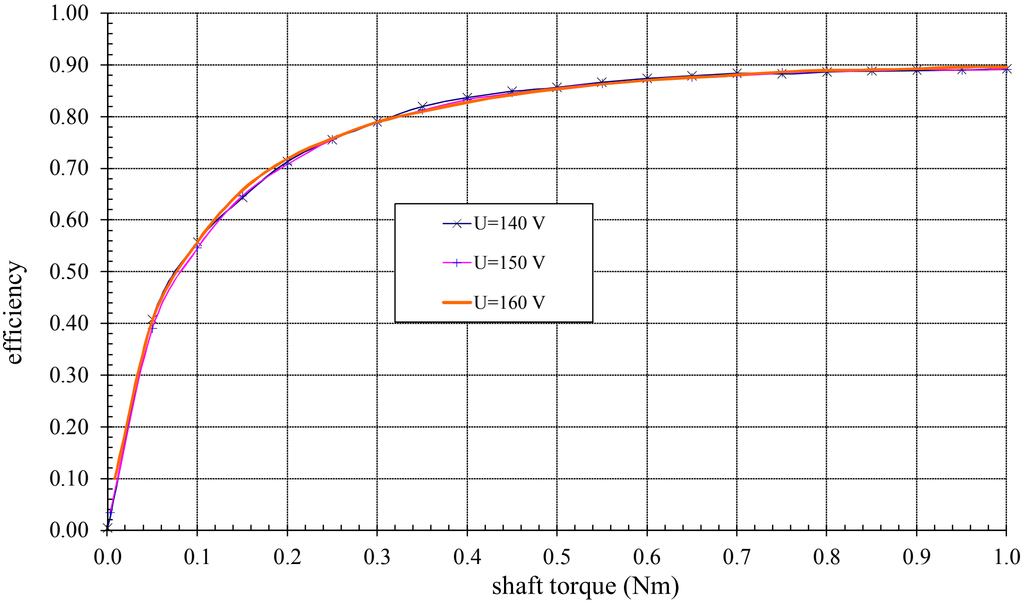

Fig. 6 Efficiency of 12 slot/10 pole FSCW IPM motor with tangential PM configuration versus shaft torque at 4300 rpm for different value of line-to-line voltage

4 Conclusion

According to the presented results it can be concluded that the best torque capability at low and high speed level can be obtained with 12 slot/10 pole FSCW IPM motor with tangential PM configuration. The similar statement is valid for the efficiency over the wide range of speed and torque level. The highest efficiency can be obtained with 12 slot/10 pole FSCW IPM motor with tangential PM configuration.

Acknowledgement

This work was supported in part by the Slovenian Research Agency (ARRS) under the research grant for research programme Applied Electromagnetics P2-0114.

References

[1] E. Carraro, N. Bianchi, S. Zhang, M. Koch, (2018), “Design and performance comparison of fractional slot concentrated winding spoke type synchronous motors with different slot-pole combinations”, IEEE Transactions on Industry Applications, Vol. 54, No. 3, May/June 2018, pp. 2276-2284.

[2] S. G. Lee, J. Bae, S. W. H. Kim, (2018), “A study on the maximum flux linkage and the goodness factor for the spoke-type PMSM”, IEEE Transactions on Applied Superconductivity, Vol. 28, No. 3, April 2018, Art. No. 5200705.

PM-SynRM rotor design and optimization with multi objective differential evolution for better torque and torque ripple performance

Gregor Srpčič[1], Miralem Hadžiselimović[1,2], Iztok Brinovar[1], Klemen Sredenšek[1], Sebastijan Seme[1,2], Bojan Štumberger[1,2]

[1] Faculty of energy technology, University of Maribor, Hočevarjev trg 1, 8270 Krško, Slovenia, grega.srpcic@um.si,
[2] Faculty of Electrical Engineering and Computer Science, University of Maribor, Koroška cesta 46, 2000 Maribor, Slovenia

***Abstract** –This paper will present the results of the design and optimization of a permanent magnet synchronous reluctance motor rotor (PM-SynRM) with multi objective differential evolution (MODE) algorithm based on finite element analysis. Based on the design of a stator, a basic reluctance rotor was designed and optimized with MODE algorithm. Maximization of torque and minimization of torque ripple were the objectives of the optimization, which was carried out for a reluctance rotor without magnets, with ferrite magnets, and with permanent magnets for the cases of 3 segmental flux barriers.*

1 Introduction

Synchronous reluctance motors (SynRm) are an attractive alternative to induction motors because they allow better torque to weight ratio, higher efficiency, and higher overload capability. The stator of the reluctance motor is similar to that of a standard induction machine. Hence rotor geometry is different with multiple flux barriers. Various configurations of flux barriers are possible regarding their number, shape, and dimension. The advantages of reluctance motors can be further improved by inserting ferrite or neodymium permanent magnets into rotor flux barriers. The obtained machine can be referred to as a permanent magnet synchronous reluctance motor (PM-SynRM). [1-3]

The basic idea of the paper is to evaluate two performance goals for the SynRM and PM-SynRM using multi objective differential evolution (MODE) algorithm in SyRE software and finite element analysis (FEA) in software FEMM. By alternating the dimensions and position of flux barriers and the dimension, position and number of ferrite and neodymium magnets, maximization of torque and minimization of torque ripple will be the two performance goals for both machine types. Minimizing torque ripple is a fundamental aspect since torque ripple can be very high in case of poor design choices. [1-2]

2 Initial reluctance motor design and data

The stator of the designed machine is Kienle Spiess IEC 71/4.62. The length of the stator and rotor are 60 mm made of steel M330-50A. The winding of the motor is a four-pole single-layer winding.

The initial SynRM rotor design was basic. The radius of the rotor was 31 mm, and shat radius was 10 mm. The rotor of the SynRM had three segmental flux barriers. For the optimization of torque and torque ripple performance following MODE algorithm parameters were used: 30 generations with a population size of 60. Optimization goals were 2,4 Nm torque and a maximum 10 % torque ripple peak-to-peak.

MODE algorithm initially had two degrees of freedom – flux barrier positions and width. As soon as the SynRM rotor was designed, ferrite and permanent magnets were added to flux barriers, and the position and dimension of magnets were optimized. Finally, designed PM-SynRMs were optimized again for better torque and torque ripple performance by allowing only one degree of freedom – offset of flux barriers. The same procedure was made for the same parameters for the stator and the rotor of the initial design, but this time the optimized rotor had four flux barriers.

The main FEA simulation parameters were: electric current 1,7 A, current phase angle was at 50 elt°, current overload 2, and motor speed at 2400 rpm for 20 rotor positions. According to [3], optimizing SynRM at current overload produces better results in torque ripple performance since motors with low torque ripple at overload conditions are likely to have low torque ripple at lower currents. However, if a machine is optimized at low currents, it usually has a higher torque ripple at overload currents. [3]

The initial design had a maximum calculated torque of 4 Nm and 10,5 % of torque ripple peak-to-peak.

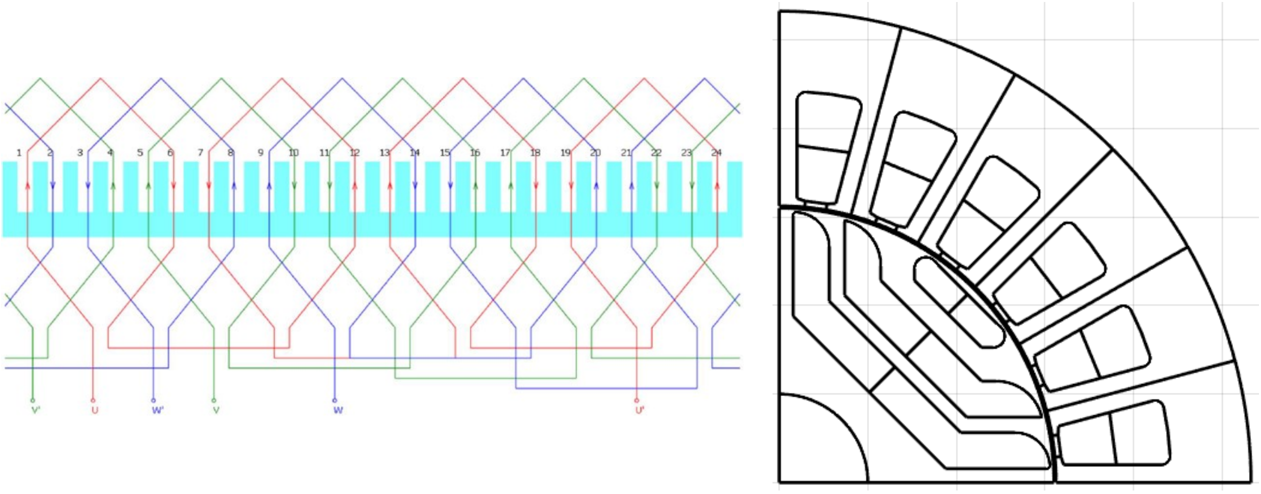

Fig. 1 Winding of the considered motor (left), initial SynRM geometry (right)

3 Results

The SynRM rotor optimization results are shown in Fig 1, which shows the Pareto front of the optimized 3 barrier rotor for maximum torque and minimum torque ripple. Pareto fronts were also obtained for the case of SynRM with Ferrite 35H magnets and SynRM with N30UH permanent magnets.

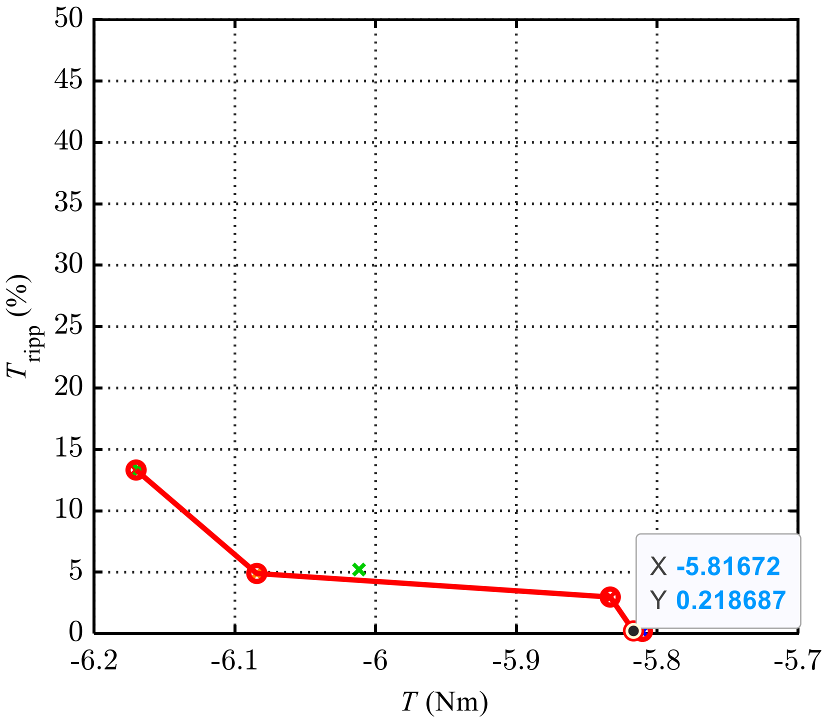

Fig. 2 Pareto front for maximum torque and minimum torque ripple of the designed SynRM with 3 flux barriers

The best cases for each optimized design are arranged in Table 1, and their geometry is shown in Fig 3. For the reluctance motor with segmental flux barriers, where flux barrier position and width were optimized, maximum calculated torque was 5,8 Nm and minimum torque ripple 0,22 percent. This geometry was taken as the base for inserting permanent magnets. First, optimization of the number and width of ferrite permanent magnets was made. Compared to the reluctance motor, the torque was higher in this case, namely 7,22 Nm, but also torque ripple was higher, but still in the desired range of 10 % peak to peak. Furthermore, ferrite magnets were changed to neodymium N30UH permanent magnets, and again number and dimensions of the magnets were changed during the optimization. In this case, as expected, torque was even higher compared to previous cases, but also torque ripple was too high at 15,5 %. In order to further lower the torque ripple, more local search optimization runs for the SynRM with N30UH permanent magnet design regarding position, number, and dimensions of magnets should have been done.

Table 1 Optimization results for the 3 barrier rotor

	SynRM	SynRM with Ferrite 35H magnets	SynRM with N30UH permanent magnets
T (Nm)	5,8	7,22	10,31
Tripp (%)	0,22	8,27	15,57

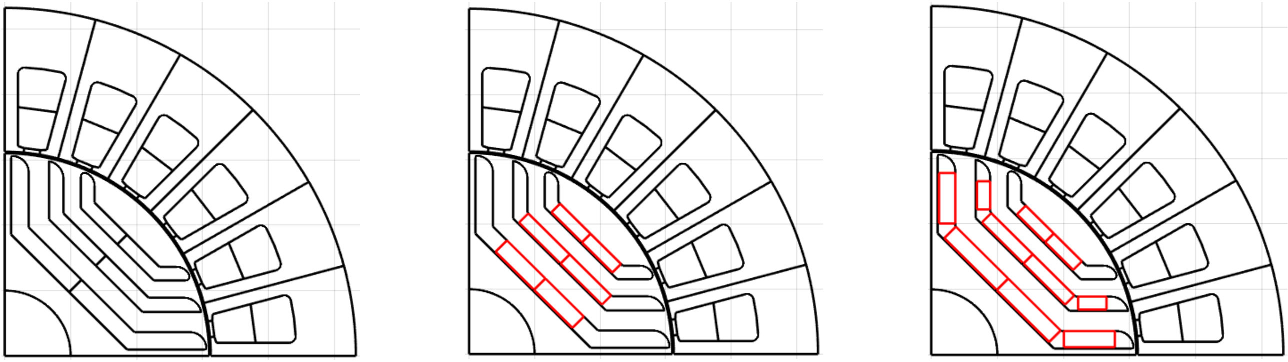

Fig. 3 Optimized rotor with 3 flux barriers geometries for Syn RM (left), SynRM with Ferrite 35H magnets (middle), and SynRM with N30UH permanent magnets (right)

Fig 4 shows the Pareto front of the optimized 4 barrier rotor for maximum torque and minimum torque ripple. Pareto fronts were also obtained for the case of SynRM with Ferrite 35H magnets and SynRM with N30UH permanent magnets for the 4 barrier rotor, and the results for best cases are shown in table 2, together with rotor geometries shown in Fig.5

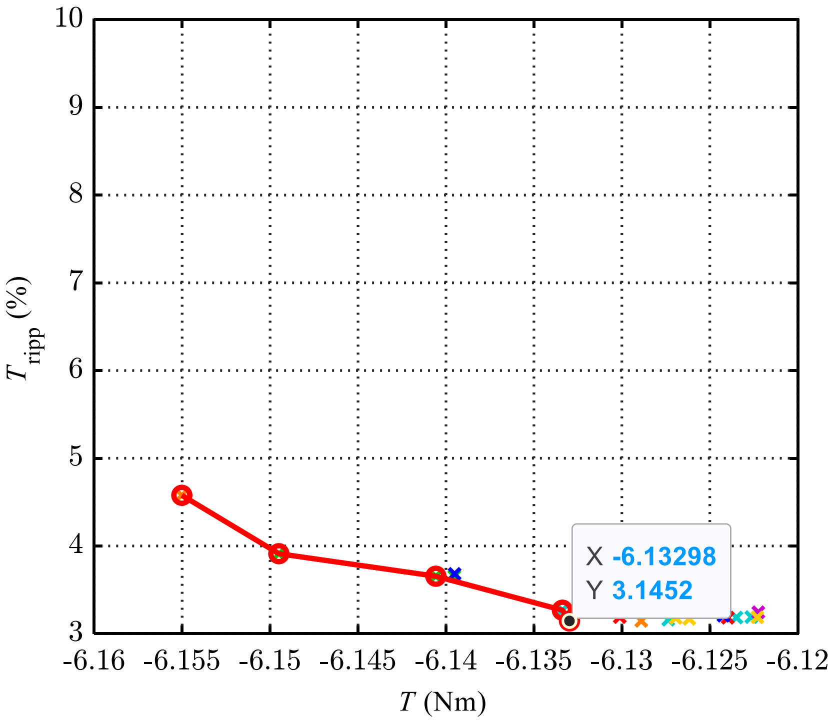

Fig. 4 Pareto front for maximum torque and minimum torque ripple of the designed SynRM with 4 flux barriers

As stated in [4] and [5], if the number of rotor flux barriers increases, the motor is more likely to produce a low torque ripple since it produces a lower magneto motive force harmonic content. As can be seen from Table 2, maximum torque remained similar in the case of the 4 barrier rotor compared to the previous one. Nevertheless, torque ripple was much lower for the rotors with ferrite 35H magnets and neodymium N30UH permanent magnets and is now in the desired range of 10% peak to peak for all three variations.

Table 2 Optimization results for the 4 barrier rotor

	SynRM	SynRM with Ferrite 35H magnets	SynRM with N30UH permanent magnets
T (Nm)	6,14	7,45	9,05
Tripp (%)	3,15	5,13	8,67

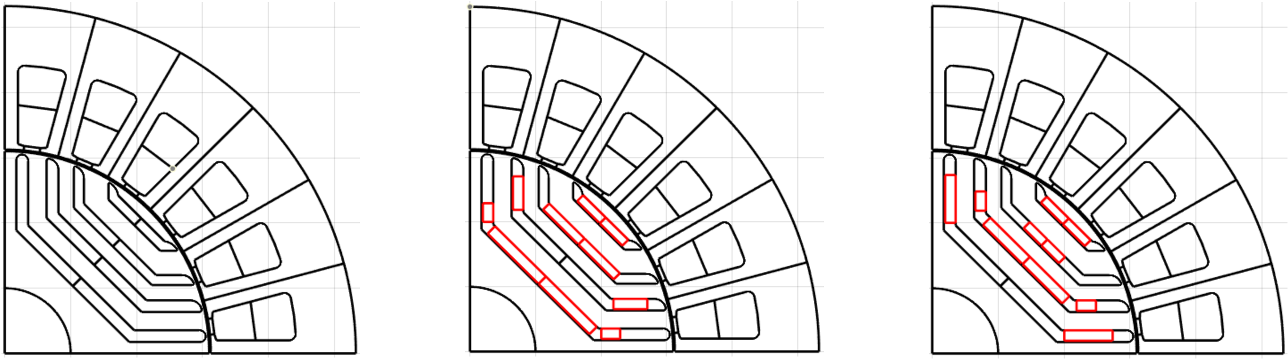

Fig. 5 Optimized rotor with 4 flux barriers geometries for Syn RM (left), SynRM with Ferrite 35H magnets (middle), and SynRM with N30UH permanent magnets (right)

4 Conclusion

This paper presented a rotor geometry optimization of SynRM and PM-SynRM for better torque and torque ripple performance by optimizing flux barrier positions and width, and later also position, number, and the dimension of magnets. This was done for rotors with 3 and 4 segmental flux barriers since a higher number of flux barriers generally produces lower torque ripples.

Compared to the initial design for the best case of SynRM, maximum torque is 50% higher. Ferrite and neodymium magnets further improved torque production. In terms of torque ripple for the case of SynRM, it was more than 3 times lower. Torque ripple was also lower for both PM-SynRM cases compared to the initial design. As expected, the optimized SynRM had the lowest torque ripple, and the highest torque was obtained with the optimized rotor with neodymium permanent magnets. In all cases, optimization goals were achieved.

As further work, obtained rotors will be checked for mechanical properties (von Misses stress and deformation) at different rotational speeds, and in case of good results, prototypes will be made in order to confirm the results of the optimization with the MODE algorithm.

References

[1] F, Cupertino, G. M. Pellegrino, C. Gerada, “A SyR an IPM machine design methodology assisted by optimization algorithms”, *IEEE Energy conversion congress and exposition*, 2012, pp. 3686-3691.

[2] F, Cupertino, G. M. Pellegrino, C. Gerada, “Design od synchronous reluctance motors with multiobjective optimization algorithm”, *IEEE Transactions on industry applications”*, **Vol. 50**, No. 6, pp. 3617-3627.

[3] G. Pellegrino, F. Cupertino, C. Gerada, “Automatic design of synchronous reluctance motors focusing in barrier shape optimization”, *IEEE Transactions on industry applications”*, **Vol. 51**, No. 2, pp. 1465-1474.

[4] F. Uberti, L. Frosini, L. Szabo, “An optimization procedure for a synchronous reluctance machine with fluid shaped flux barriers”, *2020 International Conference on Electrical Machines (ICEM)*, 2020, pp. 389-395.

[5] M. Palmieri, M. Perta, F. Cupertino, G. Pellegrino, "Effect of the numbers of slots and barriers on the optimal design of synchronous reluctance machines", *2014 International Conference on Optimization of Electrical and Electronic Equipment (OPTIM)*, 2014, pp. 260-267

The 8th International Symposium on Applied Electromagnetics – SAEM'2022

Struga, North Macedonia, 26-29 June 2022

Analysis of the Country's Energy Efficiency

Janusz Sowiński
Czestochowa University of Technology, Czestochowa, Poland, E-mail janusz.sowinski@pcz.pl

Abstract ***–One of the priority tasks in the country's energy economy is the improvement of energy efficiency. Sectoral energy consumption indicators enable the monitoring of the country's energy economy. The analysis of sectoral ODEX indicators is essential for predicting energy savings. The courses of the ODEX indicators were modeled with stochastic differential equations. Solving the equations using the Euler method enables the simulation of curves in the medium-term horizon. The results of simulation and analysis of the ODEX indicators were presented.***

1 Introduction

Improving energy efficiency on a national and EU scale requires the observation of trends in energy consumption of end users, sectors of the economy and the entire economy. Assessing progress in improving energy efficiency allows policymakers to make decisions that support positive change. Hence the necessity for researchers to undertake projects aimed at developing tools for energy efficiency analysis. A valuable method of analysis was developed within the Odyssee-Mure project coordinated by ADEME, France and sponsored by the H2020 EC program [1]. ODEX coefficients [2] have been defined to assess energy savings and thus improve energy efficiency. The method was also recognized in Poland and the above coefficients were used in the GUS database [3]. The article attempts to assess the improvement of energy efficiency by 2030 on the basis of the forecast of ODEX coefficients and to confront the results with the EU requirements in this regard.

2 Definition of ODEX indicators

The ODEX indicator is the index used in the ODYSSEE-MURE project [1]. The purpose of the ODEX index is to measure the energy efficiency progress by main sector (industry, transport, households) and for the whole economy (all final consumers). The Energy Efficiency Index ODEX is the weighted average of the unit consumption rates of end-users or sectors. The weights are the shares of each end-user or sectors in the total energy consumption of those consumers or sectors. Using the ODEX indicator, it is possible to determine savings in energy consumption.

3 Requirements for energy efficiency imposed by the EU and Polish Government

The legal status of energy efficiency in Poland is currently defined by three documents:

- Directive 2012/27/EU of the European Parliament and of the Council of 25 October 2012 on energy efficiency [4]
- New Act on Energy Efficiency(AEE) adopted by the Polish Parliament on May 20, 2016 [5]
- Directive 2018/2002/EU of the European Parliament and of the Council of 11 December 2018 amending Directive 2012/27/EU on energy efficiency [6]

Directive 2012/27/EU of 25 October 2012 on energy efficiency, adopted in order to intensify activities in this area, obliges EU Member States to introduce energy efficiency improvement instruments in order to achieve the target of 20% savings in primary energy consumption by 2020 year. In the case of Poland, the primary energy consumption target was set at 96.4 Mtoe. Directive 2018/2002 of 11 December 2018 amending Directive 2012/27/EU on energy efficiency introduced the target of improving energy efficiency of 32.5% by 2030.

The new AEE Act should be adopted in achieving a specified energy savings level by the end of 2020 by means of modernization of energy installations in private and public buildings. The new AEE Act will provide for more efficient energy usage and will increase the innovativeness of the Polish economy. The AEE Act sets forth an obligation of the Minister of Energy to prepare every three years a national plan for energy efficiency. The AEE encourages to participate in public tenders for "white certificates" (i.e. energy efficiency certificates issued by the President of the Energy Regulatory Office for companies supporting efficiency) and trade them on the Polish Power Exchange (currently companies selling energy, heat or gas to end users are obliged to obtain and present a certain number of white certificates for redemption in order to meet the requirements of the current AEE, otherwise they are required to pay a substitution fee).

In Poland, the current Act of 20 May 2016 on Energy Efficiency and the amendment to the Act of 20 April 2021 introduce a national final energy savings target to be achieved by the end of 2030. From 2021 to 2030, energy savings should amount to 5.58 Mtoe. The target set for 2030 will be implemented through a system of energy efficiency certificates and the so-called alternative measures. The system of energy efficiency certificates is commonly known as white certificates and imposes an annual obligation on obliged entities to save energy. An alternative method of fulfilling the statutory obligation is the payment of a substitute fee by the obliged entity. Alternative measures were introduced as a way to achieve the national final energy savings target for 2030. There are programs and instruments to improve energy efficiency. The obligation to achieve certain energy savings was imposed on energy companies operating in the field of production or trade in electricity, heat or natural gas.

4 Statistical data

The statistical data in the publication [3] are prepared by the Polish National Energy Conservation Agency and Statistics Poland, Enterprises Department according to the Eurostat methodology (ODYSSEE database).

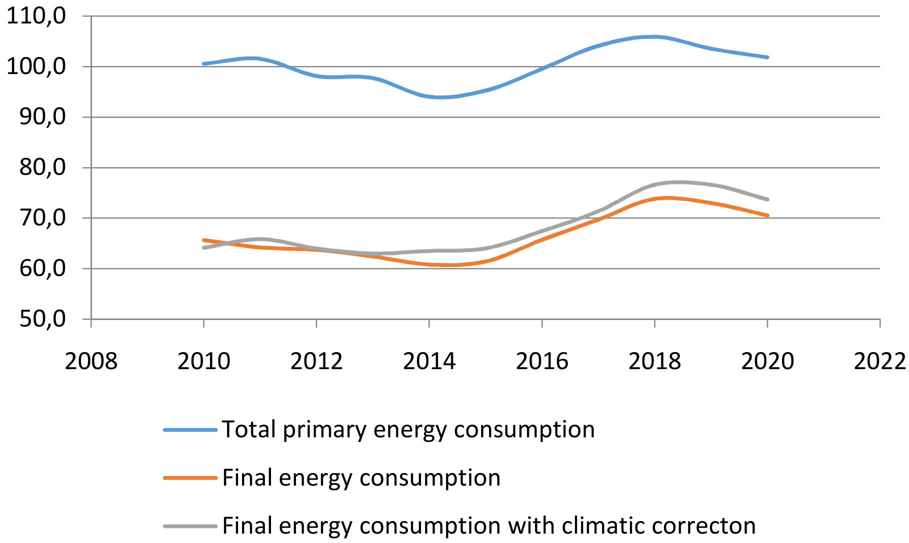

Fig. 1 Total primary energy consumption and final energy consumption in Mtoe (Source: [3])

The data includes total primary energy consumption and final energy consumption by economy sectors (Fig. 1). The growth rate of total primary energy consumption in 2010–2020 in Poland was small and amounted to 0.1%/year and increased during this period from 100.5 Mtoe to 101.8 Mtoe. This consumption peaked at 105.9 Mtoe in 2018. A slight increase in total primary energy consumption, coupled with economic growth, is a trend that will continue in the future. The final energy consumption is characterized by a similar trend, with the average annual growth rate amounting to 0.7%. Final energy consumption increased in the analyzed period from 65.6 to 70.5 Mtoe.

The climatic correction takes into account the influence of the outside temperature, characterized by the number of degree days *Sd*, on the energy consumption for heating. Final energy consumption with ZEF^{kk} climatic correction is determined from the formula:

$$ZEF^{kk} = \frac{ZEF}{1-0{,}9\alpha\left(1-\frac{Sd}{Sd_{sr}}\right)} \tag{1}$$

where: *ZEF* - final energy consumption, *Sd* - number of degree days, Sd_{sr} - long-term average number of degree days, α - share of heating energy consumption in total energy consumption in the housing sector. The number of degree days is the product of the number of heating days and the difference between the average temperature of the heated room and the average outdoor temperature. The heating days are those with the average daily outdoor temperature below 15ºC. The average long-term number of Sd_{sr} calculated for the years 1980-2004 is 3615.77.

The analysis of GDP energy consumption shows favorable changes, because in relation to 2010, the energy intensity of GDP in 2020 decreased by 24.7% (primary) and 20.3% (final). Taking into account the climatic correction, the rate of efficiency improvement was slightly lower. Primary energy consumption with climatic correction decreased by 21.1% and final energy consumption with climatic correction decreased by 14.5%. A worrying symptom is the slowdown in the rate of improvement in 2016–2020 compared to 2010-2015.

The energy intensity of sector was defined as the final energy consumption in this sector in relation to its added value. The statistics [3] also compiled the so-called energy consumption in a constant structure, determined using the Divisia method. The energy intensity calculated using the Divisia method is the so-called energy consumption in a constant structure. The dynamics of energy consumption in the Divisia method is determined as the product of the dynamics of energy consumption in a constant structure and the effect of structural changes. The effect of structural changes was calculated as the weighted sum of the growth rates of individual elements, in this case sectors of the economy. Growth rates are defined as the natural logarithm of the change in the relative value added in a given sector relative to the total in subsequent years, and the weights are the shares of the average energy consumption in a given sector in the total consumption of the economy in subsequent years.

The analysis of energy consumption is enriched by the ODEX energy efficiency indicators, which are characterized by changes in efficiency in relation to the base year (2000=100). The ODEX indicator shows the progress in the energy consumption compared to the base year. The ODEX indicator is calculated for each year as the quotient of the actual energy consumption in a given year to the energy consumption calculated assuming the current energy consumption of the production processes of the given sector. Additionally, to reduce the impact of random fluctuations, a 3-year moving average of the ODEX is calculated in [3]. A decrease in the ODEX indicator value means an increase in energy efficiency.

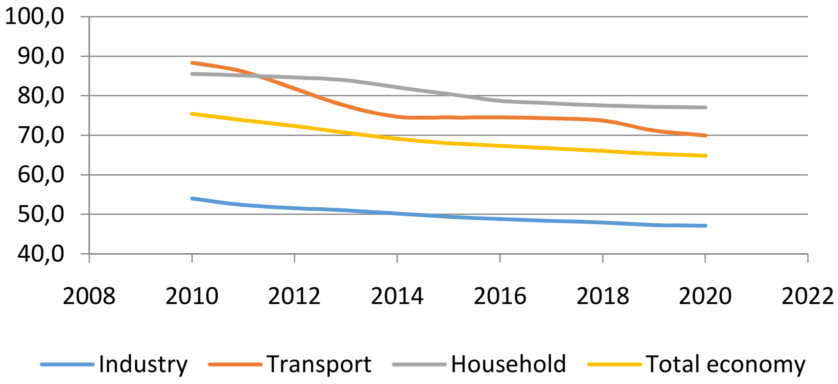

Fig. 2 Total economy and sectoral ODEX indicators for Poland (2000=100) (Source: [3])

According to [3], the ODEX indicator for Poland decreased in the years 2010–2020 from 75.4 to 64.8 points. The average efficiency growth rate was 1.5 %/year. Energy savings in the sectors were achieved in all the years presented in Fig. 2, although changes have slowed down. The highest total savings were achieved in 2014 and amounted to 1.2 Mtoe.

5 Simulation of ODEX indicators described by stochastic differential equations

A series of dynamic processes in economy and energy, in which random disturbances occur, can be modeled using stochastic equations of the Ito type [7]. The application of the Euler method [8] to solve stochastic differential equations (SDE) enables the simulation of the future development of ODEX indicators. The stochastic process of many continuous variables over time can be described by differential equations of the general form:

$$dX_t = F(t, X_t)\, dt + G(t, X_t)\, dW_t \tag{2}$$

where: X - state variable, W - Wiener process variable (Brownian motion), F - trend determining function, G - random variable distribution function.

Based on the general form (2), it is possible to define special variants of the model. The analysis uses the form of the SDE model, in which the state variables are the annual relative increases in the ODEX indicators of the basic sectors of the economy. The Geometric Brownian Motion GBMC model takes into account the correlations between the ODEX indicators of the sectors in the Wiener processes. The GBMC formula:

$$dX_t = \mu X_t\, dt + \sigma X_t\, dW_t \tag{3}$$

where: μ - mean value of the variable X_t, σ - standard deviation of the variable X_t.

The measure of uncertainty is the standard deviation in the SDE model.

6 Simulation results of the ODEX indicators

The simulations of the ODEX indicators were performed using the SDE model with the GBMC formula (3). The simulation results are shown in Fig. 3.

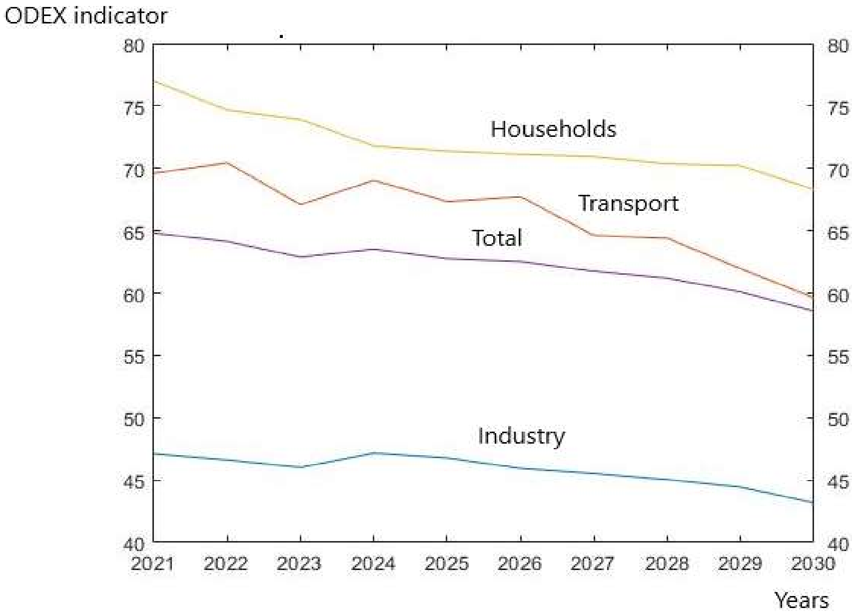

Fig. 3 Simulation results of total economy and sectoral ODEX indicators for Poland (2000=100)

The simulations of the ODEX indicators in the horizon until 2030 indicate a decrease in the energy consumption. The results of the analyzed GBMC model can be treated as a future scenario for the changes of the ODEX indicators.

7 Conclusions

The ODEX indicator of total economy calculated to the base of 2000 = 100 decreased in the years 2009–2020 from 76.9 to 64.8 points. The average efficiency growth rate was 1.57%/year. The simulation result in 2030 is the ODEX value of 58.5 points, which means an annual increase in energy efficiency by 1.15%.

The fastest rate of improvement (2.29%/year) was recorded in transport, for which the value of the index was 69.9 points in 2020. Estimation in 2030 from the SDE model is 68.3, so the average growth rate in the years 2020-2030 is 0.23%. The slowest improvement took place in the household sector, where the annual efficiency increase in 2010–2020 amounted to 1.01%. But the value in 2030 is equal to 59.6 that's why the growth rate is 2,57%/year. In the industrial sector, the rate was 1.67%, and the value of the indicator in 2020 is equal to 47.1 points. Simulation model calculated the value 43.2 in 2030, so the growth rate is 0.87%/year.

The decrease in the demand for primary energy in the period 2009-2020 was mainly due to the improvement in the efficiency of thermal power plants (decrease by 3.3 Mtoe) and the increase in the use of energy from renewable sources (decrease by 2.5 Mtoe). According to presented analysis it seems possible to reach the target in 2030 (savings 5.58 Mtoe in the period 2021-2030).

The conducted research shows that the Euler method enables the determination of a simulation of the course of stochastic variables described by differential equations, taking into account the uncertainty of the shaping of energy processes resulting from the influence of the model environment.

References

[1] Odyssee-Mure project co-ordinated by ADEME, France, supported by Horizont 2020 programme of European Union, Available online: https://www.odyssee-mure.eu/ (accessed on 14 September 2022)

[2] B. Lapillonne, Definition of energy efficiency index ODEX in ODYSSEE data base, Grant agreement n° 847082 – ODYSSEE MURE, October 2020

[3] Statistics Poland GUS, Energy efficiency in Poland in years 2010-2020, Statistical analyses, Warsaw, (2022), Available online: https://stat.gov.pl/ (accessed on 14 September 2022)

[4] Directive 2012/27/EU of the European Parliament and of the Council of 25 October 2012 on energy efficiency, Available online: https://www.eea.europa.eu/policy-documents/directive-2012-27-eu (accessed on 24 September 2022)

[5] New Act on Energy Efficiency(AEE) adopted by the Polish Parliament on May 20, 2016 (in Polish), Ustawa z dnia 20 maja 2016 r. o efektywności energetycznej, Available online: https://www.ure.gov.pl/pl/urzad/prawo/ustawy/4928,Ustawa-z-dnia-20-maja-2016-r-o-efektywnosci-energetycznej.html (accessed on 24 September 2022)

[6] Directive 2018/2002/EU of the European Parliament and of the Council of 11 December 2018 amending Directive 2012/27/EU on energy efficiency (Text with EEA relevance) Available online: https://eur-lex.europa.eu/eli/dir/2018/2002/oj (accessed on 24 September 2022)

[7] J. Sowiński, Investing in the production of electric energy in the market conditions (in Polish), Inwestowanie w źródła wytwarzania energii elektrycznej w warunkach rynkowych, Wydawnictwa Politechniki Częstochowskiej, Częstochowa, Poland (2008)

[8] B.K. Øksendal, Stochastic Differential Equations: An introduction with applications, Berlin Springer, (2003)

Implementation of Different Types of Photovoltaics on Greenhouses: A Case Study

Angela Najdoska, Goga Cvetkovski
Ss. Cyril and Methodius University, Faculty of Electrical Engineering and Information Technologies, Skopje, North Macedonia, anenajd9@gmail.com, gogacvet@feit.ukim.edu.mk

***Abstract** – In the past few years, during the global pandemic and now the energy and economic crisis, the demand for electrical energy is constantly rising. Consequently, the implementation of photovoltaic power plants on a big scale is rising. Most of the time, these photovoltaic power plants are installed on the ground, and in most of the cases it is a fertile soil, meaning we are using the land for making electrical energy. This study aims to presents a case study in which the photovoltaics are implemented on greenhouses in order to be energy neural. Also, to produce electrical energy, so that the land is used for growing plants and producing electrical energy.*

1 Introduction

According to European Environment Agency, the agricultural sector consumes around 3% of the total energy consumed in the European Union in 2016. Greenhouses constitute a major energy consumer of the agricultural sector in the European Union [1]. Thanks to the modern agriculture there are many strategies that can lead to reducing the need of energy. One of the strategies is using technologies based on renewable energy sources, such as photovoltaic (PV) system, wind turbines, heat pumps, solar panels and hybrid PV thermal systems. PV greenhouse (PVG) is an agro-system potentially able to combine food and energy production on the same land unit, by integrating the PV system on the greenhouse roof/construction [2].

The only thing that plants and PV have is that they both use solar light. Apart from the fact that they both need sunlight, photosynthetic and photovoltaic systems have distinct requirements in light quality and quantity. The quality of light absorbed by PV can be customized to harness the entire solar spectrum. For plants, absorption spectra depend on their photosynthetic pigments. Plants can be grown in order to produce food or biomass, whereas PV generate electricity cooperatively on the same plot of land. This is termed agrivoltaics or solar sharing [3].

Agrivoltaic has been reported to bring several positive benefits such as: reducing electricity costs, increased ability to install high-value, shade-resistant crops for new markets – the shading by the PV panels provides multiple additive and synergistic benefits, including reduced plant drought stress and more constant temperature as the panel will maintain the temperature higher at night and cooler during the day, potential to extend growing seasons, ability to maintain crop production during solar generation, allow for nutrient and land recharge of degraded lands, potential for water reduction [4, 5, 6].

However, greenhouse operation comes with its own set of challenges. The air temperature, relative humidity and solar radiation are the most important variables of the greenhouse climate that must be controlled. These variables affect the crop production, as well as the energy consumption of the greenhouse, which can reach up to 40% of the total production costs [2].

The purpose of this case study is to present advancements in the implementation of different types of PV on greenhouses in order to achieve net zero energy, with focus on plant growth and other benefits. An extensive literature review, which presents the current trends in the field of agrivoltaics and different types of greenhouse construction. This study aspires to stimulate using the land efficiently, with growing plants and photovoltaics.

2 Photovoltaics on Greenhouses

Over the years, studies concerning this topic are classified in two major fields: implementation of conventional/rigid PV on greenhouses and implementation of flexible semi-transparent or transparent PV on greenhouses. In Fig. 1 an example of the two scenarios of implementation of PVs on greenhouses is presented. Given the availability of the conventional PV, also their price, they are more attractive to work with, compared with the semi-transparent or transparent PV modules that are more expensive. Also, the conventional PV modules are more efficient compared with other types of modules [2].

Fig. 1 Example of greenhouse with conventional PV (right) and colored transparent PV (left)

During the past few years, the conventional PV modules implemented on greenhouses have become an interesting topic for research. Studies show that with the use of this types of PV modules the yearly global radiation in the greenhouse decreased averagely by 0.8% for each additional 1% PV cover ratio. Also, when using these types of PV modules, the orientation of the greenhouse has major impact on the solar yield of the investigated PV modules. The study shown that the N-S orientation increased the average cumulated global radiation on the greenhouse area by 24% compared to the E-W orientation [7, 8]. The idea of using this type of photovoltaic modules was even more discouraging in another study by Cossu et al. [9]. In this study the solar radiation and temperature inside an east-west oriented greenhouse with PV coverage of 50% was investigated. The greenhouse was located in Sardinia, Italy. Furthermore, in this study the south-oriented roof was completely covered with multicrystalline silicon PV panels, with installed rated power of 68 kWp. Figure 2 shows the PV greenhouse (left) and the model (right) showing the shadow casting over the greenhouse area.

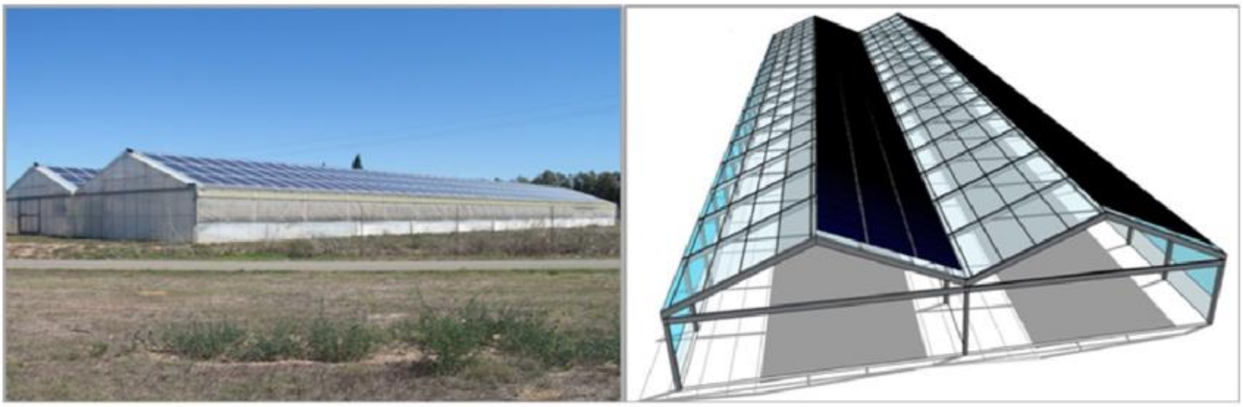

Fig. 2 PV greenhouse (left) and model of the PV greenhouse (right)

A high-light demanding crop was chosen for comparing the environmental data with the achieved yield. The PV array decreased the yearly sunlight availability inside the greenhouse by 64% compared to the situation without PV modules, while the temperature was averagely 2.8 °C higher than outside. Also, the solar radiation under the conventional plastic rood was 305% higher than under the PV roof, causing a high variability of total production between the plant rows, which ranged from 1.9 kgm^{-2} in some rows under the PV cover, where plants showed a negative photosynthetic rate (up to -3.72 mmol CO_2 $m^{-2}s^{-1}$), to 5.1 kgm^{-2}. The conclusion of this study was that new design criteria for PV greenhouses, concerning the decrease of the PV array coverage and different installation patterns of the PV modules on the roof were required.

The interest for this topic increases with the use of semi-transparent or transparent PV modules. According to several studies, plants can benefit from the implementation of PV modules on the roof of the greenhouse: they can reduce the amount of water needed, also with them energy neutral greenhouse could be achieved. In most cases they are using organic flexible PV modules, but the news trend is using colored organic PV modules in order to have more benefits for the plants growing inside the greenhouse [3, 4, 5, 6, 9].

Furthermore, Hassanien et. al [10] was investigating the effect of semi-transparent building integrated photovoltaics (BIPV) mounted on top of a greenhouse, on the growth of tomatoes and microclimate conditions as well as to estimate the generated energy and the payback period of the system. Three modules were settled at 20% of the greenhouse roof area at a tilt angle of 30° facing south at a distance of 0.08 m between the plastic cover and the BIPV. Each module had a peak power of 170 Wp and efficiency of 8.25%. The experiment has been conducted in Kunming, China. Figure 3 shows a photo of the greenhouses presented from different views, as well as their constructional parts.

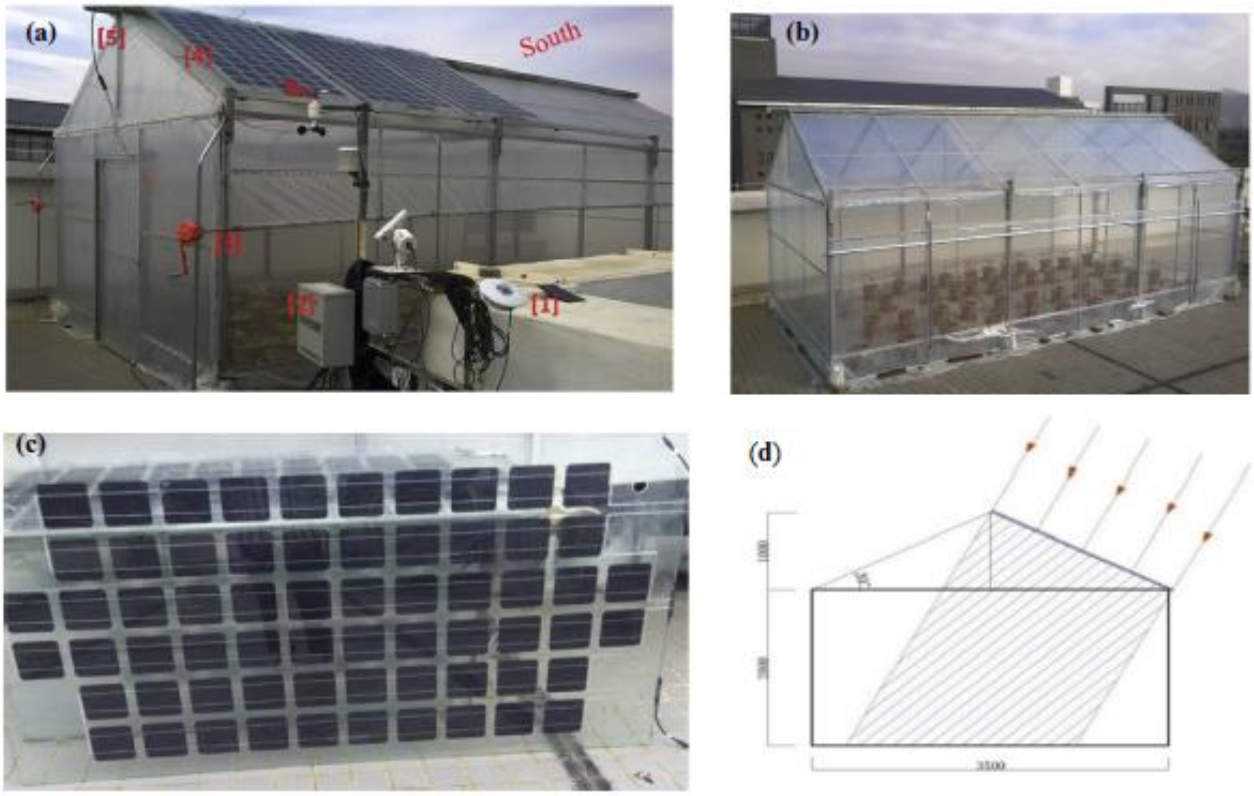

Fig. 3 Photo of the greenhouses (a) Shaded greenhouse: pyranometer, Recording station, Side ventilation system, The distance between the BIPV panels and plasticcover , Micro-inverter’s cable. (b) Un-shaded greenhouse, (c) BIPV panel, (d) greenhouse diagram

The results from this study show that the integration of the semi-transparent BIPV panels with a transmittance ratio of 47% on the roof of the greenhouses not only decreases the energy load, but also generates appropriate energy for the supplemental lighting and heating in winter as well as forced ventilation in summer. The annual generated electric energy of the BIPV modules per unit floor area of greenhouse was ranged from 24.5 kWh/m^2 to 47.5 kWh/m^2 at 20%-40% of greenhouse roof covering area. Furthermore, the results showed that the perfect orientation for producing more electrical energy on the South roof of the greenhouse was 25° and the best tilt angle in the North roof was 20°. The BIPV shading decreases the air temperature by approximately (1°C-3°C) on clear days and insignificantly increases the relative humidity by 2% as well as decreases the solar radiation by 35%-40% compared to un-shaded greenhouse. Moreover, the BIPV insignificantly affected the growth of tomato. Also, the study shows that the annual electrical energy production of the BIPV can be increased particularly in high irradiation regions and remote area. Therefore, it can be recommended that the most suitable crops, vegetables and omamental plants under the BIPV system those which need low light intensities.

Furthermore, the authors gave a suggestion that: an external integration of a mobile BIPV with a high efficiency or spherical micro-cells as a semi-transparent photovoltaic (PV) technology on the greenhouse roof are highly recommended in the subtropical regions.

Moreover, wavelength-selective photovoltaic systems (WSPVs) combine luminescent solar cell technology with conventional silicon-based PV, thereby increasing efficiency and lowering the cost of the electricity generation. WSPVs absorb some of the blue and green wavelengths of the solar spectrum but transmit the remaining wavelengths that can be utilized by photosynthesis for plants growing below. WSPVs are ideal for integrating electricity generation with glasshouse production, but it is not clear how they may affect plant development and physiological processes. In the research [6] a study of implementing WSPVs was made at the University of California Santa Cruz Arboretum (Fig. 4).

Fig. 4 Glasshouse constructed with Wavelength Selective Photovoltaic panels, at the University of California Santa Cruz Arboretum.

Key to the efficiency of the WSPVs are luminescent solar concentrators (LSCs). An LSC utilizes a luminescent material to absorb solar radiation, which waveguides a fraction of the photons to optically attaches Si-PV cells where they are converted into electricity. LSCs have been limited in power efficiency by low absorption of the solar spectrum, self-absorption of the emitted light, and waveguide losses. The WSPV improves the power efficiency of LSCs by (1) using a luminescent material that efficiently absorbs and emits radiation without excessive re-sorption and quenching, (2) the use of face-mounted (rather than edge-mounted) PV cells, which yields substantial power gains through direct illumination of the PV cell, and (3) the much shorter distances that the absorbed light energy needs to travel before being converted to electrical power.

The effects of tomato photosynthesis under WSPVs showed a small decrease in water use, whereas there were minimal effects on the number and fresh weight of fruit for a number of commercial species. Although more research is required on the impacts of WSPVs, they are a promising technology for greater integration of distributed electricity generation with food production operations, for reducing water loss in crops grown in controlled environments, as building-integrated solar facilities, or as alternatives to high-impact PV for energy generation over agricultural or natural ecosystems.

Case Study

According to the many researches and results obtained in this field of research, it can be concluded that there is still room for research and improvement. As the main conclusion, all of the above researches point out that the success of such researches depends on the location where the research will be carried out, as well as on the horticultural culture that will be grown in the greenhouse itself. At the same time, the most important condition is the photovoltaic modules, the technology from which they are made. Our goal is to continue and hopefully improve the previous research in this issue. The greenhouse where the photovoltaic modules would be installed would be located in Bitola, North Macedonia. The area of the greenhouse would occupy no more than 40 m^2. A photovoltaic module technology that would be installed on the roof of the greenhouse is organically colored photovoltaic modules. The horticultural crop that would be grown in the greenhouse is lettuce. The orientation of the greenhouse would be east-west. The attractiveness of the location is that it is characterized by quite cold winters and mild summers. That is, during the winter, temperatures can drop to -40°C in the mountainous area, while in the city itself, it can drop to -25°C. Before the realization of the research, a simulation of the greenhouse itself will be done using the Hortinergy program [11].

Conclusion

As a result of the world pandemic, various crises have appeared on a global level. One of the crises, which actually causes the others, is the energy crisis. Consequently, the need for cheaply produced energy has arisen, thus also the massive interest in investing in the installation of photovoltaic modules. Mostly large installations of the type of several MWp in Macedonia are installed on fertile land. Such policy will result in a violation of the ratio of fertile lands, and thus a violation of food production. Encouraged by this, we got the idea to make a mix between energy and agriculture. The befits of this idea are:

- Reducing electricity costs
- Increased ability to install high-value, shade-resistant crops for new markets – the shading by the PV panels provides multiple additive and synergistic benefits, including reduced plant drought stress and more constant temperature as the panel will maintain the temperature higher at night and colder during the day
- Potential to extend growing seasons
- Ability to maintain crop production during solar generation
- Allow for nutrient and land recharge of degraded lands
- Potential for water reduction

References

[1] https://ec.europa.eu/eurostat/statistics-explained/index.php?title=Agrienvironmental_indicator_-_energy_use (02.05.2022).

[2] A. Kavga, J. Vaiciunas et. al, (2020), "Recent Advancements in the Energy Performance of Intelligent Green Houses: A Case Study", *IOP Conf. Series: Earth and Environmental Science*, vol. 410(1), pp. 1-12.

[3] E. P. Thompson, E. L. Bomlelli et. al., (2020), "Tinted Semi-Transparent Solar Panels Allow Concurrent Production of Crops and Electricity on the Same Cropland", Advanced Energy Materials, vol. 10 (35), 2001189, pp. 1-9.

[4] E. Ravishankar, R. E. Booth, (2020), "Achieving Net Zero Energy Greenhouses by Integrating Semitransparent Organic Solar Cells", *Joule*, vol. 4, pp. 1-17.

[5] J. Barichello, L. Vesce, (2021), "Stable Semi-Transparent Dye-Sensitized Solar Modules and Panels for Greenhouse Application", *Energies*, vol. 14(19), 6393, pp. 1-17.

[6] M. E. Loik, S. A. Carter, (2017), "Wavelength-Selective Solar Photovoltaic Systems: Powering Greenhouses for Plant Growth at the Food-Energy-Water Nexus, *Earth's Future*, vol. 5, pp. 1044–1053.

[7] M. Cossu, A. Cossu, et. al, A., (2018), "Assessment and comparison of the solar radiation distribution inside the main commercial photovoltaic greenhouse types in Europe", *Renewable & Sustainable Energy Reviews*, vol. 94, pp. 822-834.

[8] M. Cossu, A. Yano et. al, (2017), "Effects of the photovoltaic roofs on the greenhouse microclimate", *Acta Horticulturae,* vol. 1170, pp. 461-468.

[9] R. U. Sanchez, A. J. C. Ferre et al., (2012), "Greenhouse Tomato Production with Electricity Generation by Roof-Monted Flexible Solar Panels", *Scientia Agricola*, vol. 69(4), pp. 233-239.

[10] R. Hassanien, M. Li et al., (2017), "The integration of semi-transparent photovoltaics on greenhouse roof for energy and plant production", Renewable Energy, vol. 121, pp. 377-388.

[11] https://www.hortinergy.com/ (10.09.2022).

Optimal Power Injection Placement in Radial Distribution Systems Using Clustering Optimisation

Angela Popova[1],
[1] Technical University of Munich, Moosacher Str. 81, 80809 Munich, Germany,
ge75jit@mytum.de,

Jovica Vuletić[2],
[2] Ss. Cyril and Methodius University, Faculty of Electrical Engineering and Information Technologies,
Rugjer Boskovic 18,
P.O.Box 574 1000 Skopje,
R. N. Macedonia
jovicav@pees-feit.edu.mk,

Jordančo Angelov[3],
[3] Ss. Cyril and Methodius University, Faculty of Electrical Engineering and Information Technologies,
Rugjer Boskovic 18,
P.O.Box 574 1000 Skopje,
R. N. Macedonia
jordanco@pees-feit.edu.mk,

Mirko Todorovski[4]
[4] Ss. Cyril and Methodius University, Faculty of Electrical Engineering and Information Technologies,
Rugjer Boskovic 18,
P.O.Box 574 1000 Skopje,
R. N. Macedonia
mirko@pees-feit.edu.mk,

Abstract ***– Nowadays, distributed generation plays a vital role in distribution systems. It makes an indisputable contribution towards power loss minimization and voltage profile improvement. To maximize the benefits of distributed generators, their location and size is of crucial importance. This paper describes the use of clustering optimization (CO) as a highly effective method for determining the optimal placement and sizing of distributed generators. Assessment of the effectiveness from the clustering optimization method is achieved by its demonstration on a 69-bus and 119-bus distribution systems. It is concluded that clustering optimization is a simple and efficient method in terms of optimal allocation and sizing of distributed generators. It outweighs other approaches in terms of simplicity, results, and computation time.***

Keywords*: Distributed generation, Power injection placement, Clustering optimisation, Distribution system, Losses*

1 Introduction

Increasing climate changes, dwindling resources and greenhouse gas emissions have led to an increase in the exploitation of renewable energy sources for electricity production. As renewables are scattered around the country, their potential can mostly be tapped through integration to the distribution system as a form of distributed generation (DG). In recent years, the share of DGs in power systems has been significantly increasing. Distributed generation can be defined as any electricity generating technology, installed by the utility system or at the site of a utility customer, connected at the distribution system level of the electric grid [1]. Therefore, DG integration undoubtedly affects the power system, especially at the distribution level. Properly located and sized units have the potential to reduce total power losses in the system, improve the voltage profile, enhance reliability, enable greater available capacity for power transmission and reduce equipment stress [2]. On the other hand, if not optimally placed and sized, the installation of DGs in the grid could cause an increase of system losses, crippling of the voltage conditions, voltage flicker and an increased level of harmonics, all leading to considerably greater costs [3]. Hence, the use of an efficient optimisation method for sizing and placement is of immense importance to fully utilize the benefits of DG's [4-7].

Numerous technologies can be considered as DG's. Photovoltaics and solar-thermal units, wind turbines, small hydro plants, geothermal units, all types of fuel cells and battery storage technologies can be categorized as DG's [8]. However, from power system analysis point of view, any type of DG technology depending on its specifics can be presented as an active, reactive, or apparent power injection (PIN).

This paper outlines a new approach to solving the problem of optimal allocation and sizing of PINs by presenting a simple search-based algorithm that in its essence is a pattern of using a load flow procedure. Main motivation behind this research is to introduce a simple solution to a highly complex non-linear problem. By iteratively looping through the network buses, the algorithm places a PIN of a defined size and type (active, reactive, or apparent) at specific locations yielding minimum power losses while keeping all voltages at their acceptable levels. Moreover, the optimal power factor is also determined in the case of apparent type of PIN. The proposed method is demonstrated on a 69-bus and 119-bus distribution system. Results from the proposed method suggest that it is superior; it produces repetitive and unique results; it is extremely easy to implement and has a short computation time.

2 Problem formulation

Determining the optimal location and size of a PIN in the distribution system is a complex non-linear problem. As previously mentioned, for a certain location (bus) in the network, as the size of the PIN increases, an adequate decrease in losses can be noticed. However, after exceeding a certain PIN threshold, the losses start to increase again due to a reverse power flow towards the slack/supply bus. The size of the PIN should at most be such that it is consumable within the distribution substation limits [12].

The problem of determining the optimal PIN size and locations is quantified through objective function that can take any mathematical formulation in terms of complexity. For purposes of comparison to other relevant research, objective function introduced in this paper includes costs for energy and power losses only and should yield a least possible value, i.e., minimum:

$$\min F = c_e \cdot \Delta W + c_p \cdot \Delta P_{max} \tag{1}$$

with c_e being the cost for kilowatt-hour of electricity (\$/kWh), ΔW being the electricity losses within the observed period (kWh), c_p being the cost per kilowatt for reduction in losses (\$/kW) and $\Delta P_{\max}$ being the maximum power losses during the same period (kW). To determine the minimum value of the objective function, it is necessary to obtain the minimum value of power losses which would also result in a minimum value of electricity losses during the observed period.

The number of constraints and their formulation can be regarded as a way of guiding the optimisation algorithm towards a feasible and possibly optimal solution because not necessarily always these two go hand in hand. Imposing a high number of constraints generally narrows the optimisation algorithm search path and while providing a more accurate and realistic approach, the trade-off is a feasible but not necessarily optimal solution and vice versa. For purposes of comparison to other relevant research, during all calculations, constrains on bus voltage values are imposed by setting an upper and lower bound [44], resulting in the following constraint:

$$V_{min} \le V_i \le V_{max}, \text{ for } i = 1, \ldots, NB \tag{2}$$

where $V_{\min}$=0.9 pu, $V_{\max}$=1.1 pu and NB being the number of buses in the given network.

3 Load Flow

Aiming for optimal placement and sizing of PIN, it is first and foremost indispensable to determine the parameters of interest in the distribution system, i.e., bus voltages and power losses. Due to distribution systems specific nature such as high R/X ratio and radial structure, conventional load flow methods usually fail to give satisfactory results [45]. Of all proposed power flow solution methods for distribution systems, backward/forward sweep methods are most widely used because of their computational efficiency and robust convergence characteristics [46-48]. The efficiency of the sweeps can be enhanced with oriented branch numbering [49], the only requirement being that the sending bus number i is smaller than the receiving bus number k, i.e., $i < k$ (Fig. 1). Indices from the branch's sending buses are stored in a vector $\mathbf{f}$, such that $i = \mathbf{f}(k)$, where k is the index of the branch's receiving bus. Additionally, by introducing a fictitious branch with index 1 (sending end index 0), the number of branches NL becomes equal to the number of buses NB, making the sweep procedure very simple and efficient.

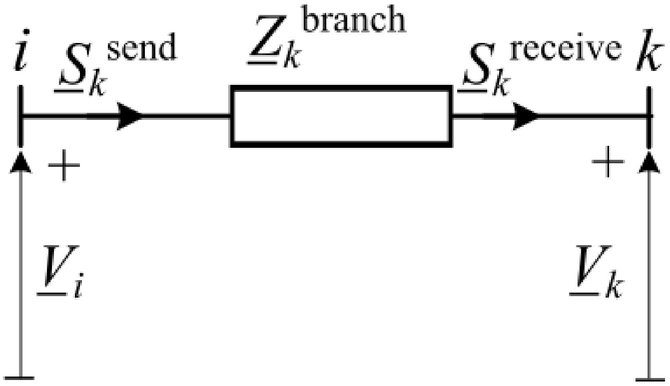

Figure. 1 Branch representation: branch *k* between buses *i* (sending end) and *k* (receiving end)

Backward sweep consists of equations that calculate the power flow through branches starting from the last one and proceeding in a backward direction towards the supply/slack bus. First, receiving end branch flows are calculated using (3), where $\underline{S}_{demand}^{receive}$ is the power demand at the branch's receiving end and $\underline{Y}_k^{shunt}$ is shunt admittance connected to bus *k* due to capacitance of the lines and/or connected capacitors (4).

$$\underline{S}_k^{receive} = \underline{S}_{demand}^{receive} + (\underline{Y}_k^{shunt})^* \cdot V_k^2, \text{ for } k = 1\ldots, NB \tag{3}$$

$$\underline{Y}_k^{shunt} = j(B_k^{lines} + B_k^{cap}), \text{ for } k = 1\ldots, NB \tag{4}$$

If a PIN of certain size is considered at bus *k*, the value of $\underline{S}_{demand}^{receive}$ from (3) is appropriately modified. To account for PIN of size $\underline{S}_k^{PIN}$, $\underline{S}_{demand}^{receive}$ is updated using (5):

$$\underline{S}_{demand,new}^{receive} = \underline{S}_{demand}^{receive} - \underline{S}_k^{PIN}, \text{ for } k = 1\ldots, NB \tag{5}$$

Afterwards, sending end branch flows are calculated using (6) and added to the branch's receiving end that supplies them (7).

$$\underline{S}_k^{send} = \underline{S}_k^{receive} + \underline{Z}_k^{branch} \left| \frac{\underline{S}_k^{receive}}{\underline{V}_k} \right|^2, \text{ for } k = NL, NL-1\ldots, 2 \tag{6}$$

$$\underline{S}_{i,new}^{receive} = \underline{S}_i^{receive} + \underline{S}_k^{send}, \text{ for } k = NL, NL-1\ldots, 2 \tag{7}$$

Forward sweep is performed to determine the voltage drops and actual voltages of each bus starting from the slack bus and proceeding in the forward direction towards the last bus using (8).

$$\underline{V}_k = \underline{V}_i - \underline{Z}_k^{branch} \cdot \left(\frac{\underline{S}_k^{send}}{\underline{V}_i} \right)^*, \text{ for } k = 2,\ldots, NL \tag{8}$$

After completing a sweep, the calculated voltages of the present iteration are compared to those from the previous one. If the voltage mismatch between two consecutive iterations is less than the specified tolerance of $\varepsilon = 10^{-4}$, convergence can be achieved. Otherwise, the procedure is repeated until convergence of the solution is attained. After determining the power flow through the branches, it is easy to calculate the active power losses by simply subtracting the real parts from the complex sending and receiving end branch power flows (9):

$$\Delta P_{loss} = \sum_{k=1}^{NL} (P_k^{send} - P_k^{receive}), \text{ for } k = 1,\ldots, NL \tag{9}$$

where P_k^{send} is active power from the branch's sending bus and $P_k^{receive}$ is active power from the branch's receiving bus.

4 Clustering Optimisation

As it has been previously mentioned, many approaches have been proposed in terms of determining the best possible location and size of PINs in an existing distribution system. However, some of them only consider PINs with unity power factor, some are applicable only for single power injecting unit allocation, others offer nearly optimal solutions, and some have inconveniently high computation time. To overcome these shortcomings, a simple search-based clustering optimisation (CO) is presented in this paper.

Basic idea behind the CO is by iteratively probing all buses from the distribution system apart from the slack bus, to place PINs of user-defined size and number of locations at locations that would yield least possible losses, which is quantified through (1). Power injections can be considered as purely active, purely reactive, or apparent. Iterative bus probing eliminates the need of using any kind of sensitivity analysis for bus selection as the process itself implicitly does that.

In case of apparent power injection, the optimal value of the power factor is also determined. Proposed approach doesn't constrain the power factor value when searching for its optima due to several reasons [4-7]:

- Most if not all utility owners demand from their dispersed generation PINs reactive power support without any specified value or quantity.
- Most dispersed generation PINs are owned by private entities which are usually if not exclusively more incentivised when injecting purely active power, i.e., they tend to operate at unity power factor. In some cases, they're required to operate at unity power factor at their point of common coupling, i.e., they should only produce reactive power for their own personal operational requirements.
- Imposing constraints on power factor value implicitly disables the proposed approach in reaching competitive and comparable results to other relevant methods.

During the CO procedure, all buses apart from the slack are considered candidate buses for optimal PIN placement, i.e., there is no bus selection procedure nor weak bus sensitivity analysis. There are many reasons for avoiding this type of bus pre-processing. Not all buses possess the same sensitivity trend when subjected to a same rate of power injection change. This is owed to network topology, load, and voltage profile. For example, if a single small power injection is placed on every bus successively, they will attain a certain sensitivity index based on the applied analysis. This index can be used to rank the buses in terms of their susceptibility towards receiving that particular power injection. However, adding a successive power injection of same size introduces a shift in bus sensitivity index following its appropriate trend that is unknown, meaning there may be a shift in position from the previous bus ranking. For a fixed number of locations for PIN placement this is a huge problem since the set of locations potentially changes by successively adding more power injections per bus and the analysis becomes obsolete. There are ways one can alleviate that, i.e., sensitivity analysis and bus ranking can be performed for base case scenario and the obtained set of buses can be kept constant throughout the process of optimisation. However, one should bear in mind that different sensitivity analysis imposes different set of candidate buses and consequently a different solution that may or may not be optimal [50].

The proposed approach alleviates this drawback by probing each bus with a small power injection, i.e., implicitly choosing locations that yield least possible losses while inherently following the buses sensitivity trend, hence avoiding the bus selection procedure. The CO algorithm calculates power losses in the distribution network using a linearised (flat start, single iteration) load flow [48] while keeping the voltage profile of the system within prescribed limits. The use of linearised load flow implies that load flow procedure finishes after one iteration, i.e., the resulting power losses and voltages are obtained after a single iteration of backward/forward sweeps. The latter enables placing PINs at each bus successively while keeping the computation time for the entire procedure significantly short.

Values of power losses obtained from a linear load flow are smaller compared to those obtained from regular iterative load flow due to flat start, i.e., all bus voltages are equal to the distribution system nominal voltage. Therefore, to obtain the actual values of power losses and voltages, another non-linear load flow is performed at the end of the clustering procedure. This approach is legitimate as the difference in values obtained from both linear and non-linear load flow solution is equal for each bus, therefore the optimal PIN size and their optimal locations do not change. The number of locations for PIN placement, type, size and φ_{step} (in case of apparent PIN for attaining optimal power factor) are all user-defined. The CO algorithm performs through the following steps:

- *Step 1*. Read distribution system line and load data and obtain total number of buses N_B. Initialise user-defined PIN size and type, desired number of locations for PIN placement N_{loc}, power factor angle step φ_{step} and counter $n=0$ (current number of buses where PINs are placed). Perform base case load flow and obtain values for distribution system power losses ΔP_0 and minimum voltage $U_{min,0}$.
- *Step 2*. Place PIN units with predefined size $\left(\underline{S}_{unit}^{PIN}\right)$ and type (active, reactive, or apparent) at each bus $i=2,3,\ldots N_B$. Perform subsequent linearised load flows (flat start, single iteration) for each PIN at each bus *i*, to check for power loss reduction. If apparent PIN type is considered, perform additional linearised load flows for each value of φ_{step} to check for optimal power factor as well, for each $\underline{S}_{unit}^{PIN}$ at each bus. The value of φ goes from $-\pi/2$ to $+\pi/2$ with a resolution of φ_{step}. Stop placing PINs per bus *i* if no loss reduction and no voltage improvement is achieved. Store the cumulative PIN for bus *i* as $\underline{S}_i^{PIN}$ and its appropriate losses ΔP_i and minimum voltage $V_i^{\min}$.
- *Step 3*. Using the results from *Step 2*, for the set of buses $i=2,3,\ldots N_B$, find bus *m* that ensures minimum active power losses $\Delta P_m=\min(\Delta P_2,\Delta P_3,\ldots,\Delta P_{N_B})$. Place the power injection $\underline{S}_m^{PIN}$ at location *m* and increase the counter *n* by 1.
- *Step 4*. Update the power demand with $\underline{S}_m^{PIN}$ at the target bus *m* obtained from *Step 3* using (5) and repeat the previous two steps until the desired number of locations is achieved ($n=N_{loc}$) or no power loss reduction is detected.
- *Step 5*. Perform final non-linear load flow for the cumulative PINs and placement locations to obtain actual values for power losses and voltages.

Additionally, an example for illustrative purposes is presented below.

Example: The CO algorithm is illustrated on a 12.66 kV, 69-bus distribution system searching a single location by placing apparent PINs of size $\underline{S}_{unit}^{PIN}=200\cdot e^{j\varphi_{step}}$ kVA. The value of φ goes from $-\pi/2$ to $+\pi/2$ with $\varphi_{step}=\pi/9$. The main purpose is power loss minimization, i.e., minimum value of (1) with $c_e=0$ and $c_p=1$ Base case losses are $\Delta P_0=225$ kW and lowest voltage occurs at bus 65, i.e. $U_{min,0}^{@65}=0.9092$ pu. All buses apart from the slack bus are considered for potential PIN placement.

Considering the use of apparent PIN in this example, the procedure also determines the optimal value of φ which yields minimum losses, by performing subsequent linearised load flows for each value of $\varphi_{step}=\pi/9$ from $-\pi/2$ to $+\pi/2$. The latter is done for each $\underline{S}_{unit}^{PIN}$ per bus. The CO builds the cluster by continuously adding $\underline{S}_{unit}^{PIN}$ per bus and obtaining the optimal value of φ until no further loss reduction is detected. When no further power loss reduction is detected by adding additional $\underline{S}_{unit}^{PIN}$ at a certain bus, the cluster, i.e., cumulative PIN with size $\underline{S}_i^{PIN}$ and cumulative value of φ is formed. Figure 3 shows a normalized histogram of PINs and power losses for every candidate bus. Losses are normalized to ΔP_0 and PINs are normalized to the maximum system injection per bus, which for this example is 4944.7 kVA.

Once the cumulative PIN for every bus ($\underline{S}_{@bus}^{PIN}$) is determined along with its appropriate losses, the CO performs a simple search for minimum losses and optimal bus for PIN placement. The cumulative PIN is then placed at the determined/optimal location. In this example, the optimal location is bus 61 (Fig. 2) and the cumulative PIN value is $\underline{S}_{@61}^{PIN}=2173.5\cdot e^{j35.42^{o}}$ kVA. The cluster formation for the optimal location is visually presented in Fig. 3 and Tab. 1.

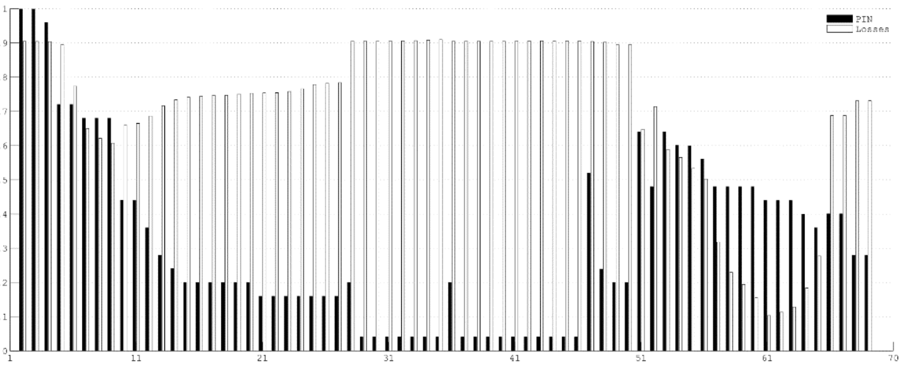

Figure. 2 Normalized histograms of PINs and power losses for all candidate buses from the 69-bus distribution system

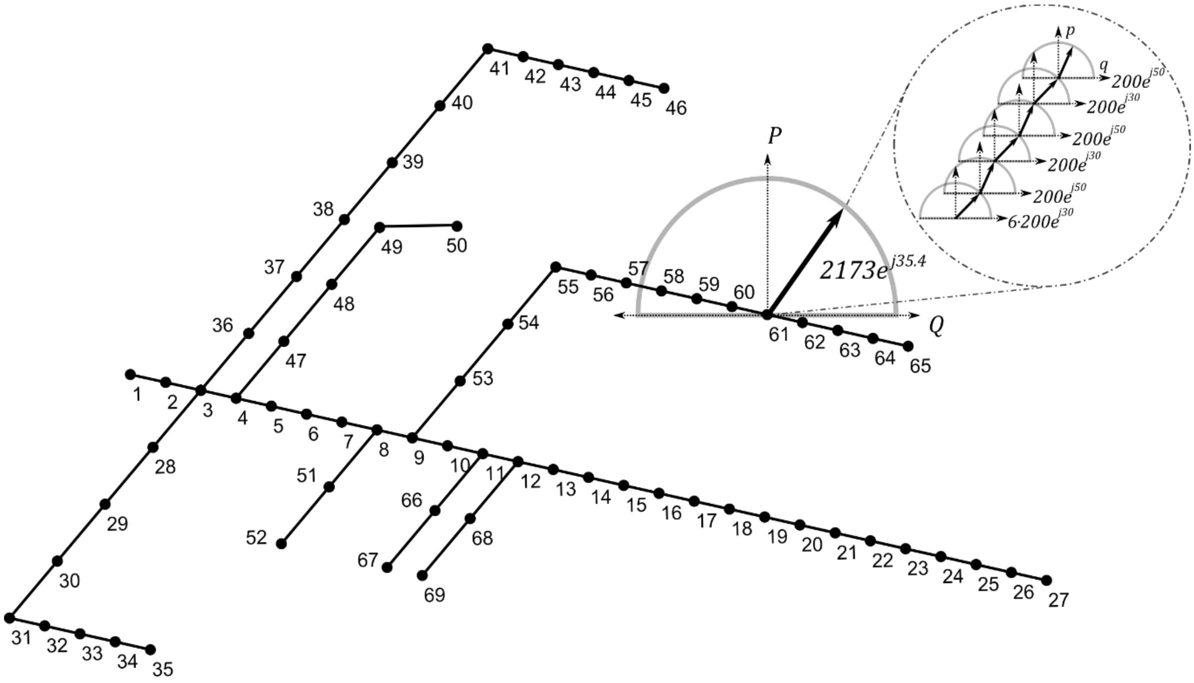

Figure. 3 Cluster formation at bus 61 from the 69-bus distribution system

Table 1 Cluster formation at bus 61 from the 69-bus distribution system

Iteration №	$\underline{S}_{unit}^{PIN}$	φ
1-6	$200e^{j30}$	30^0
7	$200e^{j50}$	50^0
8	$200e^{j30}$	30^0
9	$200e^{j50}$	50^0
10	$200e^{j30}$	30^0
11	$200e^{j50}$	50^0
$\underline{S}_{@61}^{PIN}$	$2173e^{j35.42}$	35.42^0

Step 4 is omitted in this example since there is only one potential location for PIN placement. However, the updating of power demand at bus 61 ($\underline{S}_{demand,new}^{@61} = \underline{S}_{demand}^{@61} - \underline{S}_{@61}^{PIN}$) is still performed considering the new condition in the distribution system.

Next, the CO performs a final non-linear load flow to determine the actual power losses $\Delta P = 23.3370$ kW and minimum voltage $U_{min}^{@27} = 0.9720$ pu in the distribution system.

5 Robustness, Convergence Properties and Computation Time

The proposed CO method possesses several remarkable features making it superior in terms of complexity/simplicity, implementation and results for optimal power injection sizing and allocation.

- There is no bus selection procedure, nor any form of mathematical modelling and analysis for bus selection. The CO method implicitly chooses locations/buses based on a simple search described in Section 4.
- CO method produces unique, mostly superior, repetitive, and easily reproducible results compared to other search-oriented methods.
- The algorithm operates in relatively short computation time that is dependent on distribution system size and PIN type/size. In case of apparent PINs, computation time is generally longer because optimal power factor is also being determined. Moreover, smaller size of PIN units engenders longer computation time due to an increased number of performed calculations per bus.
- Users are disburdened from complex mathematical formulations or models as in its essence, the CO method is a "pattern of using a load flow procedure" making it extremely easy to implement.

Table 2 summarises the CO's performance for the 69-bus distribution system. It can be noted that for rather large range of PIN sizes the power loss and cumulative PIN deviations are small. This is owed to the fact that cluster formation with a certain PIN size can be considered as cluster resolution. Larger PIN size imposes faster and rougher cluster formation, i.e., shorter computation time. Smaller PIN size imposes slower and smoother cluster formation but at the expense of longer computation time. Furthermore, PIN size and type are user-defined variables which can be considered a drawback if one's so insistent on that tenth or hundredth of a kilowatt losses delta. Real-life distribution system line and load data acquisition can be quite a difficult task. Additionally, distribution system data collection can introduce errors of magnitude in several tens of percent so it can be safely said that the method is as accurate as the accuracy of the input data. Tab. 2 should only serve for user's illustrative and indicative purposes when choosing PIN size regarding output results and computation time.

The CO algorithm is implemented in MATLAB R2018a. All calculations are performed on a laptop configuration with a 2.6-GHz Intel Core i5-4210M processor with 8Gb of RAM. All solutions from references subject to comparison with the CO algorithm are ran through a load flow procedure to check for accuracy of the results. Figure. 4 illustrates convergence curves for the CO algorithm when searching for a single location and three locations accordingly. It should be noted that the ending point of the single location convergence curve is a starting point for the next one etc. The latter is owed to the fact that CO algorithm successively chooses buses (one by one) for PIN placement which is explained in detail in Section 4.

Table 2 Power loss deviation and calculation time depending on PIN size, type, and number of locations for the 69-bus distribution system

№	**PIN Size (kVA)**	**Active PIN**			**Reactive PIN**			**Apparent PIN**		
		ΔP_P (kW)	**t_P (sec.)**	**Total (kW)**	**ΔP_Q (kW)**	**t_Q (sec.)**	**Total (kVAr)**	**ΔP_S (kW)**	**t_S (sec.)**	**Total (kVA)**
1	1	83.26	8.69	1841	152.06	6.01	1307	23.17	113.13	$2237.65e^{j35.45}$
	50	83.24	0.20	1850	152.08	0.13	1300	23.19	2.23	$2223.31e^{j35.30}$
	100	83.41	0.09	1800	152.08	0.07	1300	23.2	1.15	$2273.10e^{j35.18}$
	200	83.41	0.06	1800	153.43	0.04	1200	23.34	0.60	$2173.52e^{j35.42}$
2	1	71.8	12.24	2353	146.49	8.34	1654	7.57	149.32	$2851.33e^{j35.16}$
	50	71.85	0.25	2350	146.51	0.23	1650	7.51	3.00	$2797.55e^{j34.27}$
	100	71.83	0.19	2300	146.61	0.11	1600	7.88	1.62	$2867.80e^{j34.79}$
	200	72.42	0.10	2300	147.78	0.06	1600	7.5	0.91	$2765.32e^{j35.68}$
3	1	70.28	13.39	3072	145.70	9.99	2168	5.29	159.29	$3734.45e^{j35.24}$
	50	70.34	0.29	3050	145.72	0.25	2150	5.22	3.67	$3706.98e^{j35.03}$
	100	70.32	0.17	3000	145.83	0.17	2100	5.59	1.87	$3755.30e^{j35.23}$
	200	69.78	0.10	2600	146.99	0.10	2200	5.24	1.41	$3556.18e^{j35.52}$

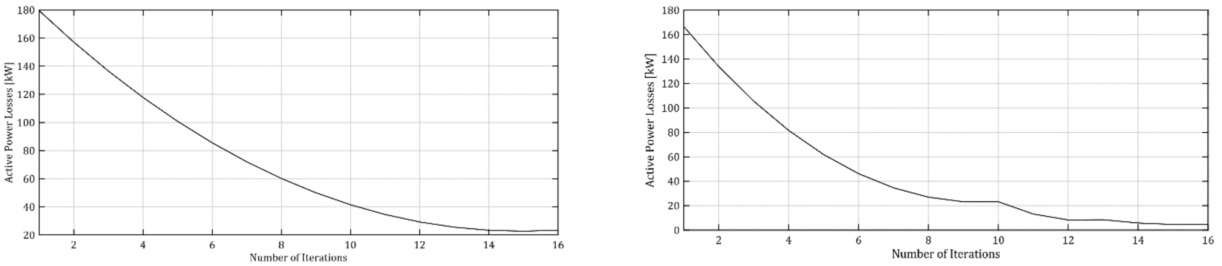

a) b)

Figure. 4 Convergence curves for power losses of the CO method: a) single location 69-bus, b) three locations 69-bus

6 Case Studies

Assessment of the effectiveness of the proposed CO method is achieved by its application on two distribution systems: 12.66 kV, 69-bus distribution system [51] and an 11 kV, 119-bus distribution system [52]. Objective function values in Tab. 3 and Tab. 4 are calculated with $c_e = 0.067$ \$/kWh and $c_p = 16$ \$/kW. Base-case values for power losses, minimum voltages, and objective function (1) for both systems are:

- *69-bus*. $\Delta P_0 = 225\,(\text{kW})$, $U_{min} = 0.9092$ (pu) and $F_0 = 135657\,(\$/\text{year})$
- *119-bus*. $\Delta P_0 = 1298\,(\text{kW})$, $U_{min} = 0.8690$ (pu) and $F_0 = 782590\,(\backslash\$/\text{year})$

6.1 69-bus distribution system

Table 3 shows results from the performed analysis using the proposed CO method on the 69-bus distribution system. Nine different scenarios are considered, i.e., three scenarios for each PIN type (active – P, reactive – Q and apparent – S) for one, two and three locations. For each scenario, minimum voltages and computation time is also presented. Table 3 suggests that CO method performs remarkably well presenting unique results in terms of power losses, minimum voltage, and computation time.

Table 3 Results from CO for 69-bus distribution system (power injection size is expressed in P(kW), Q(kVAr) and S(kVA); voltages in pu)

PIN № & Type	Size@Bus			U_{min}@Bus	ΔP (kW)	F (\$/year)	t (sec)
1P	1869.3@61			0.9683@27	83.22	50175	0.14
2P	1836@61	516@17		0.9807@65	71.77	43272	0.81
3P	1755@61	390@21	390@11	0.9795@65	69.7	42024	0.09
1Q	1313@61			0.9305@65	152.05	91674	0.38
2Q	1296@61	336@17		0.9314@65	146.48	88316	0.16
3Q	1302@61	350@17	518@50	0.9315@65	145.68	87833	0.57
1S	$2249.5e^{j35.33}$@61			0.9725@27	23.17	13970	2.22
2S	$2209.5e^{j35.29}$@61	$649.6e^{j34.00}$@17		0.9943@50	7.44	4486	3.64
3S	$2120.5e^{j35.55}$@61	$471.4e^{j35.00}$@21	$471.4e^{j35.00}$@11	0.9973@50	4.6	2773	2.90

6.2 119-bus distribution system

Performance evaluation of the CO method for the 119-bus distribution system is attained through five scenarios including: three scenarios for optimal placement and sizing of active, reactive, and apparent PINs at five locations, and two more scenarios including optimal placement and sizing of active and apparent PINs with optimal power factor at seven locations.

Table 4 Results from CO for 119-bus distribution system (power injection size is expressed in P(kW), Q(kVAr) and S(kVA); voltages in pu)

	Size@Bus				
PIN № & Type	**5P**	**5Q**	**5S**	**7P**	**7S**
	2800@50	4400@29	$3942e^{j42.0}$@50	1760@20	$2072e^{j36.6}$@20
	2800@71	2600@50	$3179e^{j32.5}$@72	1870@41	$2420e^{j35.7}$@41
	2400@79	1800@72	$2765e^{j35.7}$@80	2860@50	$3796e^{j42.8}$@50
	1600@96	1700@80	$1981e^{j34.0}$@96	2860@71	$3131e^{j32.2}$@72
	2800@110	2300@110	$3546e^{j38.9}$@110	2200@80	$2760e^{j37.5}$@80
				1540@97	$2082e^{j33.3}$@96
				3080@109	$3447e^{j40.0}$@110
Total PIN (kVA)	12400	12800	15413	16170	19708
ΔP (kW)	574.33	857.69	211.58	515.82	127.61
$U_{\min}$ (pu)	0.955	0.9074	0.9608	0.9582	0.9764
F ($/year)	346280	517120	127570	311000	76940
t (sec)	0.82	2.14	9.42	3.13	13.08

7 Conclusion

This paper presents a Clustering Optimisation (CO) method for optimal placement and sizing of DG's presented as active, reactive, or apparent power injections (PINs) with the aim of obtaining minimum power losses while maintaining an acceptable system voltage profile. The effectiveness of the proposed method is assessed through simulations performed on a 69-bus and 119-bus distribution systems. It can be concluded that the proposed method performs outstandingly, presenting unique results in all considered scenarios.

The CO method in its essence is a pattern of using a load flow procedure. It does not include solving complex mathematical formulations, it doesn't operate with population, its creation and iterative updating, it doesn't use problem coding and/or solution decoding and it has no convergence problems which makes the method superior in terms of simplicity/complexity and easy implementation. Furthermore, the lack of laborious procedures makes the method significantly intelligible, simple, and easy to reproduce. Because the methods working principle is based on simple mathematical formulations and there is no dedicated bus selection procedure, optimal or nearly optimal solutions are obtained remarkably quickly. Short computation time enhances the convenience of using this method. Another salient advantage of the proposed method is the recurrence of results, i.e., obtained results are repetitive from simulation to simulation, which is not the case for some of the other existing methods.

8 References

[1] T. Ackermann, G. Andersson, L. Soder, Distributed generation: a definition, *Electric Power Systems Research* 57 (3) (2001) 195 – 204. doi: https://doi.org/10.1016/S0378-7796(01)00101-8.

[2] T. Griffin, K. Tomsovic, D. Secrest, A. Law, Placement of dispersed generation systems for reduced losses, in: *Proceedings of the 33rd Annual Hawaii International Conference on System Sciences*, 2000, pp. 9 pp.–. doi:10.1109/HICSS.2000.926773.

[3] N. S. Rau, Y. H. Wan, Optimum location of resources in distributed planning, *IEEE Transactions on Power Systems* 9 (4) (1994) 2014–2020. doi:10.1109/59.331463.

[4] M. Aman, G. Jasmon, A. Bakar, H. Mokhlis, M. Karimi, Optimum shunt capacitor placement in distribution system - a review and comparative study, *Renewable and Sustainable Energy Reviews* 30 (2014) 429 – 439. doi: https://doi.org/10.1016/j.rser.2013.10.002.

[5] M. Pesaran, P. D. Huy, V. K. Ramachandaramurthy, A review of the optimal allocation of distributed generation: Objectives, constraints, methods, and algorithms, *Renewable and Sustainable Energy Reviews* 75 (2017) 293 – 312. doi: https://doi.org/10.1016/j.rser.2016.10.071.

[6] A. Ehsan, Q. Yang, Optimal integration and planning of renewable distributed generation in the power distribution networks: A review of analytical techniques, *Applied Energy* 210 (2018) 44 – 59. doi: https://doi.org/10.1016/j.apenergy.2017.10.106.

[7] Z. Abdmouleh, A. Gastli, L. Ben-Brahim, M. Haouari, N. Al-Emadi, Review of optimization techniques applied for the integration of distributed generation from renewable energy sources, *Renewable Energy* 113 (05 2017). doi: 10.1016/j.renene.2017.05.087.

[8] T. Gozel, M. H. Hocaoglu, An analytical method for the sizing and siting of distributed generators in radial systems, *Electric Power Systems Research* 79 (6) (2009) 912 – 918. doi: https://doi. org/10.1016/j.epsr.2008.12.007.

[9] N. Acharya, P. Mahat, N. Mithulananthan, An analytical approach for DG allocation in primary distribution network, *International Journal of Electrical Power & Energy Systems* 28 (10) (2006) 669 – 678. doi: https://doi.org/10.1016/j.ijepes.2006.02.013.

[10] EN 50160 - voltage characteristics of electricity supplied by public electricity networks.

[11] S. C. Tripathy, G. D. Prasad, O. P. Malik, G. S. Hope, Load-flow solutions for ill-conditioned power systems by a newton-like method, *IEEE Transactions on Power Apparatus and Systems* PAS-101 (10) (1982) 3648–3657. doi:10.1109/TPAS.1982.317050.

[12] D. Shirmohammadi, H. W. Hong, A. Semlyen, G. X. Luo, A compensation-based power flow method for weakly meshed distribution and transmission networks, *IEEE Transactions on Power Systems* 3 (2) (1988) 753–762. doi:10.1109/59.192932.

[13] G. X. Luo, A. Semlyen, Efficient load flow for large weakly meshed networks, *IEEE Transactions on Power Systems* 5 (4) (1990) 1309–1316. doi:10.1109/59.99382.

[14] M. E. Baran, F. F.Wu, Network reconfiguration in distribution systems for loss reduction and load balancing, *IEEE Transactions on Power Delivery* 4 (2) (1989) 1401–1407. doi:10.1109/61.25627.

[15] D. Rajicic, R. Ackovski, R. Taleski, Voltage correction power flow, *IEEE Transactions on Power Delivery* 9 (2) (1994) 1056–1062. doi:10.1109/61.296308.

[16] S. Raj, B. Bhattacharyya, Weak bus-oriented optimal var planning based on grey wolf optimization, in *2016 National Power Systems Conference (NPSC)*, 2016, pp. 1–5. doi:10.1109/NPSC.2016.7858929.

[17] D. Das, Optimal placement of capacitors in radial distribution system using a Fuzzy-GA method, *Int. J. Elect. Power Energy Syst.* 30 (6-7) (2008) 361 – 367. doi: http://dx.doi.org/10.1016/j.ijepes.2007.08.004.

[18] S. Ghasemi, Balanced and unbalanced distribution networks reconfiguration considering reliability indices, *Ain Shams Engineering Journal* 9 (4) (2018) 1567 – 1579. doi: https://doi.org/10.1016/j.asej.2016.11.010.

Flexibility assessment of the Macedonian power system: a high-level screening method for the future flexibility needs

Stojan Malcheski[1],
[1] Power System Planning & Analysis, Macedonian Transmission System Operator, Maksim Gorki No. 4, Skopje, North Macedonia, stojan.malcheski@mepso.com.mk

Sime Kuzarevski[2],
[2] Power System Planning & Analysis, Macedonian Transmission System Operator, Maksim Gorki No. 4, Skopje, North Macedonia, sime.kuzarevski@mepso.com.mk

Jovica Vuletić[3]
[3] Ss. Cyril and Methodius University, Faculty of Electrical Engineering and Information Technologies, Rugjer Boskovic 18, P.O.Box 574 1000 Skopje, R. N. Macedonia jovicav@pees-feit.edu.mk

Jordančo Angelov[4],
[4] Ss. Cyril and Methodius University, Faculty of Electrical Engineering and Information Technologies, Rugjer Boskovic 18, P.O.Box 574 1000 Skopje, R. N. Macedonia jordanco@pees-feit.edu.mk

Mirko Todorovski[5]
[5] Ss. Cyril and Methodius University, Faculty of Electrical Engineering and Information Technologies, Rugjer Boskovic 18, P.O.Box 574 1000 Skopje, R. N. Macedonia mirko@pees-feit.edu.mk

Abstract* – To achieve the strategic goals in the energy sector during the ascension path towards the European Union, North Macedonia has set ambitious goals in the Macedonian strategic framework for the power sector. Namely, the investment plans in conventional generation technologies are ambiguous, while the planned investments in variable renewable energy sources (VRES) are quick paced. Furthermore, with interest in VRES investment with total installed capacities above the hourly load during hours of maximal VRES generation, it is crucial to assess the future flexibility needs of the Macedonian power system. This paper uses multiple metrics to obtain a high-level estimate of the system inertia and flexibility needs of the Macedonian power system on a mid-term planning horizon. The system inertia and flexibility need estimates are calculated using a multi-scenario approach where the model dispatch is calculated using a Monte Carlo optimization on a market model enclosing Southeast Europe. The obtained results give a high-level estimate of the evolution of flexibility needs and system inertia of the Macedonian power system on a mid-term planning horizon.

1 Introduction

With the evolution of the Macedonian power sector towards a green energy sector, the Macedonian generation portfolio is supposed to undergo drastic structural changes in the years to come where the plan is to substitute the heavy emission power plants with VRES. According to the Macedonian strategic framework [1-3], the decommissioning of the lignite and fuel oil power plants will take place from 2019 to 2027. While the strategic goals for investments in VRES are ambitious, the investment plans in conventional generation technologies remain ambiguous. The possible changes to the conventional generation portfolio, combined with ambitious investment plans in VRES, will result in increased flexibility needs [4]. The difficulties of VRES integration and exploitation in the Macedonian power system will vary depending on the VRES production and installed capacity, the system load profile for the analyzed time horizon, and the flexibility of the power system [5]. Hence, the uncertain nature of the Macedonian energy strategy is analyzed using a multi-scenario approach to cover a broad spectrum of possible future scenarios.

As defined by [6], *power system flexibility is the capability of a power system to cope with the variability and uncertainty that VRES generation introduces into the system in different time scales, from the very short to the long term, avoiding curtailment of VRES and reliably supplying all the demanded energy to customers*. For a transmission system operator tasked to integrate large-scale VRES projects in their power system, a reasonable estimate of the future system flexibility needs is essential. There are multiple approaches to assessing the flexibility of a power system differing in their complexity and computation resource requirements. So far, in academia and power sector, there is no consensus on the best approach to tackle this problem since power system flexibility is system-specific [4].

There are numerous papers and technical reports covering the assessment of flexibility needs on a planning horizon written to this date. While the research focus is on algorithms that treat time series to assess the flexibility needs of a power system, such as in [7] and [8], there are not many papers that treat the problem using a stochastic market modeling approach.

Recent papers that treat the problem using a stochastic market modeling approach are [9], where the authors use flexibility metrics to analyze the flexibility needs from a ramp requirements point of view, while in [10], the authors focus on the impact of time-step granularity of the stochastic market modeling approach. The authors in [9] and [10] opt for a stochastic modeling approach using a European market model. In [11], the authors explore various scenarios and flexibility mechanisms to analyze a high share of RES scenarios. Furthermore, the authors in [11] developed a linear programming model POWER to solve a US-based market model.

Additionally, there are papers and studies on system flexibility that treat the problem on a national level while considering the regional implications on the national results. Such is the case in [12], where the authors examine the impact on system inertia during high penetrations of wind power to the power system of Ireland using the non-synchronous penetration ratio (SNSP) metric, and in [13], where the authors assess the flexibility needs of the Greek power system using two metrics, the flexibility index (FIX) and present VRE penetration potential (PVP). From the power system sector in Europe, two reports are of outstanding quality, namely [14] and [15].

When analyzing system flexibility, it is crucial to get a rough estimate of future system flexibility needs before developing a complicated methodology that would cover the system specifics. In this paper, the flexibility assessment of the Macedonian power system is based on the net load, which represents the difference between system load and non-dispatchable power generation [16]. More specifically, the research focus is on the following flexibility metrics: a renewable penetration index (RPI) and renewable energy penetration index (REPI) [17], system probability for VRES curtailment (LORE) [18], and system inertia metric SNSP [19]. Furthermore, the ramp span occurrence was analyzed to obtain an estimate of the most frequent ramp span durations in the future. The analysis was done, and the parameters were calculated using a regional market model of Southeast Europe, where each country is modeled with one/or multiple areas on the copper plate principle where the total production and load on a power system level is aggregated to the area/s representing a given country and interconnected with other neighboring countries on NTC-based interfaces [20].

The remainder of this paper is organized as follows: Section 2 gives an overview of the market model from a national and regional point of view and scenario definitions for analysis, Section 3 gives a detailed overview of the methodology for calculation of the selected metrics, Section 4 presents the results of the analysis while Section 5 presents a summary of the findings.

2 Market Analysis and Scenarios

The developed market model is for a mid-term time horizon (2030), based on the Pan-European Market Modelling Database (PEMMDB) and Pan-European Climate Database (PECD), for which details relevant to the market model, are publicly available on the link given in [20]. The simulation scope is the area of Southeast Europe in light gray in Figure 1. The exchanges with the exogenous power systems, given in dark gray in Figure 1, are modeled as hourly market-driven power flows.

The model consists of thirty-five climatic years for load, solar, wind, and hydro generation to account for VRES and load variability, paired with twenty outage patterns for the thermal power plants yielding seven-hundred Monte Carlo years. The solution is obtained using a commercial-grade market simulator ANTARES [21], and the obtained results are with hourly resolution on an annual basis.

The Macedonian strategy framework for the power sector is ambiguous when it comes to the investment plan in conventional power plants. Namely, there is uncertainty in the mid and long term whether the investments will be in gas power plants or a pump storage power plant (PSP). According to the Macedonian strategy framework, the investments in gas power plants by 2030 might amount to 450 MW. On the other hand, the PSP potential is around 333 MW in turbine mode and 363 MW in pump mode, based on the authors' best estimate.

Figure 1. Modeling scope of the Regional Market Model

Since both investments in gas power plants and PSP contribute to power system flexibility, both scenarios are analyzed, comparing the results of both scenarios to a base case scenario that takes no investment decision in conventional power plants. Moreover, the analysis considers two VRES profiles (wind and solar) named slow-paced and rapid development. The two VRES development profiles paired with the business-as-usual and the investment in gas and PSP scenarios yield a total of six scenarios:

- **Scenario 1:** a base case with **slow-paced VRES** development.
- **Scenario 2:** investment in gas power plants with **slow-paced VRES** development.
- **Scenario 3:** investment in PSP with **slow-paced VRES** development.
- **Scenario 4:** a base case with **rapid VRES** development.
- **Scenario 5:** investment in gas power plants with **rapid VRES** development.
- **Scenario 6:** investment in PSP with **rapid VRES** development.

Figure 2 shows the installed capacities of different production technologies for the six scenarios of the Macedonian power system analyzed in this paper.

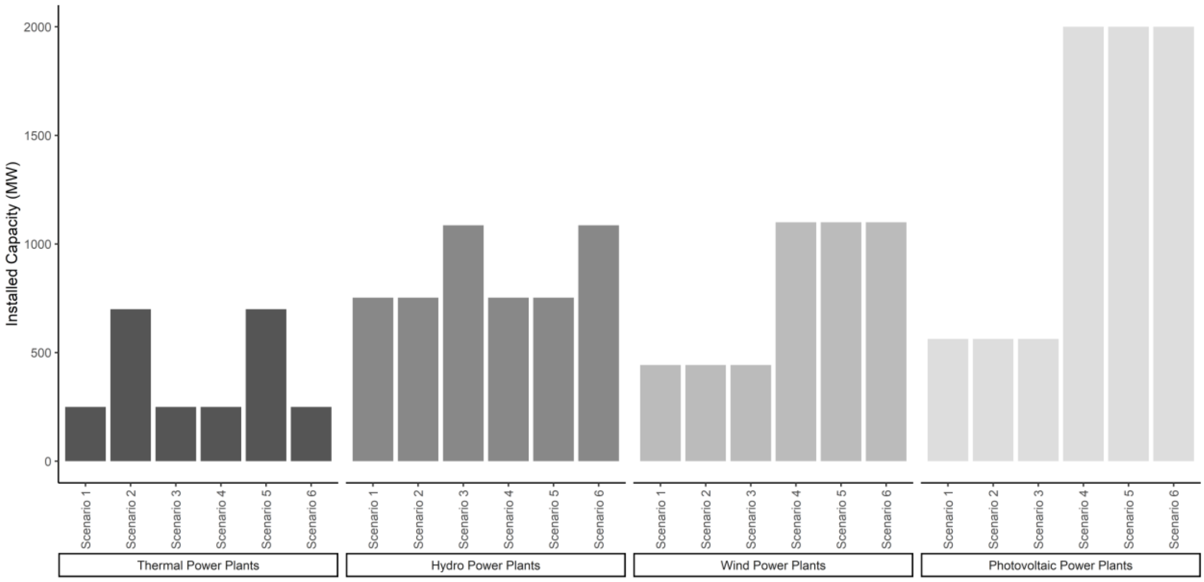

Figure 2. Installed capacity per generation technology for the six scenarios in North Macedonia on a mid-term planning horizon

Figure 3 and Figure 4 present the annual shares of the demand being met by VRES on a regional basis for the slow-paced and rapid VRES development scenario in MK, respectively. Figure 3 and Figure 4 show that the VRES data in PEMMDB and PECD for Southeast Europe is modest at best, while in most cases, it can be considered quite low, with VRES participation usually below 30%. Hence, the calculated flexibility metrics for North Macedonia might underestimate the flexibility needs since the needs are dependent on the development of the VRES generation portfolios in the region.

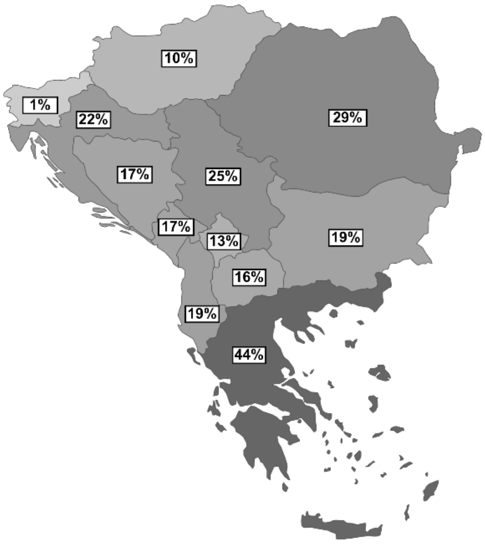

Figure 3. Share of demand being met by VRES on annual level on regional basis with slow-paced VRES development scenario in MK

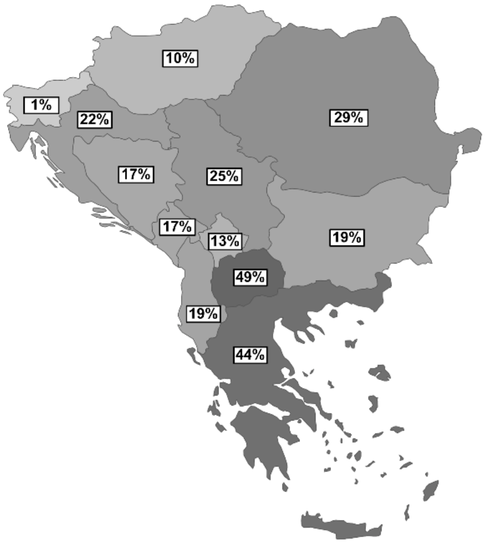

Figure 4. Share of demand being met by VRES on annual level on regional basis with rapid VRES development scenario in MK

3 Flexibility Metrics

The flexibility analysis is based on the following flexibility metrics: RPI, REPI, LORE, and SNSP. The RPI and REPI metrics are calculated based on the climatic years' data (correlated load, wind, PV, and Run-of-river time series). The LORE and SNSP metrics are calculated by analyzing the annual dispatch results from the market simulation on an hourly level. Additionally, net load (NL) and net load ramp (NLR) were calculated before calculating the LORE metric.

3.1 Calculation of RPI and REPI

The RPI is calculated as:

$$RPI = \max\left(\frac{Wind(t)+PV(t)}{Load(t)}\right), \forall t \in [1,8760] \tag{1}$$

and the REPI is calculated as:

$$REPI = \frac{\sum_{t=1}^{8760}\left(Wind(t)+PV(t)\right)}{\sum_{t=1}^{8760}\left(Load(t)\right)} \tag{2}$$

where $Wind(t)$ is the hourly production of wind power plants in (MW), $PV(t)$ is the hourly production of solar power plants in (MW), and $Load(t)$ is the hourly load in (MW).

3.2 Calculation of LORE

The system probability for VRES curtailment is calculated similarly to the Loss of Wind Estimation (LOWE) metric presented in [18]. Since, in this paper, the research is extended to cover Wind and PV curtailment probability, the metric name is modified to Loss of renewable energy estimation (LORE).

Before calculating LORE, the NL and NLR were calculated where NL is calculated as:

$$NL(t) = Load(t) - Wind(t) - PV(t) - Must\_Run(t) \tag{3}$$

while NLR is calculated as:

$$NLR(t) = NL(t+1) - NL(t) \tag{4}$$

$$NLR_{+}(t) = NLR(t), \forall NLR(t) \geq 0 \tag{5}$$

$$NLR_{-}(t) = NLR(t), \forall NLR(t) < 0 \tag{6}$$

where $Must\_Run(t)$ consists of the production of all technologies that are hard constrained to produce energy during predetermined periods on annual level in (MW).

Calculating the NLR with different time steps, e.g., two, four, or an arbitrary system-specific time step will yield different results. NL and NLR were calculated with an hourly time step.

The periods during which VRES curtailment might occur are similar to the ones described in [18], which are: NL lower than zero, NLR_{+} is higher than the ramp-up[1] capability of online generators and offline generators that cannot be brought online, and NLR_{-} is higher than the ramp-down capability of online generators and online generators that can be shut down.

The first recognized period during which VRES curtailment might occur is when NL is lower than zero, so the probability of this event is computed as:

$$P(Period_1) = P(NL(t) \leq 0) \tag{7}$$

The second period is the one where NLR_{+} is higher than the ramp-up capability of online generators and offline generators that cannot be brought online, for which the probability of occurrence is calculated as:

$$P(Period_2) = P(NLR_{+}(t) \geq \sum Ramp\_up(t)) \tag{8}$$

The last period is the one where NLR_{-} is higher than the ramp-down capability of online generators and online generators that can be shut down, for which the probability of occurrence is calculated as:

$$P(Period_3) = P(|NLR_{-}(t)| > \sum Ramp\_down(t)) \tag{9}$$

Finally, the $LORE$ metric is calculated as:

$$LORE = 1 - (1 - P(Period_1)) \cdot (1 - P(Period_2)) \cdot (1 - P(Period_3)) \tag{10}$$

---

[1] The Ramp-up or Ramp-down Capability more commonly known as the Ramping Capability of a generator is defined as the sustained rate of change of generator output, in (MW/s). In this paper the Ramp-up and Ramp-down capability of the generators is expressed in (MW/h) due to the time step granularity of the market simulation.

3.3 Calculation of SNSP

The Non-synchronous penetration ratio (SNSP) is calculated as:

$$SNSP(t) = \frac{\sum P_{in_{inverter}}(t)}{\sum P_{out}(t)} = \frac{Wind(t)+PV(t)}{Load(t)+Export(t)} \tag{11}$$

where $Export(t)$ is the export to the neighboring countries in (MW), [19].

4 Results and Discussion

The flexibility analysis of the Macedonian power system was carried out using a regional market model covering Southeast Europe with six different scenarios for the national generation portfolio. To account for the stochastic nature of VRES, in the analysis, thirty-five unique climatic year scenarios for VRES and twenty outage patterns for the conventional power plants were used, which accounts for a total of seven hundred Monte Carlo years per scenario. Four main metrics were calculated: RPI, REPI, LORE, and SNSP. Additionally, an analysis of the ramp span occurrence based on the net load ramps was done.

Table 1 shows the results for RPI and REPI for the Macedonian power system. For the slow-paced development scenario of VRES, the values for RPI and REPI are 1.81 and 0.16, respectively, while for the rapid development scenario of VRES, the values for RPI and REPI are 5.4 and 0.49, respectively. In both VRES development scenarios, RPI is, on average, eleven times higher than REPI because the load is already low during hours of high VRES production, especially during the summer period. In the future, to avoid VRES production curtailment, the Macedonian strategic framework should be reworked to consider different energy storage technologies or a shift from a fossil fuel-powered industry to an electricity-powered industry to increase the overall load profile [22]. As an alternative approach, the Macedonian strategic framework may be reworked to develop a generation portfolio with suitable flexibility, which would allow the country to become export oriented.

Table 1. RPI and REPI for the Macedonian power system on a mid-term planning horizon

VRES development scenario	**RPI**				**REPI**			
	min	**max**	**mean**	**Standard Deviation**	**min**	**max**	**mean**	**Standard Deviation**
slow-paced	0.938	1.811	1.114	0.148336	0.14	0.17	0.16	0.00004
rapid	2.804	5.403	3.320	0.447087	0.46	0.52	0.49	0.00030

Table 2 shows the loss of renewable energy estimation (LORE) for the six analyzed scenarios. The results show a similarity between the LORE values for Scenario 2 and Scenario 3 compared to Scenario 1 and Scenario 5 and Scenario 6 compared to Scenario 4. Hence, when the curtailment of VRES is considered, both investments in gas power plants and a pump storage power plant have similar effects. In all six scenarios, the main driver for VRES curtailment is the period during which VRES production is higher than system load. It is important to note that the results from the market model did not show curtailment of VRES as a result of the well-developed interconnections in the region of interest, but at the same time, the installed VRES capacities in the neighboring countries are quite modest, with exception to the installed capacities in Romania, Greece, Bulgaria, and the rapid development VRES scenarios for North Macedonia. From the results, it is expected that if each country follows a VRES development scenario, such as the one we are using for North Macedonia, the region will experience curtailment of VRES.

Table 2. LORE for the analyzed scenarios for the Macedonian power system on a mid-term planning horizon

Scenario	**Scenario 1**	**Scenario 2**	**Scenario 3**	**Scenario 4**	**Scenario 5**	**Scenario 6**
LORE value	4.290	1.478	1.110	30.229	25.535	25.092

Figure 5 and Figure 6 show the rate of occurrence of ramps for the slow-paced and rapid VRES development scenario, respectively. The rate of occurrence of ramps is calculated as an average of the measurement of the duration of up and down periods of $NLR(t)$ for the thirty-five climatic years for the slow-paced and rapid VRES development scenarios, respectively. Based on the obtained results, we can conclude for both VRES development scenarios that the one-hour ramps are the most frequent. Moreover, the two-hour, three-hour, four-hour, eight-hour, nine-hour, ten-hour, and eleven-hour ramps occur frequently enough so that their effects should be analyzed in more detail in future flexibility studies of the Macedonian power system.

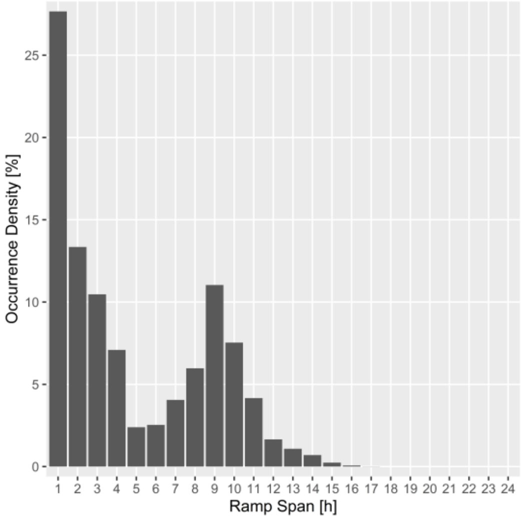

Figure 5. Ramp span occurrence for the slow-paced VRES development scenario

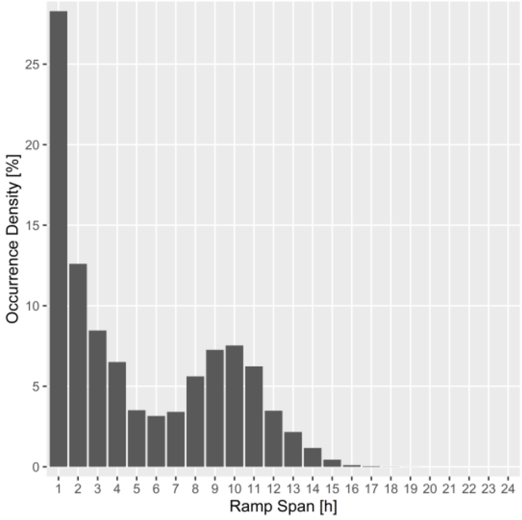

Figure 6. Ramp span occurrence for the rapid VRES development scenario

Figure 7 shows the SNSP density for the analyzed scenarios of the Macedonian power system. In comparison to the slow-pace VRES development scenarios (Scenario 1, 2, and 3), the rapid VRES development scenarios (Scenario 4, 5, and 6) have a notable SNSP evolution which suggests that with the development of VRES and decommissioning of conventional brown power plants in MK and the region, the system inertia might be inadequate to maintain system stability. From the results for Scenario 4, 5, and 6 in Figure 7, we can see that the tail of the graph goes to 1, and for Scenario 6, even above 1, which suggests that in the future in MK, we will have numerous regimes with extremely low inertia.

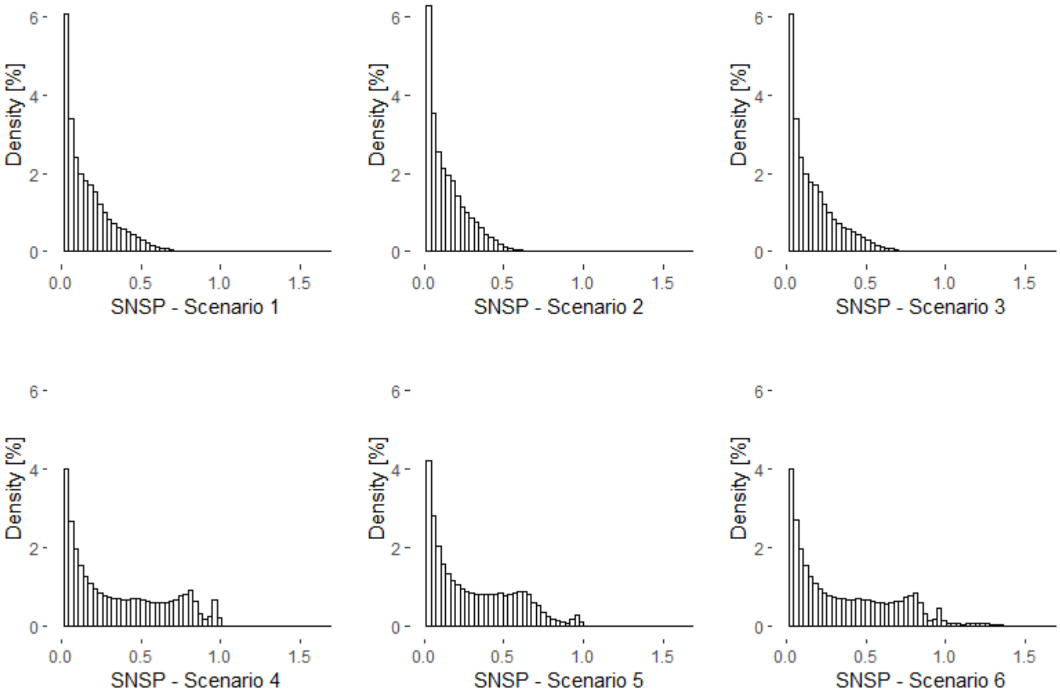

Figure 7. Non-synchronous penetration ration (SNSP) on national level for the analyzed scenarios

The results in Figure 8 clearly show that as the VRES profile in MK evolves, the Macedonian power system would rely on the neighboring power systems for system inertia provision. Additionally, as more and more conventional brown power plants get decommissioned, the region will have even fewer power plants that could provide the needed system inertia. Hence, with the VRES evolution on a regional level, the focus should be on a share of reserves and regional balancing market in Southeast Europe, which will lead to an optimal interconnection use and investments in synthetic inertia from large VRES plants.

5 Conclusion

The flexibility analysis for the Macedonian power system was done using a probabilistic market-based calculation on a PEMMDB-based market model for Southeast Europe. For North Macedonia, six national scenarios were analyzed as a combination of three development scenarios for the conventional power plants in MK and two VRES development scenarios, Section 3. The flexibility was assessed by computing the RPI, REPI, LORE, and SNSP metrics. Additionally, an analysis of the ramp span occurrence was done for the two VRES development scenarios.

The introduction of VRES to the system leads to a high ratio between RPI and REPI, which is mainly driven by the low load levels during the periods where the VRES production is highest. Moreover, as shown in Table 2, the LORE parameter increases as more VRES are introduced to the system, which means that the risk for VRES curtailment in the future will be high. Since the flexibility needs are dependent on the regional evolution of the generation profiles in the neighboring countries, it is expected that as more VRES are introduced, the curtailment risk in MK and the region will be even higher. To avoid future VRES curtailment, it is important to run dedicated flexibility studies to assess the flexibility needs and optimize the conventional generation portfolio to a sufficiently flexible one while introducing smart technologies and techniques for flexibility provision. Furthermore, the Macedonian strategic framework for the energy sector should be reworked to consider different energy storage technologies, a shift from a fossil fuel-powered industry to an electricity-powered industry so to increase the overall load profile, or a redesign of the investment plan in the generation and storage portfolio to be suitably flexible to allow the country to become export oriented. Lastly, as the evolution of the generation profile is optimized, the national and regional legislation must be appropriately updated to support the needed changes.

Figures 5 and 6 show the ramp span occurrence for the slow-paced and rapid VRES development scenarios, respectively. As the results show, the one-hour ramp is the most frequent, followed by the two-hour, three-hour, four-hour, eight-hour, nine-hour, ten-hour, and eleven-hour ramps. In future flexibility studies, the one, two-hour, three-hour, four-hour, eight-hour, nine-hour, ten-hour, and eleven-hour ramps on system flexibility should be analyzed in more detail on a national level.

With the rapid development of the VRES profile in the region, a decarbonization phase is envisioned where conventional brown power plants are planned to be decommissioned. This will lead to a reduction of the available system inertia in the region, and in MK, it is expected that there will be periods with extremely low system inertia in the future if the evolution of the generation profile follows the rapid VRES development scenario. To avoid long periods of system instability, the focus should be on participation in regional markets for a share of reserves to optimally use the well-developed interconnections as well as developing the national markets to facilitate synthetic inertia provision from the large VRES parks.

The metrics in this paper are relatively easy to compute, and their computation isn’t computationally intensive compared to other more detailed methods. The obtained results represent a first-of-a-kind screening of the future flexibility needs in the Macedonian power sector, and they pave the way for future developments in this field on a national level. In the future, on a national level, the research focus should be on optimizing the flexibility portfolio from two aspects: reduction of cost for adequate flexibility provision and introduction of a flexibility analysis as an integrated part of the national adequacy studies. Furthermore, since the analysis of the system inertia showed that in the future, with the rapid development of VRES, the Macedonian power system would experience periods of extremely low system inertia, an analysis of the expected Rate of Change of Frequency (RoCoF) should be carried with a regional scope.

References

[1] PwC, MANU, The Strategy for Energy Development of the Republic of North Macedonia until 2040, October 2019.

[2] GIZ, National Energy and Climate Plan of the Republic of North Macedonia, July 2020.

[3] TAF-WB, Programme for the realisation of the Energy Development Strategy 2021 – 2025, March 2021.

[4] Cochran, J & Miller, Mackay & Zinaman, Owen & Milligan, Michael & Arent, Doug & Palmintier, Bryan & O'Malley, Mark & Mueller, S & Lannoye, Eamonn & Tuohy, Aidan & Kujala, B & Sommer, M & Holttinen, Hannele & Kiviluoma, Juha & Soonee, Sushil. (2014). Flexibility in 21st Century Power Systems.

[5] E. Lannoye, D. Flynn and M. O'Malley, "Evaluation of Power System Flexibility," in IEEE Transactions on Power Systems, vol. 27, no. 2, pp. 922-931, May 2012, doi: 10.1109/TPWRS.2011.2177280.

[6] IRENA (2018), Power System Flexibility for the Energy Transition, Part 2: IRENA FlexTool methodology, International Renewable Energy Agency, Abu Dhabi.

[7] D. A. Tejada-Arango, G. Morales-España, S. Wogrin and E. Centeno, "Power-Based Generation Expansion Planning for Flexibility Requirements," in _IEEE Transactions on Power Systems_, vol. 35, no. 3, pp. 2012-2023, May 2020, doi: 10.1109/TPWRS.2019.2940286.

[8] M. Cañas-Carretón and M. Carrión, "Generation Capacity Expansion Considering Reserve Provision by Wind Power Units," in _IEEE Transactions on Power Systems_, vol. 35, no. 6, pp. 4564-4573, Nov. 2020, doi: 10.1109/TPWRS.2020.2994173.

[9] Matthias Huber, Desislava Dimkova, Thomas Hamacher, Integration of wind and solar power in Europe: Assessment of flexibility requirements, Energy, Volume 69, 2014, Pages 236-246, ISSN 0360-5442, https://doi.org/10.1016/j.energy.2014.02.109.

[10] Hans-Kristian Ringkjøb, Peter M. Haugan, Pernille Seljom, Arne Lind, Fabian Wagner, Sennai Mesfun, Short-term solar and wind variability in long-term energy system models - A European case study, Energy, Volume 209, 2020, 118377, ISSN 0360-5442, https://doi.org/10.1016/j.energy.2020.118377.

[11] Bethany A. Frew, Sarah Becker, Michael J. Dvorak, Gorm B. Andresen, Mark Z. Jacobson, Flexibility mechanisms and pathways to a highly renewable US electricity future, Energy, Volume 101, 2016, Pages 65-78, ISSN 0360-5442, https://doi.org/10.1016/j.energy.2016.01.079.

[12] J. O'Sullivan, A. Rogers, D. Flynn, P. Smith, A. Mullane and M. O'Malley, "Studying the Maximum Instantaneous Non-Synchronous Generation in an Island System—Frequency Stability Challenges in Ireland," in _IEEE Transactions on Power Systems_, vol. 29, no. 6, pp. 2943-2951, Nov. 2014, doi: 10.1109/TPWRS.2014.2316974.

[13] A. C. Stratigakos, K. F. Krommydas, P. C. Papageorgiou, C. Dikaiakos and G. P. Papaioannou, "A Suitable Flexibility Assessment Approach for the Pre-Screening Phase of Power System Planning Applied on the Greek Power System," _IEEE EUROCON 2019 -18th International Conference on Smart Technologies_, 2019, pp. 1-6, doi: 10.1109/EUROCON.2019.8861888.

[14] ELIA, Adequacy and Flexibility Study for Belgium 2022-2032, https://www.elia.be/en/electricity-market-and-system/adequacy/adequacy-studies

[15] European Commission, Directorate-General for Energy, Bardet, R., Khallouf, P., Fournié, L., et al., Mainstreaming RES : flexibility portfolios : design of flexibility portfolios at Member State level to facilitate a cost-efficient integration of high shares of renewables, Publications Office, 2019, https://data.europa.eu/doi/10.2833/97595

[16] IEA (2011), Harnessing Variable Renewables: A Guide to the Balancing Challenge, OECD Publishing, Paris, https://doi.org/10.1787/9789264111394-en.

[17] Dierk Bauknecht, Christoph Heinemann, Moritz Vogel, Study on the impact assessment for a new Directive mainstreaming deployment of renewable energy and ensuring that the EU meets its 2030 renewable energy target, Task 3.1: Historical assessment of progress made since 2005 in integration of renewable electricity in Europe and first-tier indicators for flexibility, July 2019, https://energy.ec.europa.eu/design-flexibility-portfolios-member-state-level-facilitate-cost-efficient-integration-high-shares_en

[18] J. Ma, V. Silva, R. Belhomme, D. S. Kirschen and L. F. Ochoa, "Exploring the use of flexibility indices in low carbon power systems," 2012 3rd IEEE PES Innovative Smart Grid Technologies Europe (ISGT Europe), 2012, pp. 1-5, doi: 10.1109/ISGTEurope.2012.6465757.

[19] Poncela Blanco, M., Purvins, A. and Chondrogiannis, S., Pan-European analysis on power system flexibility, ENERGIES, ISSN 1996-1073, 11 (7), 2018, JRC110658.

[20] ENTSOE, European Resource Adequacy Assessment 2021 Edition – Executive Report, Brussels, 2021, link: https://www.entsoe.eu/outlooks/eraa/eraa-downloads/

[21] RTE, Antares Simulator 7.1.0 - OPTIMIZATION PROBLEMS FORMULATION, https://antares-simulator.org

[22] B. Ćosić, G. Krajačić, and N. Duić, “A 100% renewable energy system in the year 2050: The case of Macedonia,” Energy, vol. 48, no. 1, pp. 80–87, Dec. 2012, doi: 10.1016/j.energy.2012.06.078.

Electromagnetic Coupling of Overhead High Voltage Transmission Lines to Pipelines in Multilayer Soil: Parametric Analysis

Blagoja Markovski[1], **Leonid Grcev**[2], **Vladimir Gjorgievski**[3],
Bodan Velkovski[4], **Marija Markovska Dimitrovska**[5]
Ss. Cyril and Methodius University in Skopje,
Faculty of Electrical Engineering and Information Technologies, Skopje, Macedonia,
[1]bmarkovski@feit.ukim.edu.mk, [3]vladgjor@feit.ukim.edu.mk, [4]bodan@feit.ukim.edu.mk, [5]marijam@feit.ukim.edu.mk
Macedonian Academy of Sciences and Arts, Macedonia, [2]leonid.grcev@ieee.org

Abstract* – Faults in electric power system may give rise of pipeline-to-soil voltages on nearby pipelines due to mutual electromagnetic coupling. Excessive voltages may endanger people and disrupt pipeline system safety and reliability. To prevent hazardous situations, accurate modelling of the electromagnetic interactions between such complex systems is required. In this paper, we perform parametric analysis of the electromagnetic coupling of overhead high voltage transmission lines and tower grounding to buried pipelines. The objectives of the analysis are: 1) to determine the effects of the characteristics of multilayer soil on the induced voltages due to different coupling mechanisms; 2) to analyse the effectiveness of some typically used mitigation methods for reducing the induced voltages. Analysis are performed by full-wave electromagnetic model, based on the method of moments, that accurately accounts for the electromagnetic coupling of large and complex systems in presence of multilayer soil.

1 Introduction

Metallic pipelines and power transmission lines often share common corridors. As result of their electromagnetic coupling, lightning and power system faults may give rise to excessive transient pipeline-to-soil voltages that may endanger people and disrupt pipeline system safety and reliability. Therefore, safety analysis require accurate modelling of the electromagnetic interactions between such complex systems [1].

Due to the adopted approximations, the accuracy and capability of the widely used numerical models is often limited to low-frequency analysis in uniform soil [2]. Such models can provide fast assessment of the induced voltages on pipelines, for normal operating conditions and faults at power frequencies on nearby power systems. However, they are not well optimized for dealing with the conductive coupling in case of using protective grounding on the pipeline and the treatment of the soil stratification [3].

In this paper, we perform parametric analysis of the electromagnetic coupling of overhead high voltage transmission lines and tower grounding to buried pipelines. We analyse the effects of the characteristics of the multilayer soil on the induced pipeline voltages due to conductive and inductive coupling. The parametric analysis should help to identify which scenarios of electromagnetic coupling are most unfavourable for the safety of the pipeline system. We also analyse the effectiveness of some typically used mitigation methods in reducing the induced voltages due to different coupling mechanisms.

Analysis are performed by full-wave electromagnetic model, based on the method of moments (MoM), that enables precise modelling of both systems and accurately accounts for the electromagnetic coupling in presence of multilayer soil [4]. Due to the size and complexity of the systems, the numerical model requires some optimization methods that are also discussed in this paper.

2 Description of the electromagnetic model

The analysed structures are assumed to comprise a network of N straight thin cylindrical conductors in multilayer soil, with an equivalent circular cross-section and in an arbitrary position along which a constant longitudinal current I_n for the n-th conductor is assumed. The application of MoM [5] enables to determine the electromagnetic interactions between these conductors by solving the following matrix equation:

$$[Z]\cdot[I]=[V] \tag{1}$$

where $[I]$ is a column matrix with unknown longitudinal currents, $[V]$ is related to energization of the structures and $[Z]$ is a square matrix of order N with elements calculated as:

$$Z_{mn}=\frac{\Delta\ell_m}{4\pi}\left(j\omega\mu_0\int_{\ell'_n}\overline{\overline{G}}_A d\ell'_n-\frac{1}{\underline{\sigma}_i}\frac{\partial}{\partial\ell_m}\int_{\ell'_n}\frac{\partial}{\partial\ell'_n}G_\Phi d\ell'_n\right) \tag{2}$$

where n and m are numerals of interfering and interfered conductor, $\underline{\sigma}_i$ is complex conductivity of the *i-th* layer where the interfered conductor is located, and $\overline{\overline{G}}_A$ and G_Φ in (2) are dyadic Green's function for the magnetic vector potential and Green's function for the electric scalar potential, respectively [6]. The interested reader can find details for the application of different formulations of Green's functions and their approximations in [4] and [7]. Once the longitudinal currents I_n from (1) are determined, follows the evaluation of other parameters such as electric fields, voltages, leaking currents, for different types of energization of the structures [8].

Analysis in this paper are performed using full-wave electromagnetic model that is based on a minimum approximations with respect to other commonly used models for analysis of electromagnetic interference between electric power system and pipelines. Some of the advantages of this model are:

- Accurate analysis in frequency domain from dc to tens of MHz. If time domain responses are required, they can be obtained by the application of a suitable Fourier inversion technique.
- Supports modeling of bare or insulated wires, cables, pipes or other complex and arbitrary shaped underground or aboveground structures that can be thought as constructed by cylindrical conductors.
- Supports modeling of different types of energization such as voltage and current sources, external electromagnetic sources, elevated earth potentials, etc.
- Analysis of electromagnetic problems in multilayer soil with horizontal stratification.
- Accurate modeling of simultaneous mutual interactions between pipeline and multiple elements of the electric power systems.

However the application of such complex model also introduces some disadvantages and limitations:

- Unable to model non-linear phenomena.
- Unable to model variations of soil characteristics at different locations along the analyzed systems, which is especially unfavorable for analyzing of pipeline systems that span tens of kilometers.
- Requires large amount of CPU and memory resources for large structures.

The first limitation is implied by the use of MoM since it is applicable only for linear systems. The solution of the second limitation is considered for a future research work. Authors have recently addressed the latter issues [5] and some of the utilized optimization methods in this model, that reduce the need of CPU and memory resources are briefly described in Section 5.

3 Description of the interfering and interfered systems

As interfering system we consider 110 kV single-circuit transmission line with phase sequence and geometry described on Fig. 1. The tower grounding electrodes are buried at depth of 0.8 m. As interfered system we consider 1 km long metallic pipeline section that is well insulated from the surrounding soil using PE isolation and terminated at both ends by insulating joints. The pipeline is buried at depth of h = 1.5 m in a two-layer soil. The upper soil layer has conductivity σ_1 = 0.01 S/m and a thickness of H = 1 m (for a case where pipeline and tower grounding are in same layer) or H = 2 m (for a case where pipeline and tower grounding are in different layers). Three different alternative values of the conductivity σ_2 of the lower layer are considered, that are also expressed in terms of the reflection coefficient K [9]: 0.19 S/m (K = –0.9), 0.01 S/m (K = 0), and 0.000526 S/m (K = 0.9), where:

$$K=(\sigma_1-\sigma_2)/(\sigma_1+\sigma_2) \tag{3}$$

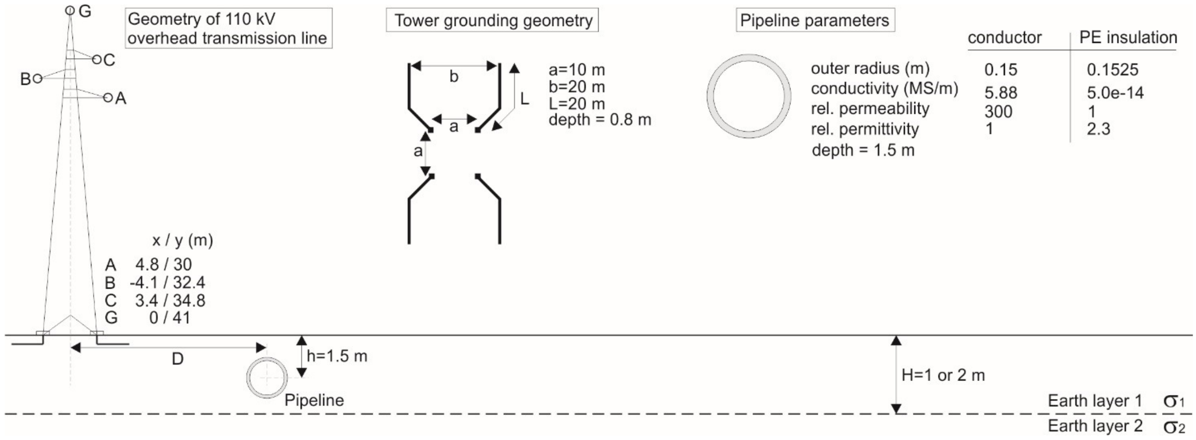

Fig. 1 Details for the analysed systems.

Since the interfered system is buried pipeline, following the guidelines provided in [1], only the effects of conductive and inductive coupling are of particular interest, while the effects of capacitive coupling are negligible. The conductive coupling is related to the effects of elevated soil potentials due to dissipated current from nearby grounded structures of the power system during fault conditions. The inductive coupling is related to the induced voltages on pipeline, caused by the alternating magnetic field from electric power lines in normal operating and fault conditions. Here we consider only short-term inductive coupling during fault conditions.

4 Parametric analysis and discussions

4.1 Effects of multilayer soil on conductive coupling

In the following analysis, we consider pipeline that runs near grounding electrodes of 110 kV transmission line tower. The minimal distance between grounding electrodes and pipeline is varied between 2 m, 10 m and 20 m. According to [1], such distances correspond to the minimum allowed (for 2 m) and the maximum separation distances (for 20 m) that require analysis of conductive coupling. Figure 2 shows the maximum values of soil potentials surrounding the insulated pipeline, with respect to remote earth. Since in this analysis other coupling effects are neglected, the metal part of the pipeline can be considered to be at 0 V of potential and therefore calculated potentials correspond to the coating stress voltages when the pipeline is subjected to conductive coupling. Calculated voltage values are normalized to 1 A current that is injected in the grounding electrodes.

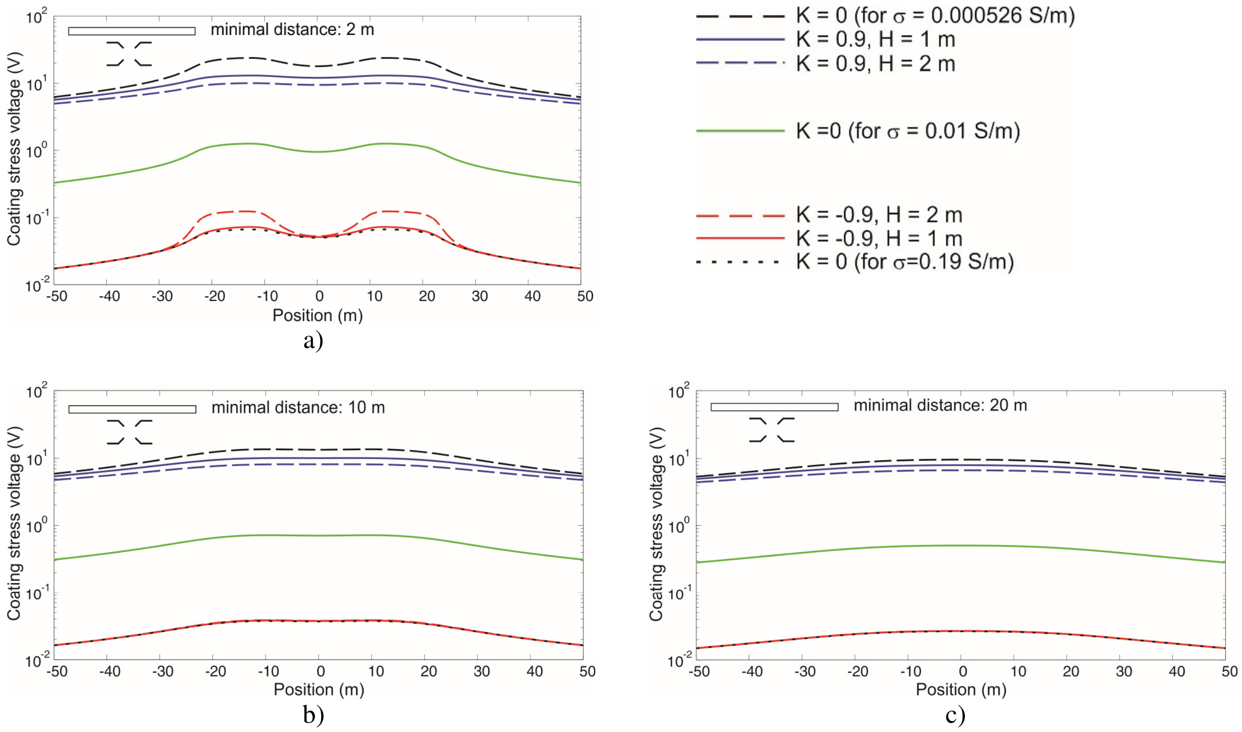

a)

b)

c)

Fig. 2 Effects of multilayer soil on coating stress voltage due to conductive coupling (normalized values per dissipated current of 1 A through the tower grounding).

Results show that resistivity of the deeper soil layer have strong influence on the coating stress voltages and these voltages increase with the increase of the deeper soil resistivity. The voltages are affected by the position of the pipeline in multilayer soil and significant increase of voltages is observed when pipeline is within the more resistive soil layer. The assumption of homogeneous soil related either to the characteristics of the upper or deeper soil layer, or to the mean value of layered soil resistivity, will lead to erroneous results and substantial underestimation or overestimation of the calculated voltages. Therefore, accurate modelling of layered soil is required for proper risks assessment.

4.2 Effects of multilayer soil on soil ionization

When high intensity currents are dissipated through small-sized grounding such as tower grounding electrodes, despite of the local increase of soil potentials, strong electric field surrounding the grounding electrodes may also appear. The zone where the intensity of the electric field is above a critical strength (here we consider $E_{cr} = 300$ kV/m) can be considered as ionized and arcing from the electrodes within the ionized soil may appear. Hazardous situation may appear if such ionized channel is attached to the metallic pipeline, leading to possible successive discharge of high intensity fault currents into the pipeline.

In this analysis we calculate the electric field within soil for the minimal separation distance of 2 m between pipeline and the tower grounding. Fig. 3 shows the spatial distribution of electric field surrounding the pipeline along a profile perpendicular to the pipeline. The electric field values are normalized for current of 1 A that is dissipated through the tower grounding. For better clarity of the results, only the variations of the electric field within the range 0.1 – 2 V/m are displayed.

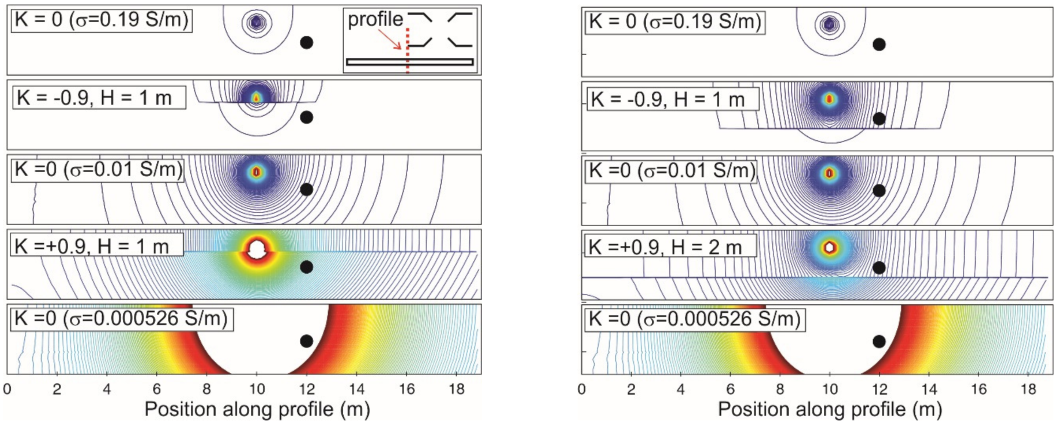

a) b)

Fig. 3 Effects of multilayer soil on the intensity of electric field in the soil
(normalized values per dissipated current of 1 A through the tower grounding).

Results show that the risk of entering the pipeline into ionized zone of soil is increasing with the increasing resistivity of deeper soil layer. Similarly to the previous observations, such risk increases when pipeline is within the more resistive soil layer. For example if we consider that entire lightning current with intensity of 200 kA (attributed to first lightning stroke with $T_1 / T_2 = 10/350$ μS) is discharged through the tower grounding electrodes, then the pipeline may enter in the ionized zone when $K = 0.9$, but only when pipeline is within the more restive layer. The most hazardous situation is observed for homogeneous soil with $\sigma = 0.000526$ S/m, i.e. when grounding electrodes and pipeline are at small distance and within highly resistive soil.

4.3 Effectiveness of some typically used mitigation methods for conductive coupling

In this Section the full-wave electromagnetic model is used to accurately model some typical mitigation methods and estimate their effectiveness in reduction of the effects of conductive coupling. The use of gradient control wire, buried in the same trench close to the pipeline, is a commonly used method [10]. Here, as interfering system we consider grounding electrodes of transmission line tower, that have 10 m minimum separation from the pipeline section described in Section 3. For simplicity, in these analysis we consider only homogeneous earth with $\sigma = 0.01$ S/m. We assume that grounding system is energized by fault current with intensity of 1A, so the results in Fig. 4 and Fig. 5 show normalized values of coating stress voltages for the different mitigation methods.

The results provided in Fig.4, for a case without mitigation, will be used as reference in the evaluation of the effectiveness of the mitigation methods. Since the pipeline is well insulated from the surrounding earth by PE coating and has no electrical continuity with the rest of pipeline outside the analyzed section due to the use of insulating joints, the potentials of the metallic part of the pipeline will be elevated above 0 V and maintained constant within the analyzed section. In the considered scenario, the maximum coating stress voltage is 0.6 V. It is obtained as difference of potentials between the metallic part of the pipeline and the surrounding soil.

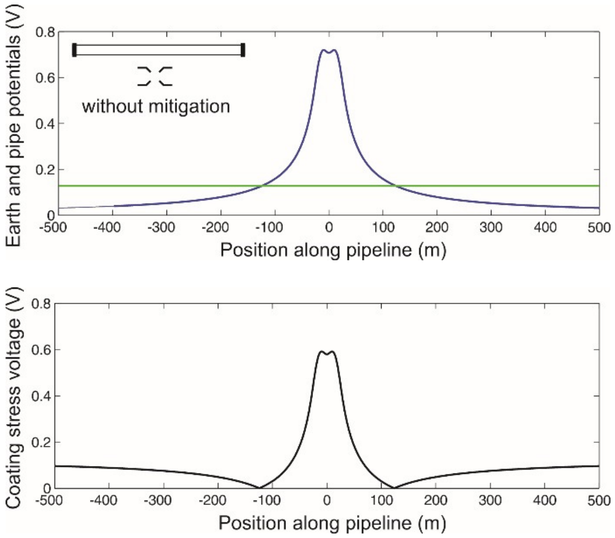

Fig. 4 Normalized values of soil potentials (blue), pipe potentials (green) and coating stress voltage (black) due to nearby grounding electrodes, energized with fault current of 1 A.

In the following analysis we consider the effectiveness of using FeZn ribbons as gradient control wires with lengths of 30, 100 and 200 m, that can be attached or detached to the pipeline. Results are provided in Fig. 5.

Similarly to the previous observations, the FeZn ribbon is energized by the locally elevated soil potentials in the interfering zone of the tower grounding. Since the ribbon is in direct contact with soil, it will dissipate part of the energy outside of the interfering zone of the tower grounding, thus increasing the potentials of surrounding soil, but it will contribute to reduction of the soil potentials within this zone. The effectiveness of this mitigation is very sensitive to variety of parameters: geometry of grounding electrodes, geometry and characteristics of FeZn ribbon, soil characteristics, configuration of pipeline system, and therefore accurate model is required for precise and proper modeling of such mitigation.

The use of attached FeZn ribbon to pipeline will elevate the pipe potentials to the mean value of the soil potentials to which the FeZn ribbon is subjected within the interfering zone. Since in the analyzed scenario the pipeline section is well insulated, these potentials will maintain elevated at high value and constant over the entire pipeline section. Results indicate that the use of attached FeZn ribbon will reduce the coating stress voltages near the HV tower grounding, but it will increase the hazardous zone on the remaining part of the pipeline section, therefore leading to even worse situation than the case of pipeline without mitigation. Although the length of the ribbon contributes to reduce the elevated voltages over the entire length of the pipeline section, the previously noted problem still remains.

Results also indicate that the most effective measure for the analyzed scenario is using long detached FeZn ribbon buried parallel in the same trench with the pipeline, whose length is much larger than the interfering zone of the HV tower grounding, as illustrated on Fig. 5. This mitigation is easy to implement and leads to nearly 50% reduction of the coating stress voltages that appear near the HV tower grounding.

It should be emphasized that the analyzed mitigation may have different effect on other configurations of pipeline systems, for example ones with electrical continuity over tens of kilometers and the effects on such systems will require suitable simulation that can be also performed by the electromagnetic model.

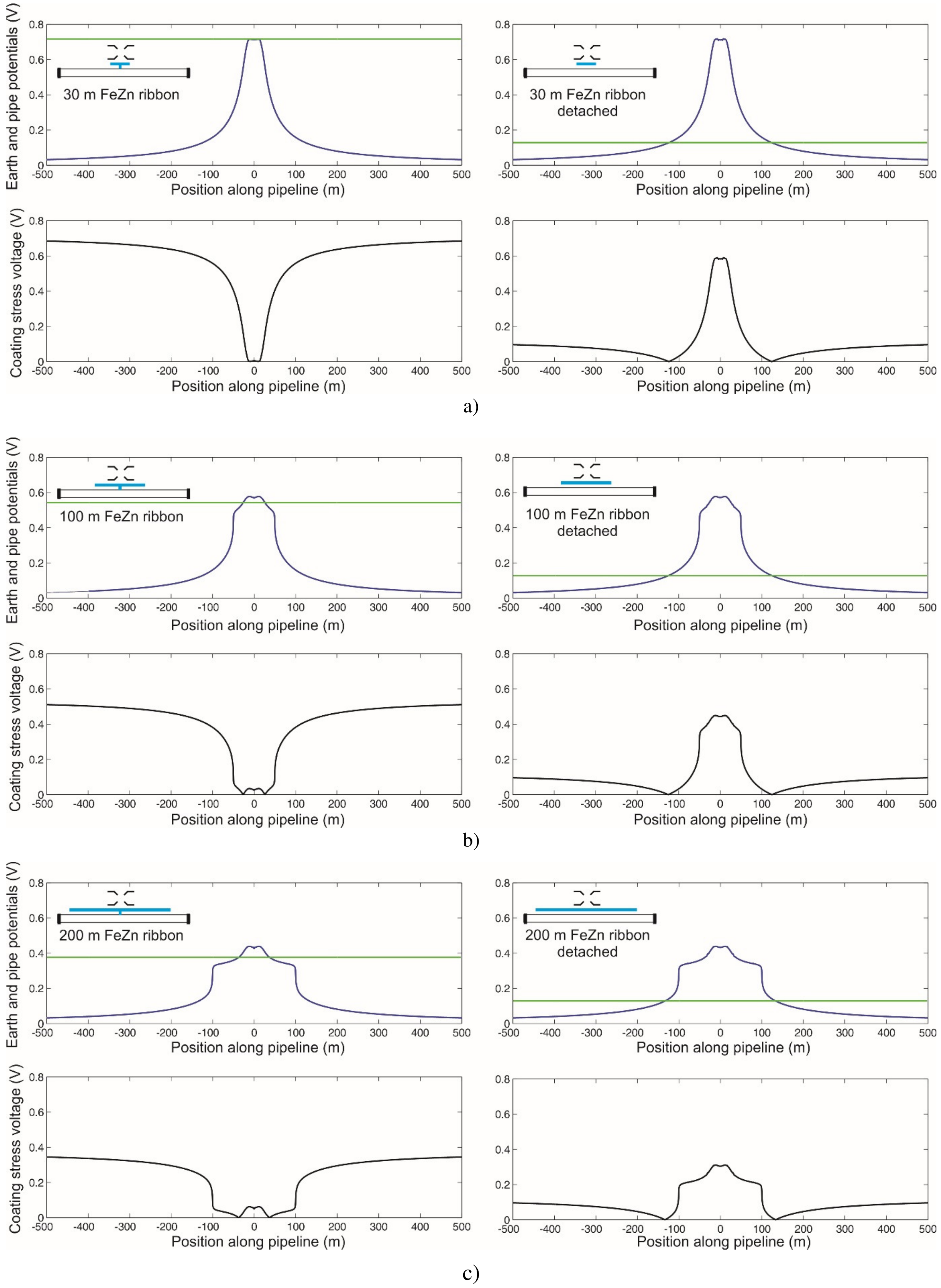

a)

b)

c)

Fig. 5 Normalized values of soil potentials (blue), pipe potentials (green) and coating stress voltage (black) due to energized nearby grounding electrodes with fault current of 1 A for different mitigation methods on the pipeline side.

4.4 Effects of multilayer soil on Inductive coupling

In this section we analyse the effects of the characteristics of multilayer soil on the induced voltages on pipeline system due to inductive coupling. We consider a well insulated 1 km pipeline section with PE coating and terminated at both ends by insulating joints, buried in two-layered soil with characteristics given in Section 3. The interfering system is 110 kV overhead transmission line that is parallel with the pipeline at distances D of 12, 62 and 112 m. Simulation results show normalized values of coating stress voltages due to 1 A earth fault current at 50 Hz over the entire length of phase A of the HV line. In these simulations we consider only the effects of inductive coupling, while the conductive coupling is neglected, therefore the surrounding soil is assumed to be at potential of 0 V.

On Fig. 6 we consider scenario when entire pipeline section is subjected to the magnetic field of the faulted line, and on Fig. 7 only portion of the pipeline section is energized since part of the HV line is perpendicular to the pipeline. On both figures, families of curves show that the earth characteristics have significant influence on the induced voltages on the pipeline and increasing earth resistivity leads to increased coating stress voltages. However, the overlapping families of curves also indicate that the induced voltages are not significantly affected by the position of the pipeline in multilayer soil, but only by the characteristics of the deeper soil layer.

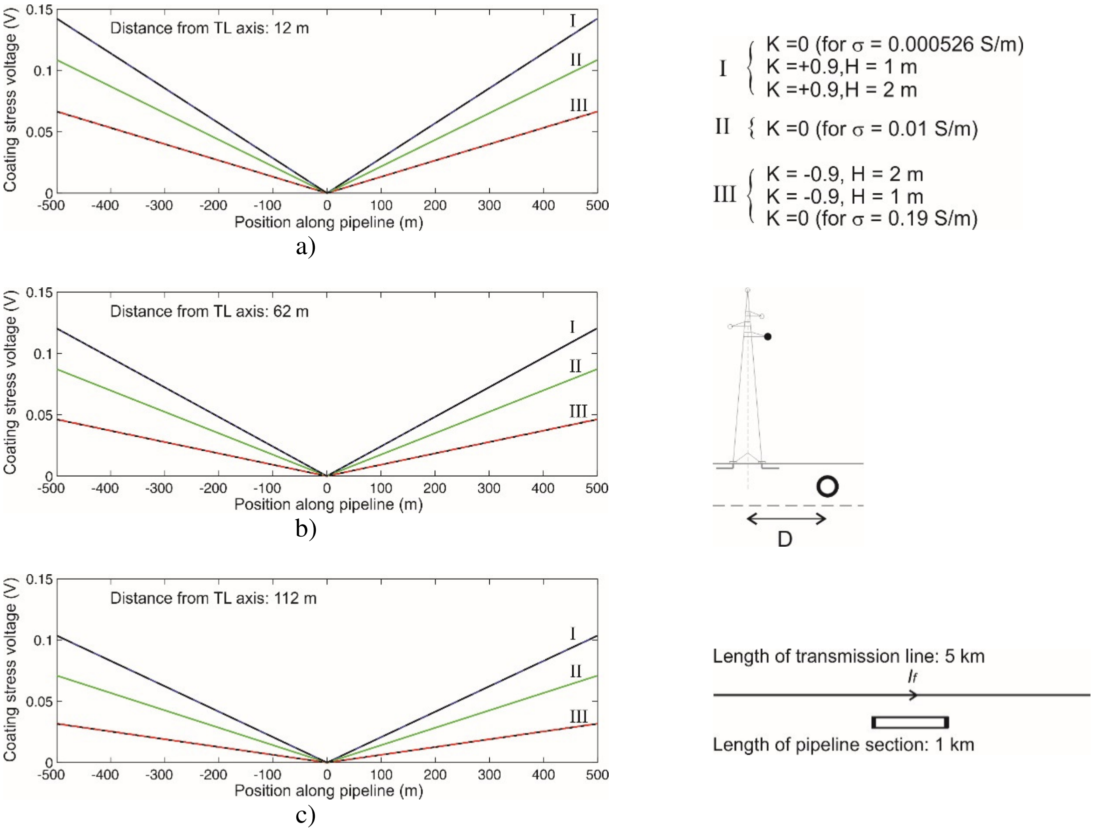

a)

b)

c)

Fig. 6 Effects of multilayer soil on coating stress voltage due to inductive coupling on the entire pipeline section (normalized values per fault current of 1 A in phase A of the 110 kV transmission line).

4.5 Effectiveness of some typically used mitigation techniques for inductive coupling

In this section we analyse the effectiveness of some typical mitigation methods for dealing with inductive coupling. The commonly used approach proposed in the textbooks for pipeline protection is using screening conductors between the interfering and interfered systems, buried in the same trench with the pipeline. According to [10], such conductors can be attached or detached to the pipeline. Basically this is the same approach as for dealing with conductive coupling, where FeZn ribbon was considered.

Fig. 8 shows the normalized values of coating stress voltages for a well insulated 1 km pipeline section in a homogeneous earth with σ = 0.01 S/m, that is partially energized (over 50% of its length) by fault current in phase A. The distance between central axis of both systems is 12 m.

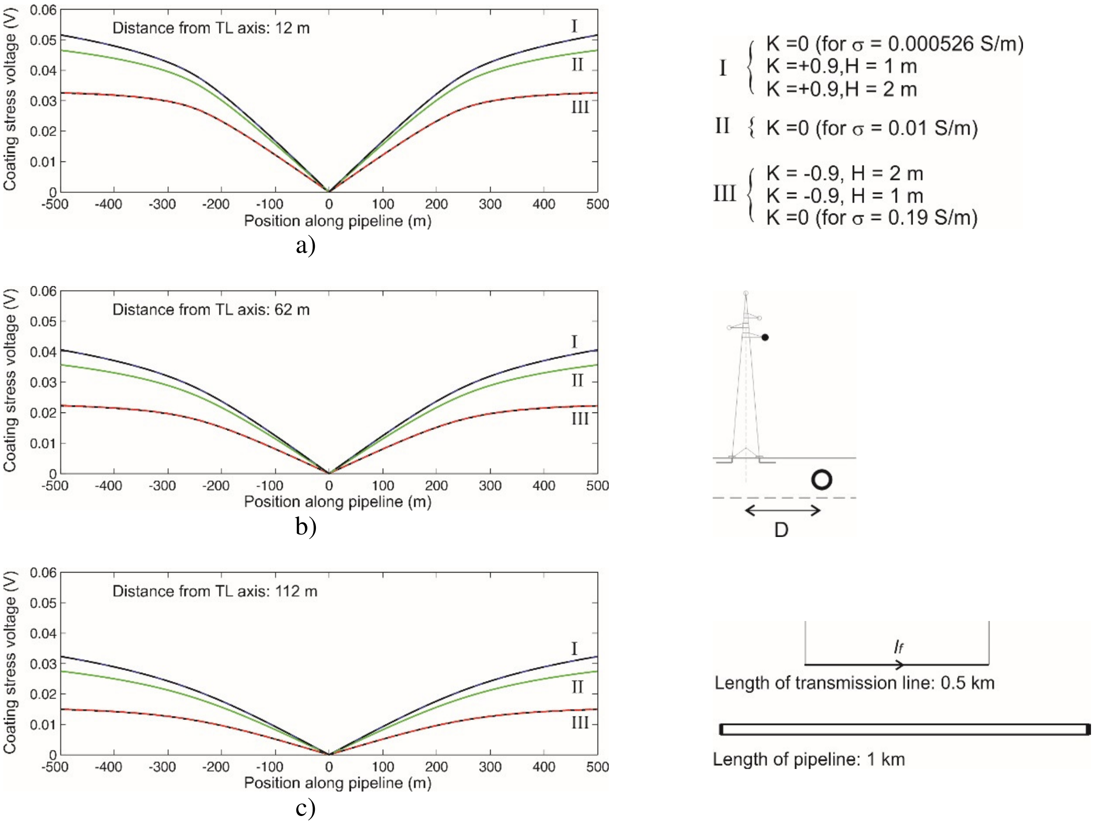

a)

b)

c)

Fig. 7 Effects of multilayer earth on coating stress voltage due to inductive coupling on 50% of the pipeline section (normalized values per fault current of 1 A in phase A of the 110 kV transmission line).

As a reference case, we consider induced voltages on the pipeline section without using mitigation. Since in this case the conductive coupling is neglected and the pipe is well insulated, the surrounding soil has potential of 0 V. Therefore the coating stress voltages are equal with the pipe potentials with respect to remote earth, as illustrated on Fig. 8.

The results in Fig. 9 show that the screening conductor has small contribution in reducing the induced potentials on the pipeline. However since it is also energized by inductive coupling with the faulted line, and is in direct contact with soil, it dissipates currents to the soil that increase the surrounding soil potentials. The coating stress voltage, which is calculated as difference of potentials between metallic part of the pipe and surrounding soil, become fraction of the pipeline potentials with respect to distant earth. For the analysed scenarios, this mitigation method is more effective for attached screening conductor and in cases where this conductor spans beyond the interfering zone. Similar observation can be made for detached screening conductor that spans beyond interfering zone, but this method is less effective. Extended analysis, not provided in this paper, have shown that the analysed mitigation methods are very sensitive to the geometry of the systems and different effectiveness can be obtained for less symmetric scenario, or in case of pipeline with electrical continuity that spans tens of kilometres beyond interfering zone. Therefore the application of such mitigation requires case-specific and accurate modelling of the coupled systems to obtain optimal mitigation from inductive coupling.

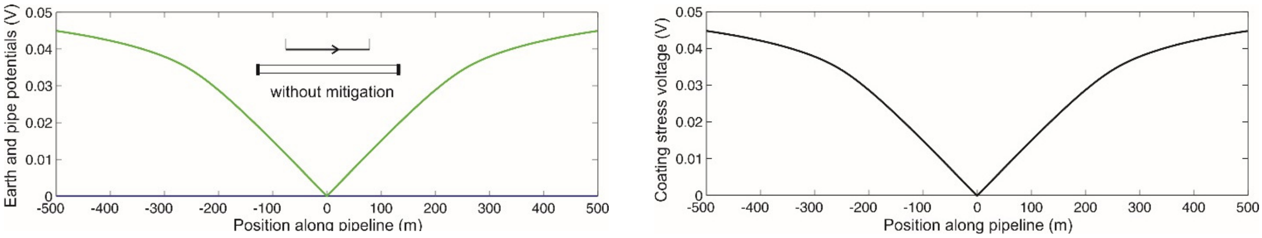

Fig. 8 Normalized values of earth potentials (blue), pipe potentials (green) and coating stress voltage (black) due to fault current of 1 A in phase A of the 110 kV transmission line, without mitigation on the pipeline side.

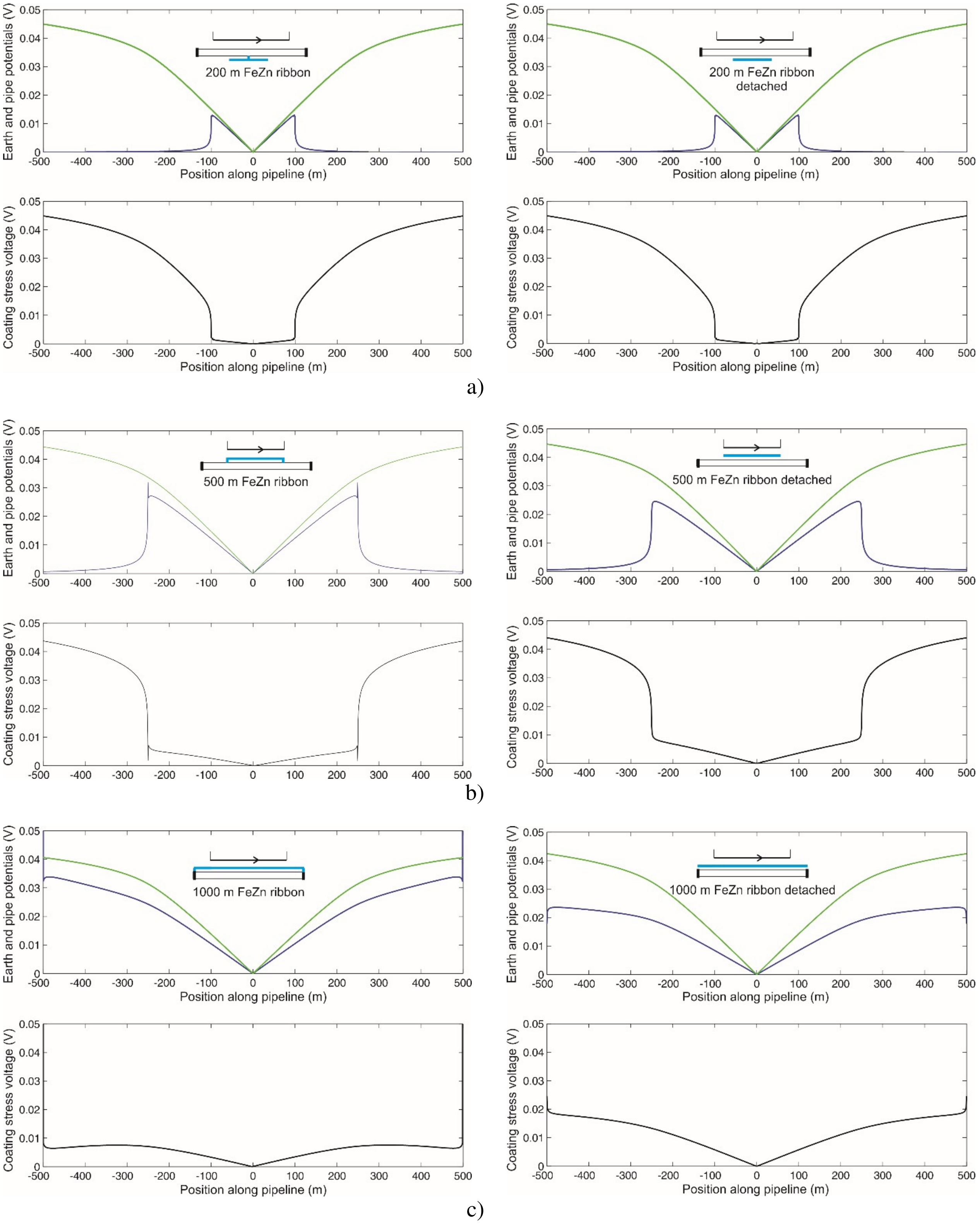

a)

b)

c)

Fig. 9 Normalized values of soil potentials (blue), pipe potentials (green) and coating stress voltages (black) due to fault current of 1 A in phase A of the 110 kV transmission line, for different mitigation methods on the pipeline side.

5 Methods for improving the efficiency of the full-wave electromagnetic model

The application of the full-wave electromagnetic model requires numerical integration of oscillatory and slowly convergent Sommerfeld integrals, and evaluation of mutual electromagnetic interactions between large number of segments that are obtained by the system discretization. These calculations can be lengthy and require large amount of CPU and memory resources, which is one of the main drawbacks of practical application of the model in analysis of large systems. To make the model practical, different methods have been used to optimize the numerical model, minimize the computations of the Sommerfeld integrals and minimize the evaluation of mutual electromagnetic interactions between segments. Here we provide non-exhaustive list of optimization methods used in the full-wave electromagnetic model [4]:

- Extraction of singularities from Sommerfeld integrals improves their convergence and reduces the number of iterations during the procedure of numerical integration. This method results in substantial reduction of computation time required for numerical integration, but also makes the solutions of Sommerfeld integrals suitable for interpolation. The procedure considers only extraction of singular terms that have analytical solution.
- The application of 3D interpolation over a small number of points, minimizes the number of direct numerical computations of the Sommerfeld integrals. The times required to estimate the mutual interactions between segments, that are expressed in terms of Z_{mn} in Eq. (2), then become comparable to the ones required when approximate image-theory models are used, while the introduced error is negligible for practical applications. Maximum efficiency of this method is obtained for systems with small height variations, relative to the earth surface.
- The number of evaluations of mutual electromagnetic interactions between segments can be minimized by using lookup tables and efficient sorting algorithms. This approach enables to reuse already calculated elements of the impedance matrix Z_{mn} from previously evaluated identical situations of mutual interaction between segments. Maximum efficiency of this approach can be obtained in analysis of large grounding grids with regular mesh or long systems with homogeneous characteristics, such as the ones analysed in this paper.
- Use parallelization over the available CPU cores or distribution of calculations on multiple computers.

The implementation of these methods leads to substantial reduction of computation times and need for CPU and memory resources, while enabling accurate modelling of electromagnetic problems in large systems on a computers with moderate performances.

6 Conclusion

In this paper, we have analysed the effects of multilayer soil on the coating stress voltages on pipelines, which can be induced due to electromagnetic coupling with electric power system in fault conditions. We have also analysed the effectiveness of some commonly used mitigation techniques for dealing with conductive and inductive coupling.

Analysis show that induced coating stress voltages from both coupling mechanisms are strongly affected by the characteristics of the multilayer soil, and that severity of the induced voltages is proportionally related to the specific resistivity of the deeper soil layers. However, accurate calculation of these voltages requires proper treatment of the characteristics of the multilayer soil, and the use of simplified model of uniform soil can introduce significant error in the calculated voltages.

The obtained results for the analysed scenarios show that the use of gradient control wire within the same trench of the pipeline, which is detached from the pipeline and spans beyond the interfering zone, can serve as optimal protection method for dealing with the conductive and inductive coupling. However analysis also show that effectiveness of mitigation is sensitive to variations of geometry and characteristics of the coupled systems. Therefore the optimal design of mitigation requires case-specific and accurate modelling of the electromagnetic interactions between the coupled systems.

Acknowledgements

This work was supported by the Ss. Cyril and Methodius University in Skopje, Project NIP.UKIM.20-21.10.

References

[1] EN 50443:2011 – Effects of electromagnetic interference on pipelines caused by high voltage a.c. electric traction systems and/or high voltage a.c. power supply systems, CENELEC, Brussels, (2011).

[2] Directives concerning the protection of telecommunication lines against harmful effects from, from electric power and electrified railway systems, Capacitive, inductive and conductive coupling: Physical theory and calculation methods – Vol. III, CCITT, Geneva (1989).

[3] R. D. Southey, F. Dawalibi, Y. Li, W. Ruan, (2005), “Increasing the cost-effectiveness of AC interference mitigation designs with integrated electromagnetic field modeling”, Corrosion, pp. 1-12.

[4] B. Markovski, L. Grcev, V. Arnautovski-Toseva, (2021), “Fast and accurate transient analysis of large grounding systems in multilayer soil”, *IEEE Transactions on Power Delivery*, Vol. 36, No. 2, pp. 598-606.

[5] R. F. Harrington, (1967), “Matrix methods for field problems”, *Proc. IEEE*, Vol. 55, No. 2, pp. 136–149.

[6] K. A. Michalski, (1985), “The mixed-potential electric field integral equation for objects in layered media,” *Arch. Elek. Ubertragung*, Vol. 39, No. 5, pp. 317–322.

[7] B. Markovski, Efficient electromagnetic model for transient analysis of large grounding systems in layered earth, PhD Dissertation, Ss. Cyril and Methodius University in Skopje, Skopje, Macedonia, (2019).

[8] L. Grcev, A. Kuhar, B. Markovski, V. Arnautovski-Toseva, (2019), “Generalized network model for energization of grounding electrodes,” *IEEE Trans. Electromagn. Compat.,* Vol. 61, No. 4, pp. 1082-1090.

[9] IEEE Std 80-2000 - IEEE Guide for Safety in AC Substation Grounding, IEEE, New York, (2000).

[10] CIGRÉ Working Group 36.02, Guide on the Influence of High Voltage AC Power Systems on Metallic Pipelines, Paris, (1995).

Smart Voltage Control and Direct Load Management

Darko Vidinikj, Goga Cvetkovski

Ss. Cyril and Methodius University, Faculty of Electrical Engineering and Information Technologies, Rugjer Boskovic 18, 1000 Skopje, North Macedonia E-mail, dvidinik89@hotmail.com, gogacvet@feit.ukim.edu.mk

Abstract* – The flexibility of the valves in power electronics and convertors, emerging IoT devices and Smart meters as well as the development of AI based on ML algorithms offer possibilities of Grid orchestration thus tackling the challenges presented with it's and society's evolution. The operation between unpredicted consumption (ex. EVs) and renewable generation (especially PVs) can be linked with Smart Grid techniques like Load and Voltage management that include Smart Inverter and Big Data modelling and real time analysis. The emerging technologies enable green and sustainable options – causing challenges for the grid, but it's technology again that tackles those challenges. Everybody, from Electrical engineers, Telecommunication and IT specialist must contribute with their unique skills in developing and make Smart Grid possible for better life of everyone.

1 Introduction

The electricity system (EES) is facing major challenges, mainly due to the mass integration of dispersed renewable sources, new ways of using electricity - electrification of heating with heat pumps and electrification of personal mobility, and the introduction of a Pan-European electricity market. All these factors certainly have a strong impact on the operation and development of the entire power system. The distribution network is particularly affected, as the vast majority of distributed generation and devices for new uses of electricity are integrated into it. The situation in the power system can be successfully managed only with the use of modern solutions for smart grids, which are based on seamless communication technologies and Common Information Model (CIM). In the following, this document will provide key use cases where we can use IoT technologies, related services and requirements.

2 Use cases

2.1 Voltage and power flow control

Dispersed sources in the distribution network affect power flows and consequently the voltage profiles. Providing an appropriate voltage profile (voltage within the standard for all network users) is one of the most pressing problems in networks with a large share of these sources. These problems can also be managed by remote control of resources, especially by setting the power factor (cos fi) – i.e. by regulating the reactive power, and in extreme conditions also by regulating the active power. In emergency situations, when the safe operation of the power system is endangered, remote shutdown of sources is also prescribed. This applies to all sources, and remote power control only to sources with an installed power greater than (according to current regulations in some countries) 250 kW. Production plant (PN) or the distributed source must enable the exchange of information (operational measurements, commands, etc.) in real time with the system of the relevant distribution system operator. Depending on the type of device, the requirements are different separated in to several groups. One of the most important use cases of the usage of data from dispersed sources and their remote control is the one that modern technology enables and that is to provide a Distributed Energy Resources Management System (DERMS) module that allows for increased observability of generation from dispersed sources, both in real time and in the future (forecasts). Observability is then the basis for controllability, which allows for optimal resource management in terms of solving current or future network problems. This is mainly about voltage regulation and management of power flows. Mandatory data exchange is already applied just on higher power installations but also the smaller ones grow in number and they need to be managed. To apply mandatory data exchange on smaller installations there is a challenge to use the (Internet of Things) IoT technologies. These processes would require multiple devices, meters and (Information Technology/Operational Technology) IT/OT systems to exchange data in real time and provide it to an (Artificial Intelligence) AI and (Machine Learning) ML algorithm or more complex AI based application. This means that the technology must enable device connectivity as well as data integration through CIM based platform.

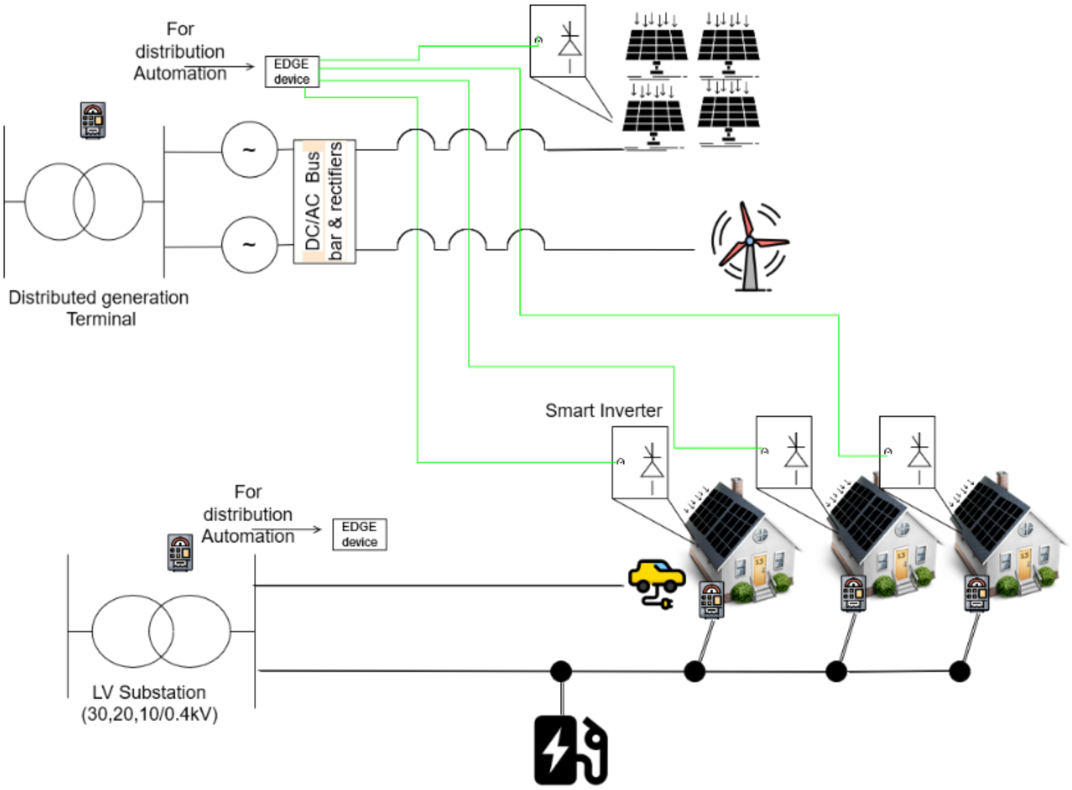

Fig. 1 HL Level Architecture of Smart Invertor control

2.2 Voltage quality monitoring

The voltage quality is monitored on the distribution network on (Middle Voltage) MV terminals in the regional substation and in some places also on (Low Voltage) LV distributors in substations. The parameters defined by the standard EN 50160 are monitored. These are mainly: interruptions, voltage fluctuations or drops, harmonics and total harmonic distortion (THD), asymmetries, flicker in frequency fluctuations.

In addition to quality data, operational P / Q / U / I measurements are also covered. It is also possible to capture digital signals; such as signals of various alarms (e.g. protection relay, entry into a building, etc.) The capture frequency is adapted to the needs of operational measurements (10-second to minute class), as much longer averages are used for the quality parameters themselves.

3 Drivers

The use of renewable energy increased by 3% in 2020 as the global demand for other fossil fuels decreased, consistent with 7% growth in electricity power generation from renewable energy resources, such as wind turbine and photovoltaic (PV) sources.

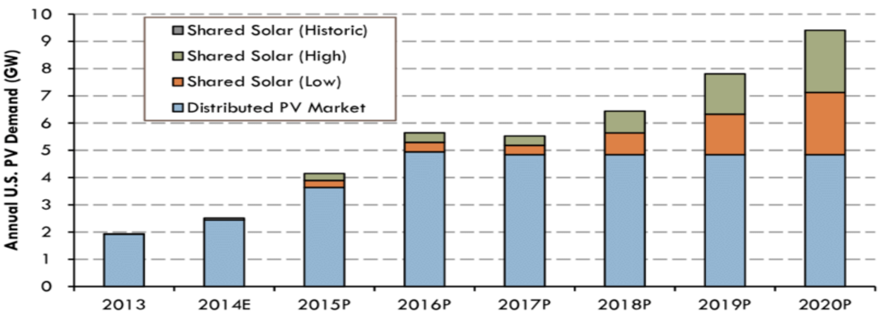

Fig. 2 PV installation trends till 2020

The electricity prices over the last year in Macedonia have tripled, causing wave of decisions of companies to invest in PVs as additional power source.

Table 1 Relevant figures that illustrate the trends for PV penetration in Macedonia

Category	Before the Energy Crisis	After and Future
Electricity price	0.11€	0.31€
TabMak price per consumption (30GWh)	219,512.20€	609,756.10€
PV demand in MK (from local PV provider for one year)	160 kWp	10.4MWp

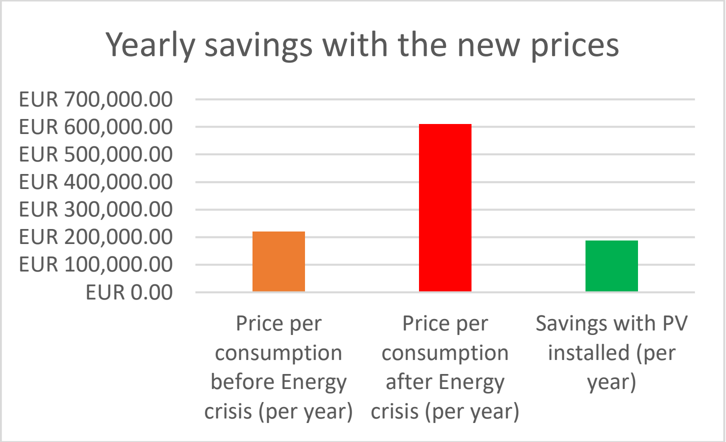

Fig. 3 Estimated saving with PV installation of one factory in Macedonia

Having the potential early savings in mind, the trend of PV installations is expected to rise even more.

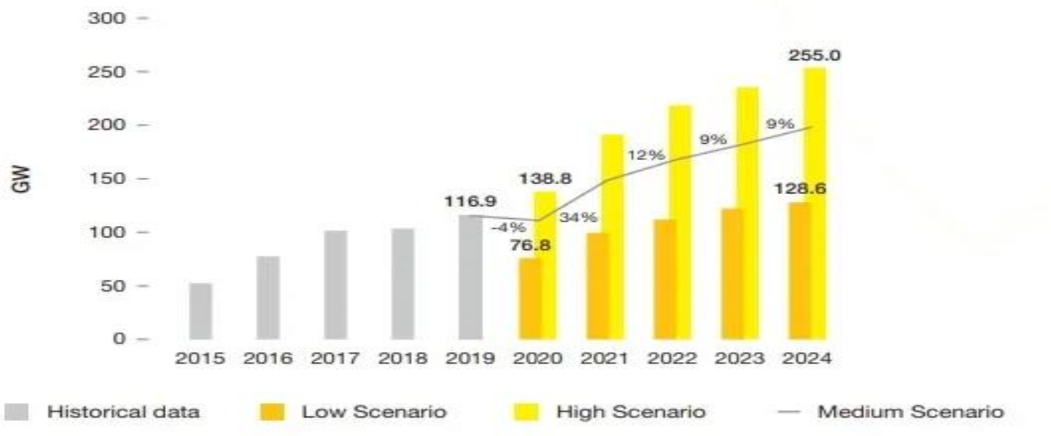

Fig. 4 PV Trends Estimation till 2024 based on data till 2020

4 Challenge definition

The intermittence of PV effects of Distribution networks cannot be ignored because it results in voltage quality problems, such as:

- voltage fluctuation
- overvoltage
- voltage sag
- voltage dip
- and unbalanced voltage.

For power grids with high PV penetration, the active power output may decrease suddenly due to weather issues, such as: solar radiation, clouds, rain, poor visibility and others.

The trend of increased power injection and penetration of solar electricity generation will make the mitigation of this problems with existing strategy and procedures will be very challenging and next to impossible.

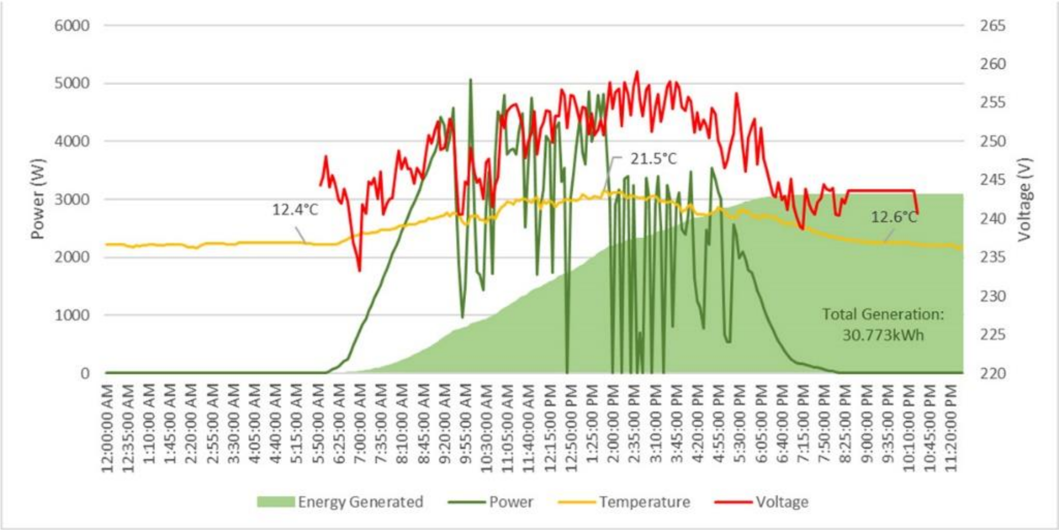

Fig. 5 Voltage profile and drops caused by sudden drop in generation from PV’s

5 History and traditional approach

Distribution grids were originally developed towards the end of IX century. So, since then a good amount of effort has been made to mitigate the reactive power impact as well as voltage drops.

First there was an introduction of local controls, applied in line voltage regulation, switch shunt capacitors and load tap changing with the following devices:

- Switch Capacitor Banks (SCB)
- Voltage regulators (VR) on the middle section of the feeder
- On Load Tap Changers (OLTC)

Such techniques were introduced to help maintain voltages within regulatory range, enable more capacity in the generation, transmission, and distribution systems and reduce active power losses. Figure 6 illustrates the major developments in distribution volt/VAR control over time.

Implementation of just local controlling and no centralized coordination of volt/ VAR devices at the system level is far from optimal operation. Additionally, there are seasonal labor costs of the trips that the field personnel need to take towards the capacitor banks. In more than 30 years ago, utilities begun to implement

Centralized radio control systems that would utilize a centralized based monitoring system, often based on heuristic methods utilizing only the VAR measurement at the distribution feeder breaker. In these systems, impacts to the entire feeder such as temperature limits and voltage drops were not modeled, neither were the loads from the consumers but only the quantity of the reactive power (VAR) flow. When distribution feeders are reconfigured due to normal switching, load balancing or isolation of certain fault, the rule-based logic could not automatically track the changes and the capacitor banks on connected feeder in that time. Because of the poor visibility following predictability and optimization, the Conservation Voltage Reduction (CVR) implementation was shown as no longer practical which made utilities to seek more advanced volt/Var optimization methods.

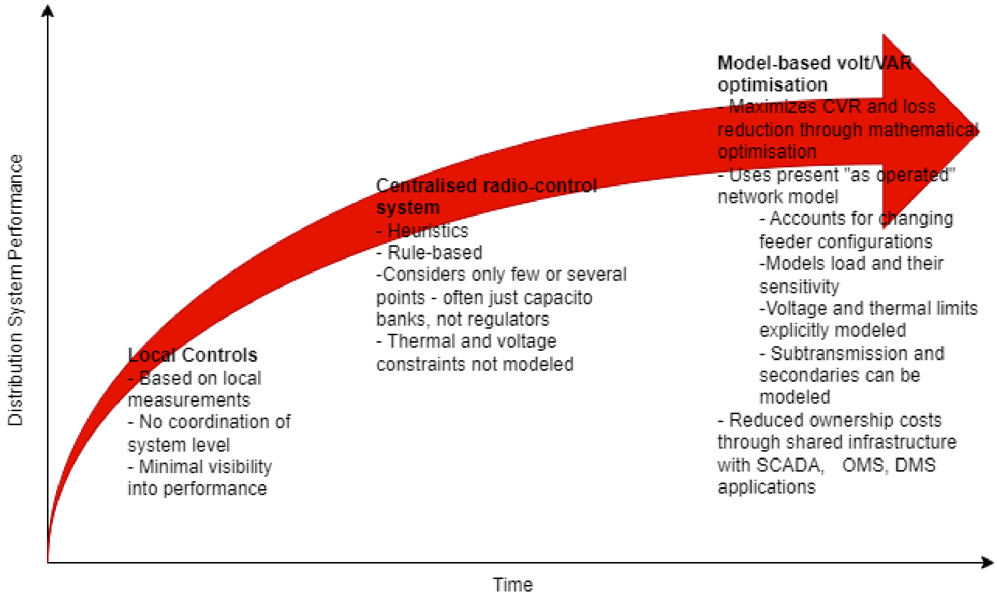

Fig. 6 Evolution and development in Volt/VAR control

6 Proposed solution

This paper will propose solution using the capability- controllability of a Smart Inverter as well as intelligent implementation of metaheuristic algorithm deployed on data modeling and data integration platform.

6.1 Use of Smart inverter possibilities

The smart inverter offers several possibilities which can be used for successful operation and direct voltage control. It’s flexibility and capability to be used both as an inverter or rectifier makes it perfect tackling some of the challenges caused by voltage irregularity. These capabilities are employed in several actions:

- Flexibility for:
    - Active power injection
    - Inductive reactive power injection
    - Capacitive reactive power injection
- Bidirectional and can simultaneously:
    - Inject Active and Reactive power
    - Absorb Active and reactive power

6.2 Mitigating voltage drops with capacitive reactive power

With the increased PV penetration in the electrical grids, due to changing weather conditions the active power output may drop suddenly. So, grid voltage drop occurs according to Equation (1):

$$\Delta V \approx \Delta P \times R + \Delta Q \times X \tag{1}$$

where R is the resistance and X is the reactance of the conductor where the voltage is measured.

As mentioned before, the smart inverter offers the capability to inject reactive power to mitigate the voltage drops as shown in the picture below.

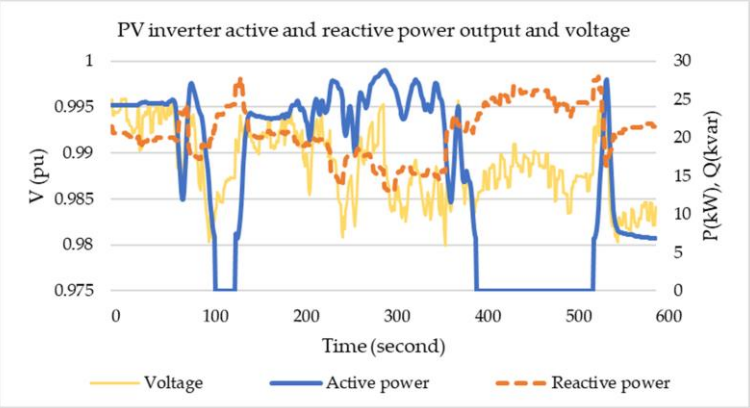

Fig. 7 Mitigating voltage drop with capacitive reactive power

When the active power drops, the inductive reactive power mitigates the voltage drop which is defined as volt-var control. Voltage regulation in the Distribution grids can be attained using On Line Tap Changers and Voltage Regulators with a tap range of 10%, as well as a Voltage Regulators positioned in the middle section of a line or the feeder. The smart inverter operation can decrease tap position changes because of the ability of flexible reactive power output with very fast response. This also reduces the switching times of the switched capacitor banks that are also traditionally used to mitigate undervoltage in the distribution grids. As additional benefit, the grid-controlled PV inverters are individually controlled by phase – feature that can lead to improvement of the 3-phase voltage unbalance as well.

6.3 V-Q control strategy

Depending on the scenario, there are two possibilities of the reactive power output which is impacted by the control curve. These volt-var control curves can be gentle or aggressive.

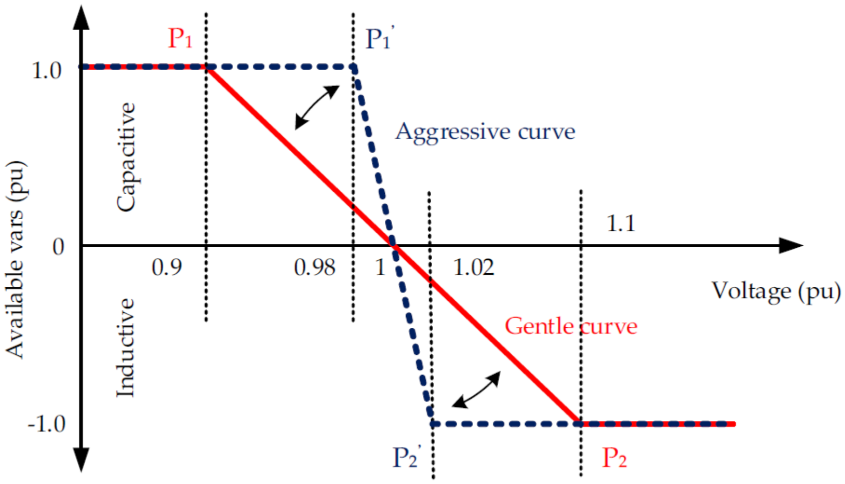

Fig. 8 Smart inverter V-Q control options and effects on voltage regulation

The advantage of the aggressive curve control is that offer faster voltage regulation rather than more smooth voltage control of the gentle curve. As a down side of the aggressive curve control strategy it can result in voltage and reactive power oscillations. On the other side, although as mentioned before the gentle curve control can offer smooth control of the voltage this type of reactive power output results in worse – slower regulation of the voltage.

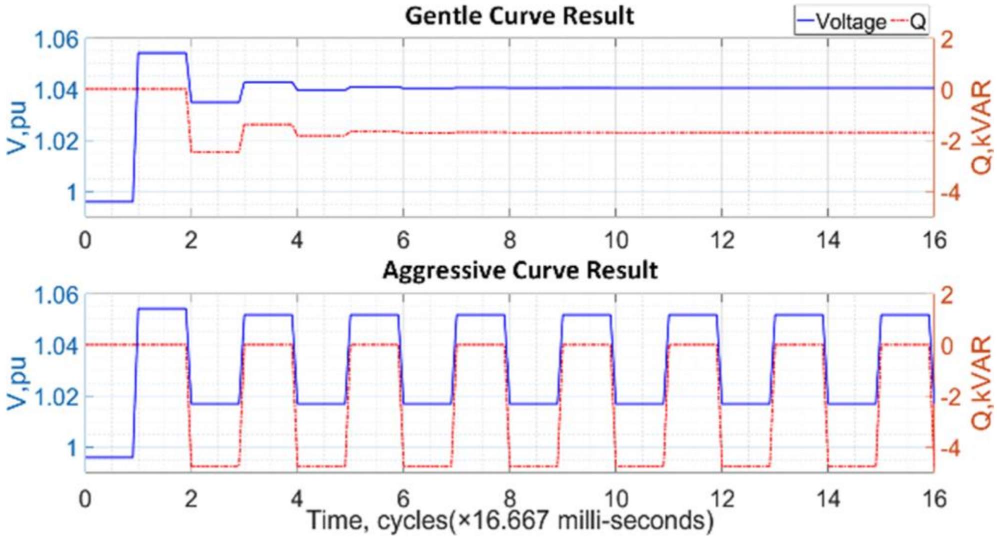

Fig. 9 Gentle vs aggressive curve for regulation

6.4 Layers of the concept

In order to successfully tackle challenges that are brought by widely distributed renewable power injections as well as the dynamic - hard to predict load (with increasing penetration of EVs) solution that utilizes voltage control through Smart Inverter should implement strategies globally in the grid, meaning on central level. Since most of the control needs to be made in real-time, the central level decision making needs to be automated and values need to be checked against the criteria of metaheuristic algorithm after which automatic actions are executed and commands are sent. However, the execution of those commands is taken locally on the smart inverter placed at the solar generation units and locally in the Intelligent Edge Devices on the substation. The data acquisition – data quality and accurate observability is of the exact same importance for the process quality and success, since the result of the implemented automated logic can be only as good as the information extracted from the measurement data used as an input. So, the proposed solution will consist of basic 2 layers: On central dispatching level through SCADA and local level through edge devices.

7 Prerequisites

7.1 Local edge Layer

The edge layer would consist of Smart Inverter devices that communicate with edge device bidirectionally through communication interface. The edge device, communicates with the equipment directly or indirectly through the local server with the SCADA system. This device would then implement commands coming from the central system, but also independently implements simple control algorithms and forms control actions to ensure reliable and secure operation of the system in case of communication loss. So, the logic of the strategy should be implemented in distributed whey locally and be coordinated from the central automation system, that can be part for DMS SCADA or even EMS when such cases are in the jurisdiction of the Transmission Operation System.

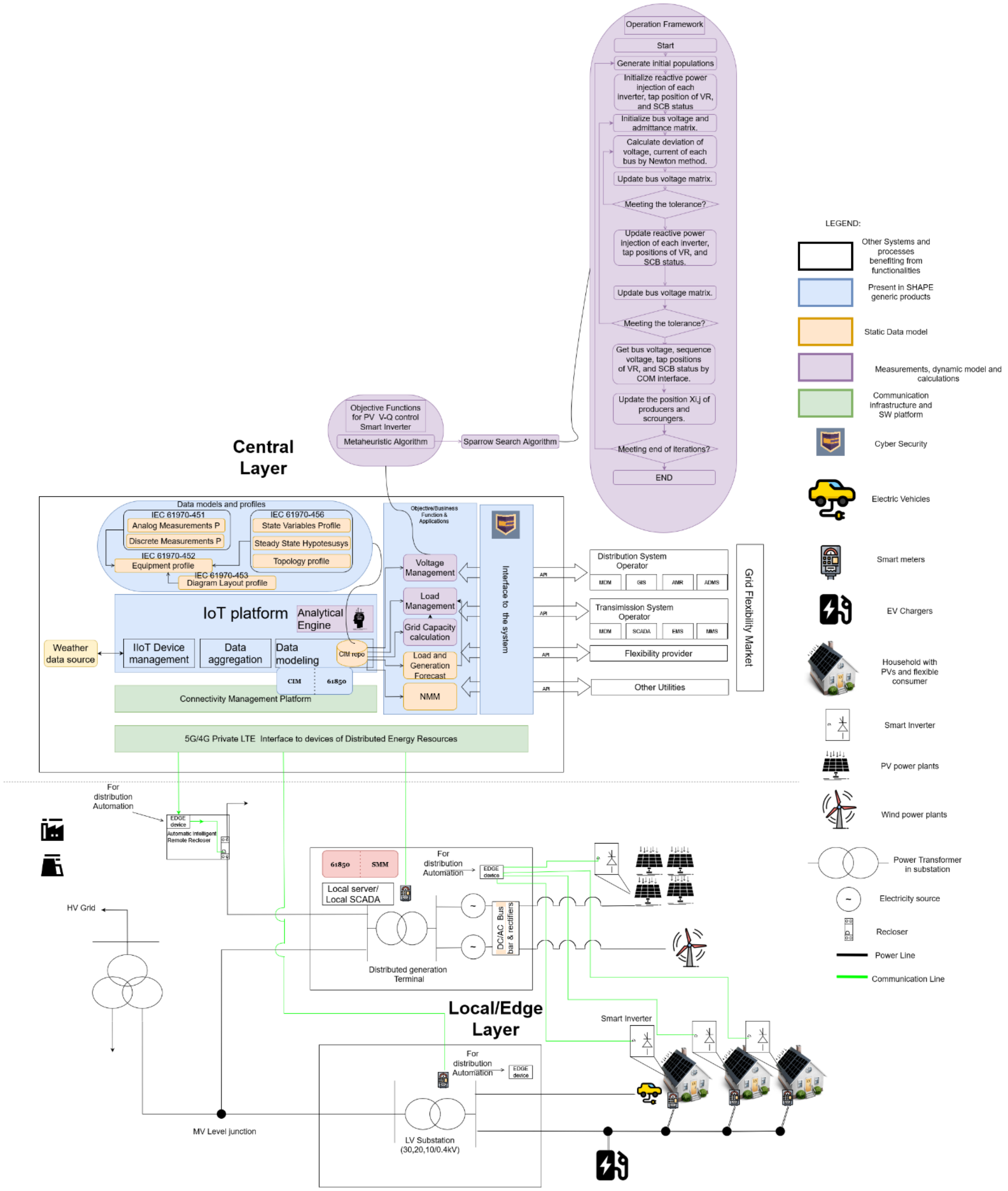

Fig. 10 High Level concept of the solution divided in two layers

7.2 Central Layer

The central layer consists of a system application that aggregates data from measurements transferred through the edge devices and local server as well as from meteorological information systems and other sources. Then it uses historic data, real time measurements and weather forecast as a basic input to employ machine learning algorithm in term providing services to solve forecasting optimization problems (Load and Generation) after which it implements metaheuristic algorithm to create optimal logic for voltage control through Smart inverter.

The logic would be created mainly on central level, but locally optimized settings would be calculated and then distributed to local servers and edge devices.

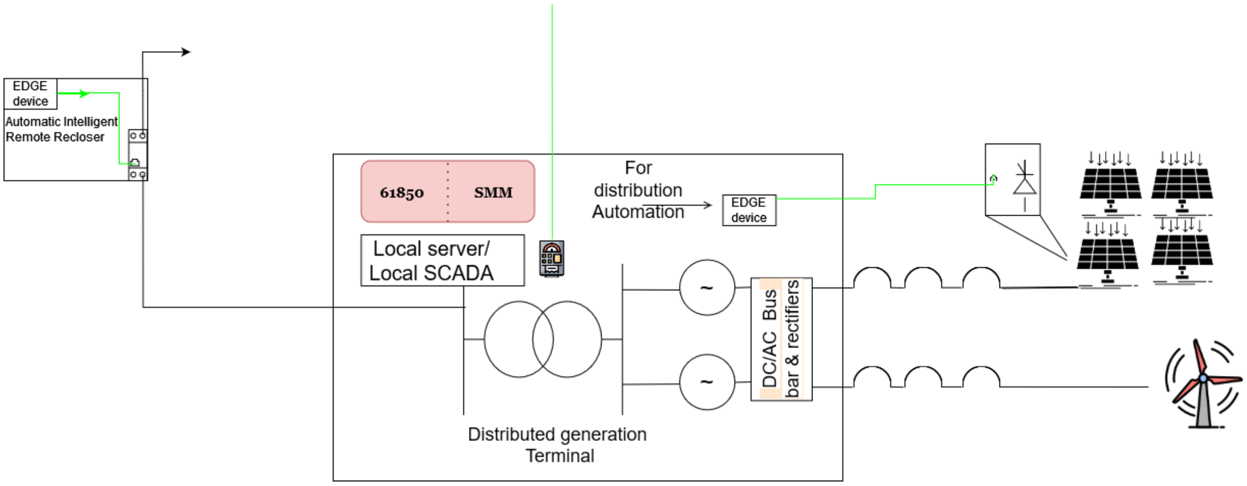

Fig. 11 Local layer consisting of Smart Inverter, Meter, Communication GW and Edge device

7.3 Operation Modeling approach

7.3.1 Choosing algorithm

Due to varied complicated planning problems especially in the Distribution grid, possibility to search all of the possible solutions makes the metaheuristic approach suitable for the application. Because of the simple mathematics it uses users only need to define the upper, lower bounds, the dimension of the problem, set number of populations and number of population. Many types of metaheuristics are inspired from evolutionary, physics, swarm, human and other bio-based behavior. Based on the research done in [1] the swarm-based types are considered as good for global searching in the solution space and use simple mathematical equations – enabling fast calculation. In the same study the Sparrow Search Algorithm showed the most optimal results finding solutions near 0.

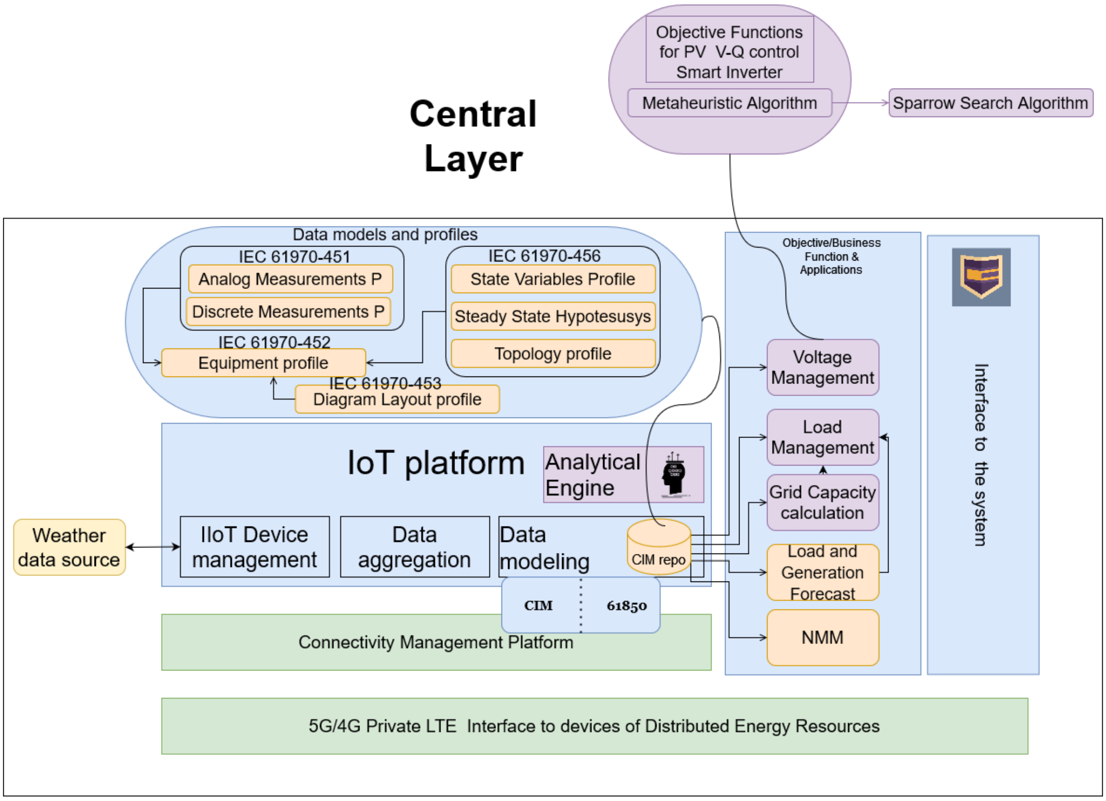

Fig. 12 Central layer for data integration, modeling and model based calculation

The SSA [5] was proposed by Xue and Shen in 2020. It is inspired by group wisdom, foraging, and anti-predation behavior of the captive house sparrow. The sparrow swarm has producers and scroungers. The producers actively search for the food source, whereas the scroungers obtain food through the producers. The producers and scroungers can flexibly switch between each other for the foraging strategy. However, their proportion must be unchanged in the whole population. Sparrows that are close to a rich food source, which represents a better fitness value and has higher energy, act by following the procedure. Several starving scroungers are more likely to fly to another place for food to gain more energy. Furthermore, once sparrows detect a predator, they begin to rise an alarm signal. The producers then need to lead all the scroungers to a safe area until the alarm value is greater than the safety threshold.

The producers are responsible for searching for food and guiding the movements of the scroungers. Thus, they are good at global searching. The location of the producers is updated as follows:

$$X_{i,j}^{t+1} = \begin{cases} X_{i,j}^{t} \cdot \exp\left(\frac{-i}{\alpha \cdot T}\right) & if\ R_2 < ST \\ X_{i,j}^{t} + Q \cdot L & if\ R_2 \geq ST \end{cases} \tag{2}$$

A total of 10% to 20% of the population of the sparrow swarm is aware of the danger. These sparrows quickly move toward the safe area, whereas the sparrows in the middle of the group randomly walk to be close to others. The mathematical model can be expressed as follows:

$$X_{i,j}^{t+1} = \begin{cases} X_{best}^{t} + \beta \cdot \left|X_{i,j}^{t} - X_{best}^{t}\right| & if\ f_i < f_g \\ X_{i,j}^{t} + K \cdot \left(\frac{\left|X_{i,j}^{t} - X_{best}^{t}\right|}{(f_i - f_w) + \varepsilon}\right) & if\ f_i = f_g \end{cases} \tag{3}$$

where X_{best} is the current global optimal location. β, as the step size control parameter, is a normal distribution of random numbers with a mean value of 0 and a variance of 1. $K \in [-1, 1]$ is a random number. Here, f_i is the fitness value of the present sparrow. f_g and f_w are the current global best and worst fitness values, respectively. ε is the smallest constant to avoid a zero-division error.

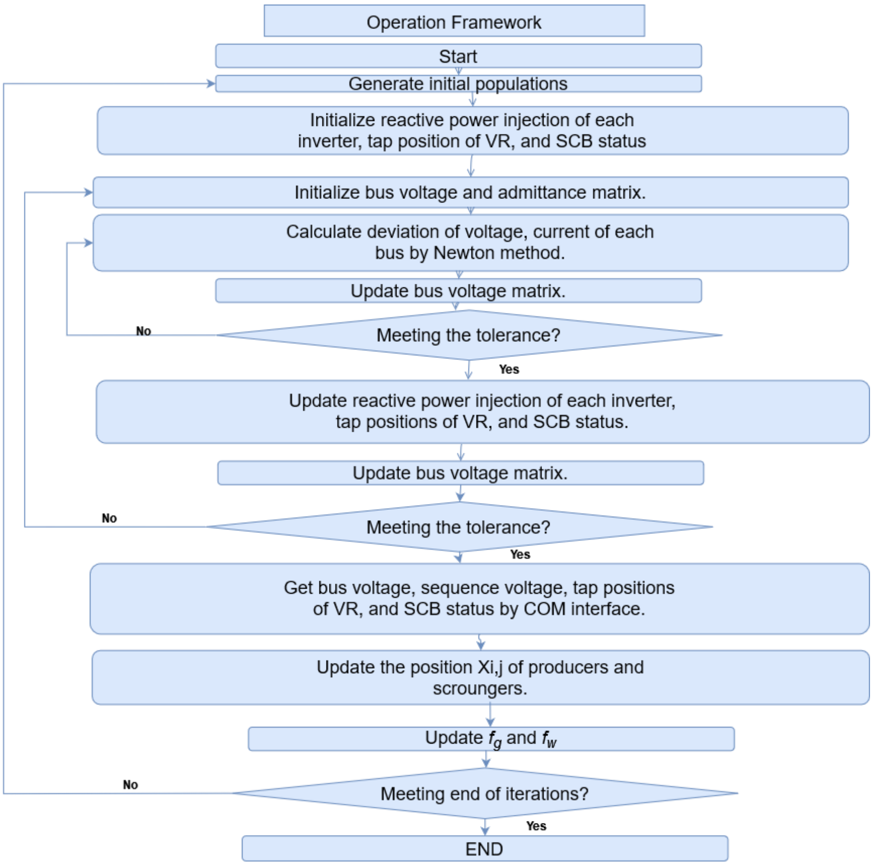

Fig. 13 Diagram of adapted Sparrow Search Algorithm

7.3.2 Implementation framework

The volt–var control settings are modified in the application according to the sparrow positions in the SSA. Then, the analytical engine calculates the bus voltage, branch current, sequence voltage, loss, tap positions of VR, and SCB status. Finally, it delivers the outcomes. First, the SSA generates the initial population of the sparrow swarm and converts the sparrows' positions to the control setting of the smart inverters. Second, to calculate the fitness value of the SSA, the analytical engine derives the power flow using the Newton method and repeatedly updates the smart inverter reactive power injection, tap positions of VR, and SCB status until convergence [1].

7.4 Data input needs and challenges

7.4.1 Data sets on the input

In order to be able to perform accurate power flow calculations which is one of the steps in the algorithm and also additional steps for the voltage regulation framework as well as application to the Load management following values are necessary to be integrated and modeled properly:

- Object data
  - object operating
    - Voltages
    - Currents
    - Active Power
    - Reactive power
    - Discrete measurements
    - Tap changers positions
    - SCB status
  - Asset info
    - Feeder Current limits
    - Substation capacity
    - Equipment maintenance and repairs schedule,
- Historical data on object consumption. Time horizon weeks to years.
- Historical observations and statistics obtained from various open sources of weather and climate data
- Calculated data of the solar position: solar zenith, azimuth, light day length, etc.
- Calendar data

7.4.2 Data challenges

As mentioned in chapter (Challenge definition) in order to make accurate use of the metaheuristic calculation the regulation needs to be done on central level as well. This leads to the need of up-to-date state of the local equipment in the central level as well. The most of the current deploys meet limitations when certain level of details of operation state are needed. These limitations occur because of several reasons:

- Lack of communication between the substation and central level
- Poor (lazy) modeling of signals on substation
- Data is distributed in different IT/OT systems and other data source
- Data intensive process 10 TB data exchange daily
- Inoperability between local and central data models

The trends of substation digitalization and even digital substations definitely go in direction of making successful implementation of such solution framework possible, but simply by digitalization and even proper implementation of IEC 61850 there is going to be missing links since most of the central systems (usually SCADA) operate with data models that defer from IEC61850 that was originally designed for message exchange on the substation level.

7.4.3 Data modeling approach

For the purposes of creation data models which will serve for building the model that will be used as an input in the calculation, after some research the following two groups of standards are chosen relevant for certain equipment, processes and calculations:

- **IEC 61850** for Real time description of the monitored and controlled objects
  - Smart inverters -IEC TR 61850-90-7
  - Power Injection points (substations) - IEC TR 61850-90-2
- **IEC CIM** to support IT/OT systems operation in the process to support several use cases:
  - Energy forecasting and scheduling (P) – IEC 61968-95, IEC 61968-9 and IEC 61968-13
  - Network steady-state analysis & optimization (V, Q) - IEC 61970-420

There are additional certain use cases that lay on the border of this standards, as well as data types that need to be mapped in to information like:

- Special case: time-series steady state – how does the network move from one state to another
- Electrical Connection Point
- Equipment nameplate
  - Static ratings
  - Dynamic (e.g., ramp-rates)
- Power management control
  - Operational constraints / maximums
  - Operational functions (autonomous control functions)
  - Dynamic characteristics
- Schedules and Forecasts

Off course, because of wider area of challenges in operation there are initiatives for harmonization of these standards for modeling, some of which mentioned in IEC 61850-90-2 and will be crucial task also for successful implementation of across the grid Volt-Var control strategy. For truly successful implementation of this advanced V-Q control future efforts on model information mapping, model integration and further harmonization need to be invested.

8 Conclusions

A successful implementation of any intelligent calculations based on analytics and advanced algorithms is highly dependent on observability, data accessibility and accuracy. Most importantly calculation accuracy – dependency for good operation (voltage regulation) is directly correlated with data model quality. The IEC standards referenced in this paper provide only the guidelines for successful modeling. It is up to the engineers to be practical in to the implementation but strict in the same time, always having in mind the bigger of near and further future Smart Grid operations that mostly depend on the quality of information

References

[1] Y.-D. Lee, W.-C. Lin, J.-L. Jiang, J.-H. Cai, W.-T. Huang, (2021), "Optimal Individual Phase Voltage Regulation Strategies in Active Distribution Networks with High PV Penetration Using the Sparrow Search Algorithm", *Energies*, **Vol.** 14, 8370, pp. 1-22.

[2] IEC 61968,

[3] IEC 61970,

[4] IEC TS 61850

[5] Xue, J.; Shen, B. A novel swarm intelligence optimization approach: Sparrow search algorithm. Syst. Sci. Control Eng. 2020, 8,22–34.

The 8th International Symposium on Applied Electromagnetics – SAEM'2022

Struga, North Macedonia, 26-29 June 2022

Utilization of the Flexibility of Consumers in Power Systems by Implementation of Demand-Side Management

Katerina Bilbiloska, Aleksandra Krkoleva Mateska, Petar Krstevski
Ss Cyril and Methodius University in Skopje, Faculty of EE and IT, Ruger Boskovic No. 18, Skopje, North Macedonia,
krkoleva@feit.ukim.edu.mk, petark@feit.ukim.edu.mk

***Abstract* – The paper presents demand – side management (DSM) application implemented for household consumers. The presented solution is based on a linear optimization technique (LP) to distribute the use of household appliances given certain constraints. Furthermore, it presents the findings of the performed sensitivity analysis of the solution as well as the potential financial benefits for the customers, given that such a solution is applied.**

1 Introduction

Fossil fuels are still among the most commonly used sources of primary energy with the highest negative impact on the environment. To counteract the negative environmental impacts, the governments throughout the world adopt strategies [1] and measures [2] to ensure the use of low-carbon technologies and renewable energy sources (RES) in the attempts to secure the path towards decarbonisation. However, the operation of power systems with high RES penetration requires dealing with various technical challenges, which emerge due to the intermittent nature of these resources. As the uncertainty in the operation of the electricity systems grows, the use of flexibility resources to support their operation becomes a necessity. The traditional approach, which is based on the load following principle (generation follows consumption), can be revised considering that the load can have certain flexibility and thus, the consumption can change to fit the available generation. This approach is introduced through the DSM concept [3]. Demand side flexibility is based on the use of load and storage through concepts as DSM, virtual storage plants and other innovative solutions. DSM is defined as measures, activities and programs that establish cooperation between electricity suppliers and consumers by encouraging a change in energy use which differs from their usual habits to achieve economic benefit to both parties. DSM strives to equalize the load curve, i.e., to reduce the occurrence of peaks and the duration peak periods. That could be achieved through several approaches: demand response (DR), energy efficiency and creating opportunities for energy storage [3].

1.1 DSM concept implementation

The concept of DSM focuses on consumers and its implementation should be structured so that consumers' comfort is not compromised [4] and their normal economic operation is maintained [5], [6]. One of the most common forms of DSM is demand response (DR). DR is usually defined as a change in energy usage by consumers compared to their normal consumption, as a response electricity price change over time or an external requirement from a grid operator. DR is an effective approach to use consumer's flexibility to change the inelastic consumption into elastic, and at the same time, provide benefits for the consumer through predetermined incentives [7]. While developing and implementing DR programs, it is important to consider the specific characteristics of the customers and maximise the utilization of their flexibility. In this context, consumers can be classified into three basic categories: industry, commercial consumers and households [5]. An industrial consumer can participate in a specific program if its implementation does not compromise the customer's production process. Similarly, the participation of the commercial consumers in DR programs depends on the availability of specific systems, as heating and cooling systems or lighting, which can be managed to a certain extent and change the consumption of these customers compared to a baseline scenario. The households have the opportunity to exercise their flexibility by changing the time and frequency of use of certain household appliances as washing machines, dish-washers, air conditioning electric water heaters, etc.

Depending on the way of implementation, DR programs can be divided into two categories, explicit (incentive) programs and implicit (price-based) programs. Explicit programs aim to change electricity usage in response to a request or signal from a supplier or aggregator, in return for receiving some benefit such as payment for service credits or other benefits [8]. These programs allow end users to participate in the wholesale, capacity and balancing markets. This category encompasses programs for direct load control, curtailable service, demand bidding, emergency demand response, capacity market and ancillary market programs. The implicit programs are based on dynamic definition of the price, i.e. the price of electricity is not the same in all periods, it fluctuates in real time. The aim is to equalize load curve through offering higher price in the periods with high demand and lower price in other periods. In contrast to explicit programs, in these programs consumers do not participate in the electricity markets, but rather, use their flexibility to reduce their electricity costs. In this category, time of use tariff, critical load pricing, extreme day price programs and extreme day price with peak (critical) load and real time price (variable price) are classified.

The practical implementation of these programs depends on several factors including appropriate regulatory framework, developed electricity markets that foster the participation of both load and generation for providing bids and offers in all market timeframes, especially related to reserve capacity and balancing energy [9]. In addition, application of appropriate information and communication technologies (ICT) is considered an enabler for the practical implementation of DSM programs. The ICT solutions should be applied both at supplier/aggregator level and customer level. It is important to use cost-effective solutions that would be affordable and simple to use, especially when these programs should be applied at small customers and households [10].

This paper presents a specific application of DSM for households, based on a simple and effective approach that optimizes household consumption and redistributes the use of various electrical appliances given certain constraints. The aim is to reduce the peak of the load curve and thus, contribute to a more efficient operation of the grid and reduction of the electricity bill for the customer. The financial aspect, reduction of the electricity bill is also described through one simple example.

2 DSM application for households based on linear optimization

The integration of DSM in the households is a complex problem primarily due to the different devices used, as well as the specific habits of the users. The main goal when implementing DSM in a household is not to change the habits of the users, but to motivate their engagement, considering their comfort constraints. The solution presented in this paper distributes the use of certain devices within a 24 hour period, aiming to minimize the household load at each hour of the observed period.

2.1 Method

LP optimization technique is used for distribution of the use of household electric appliances within specific time periods. The LP process considers the user-defined constraints related to various categories of devices. The basic idea of the developed solution is to determine in which period of the day a specific appliance should be used, with aim to reduce electricity costs, to reshape the load curve and to provide certain service for distribution system operator. If LP is used to find an optimal use schedule of household appliances, than that would mean to determine household appliance engagement in order to minimize load in each hour of the day. The LP optimization is based on the Eq. (1)-(5), [11]:

$$\min_{L, x_{a,h\in R}} L, \text{ i.e.}, \sum_{a\in A} x_{a,h} \le L, \forall h \in H \tag{1}$$

$$1^T x_a = l_a, \forall a \in A \tag{2}$$

$$\alpha_a \le x_{a,h} \le \beta_a, \forall h \in [h_{as}, h_{a(s+1)}, ..., h_{af}] \tag{3}$$

$$1^T s_t = 1, 0 \le s_t \le 1, \forall t \in T \tag{4}$$

$$x_t = P_t^T s_t \tag{5}$$

where A is set of devices, *a* is specific device, *H* is time of use of device, x is installed power of device in period h, l_a is the installed power of device, α_a, β_a, lower and upper bond of device, $h_{as}, h_{a(s+1)}, ..., h_{af}$ time of use, P_t^T is the matrix with possible use combinations of device and s_t is the vector with binary elements that indicate the state of the device.

For the purpose of this research, the household appliances are classified in three categories depending on their usual period of use, i.e. 1) appliances with constant time of use; 2) appliances with variable time of use; and 3) devices with variable energy and time of use, as described in details in [12].The first category covers appliances for which a change of use in not preferred and includes electric stoves, TVs, refrigerators with freezers etc. The second category encompasses appliances that could be used in various periods of the day like water heater, air conditioner, electric vehicle battery etc. The third category includes appliances with shiftable time of use and energy use that changes over time. It includes washing machines, dishwashers etc. Eq. (3)-(5) introduce the used-defined constraints and are related to the three categories of devices mentioned above.

The optimisation process consists of two parts: the first part, which optimises the use of the appliances from the second category (with variable time of use) based on the described LP optimisation and the second part, which aims to find the best period for the use of the devices from the third category, while achieving the least peak durations.

2.2 Optimization results

In this paper, the operation of the devices in a four-member household is optimized through the application of a DR program. The input data used for the devices are indicative, based on [12].

The optimization results are presented in Fig. 1 to Fig. 4. Fig. 1 shows the baseline scenario, without any optimization. Fig. 2 shows the case after the optimization is applied, showing that in the optimized solution the peak in the household consumption is significantly decreased. To broaden the analyses, additional cases have been considered. The sensitivity analyses applied on the proposed solution show how changes in user defined constraints influence the optimized solution. Fig. 3 shows the load curve if the devices from the second category are switched on only after 5 p.m. while Fig. 4 shows the load curve if a constraint on the number of devices switched on per hour is limited (in this case, 4 devices may be simultaneously switched on). Further sensitivity analyses are presented in [13]. It is worth to mention that the method puts the appliances in the solution once a pre-defined condition is satisfied, which explains the occurrence of the peak in early morning hours or after 5 in the afternoon in the examples below.

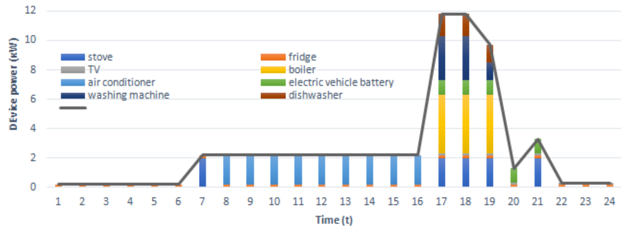

Fig. 1 Baseline scenario - without optimization

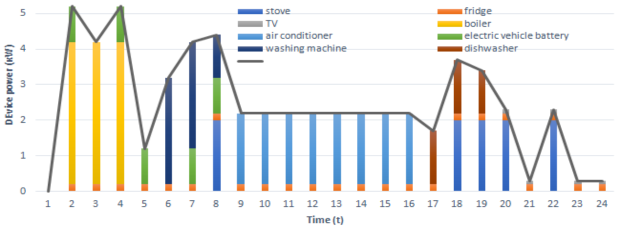

Fig. 2 Optimized use of the considered devices

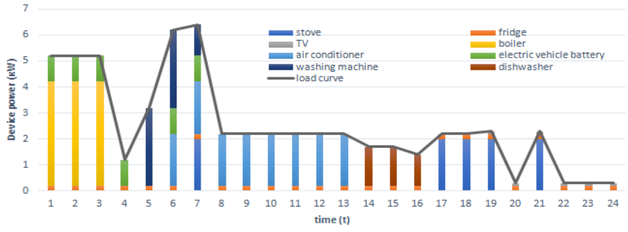

Fig. 3 Category 2 devices are switched on after 5 pm

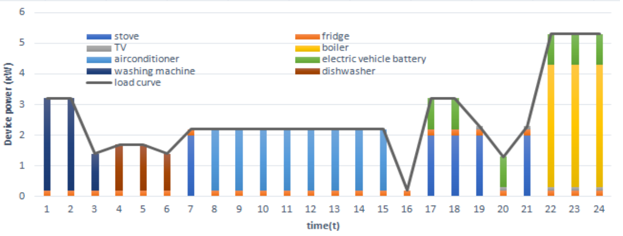

Fig. 4 Load curve with a limited number of switched devices per hour

2.3 Financial impact of implementation of DR programs

The potential benefits of the implementation of a DSM program impact both suppliers (aggregators) and customers. It is essential to note that the participation of the customers in such programs is ensured if they have the opportunity to receive some financial compensation or reduce their electricity bills. To valorise the expected benefits for the customers, the examples described in the previous subsection are compared to the baseline scenario, considering the costs of electricity for each case. The performed calculations show the amount of money spent by the household to cover the electricity costs per day if the household appliances are used as in the baseline scenario and as in the scenarios depicted in Fig. 2 to Fig. 4 (the optimised distribution of use of the devices). The calculations are performed considering the current electricity prices for households in the Republic of North Macedonia [14], i.e. low tariff of 0.6193 denars/kWh for the period between 10 pm and 7 am and first block tariff of 4,3484 denars/kWh for the rest of the day (for monthly usage up to 200 kWh). The prices are for energy only and costs for transmission and distribution of electricity are not included.

The results of the calculations are presented in Table 1 below. The period T1 is the period of the day between 7 am and 10 pm and the period T2 is between 10 pm and 7am. Although the tariff system in place considers 4 tariff blocks, the calculations are done considering the tariff for the first block only. It is a reasonable approach as the optimization should maximise the use of shiftable appliances in the off-peak period, leading to a situation where the customer monthly consumption would not exceed the limit of the first block. This is valid in the cases where electricity is not the major source for household heating. Furthermore, the calculations are done per day only, to relate to the simulation results of the previous section.

Table 1 Costs for energy for the baseline and optimized scenarios

	Baseline scenario (Fig. 1)		Optimized scenario (Fig. 2)		Optimized scenario (Fig. 3)		Optimized scenario (Fig. 4)	
Time of day	T1	T2	T1	T2	T1	T2	T1	T2
Energy (kWh)	57	4	31.6	28.2	33.2	27.6	35.4	25.4
MKD	247.9	2.5	137.4	17.5	144.4	17.1	154	15.7
Total (MKD)	250.4		154.9		161.5		169.7	
Total (EUR)	4.1		2.5		2.6		2.7	

As it could be noticed from the results presented in Table 1, the redistribution of the use of the appliances to periods with lower electricity price could significantly decrease the electricity bill. The optimization presented in Fig. 2 results with least energy costs, which is achieved in accordance with the customer’s constrains, i.e. without considerable changes of the their habits. Relieving customer’s constraints would lead to achieving higher savings. The described example presents the possible household savings on electricity if a specific DR program is in place, with pre-defined time periods and tariffs per periods. In such case, the implementation of the described LP method would allow the customer to use the shiftable household appliances in periods with low tariff following a schedule derived from the LP solution. Further analyses are required to valorise the benefits for customers in the case of dynamic prices.

3 Conclusion

This paper shows how the implementation of simple optimization solutions can ease the implementation of DSM programs at households. By introducing user-defined constraints, the solution can be tailored to the consumer, however, without the need of complex algorithms and advanced technologies. Both the system operators and the consumers benefit of the optimization of the household flexibility. The presented analyses confirm that the household peaks are decreased, which benefits the distribution system operation. Furthermore, the distribution of the appliances following the described LP optimization will lead to decrease of household electricity costs. The savings will depend on the constraints introduced by the customers and the willingness to slightly change their living habits.

References

[1] European Commission, Communication from the Commission, The European Green Deal, COM(2019) 640 final, Brussels, 11.12.2019.

[2] Clean Energy for all Europeans package https://energy.ec.europa.eu/topics/energy-strategy/clean-energy-all-europeans-package_en, accessed 10 April 2022

[3] P. Warren, (2014), "A review of demand-side management policy in the UK", *Renewable and Sustainable Energy Reviews*, **Vol 29.(C)**, pp. 941-951.

[4] S. Nojavan, K. Zare, Demand Response Application in Smart Grids – Operation Issues Vol. 2, Springer Cham, pp. 75-117, (2020).

[5] M. H. Shoreh, P. Siano, M. Shafie – khah, V. Loia, (2016), "A survey of industrial applications of demand response", *Electric Power Systems Research*, **Vol.141**, pp. 31-40.

[6] J. Ponoćko, J.V. Milanović, A. Krkoleva Mateska, P. Krstevski, S. Borozan, (2019), "Existing Approaches to Wide-scale DSM Deployment to Facilitate Transmission Network Flexibility - Results of the Survey in South-East Europe", *Proceedings, 2019 IEEE PES Innovative Smart Grid Technologies Europe*.

[7] J. Aghaei, M.-I. Alizadeh, (2013), "Demand response in smart electricity grids equipped with renewable energy sources: A review", *Renewable and Sustainable Energy Reviews*, **Vol. 18**, pp. 64-72.

[8] Abiri-Jahromi, A., Dhaliwal, N., Bouffard, F.: "Demand Response in Smart Grids", in Integration of Demand Response into the Electricity Chain - Challenges, Opportunities and Smart Grid Solutions, (ISTE Ltd, John Wiley & Sons, 2015), pp. 1-9.

[9] Smart Energy Demand Coalition, "Explicit Demand Response in Europe - Mapping the Market 2017", (SEDC), April 2017.

[10] S. Panda, S. Mohanty, P. Kumar Rout, B. Kumar Sahu, M. Bajaj, H. M. Zawbaa, S. Kamel, "Residential Demand Side Management model, optimization and future perspective: A review", *Energy Reports*, **Vol**. **8**, 2022, pp. 3727-3766.

[11] Z. Zhu, J. Tang, S. Lambotharan, W. Chin, Z. Fan, (2012) "An integer linear programming based optimization for home demand-side management in smart grid", *Proceedings, 2012 IEEE PES Innovative Smart Grid Technologies Europe.*

[12] K. Bilbiloska, Utilization of consumers’ flexibility in power systems by implementation of demand-side management, Master Thesis, Ss. Cyril and Methodius University, Faculty of EE and IT, Skopje, pp. 38-40, (2021).

[13] K. Bilbiloska, A. Krkoleva Mateska, P. Krstevski, "Optimization of Customer Flexibility within Implicit Demand Side Management Programs", *Proceedings, 18th International Conference on the European Energy Market (EEM)*, Ljubljana, September, 2022.

[14] Energy and Water Services Regulatory Commission of the Republic of North Macedonia, Electricity prices https://www.erc.org.mk/page_en.aspx?id=287

The 8th International Symposium on Applied Electromagnetics – SAEM'2022

Struga, North Macedonia, 26-29 June 2022

Analyzing the Impact of Plug-In Hybrid Vehicles in Low-Voltage Distribution Systems Using a Non-Deterministic Approach

Evica Smilkoska[1],
[1] Elektrodistribucija DOOEL, Customer Center (KEC) Gostivar, Str. Goce Delchev no.45 Gostivar,
R. N. Macedonia, E-mail: evica.smilkoska@evn.mk

Vasko Zdraveski[2],
Ss. Cyril and Methodius University, Faculty of Electrical Engineering and Information Technologies, Rugjer Boskovic 18, Skopje, R. N. Macedonia, E-mail: vaskoz@pees-feit.edu.mk

Jovica Vuletić[3]
[3] Ss. Cyril and Methodius University, Faculty of Electrical Engineering and Information Technologies, Rugjer Boskovic 18, P.O.Box 574 1000 Skopje, R. N. Macedonia
jovicav@pees-feit.edu.mk,

Jordančo Angelov[3],
[4] Ss. Cyril and Methodius University, Faculty of Electrical Engineering and Information Technologies, Rugjer Boskovic 18, P.O.Box 574 1000 Skopje, R. N. Macedonia
jordanco@pees-feit.edu.mk,

Mirko Todorovski[4]
[5] Ss. Cyril and Methodius University, Faculty of Electrical Engineering and Information Technologies, Rugjer Boskovic 18, P.O.Box 574 1000 Skopje, R. N. Macedonia
mirko@pees-feit.edu.mk,

Abstract* –The growing presence and randomness of renewable-based Distributed Generation such as solar, photo-voltaic and wind power, and heavy Plug-in Hybrid Electric Vehicle loads in residential distribution grids, results in a higher degree of imbalance, and wide range of voltage fluctuations. When increasing the number of Plug-in Hybrid Electric Vehicles that are simultaneously charged, the additional unpredicted load may cause a number of problems to the current grid in terms of voltage deviations, thermal overloads, power losses, increased aging of transformers and lines, decreased quality of supply and power outages. To investigate how the new Plug-in Hybrid Electric Vehicles impact the current distribution grid, this paper proposes an approach that models their behavior and performs power flow analysis using non-deterministic modelling on CIGRE low voltage benchmark grid.

1 Introduction

Distribution system operators (DSOs) have the responsibility to operate their grid in order to follow a predicted demand with unidirectional power flows only. Most of the conventional distribution grids are of radial type with different configurations and loads, with one objective, to offer quality of supply under certain technical and economical parameters that offer efficient and reliable grid operation [1]-[2]. Due to the fast development of power electronic technologies, the presence of Distributed Generation (DG) and connected Plug-in Hybrid Electric Vehicle (PHEV), the bi/multi-directional power flow distribution grid is growing rapidly which raises the question, are the current conventional distribution grids ready for these new rapidly growing types of loads [3].

The advancements in transportation electrification have changed the structure of traditional car manufacturing processes. That kind of rapid and increased development in the transportation electrification sector requires large scale research and evaluation, in order to measure the capability of the current conventional distribution systems to withstand the increased presence of PHEV [4].

PHEV are continuously opening new perspectives and numerous possibilities [5]. These types of vehicles currently present on the market can not only reduce the pollution, but also help in conserving natural resources. PHEV technology is one of the most promising for reducing petroleum consumption associated with reducing the use of internal combustion engine vehicles, and they are seen as an opportunity to provide environmentally friendly vehicles for transportation that do not release greenhouse gases into the atmosphere or cause smog. From an energy policy point of view, electromobility offers the opportunity to achieve the objectives of decarbonisation and decentralization of electricity sources [6].

PHEVs, as one of the types of Electric Vehicles (EVs), are recharged through a plug, connected to the electric power grid [4]. Hence, PHEVs are changing the conventional load profile [7, 8]. The main issues caused by their growing presence is mainly related to power quality. Power quality is a predominant aspect in the efficiency and security of grids and, is likely to be strongly affected by PHEV development over the forthcoming years [9].

The term ’Power Quality’ refers to providing a near sinusoidal voltage and current waveforms for the power grid at the rated magnitude and frequency [10]. Power quality can be determined by several factors such as voltage and frequency variations, imbalance, interruption, flicker, and harmonics. When the number of PHEVs that are randomly charged on the grid is increasing rapidly, the unpredicted load profile may cause a number of problems to the current conventional grid that are in terms of voltage deviations, thermal overloads, power losses, increased aging of transformers and lines, decreased quality of supply and power outages. Hence, it is of great significance to investigate the power quality concerns in distribution grids while considering PHEVs.

The impact of PHEVs on the grid parameters can be consequential or inconsequential depending upon the number of PHEVs attached to the grid, grid characteristics, and PHEVs charging features. To conclude that supplied energy is of acceptable quality, the parameters that define it must be within limits defined by the DSO distribution regulation [11].

With the increased presence of PHEVs, besides the problems associated with the quality of the distributed electric energy, as mentioned before, it is also very important the problem related with the increased aging of transformers and lines. The solution to this problem is mainly focused on grid reinforcement. Researchers studying this problem have concluded that for the proposed solution, a large economical investment will be needed. As an economic alternative to grid reinforcement, different studies have proposed different strategies [1]. One of the proposed strategies is PHEVs charging schemes as an alternative for supporting the grid and enhancing both the efficiency and the reliability of the distribution grid. An extensive amount of research shows that intelligent integration, namely smart PHEV charging, can be used for lowering the impact on the power grid or providing different ancillary services [12]. The ancillary services provided by PHEVs are associated with the mode of discharging their batteries, hence discharging the stored energy for peak power shaving, and spinning reserves [13]. On the other hand, the available energy stored in the PHEVs can be used to relive the distribution grid from overloading at certain times or to allow the grid to charge more PHEVs at any time of the day, including peak hours. The introduction of storage devices like PHEVs may result in revolutionary changes to the distribution grid [14], such as voltage support, provide backup power in case of interruption, reduce losses, and postpone the need for distribution grid reinforcements.

The way the distribution grid is connected and operated to provide power to a load that changes every minute requires a time analysis to see the effect on the grid, especially with changing household loading and the timing of PHEVs cycles of charging and discharging or in other word demand response [15]. The main purpose of this paper is to analyze a certain grid configuration, where feeders, conductors, transformers and substations, DGs and PHEVs perform well, while maintaining a radial configuration, and maintaining the desired quality of supply [16].

2 Problem Formulation

The problem of connecting the injections generated by PHEVs in the distribution grid for 24 hour analysed intervals and analysing the power quality parameters is defined in this section using MATLAB functions.

The PHEV types used in this simulation are defined in Table 1 [8]. There are four different groups of PHEVs, and every group contains three different PHEVs according to their All-Electric Range (AER). The AER is defined as the possible distance driven by a PHEV with a fully charged battery [4]. Table 1 also presents the battery capacity of PHEVs with AER of 48, 64 and 96 km respectively. As noticed from the presented data, the battery capacity of a PHEV can vary from 7.78 kWh to 27.44 kWh.

In order to precisely define the PHEVs used in this paper, the battery’s State of Charge (SOC) has to be determined, as one of the required parameters. SOC is a measure of the amount of energy stored in a battery [4]. In this paper, the battery SOC is defined as a random value between 0.3 and 0.9 of the battery capacity. These values are used a minimum energy that must be stored in the PHEVs battery and a maximum energy up to which the PHEVs battery can be charged.

Table 1. PHEVs battery capacity data

Vehicle type	$PHEV_{48}$[kWh]	$PHEV_{64}$[kWh]	$PHEV_{96}$[kWh]
Compact sedan	7.78	10.34	15.51
Mid-size sedan	8.95	11.93	17.89
Mid-size SUV	11.33	15.11	22.67
Full-size SUV	13.72	18.29	27.44

$$\Delta SOC = 0.9 - 0.3 = 0.6 \tag{1}$$

$$A = randvalue[0,1] \tag{2}$$

$$\Delta SOC' = A \cdot \Delta SOC + 0.3 \tag{3}$$

If the battery SOC of the PHEV is < 0.5 the vehicle attached to the grid has to charge, or in other words to take energy from the grid, otherwise if the battery SOC is > 0.5 and < 0.9 the vehicle must discharge or to inject energy into the grid.

$$PHEV = \begin{cases} ch\arg ing: & SOC < 0.5 \\ disch\arg ing: & 0.5 < SOC < 0.9 \end{cases} \tag{4}$$

The next parameters defining the PHEVs are the arrival and departure times of PHEVs. The arrival and departure times are used to determine their availability during the 24-hour analyzed interval. The arrival time and departure time of the PHEVs are randomly chosen from real life database [17]. If the departure time is lower than the arrival time by value, it is considered that the departure time of the vehicle is within the next day which is out of the analyzed interval and the departure time is rounded up to midnight or the last hour of the analyzed interval. After determination of the needed parameters, the injection of the PHEVs during the 24-hour analyzed interval is generated.

$$ATime_{veh} = randvalue[DataBase] \tag{5}$$

$$DTime_{veh} = randvalue[DataBase] \tag{6}$$

$$DataBase = 01:00, 02:00, ...24:00 \tag{7}$$

$$DTime = \begin{cases} DTime; & DTime > ATime \\ 24:00; & DTime < ATime \end{cases} \tag{8}$$

As far as the load of the grid is concerned, the paper uses real life data from the site of Elektrodistribucija DOOEL [18]. The loading data applies to households with and without electric heating during the year 2021. An annual data for scale of 24-hour distribution is extracted for the purpose of this simulation. Figure 1 presents a daily diagram of the households loading with and without electric heating during a 24-hour period with its minimum, maximum and mean values according to the legend shown on the diagram.

To address the uncertainty of the loads connected to the grid nodes, their load curve is randomly chosen between the maximum and minimum values from the load profile curve area presented in Figure 1. Considering all the uncertain variables used in this paper, as a method for solving the power flow analysis in each iteration, the Monte Carlo simulation is utilised. For every node of the grid, a new loading curve is generated, and the methodology is repeated for every iteration.

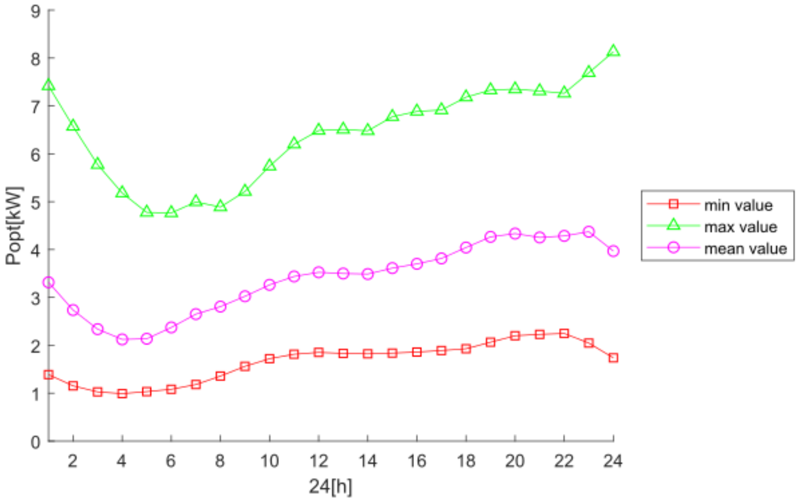

Figure 1. Domain of the household loading curves

$$P_{value,h_i} = randvalue[P_{\min value,h_i}, P_{\max value,h_i}] \tag{9}$$

$$h_i = 1,2,3....24 \tag{10}$$

The characteristic values that determine the loading data are presented in Table 2. It can be noticed that the values of the loading attached to the grid are within the interval of 0.9914 kW to 8.1298 kW, for households with and without electric heating.

Table 2. Household loading data

h_{no}	min [kW]	max [kW]	std	mean [kW]
1	1,3883	7,4191	1,7856	3,3152
2	1,1536	6,5703	1,5389	2,7366
3	1,0278	5,7731	1,3089	2,3372
4	0,9914	5,1797	1,1392	2,1233
5	1,0332	4,7751	1,0259	2,1372
6	1,0819	4,7651	1,0304	2,3738
7	1,1811	4,9939	1,0492	2,6515
8	1,3583	4,8876	0,9493	2,8087
9	1,5612	5,2129	0,8893	3,0241
10	1,7215	5,7407	0,9406	3,2629
11	1,8143	6,2004	0,9977	3,4379
12	1,8520	6,4862	1,0455	3,5247
13	1,8315	6,5069	1,0548	3,4997
14	1,8228	6,4792	1,0637	3,4883
15	1,8376	6,7738	1,1674	3,6126
16	1,8596	6,8856	1,2229	3,7013
17	1,8909	6,9139	1,2561	3,8145
18	1,9282	7,1817	1,3612	4,0425
19	2,0656	7,3305	1,3428	4,2652
20	2,2005	7,3505	1,2608	4,3337
21	2,2284	7,3101	1,2058	4,2525
22	2,2481	7,2631	1,206	4,2848
23	2,0472	7,6929	1,6033	4,3718
24	1,7388	8,1298	1,8643	3,9683

For analyzing the injection of the PHEVs on the distribution grid and the characteristics that define the power quality, in this paper the CIGRE benchmark low voltage grid is used [20]. The topology of the grid is presented in Figure 2 with household loads connected to every node of the grid.

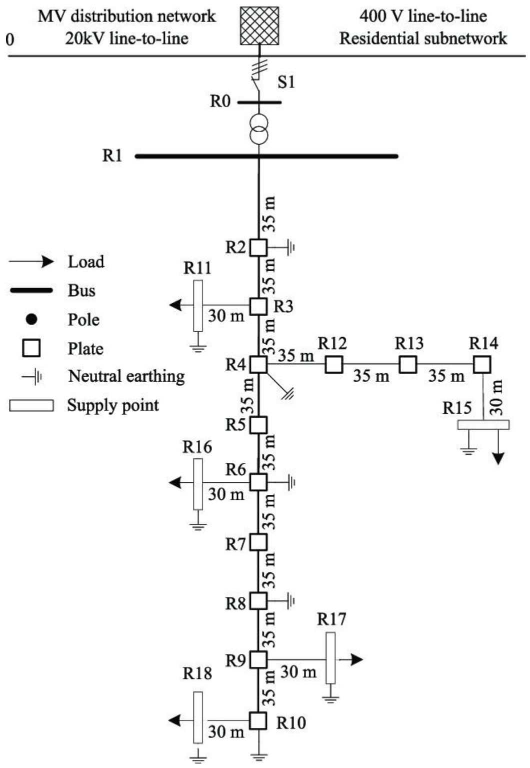

Figure 2. CIGRE Benchmark low voltage grid

The Power Flow analysis of the low voltage distribution grid is made using suitable mathematical model [21]. With the Power Flow analysis, the power distribution in the grid branches and voltages in the grid's nodes are determined.

3 Case Study

For every node of the CIGRE Benchmark low voltage distribution grid, a new injection for 24-hour analysed interval from one randomly chosen PHEV is generated and a new curve for the loading profile is generated. Because the grid has 18 nodes, 17 new PHEVs injections are generated, 17 different loading profiles are generated, and one power flow analysis is made. Node R1 is not a part of the analysis. The result from one iteration is a 24-hour probability distribution (PD) for the branch's active power loss and node's voltage drops interval.

To provide detailed information for the PD of the branch's active power losses and the PD of the node voltage magnitudes, the simulation is performed 10.000 times. To make a comparison of the results for the branch's active power loss and node voltage drops, the simulation is performed additional 10.000 times when there are no PHEVs injections attached to the distribution grid, i.e., base case scenario.

For solving the power flow simulation in this paper, the Monte Carlo method is considered, as mentioned earlier. During a Monte Carlo simulation, the values that are subject to analysis are randomly sampled. Each set of samples is called an iteration, and the resulting outcome from that sample is recorded. In this case the results that are recorded are the branch active power losses and nodes voltages. With the Monte Carlo simulation that is performed hundreds or thousands of times, the result is a probability distribution of possible outcome values of the branch active power losses and node voltages. In this way, Monte Carlo simulation provides a much more comprehensive view of what may happen.

The desired output of the power flow analysis is the domain of the active power losses in the grid, presented by its min, max and mean values, and the domain of the voltages in the nodes, respectively. It is expected that when the active power loss in the grid is maximum, the node voltages are minimum due to high values of the loading.

The comprehensive presentation for the generated PHEVs injections represented by their minimum, maximum and mean values is presented in Figure 3.

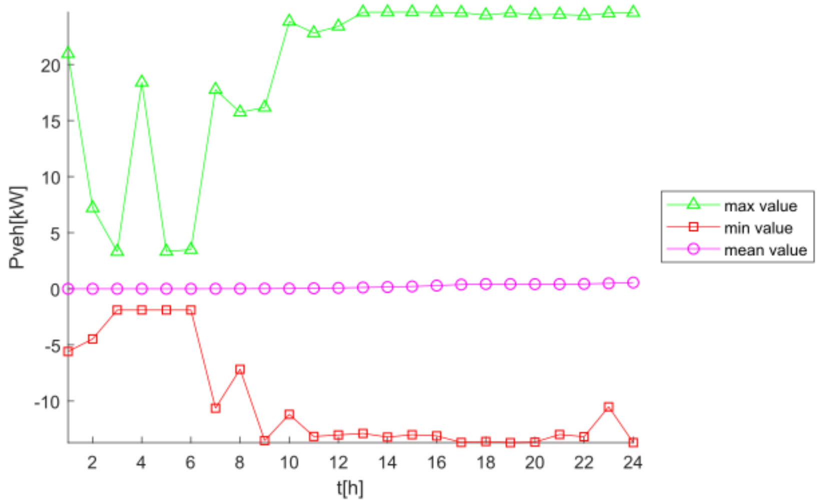

Figure 3. Domain of the generated PHEVs injections

From the presented data of the generated injections, it can be noticed that the domain of the PHEVs attached to the grid is between 24.6924 kW and -13.7090 kW.

After the simulation, the results for active power losses and node voltages are presented in Figure 4 and Figure 5, respectively.

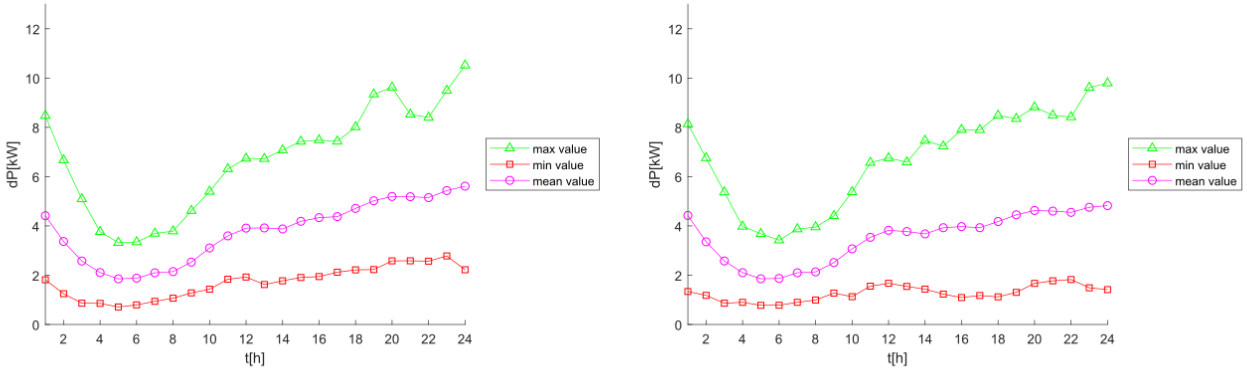

Figure 4. Active power losses - left without PHEVs, right with PHEVs

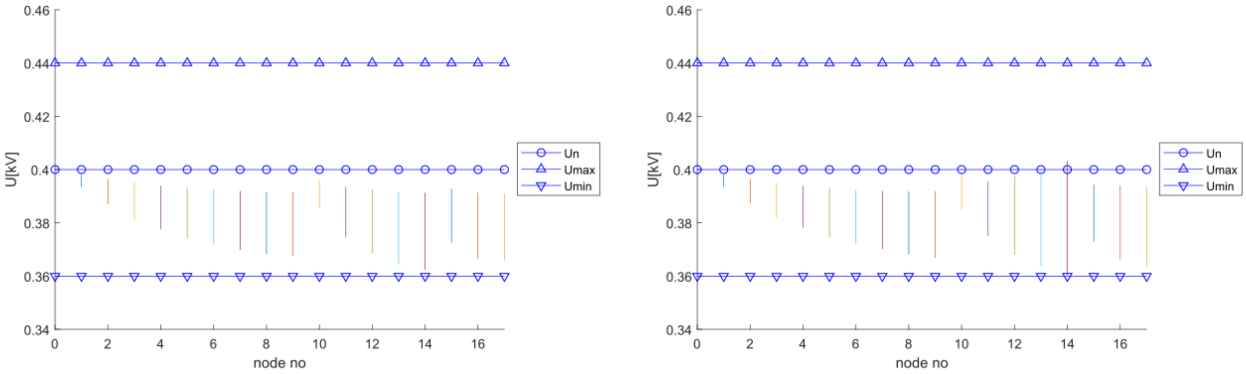

Figure 5. Histogram of node voltages - left without PHEVs, right with PHEVs

From the presented results, we can see that the domain of the grid active power losses with and without PHEVs is mainly overlapped. The domain of the active power losses consists of larger values, when there are no PHEVs connected to the grid, which is unlike when PHEVs are connected to the grid, confirmed by the presented results. When we are analysing the scenario without PHEVs, the curves of the active power losses generally follow the curve of the loading profile, which is not the case when we are analysing the scenario with connected PHEVs. In such cases the active power losses curve follow the same trend but with certain peak shaving, depending on the PHEVs injections. As for the results of the node voltages and the given constraints, almost all are beneath the grid nominal voltage (0.4kV), but besides that all the values are in the DSOs given constraints of $\Delta U = \pm 10\ \%$, with and without connected PHEVs, respectively. From the presented results, we can notice a deviation of voltage magnitudes, which is larger when PHEVs are connected to the grid and somewhat smaller when PHEVs are absent. Altogether, the distribution grid will perform well while maintaining a radial configuration and maintaining the desired quality of supply defined by the DSO distribution regulation, while PHEVs are connected.

4 Conclusion

The increasing presence of PHEVs in daily life is inevitable. Their presence in the years that follow will increase exponentially. According to the presented results the presence of PHEVs will make an impact on the current distribution grid. These impacts can be significant or insignificant, depending upon the number of PHEVs attached to the grid, grid characteristics and PHEVs charging features, despite the negative impact of the charging/discharging cycles of the PHEVs on the battery life.

To lower the impact of PHEVs on the distribution grid, solutions need to be taken into consideration which should also include technical and economic aspects of the problem. The proposed methods are in line with the integration of new charging schemes and coordinating their charging and discharging cycles [22]. With the use of smart charging of PHEV, the peak from charging the PHEVs will be shifted to periods with a lower peak from the household loading. The characteristic of PHEV for bi/multi-directional power flow can be used as a strategy for regulating the grid voltage. The active power control can adjust the operation of PHEV charging, and the reactive power control can inject reactive power into the grid to support the network voltage. The proposed methods should be subject of further research.

References

[1] Sergejus Martinenas, Katarina Knezovi´c, Mattia Marinelli, “Management of Power Quality Issues in Low Voltage Networks using Electric Vehicles: Experimental Validation”, IEEE Transactions on Power Delivery, Volume: 32 Issue: 2, 2016.

[2] Md Multan Biswas, Sultana Razia Akhter, Kamal Chandra Paul, “Power Quality Analysis for Distributed Generation and Electric Vehicle Integrated Distribution System”, IEEE 2020 55th International Universities Power Engineering Conference (UPEC), Torino, Italy, 2020.

[3] Tawfiq Aljohani and Osama Mohammed: „Modeling the Impact of the Vehicle-to Grid Services on the Hourly Operation of the Power Distribution Grid “, Energy System Research Laboratory, Florida International University, Miami, Florida, 2018.

[4] Peng-Yong Kong, George K. Karagiannidis, „Charging Schemes for Plug-In Hybrid Electric Vehicles in Smart Grid: A Survey “, IEEE Access (Volume: 4), pp. 6846 – 6875, 2016.

[5] Zahra Darabi, Mehdi Ferdowsi, “Plug-in Hybrid Electric Vehicles: Charging Load Profile Extraction Based on Transportation Data”, 2011 IEEE Power and Energy Society General Meeting, 2011.

[6] Joanna Baraniak, Jacek Starzynski, “Modeling the Impact of Electric Vehicle Charging Systems on Electric Power Quality”, Article, Energies 2020.

[7] Shengnan Shao, Manisa Pipattanasomporn, Saifur Rahman, “Challenges of PHEV Penetration to the Residential Distribution Network”, 2009 IEEE Power & Energy Society General Meeting, Calgary, Alberta Canada, 2009.

[8] V. Zdraveski, P. Krstevski, J. Vuletic, J. Angelov, A. Krkoleva Mateska, M. Todorovski: „Analyzing the Impact of Battery Electric Vehicles on Distribution Networks Using Nondeterministic Model “, IEEE EUROCON 2019 -18th International Conference on Smart Technologies, Novi Sad, Serbia, 2019.

[9] M. Sabarimuthu, N. Senthilnathan, A. M. Monnisha, V. Kamalesh Kumar, S. KrithikaSree, P.Mala Sundari, “Measurement and Analysis of Power Quality Issues Due to Electric Vehicle Charger”, IOP Conference Series Materials Science and Engineering, 2021.

[10] Abdollah Ahmadi, Ahmad Tavakoli, Pouya Jamborsalamati, Navid Rezaei, Mohammad Reza Miveh, Foad Heidari Gandoman, Alireza Heidari, Ali Esmaeel Nezhad: „Power quality improvement in smart grids using electric vehicles: a review “, IET Electrical Systems in Transportation, Volume 9, Issue 2, pp. 53-64, 2019.

[11] Energy Regulatory Commission, "Electricity Distribution Network Rules", Energy Regulatory Commission Official page, 2019.

[12] Shengnan Shao, Manisa Pipattanasomporn, Saifur Rahman, "Challenges of PHEV Penetration to the Residential Distribution Network", 2009 IEEE Power & Energy Society General Meeting, Calgary, Alberta Canada, 2009.

[13] Fucun Li, Liang Guo, Lijun Liu, Xiao Li, Qing Wang, "Method to improve charging power quality of electric vehicles", The 14th IET International Conference on AC and DC Power Transmission (ACDC 2018), The Journal of Engineering, Chengdu, China, 2018.

[14] Behzad Zargar, Ting Wang, Manuel Pitz, Rainer Bachmann, Moritz Maschmann, Angelina Bintoudi, Lampros Zyglakis, Ferdinanda Ponci, Antonello Monti, Dimosthenis Ioannidis, "Power Quality Improvement in Distribution Grids via Real-Time Smart Exploitation of Electric Vehicles", Article, Energies, 2021.

[15] Tawfiq Aljohani and Osama Mohammed: „Modeling the Impact of the Vehicle-to Grid Services on the Hourly Operation of the Power Distribution Grid ", Energy System Research Laboratory, Florida International University, Miami, Florida, 2018.

[16] Eonassis O. Santos, Joberto S. B. Martins, "Distribution Power Network Reconfiguration in the Smart Grid", CIGRÉ-BRASIL - Brazilian National Committee, International Seminar on Policies, Incentives, Technology and Regulation on Smart Grids, Rio de Janeiro, Brasil, 2017.

[17] National Highway Traffic Safety Administration, https://www.nhtsa.gov/, date of access March 2022

[18] Elektrodistribucija DOOEL – Standard annual load distribution curve 2021, https://www.elektrodistribucija.mk/, date of access March 2022

[19] Jordancho Angelov, Jovica Vuletik and Mirko Todorovski: „Optimal Locations of Energy Storage Devices in Low-Voltage Grids ", ICEST 2019, Ohrid, Macedonia, 2019.

[20] "Benchmark systems for network integration of renewable and distributed energy resources", Cigre Task Force C6.04.02, Tech. Rep, 2014.

[21] Faruk DILSIZ, "Power Flow Analysis - Power Flow Study", International University of Sarajevo, Faculty of Engineering and Natural Sciences, 2014.

[22] LI Hui-ling, BAI Xiao-min, and TAN Wen, "Impacts of Plug-in Hybrid Electric Vehicles Charging on Distribution Grid and Smart Charging", 2012 IEEE International Conference on Power System Technology (POWERCON), Auckland. New Zealand, 2012.

Numerical Calculation of the Electrical and Magnetic Fields of the High Voltage Power Distribution Network Insulator

Željko Hederić[1], Venco Ćorluka[1]
[1] Faculty of Electrical Engineering, Computer Science and Information Technology in Osijek, Croatia,
zeljko.hederic@ferit.hr

Abstract ***– The most common method of detecting insulator faults to date requires trained personnel to manually inspect a large number of insulators in a variety of locations and positions. This is a relatively simple task if there's a road next to the HV grid. When the terrain isn't so easily accessible, the difficulty of detection increases exponentially. This is where IoT technologies come in. Combination of the sensors (electric and magnetic field detection) system of the communication and control units is developing under project research where modelling of electric and magnetic field in insulator area using Finite Elements Method provide detection action for sensor network communicated via LoRa devices.***

1 Introduction

As the number of high-voltage power lines increases, so does the number of insulators that are installed on them. Since these insulators are located in many areas with varying conditions, there are almost countless ways in which failures can occur, but some of these failures occur more frequently. These failures include, for example, cracks in the insulators caused by bad weather. Also failures can be caused by polluted air or acid from the droppings of certain bird species, on the other hand, are a little harder to imagine but do occur and large enough to cause a malfunction [1].

In order for the power grid to function efficiently and for end-users not to be left without electricity, faults in the insulator must be noticed and repaired in time. Unfortunately, there's not yet an effective method to detect all types of faults. In addition, the safety of the personnel carrying out these repairs must be taken into account. By far the most common method for detecting malfunctions is a visual inspection. Visual inspection requires personnel to approach each insulator, which is a major problem if the power grid pylon is located off the road, in a forest, or on an inaccessible mountain. In order for everything to function according to modern requirements, new monitoring systems must be durable, which means they must've minimal energy consumption, but also be very reliable. The right candidate to meet these requirements is the LoRa based device [2].

2 Insulators

Insulators represent a passive electrical part on transmission lines. They prevent the current from flowing in a short way between the conductors or through the poles into the ground and thus give the transmission line the necessary electrical strength. As the conductors are attached to the poles using insulators, they must also be mechanically strong enough. From this, and from the circumstances in which the insulators are located, follow the requirements that are placed on them. Insulators must have sufficient electrical resistance to jump, which depends on the external dimensions and shape of the insulator, and it is necessary to prevent an electric arc between the conductor and the pole through the air along the insulator. They are also required to have electrical breakdown strength, which depends on the internal dimensions and properties of the material, and is necessary to prevent a breakdown and short circuit through the insulator itself. Insulators are dimensioned so that their breakdown strength is greater than jump strength, because breakdown leads to the destruction of the insulator. For the production of insulators for transmission lines, primarily ceramic insulating materials are used today, which, if they are produced in good quality, meet the set requirements. Electroporcelain is mostly used, which is basically produced from a mixture of alumina, quartz and kaolin. Recently, it has been increasingly used for insulators and tempered glass, especially in some Western countries [9,10].

For transmission lines with a voltage of 30 kV and above, suspension insulators are used, from which insulator chains are assembled. Of the porcelain suspension insulators, cap insulators are used the most (Fig. 1). A batik is inserted into the porcelain body from below, and a cap with a nest is inserted from above, into which the batik of the next article is inserted. In Central Europe, massive (Fig. 2) and stick insulators are widely used.rod insulators (Fig. 3). Their advantage is that they are insensitive to puncture, so they do not even need to be tested in operation. In order to ensure the electrical resistance to the jump, the insulators are designed so that they have a long sliding track on the surface of the insulating body, one part of which track remains dry even during rain.

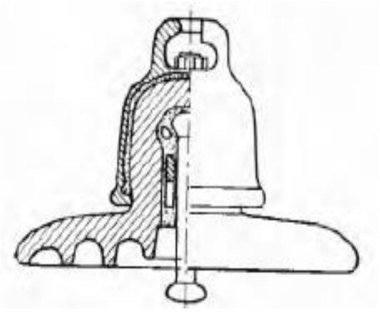

Fig. 1 Cap insulator

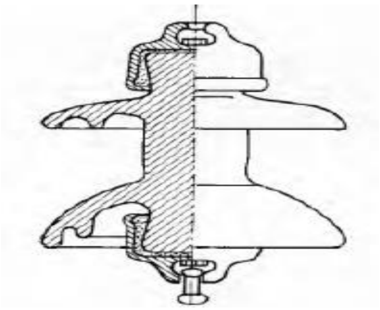

Fig. 2 Massive insulator

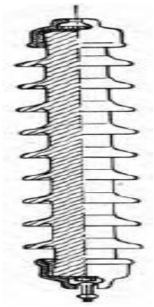

Fig. 3 Rod insulator

3 Research and development of systems for monitoring high-voltage routes using IOT technologies

The applicant's project aims to develop a new technology that will form the basis for the construction of a new company product or solution for monitoring high-voltage power lines, more specifically a digital system for detecting breaks in high-voltage insulators. The goal is to develop breakthrough detection devices and build a cloud system that reports in realtime which insulator has failed to minimize downtime and replacement costs, enable maintenance of insulators and enable monitoring of other important aspects of the transmission line for which there are no instruments in most transmission lines today (wire breakage, lightning strike). The project is being carried out in industrial research and experimental development phases.

The sensing device is designed as an independent system, completely isolated for reasons of safety of use and longevity, consisting of containing three basic units: sensors, control system, communication system, and battery. The idea of the device is based on the fact that physical damage to the insulator's body causes changes in the electric and magnetic fields around the insulator [3, 4]. Fault detection is based on two basic triggers. The first is that during normal operation, three-phase power line sensors located on the same pylon should respond the same way over a longer period of time, which can then be detected by comparison (due to a fault, a particular sensor should start giving different readings - e.g. after an insulator failure). This is important if there's major insulator damage. The second trigger is power system transients monitoring (transient of current and voltage waves), which occurs when a larger load or a smaller atmospheric discharge is switched on. Significant changes in electromagnetic field levels then occur and consequently, potential faults can be detected [5].

The first group of sensor devices was brought to the HV laboratory to test them under real conditions. The gateway was placed no more than 10 meters away to test which devices are capable of communicating with the server in the presence of a high voltage (the sensors must be functional for up to 400kV). Fig. 4 shows how the devices were placed inside of the HV laboratory.

Fig. 4. Metal plate as zero potential plane for the simulation of partial discharges in HV laboratory and arrangement of the tested devices.

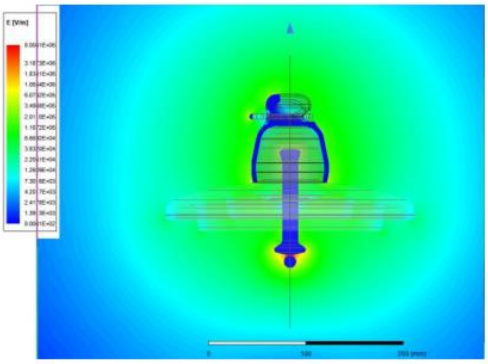

Fig. 5. FEM numerical analysis of electrical and magnetic fields around insulator chain parts

In parallel with the field tests, numerical calculations (FEM in ANSYS software) were carried out to obtain a simulation of the electric and magnetic field surrounding the HV insulator parts while they were attached to the power line to determine the position where the device should be placed [6]. Proper placement of the devices must be accompanied by correct adjustment of the sensors inside them and their calibration so that their readings match the detection of the electromagnetic fields at the actual position of the insulator chain. Fig.5 presents the contour of the electric field around single glass insulator chain parts.

Defects and pollution on insulators most often occur in industrial areas. The consequence of a contaminated insulator is a current jump or leakage current. The distribution of electric and magnetic fields is determined by the finite element method, which is widely used in numerical calculations today. For a good calculation accuracy, it is important to know the properties of the insulator material as well as the choice of the number of finite elements in the critical places of the insulator, because the electric fields in that part change rapidly. For the analysis of electric fields, Gauss's law and continuity equation are applied [10,11]:

$$\nabla \cdot \varepsilon E = \rho \qquad (1)$$

$$\nabla \cdot J = -\frac{\partial \rho}{\partial t}$$

(2)

Where: ρ - is electric charge density (C/m3), ε - is dielectric constant of dielectric material, J - is current density (A/m2), E - is electric field strength (V/m).

At determining the vector of magnetic flux density in the slots of the stator winding, we start from the fourth Maxwell's equation:

$$\mathrm{Div}\ \boldsymbol{B} = \nabla \boldsymbol{B} = 0 \qquad (3)$$

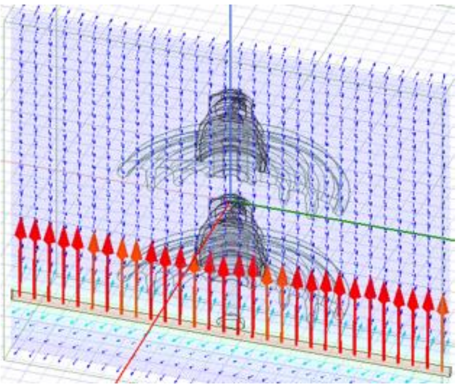

Fig. 6 The direction of the magnetic field current 1000A

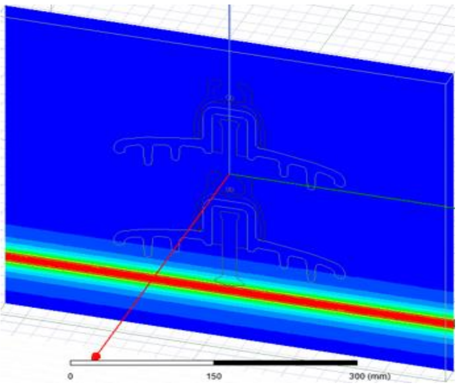

Fig.7 Magnetic flux density around insulator for conductor in the insulator for a conductor current of 1000 A

Figures 6 and 7 show the distribution of the magnetic flux density and the direction of the magnetic field vector around the insulator obtained by the finite element method for a conductor current of 1000 A. It can be seen that the densest field distribution is on the lower insulator carrying the conductor. Since faults on this insulator are the most common, the accuracy of the calculated fields will be more reliable, which means that the field detection sensors should be placed closer to the lower insulator that carries the conductor

4 Conclusion

The paper proposed a system for detecting faults on insulators by analyzing electromagnetic fields using the finite element method. By timely detection and determination of the type of failure, it contributes to the maintenance of the entire power system and its greater reliability in operation. Some types of malfunctions are difficult to detect, so various monitoring methods and systems are being developed that include more sophisticated measuring equipment, especially sensors. Sensors must be highly sensitive, have a communication system and be well isolated from harmful external influences. LoRa is a new technology for communication, and the advantage is low consumption and long-distance signal transmission. Communication is achieved by frequency modulation, which has a wide range of coverage. By calculating the field, a fault on the insulator can be observed because each damage has a different distribution of the field. This approach is applicable for all types of insulators, so based on reliable results, the right type of insulator can be selected economically. Since the insulator is made of cement, porcelain for iron, it is important to know the permittivity and conductivity of these materials for the accuracy of the calculation.

Acknowledgements

This research is supported by the European Union from the European Regional Development Fund within the Operational Program "Competitiveness and Cohesion 2014-2020", under the project: “Research and development of systems for monitoring high-voltage routes, and especially the discharge of high-voltage insulators using IoT technologies”, under the project number KK.01.2.1.02.0056.

References

[1] Bad Things Can Happen to Insulators, inmr.com, September 17, 2021. [online] https://www.inmr.com/bad-things-can-happen-toinsulators

[2] Guillermo del Campo, Igor Gomez, Silvia Calatrava, Rocio Martinez and Asuncion Santamaria CeDInt, Power Distribution Monitoring Using LoRa Coverage Analysis in Suburban Areas,Universidad Politecnica de Madrid

[3] Comparing Methodologies to Detect Damaged Composite Insulators, inmr.com, September 3, 2021. [online] https://www.inmr.com/comparing-methodologiesto-detect-damaged-composite-insulators/

[4] Othman, Nordiana & M. Piah, M. Afendi & Adzis, Zuraimy. (2017). Effect of broken skirts on voltage distribution along insulator strings. 17. 16.1-16.4.

[5] del Campo, Guillermo & Gómez, Igor & Calatrava, Silvia & Martinez, Rocio & Santamaría, Asunción. (2018). Power Distribution Monitoring Using LoRa: Coverage Analysis in Suburban Areas.

[6] X. Changfu, H. Chengbo, X. Jiayuan, L. Yunpeng, Z. Kaiyuan and P. Shaotong, "Influence of deteriorated porcelain insulator on electric field and potential distribution of insulators strings in 110kV transmission lines," 2017 IEEE International Conference on Smart Grid and Smart Cities (ICSGSC), 2017, pp. 162-166

[7] WL Vosloo, JP Holtzhausen, “The Design Principles of On-Line Insulator Test Stations to be used on Power Distribution and Transmission Networks” AFRICON96, Stellenbosch, South Africa, 1996.

[8] IEC 60305, “Insulators for overhead lines with a nominal voltage above 1000 V - Ceramic or glass insulator units for a.c. systems - Characteristics of insulator units of the cap and pin type”, 1995.

[9] A. Michaelides, C.P. Riley, A.P. Jay, G Molinari,P. Alotto, A. Zubiani, A. D’Souza, J. Madail Vaiga,“Parametric FEA for the Design of electric Insulating Components”, EU Project ADETEC,

[10] MedPower 2002, November 2002, Athens, Greece. N. Morales, E. Asenjo, and A. Valdenegro, "Field Solution in Polluted Insulators with non-symmetric Boundary Conditions," *IEEE Transactions on Dielectrics and Electrical Insulation*,, vol. 8, pp. 168-172, 2001.

Assessment of Electric and Magnetic Field Exposure Near Overhead Transmission Lines Using 2D Finite Elements Method

Bojan Glushica[1], Blagoja Markovski[2], Andrijana Kuhar[3], Vesna Arnautovski Toseva[4]
Ss. Cyril and Methodius University in Skopje,
Faculty of Electrical Engineering and Information Technologies, Skopje, Macedonia
[1]glushica@feit.ukim.edu.mk, [2]bmarkovski@feit.ukim.edu.mk, [3]kuhar@feit.ukim.edu.mk, [4]atvesna@feit.ukim.edu.mk

***Abstract* – The intensity of extremely low frequency electric and magnetic fields near transmission lines is of particular interest in studies related to environmental and equipment protection. The use of numerical tools can be considered as the most efficient method for their assessment. In this paper we numerically compute the electric and magnetic fields near different configurations of high voltage transmission lines using the open source software FEMM 4.2. Computed fields are then compared with reference levels related to human exposure to electromagnetic fields. The computed magnetic field is also used to estimate the induced currents within simplified models of human organs.**

1 Introduction

Overhead transmission lines (OTL) generate extremely low frequency (ELF) electric and magnetic fields that may interact with technical or biological systems and produce a possible harmful effects in case of excessive exposure [1], [2]. Therefore, the intensity and distribution of electric and magnetic fields near OTL are of particular interest in studies related to their possible adverse effects on the environment, human health, sensitive electronic equipment or critical infrastructures. To address the variety of problems, numerous standards and protocols have been introduced that define methods for assessment and protection from the effects of electromagnetic fields [3]-[5]. The use of electromagnetic simulation tools can be considered as the most efficient method, especially when dealing with large and complex systems where measuring procedures can be time consuming, expensive or impractical. Another advantage of the simulation tools is in the possibility of analyzing systems in the initial phase of their planning and construction, and the ability to test the effectiveness of different protection techniques.

In this paper we perform numerical analysis of the intensity and distribution of electric and magnetic fields in the vicinity of OTL using the open source software for analysing electromagnetic problems FEMM 4.2, which is based on the finite element method (FEM). The modelling procedure is briefly described and it is verified using full-wave electromagnetic model based on the method of moments (MoM). The analysis should provide general information for the expected field levels near 110 kV and 400 kV OTL, therefore different configurations of OTL and effectiveness of phase sequence transposition in double-circuit OTL are considered. Computed electric and magnetic field levels are compared with reference levels for human exposure to electromagnetic fields, established by the International Commission on Non Ionizing Radiation Protection (ICNIRP) [6]. The computed magnetic field is also used to estimate the induced currents within simplified models of human organs.

2 Procedures for modelling the electromagnetic problem in FEMM

Subject of analyses are 110 kV single-circuit, 110 kV double-circuit and 400 kV overhead transmission lines. Details for the placement of the phase conductors and ground wire (GW) are provided in Fig. 1 and Table 1. The cross-sectional area of each conductor of the 110 kV OTL is 104 mm^2 (11.5 mm diameter). For the 400 kV OTL, the cross-sectional area of the phase conductors is 2 x 245 mm^2 (17.66 mm diameter each) with mutual separation of 30 cm and for the ground wire it is 120 mm^2 (12.36 mm diameter). The shortest distance between the conductors and the ground level is represented by the parameter h_g. In our analysis we consider two values of h_g : 30 m and 15 m. The electromagnetic problems have been analyzed following a similar procedures as described in [7].

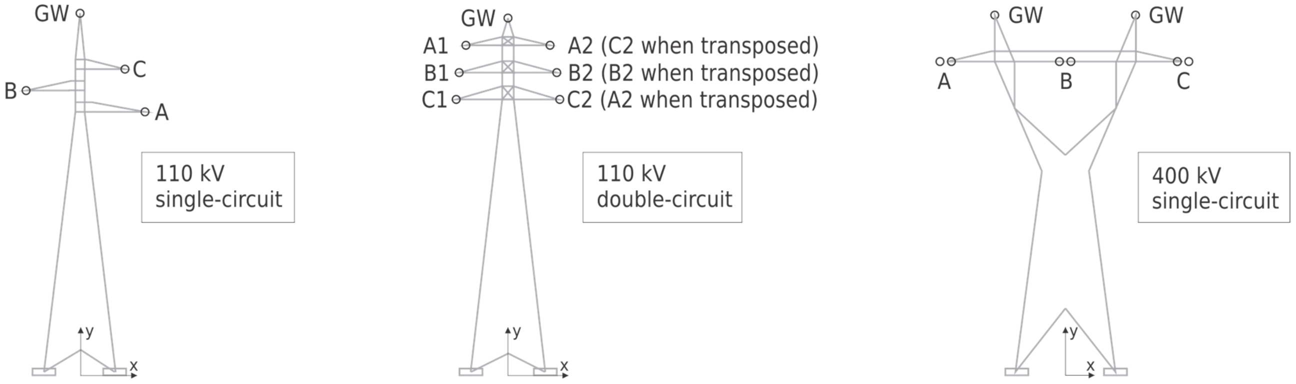

Fig. 1 Configuration of the analyzed 110 kV and 400 kV overhead transmission lines.

Table 1 Position of the phase conductors and ground wires for the 110 kV single-circuit, 110 kV double-circuit and 400 kV overhead transmission lines.

Conductor	110 kV single-circuit		110 kV double-circuit		400 kV single-circuit	
	x [m]	y [m]	x_1 / x_2 [m]	y [m]	x [m]	y [m]
Phase A	4.8	h_g	-3.2 / 3.2	h_g+6	-8.47	h_g
Phase B	-4.1	$h_g+2.4$	-3.5 / 3.5	h_g+3	0	h_g
Phase C	3.4	$h_g+4.8$	-3.8 / 3.8	h_g	8.47	h_g
GW	0	h_g+11	0	h_g+9	-5.07 / 5.07	$h_g+4.45$

Modelling of electromagnetic problems in open space using the FEMM 4.2 software requires to specify a solution domain with suitable shape and size for the analysed problem and appropriate boundary conditions at its borders. The solution domain, in which the electromagnetic problem is solved, should have a circular shape. To reduce the influence of the boundary, the radius of the domain is set to 300 m, which is 10 times larger than the size of the analysed system. The domain is divided into 2 sections. The bottom section is the ground with specific conductivity $\sigma = 0.01$ S/m. The top section is with characteristic of air. The x and y coordinates of the conductors in Table 1 are relative to the centre of the domain. Because the field computation is a time consuming process and because we focus on the fields above the ground in vicinity of the conductors, the discretization of the solution domain is done separately in sections as shown in Fig. 2. The ground has the lowest degree of discretization. The air is divided into 2 half circles with 150 m and 300 m radius, where the inner circle has the highest degree of discretization in order to obtain more accurate results. In total, the solution domain is discretized with about 340000 nodes or 685000 elements.

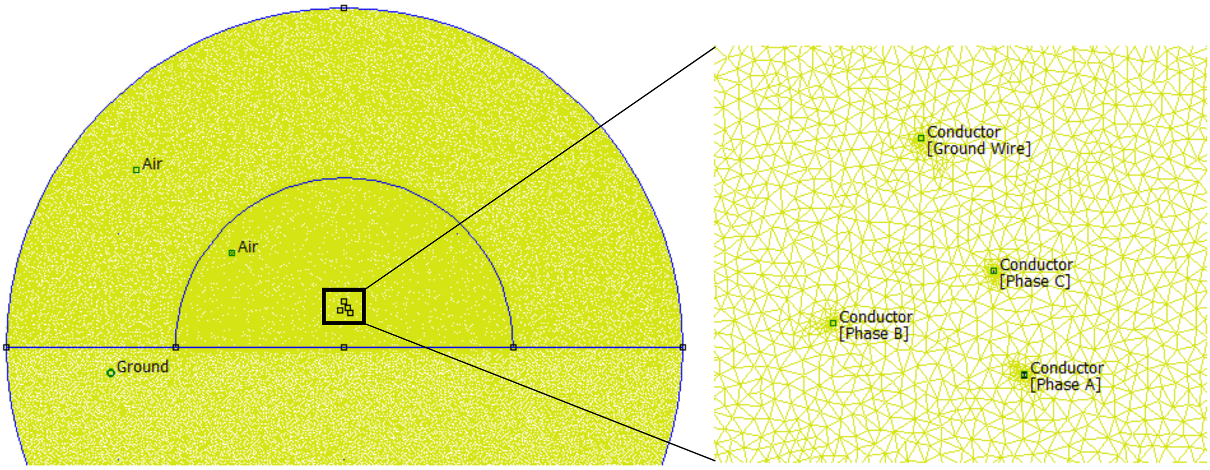

Fig. 2 Different degrees of discretization for the 110 kV single-circuit transmission line.

The FEMM 4.2 software provides instantaneous values of computed fields (electric or magnetic), while RMS values are required for further estimation of human exposure to electromagnetic fields [6]. To obtain the RMS values, we have computed multiple samples of the instantaneous field values over one period of 20 ms.

We have observed that 40 equally-spaced samples over one period can provide good estimate of the RMS values of the fields. To automate this process for all considered cases, we have used the Lua scripting language which is incorporated in the FEMM 4.2 software. The electric and magnetic field are computed in multiple points at height of 1 m above ground level, along a profile perpendicular to the center of the transmission line, as requested by the standards [3]. The above mentioned procedures are general for calculation of electric and magnetic fields. In the following sub-sections we describe some procedures that are specific for the computation of the electric field and for the computation of the magnetic field.

2.1 Procedures for obtaining the RMS values of electric field

Computation of the electric field and the electric scalar potential is performed using the “Current Flow” module of FEMM 4.2. For this module, fixed voltages are required. The boundary condition for potentials at the borders of the domain is set to 0 V. The same condition is applied for the ground wires. The phase conductors are set to instantaneous phase voltages that correspond to the appropriate time points within one period of 20 ms using a Lua script. For the double-circuit power line, two cases are observed: in the first case the phase conductors are untransposed and in the second case they are transposed. The relative dielectric permittivity of the whole domain is $\varepsilon_r = 1$.

2.2 Procedures for obtaining the RMS magnetic field

Computation of the magnetic field and magnetic vector potential is performed using the “Magnetics” module of FEMM 4.2. For this module a fixed current strength and magnetic vector potential are required. The boundary condition for the magnetic vector potentials at the borders of the domain is set to 0 Wb/m. The current strength in the ground wire is forced at 0 A. For the current strength in the phase conductors, the maximum load current of the TL is considered. Based on the previously mentioned surface area of each conductor, the maximum load current for each phase conductor is 800 A and 1920 A for the 110 kV and 400 kV towers, respectively. The instantaneous values for the current strength of each phase are set based on the time points using a Lua script. For the double-circuit power line, the untransposed and transposed cases are considered as well. The relative magnetic permeability of the whole domain is $\mu_r = 1$.

2.3 Verification of the presented procedures

Presented procedures have been implemented in FEMM for calculating the electric and magnetic field levels (latter expressed in terms of the magnetic vector potentials) near a 110 kV single-circuit OTL with h_g=15 m. To verify the obtained results, the same problem has also been simulated using full-wave electromagnetic model based on the method of moments [8]. The results provided in Fig. 3 show excellent agreement, with less than 3% differences in the calculated electric and magnetic field levels.

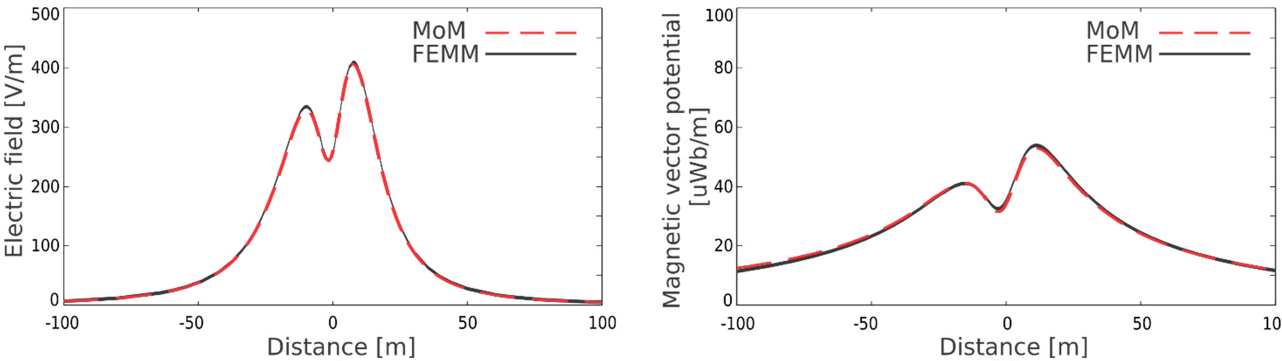

a) b)

Fig. 3 Verification of the calculated RMS values of electric field a) and magnetic vector potential b) for 110 kV single-circuit transmission line.

3 Estimation of the induced current density in human tissue

Exposure to time varying electric and magnetic fields can cause an induced electric field inside human tissue. The internal field induced by exposure to 50 Hz external electric field is several orders of magnitude lower than the inducing electric field. This is mainly due to the high charge density at the tissue-air contact area [9]. On the other hand, the induced field may have higher than average local values on sharp edges of any conducting object. Considering the human body and hair, this can cause minor annoyance to the affected persons. The redistribution of charge can also lead to uncomfortable periodic discharges (micro-electroshocks) at the body surface or to grounded objects. As a result of these factors, the calculation of the induced electric field is not of interest in this paper. The magnetic field however, is of a great significance for its effects on biological tissues. It has a uniform distribution inside the human body, mainly due to the extremely poor magnetic properties of the human body. The low frequency magnetic field in biological tissues induces currents that circulate along paths in a plane perpendicular to the direction of incidence of the field. This induced circulating electric field increases proportionally to the frequency and cross-sectional area. As a result, the intensity of induced electric fields increases from zero at the inner part of the body to the maximum at the body surface. The induced electromotive force in turn gives rise to a current density in a conductive medium such as the human tissue. The closed loops of this current create a negligible secondary induced magnetic field.

If we consider the average characteristics of human tissues, we can calculate the internally induced electric field using the Faraday's law of electromagnetic induction. For this purpose, the tissues will have a circular shape that is always perpendicular to the magnetic field. The induced current density will form a closed circular loop with radius R corresponding to the size of the tissue. The tissues of interest are heart, with estimated radius $R = 0.06$ m and conductivity $\sigma = 0.2$ S/m, and brain, with estimated radius $R = 0.1$ m and conductivity $\sigma = 0.1$ S/m. When considering the geometry of the TL models discussed in Section 2, the tissues of interest are placed at the center of the coordinate system elevated by 1 m above ground level. The endogenous current densities of the heart and brain are estimated at a minimal value of 10 mA/m^2 and 1 mA/m^2, respectively [10]. For a closed circular loop with radius R where the uniform magnetic field B is perpendicular to the surface area, the induced electric field E_i can be calculated as:

$$E_\mathrm{i} = \frac{R}{2} \cdot \frac{\partial B(t)}{\partial t} \tag{1}$$

where $\partial B / \partial t$ is the time derivative of the external magnetic field B. The time derivative is calculated numerically using the instantaneous values of B with the five-point method for the first derivative:

$$\frac{\partial B(t)}{\partial t} = \frac{-B(t+2h) + 8B(t+h) - 8B(t-h) + B(t-2h)}{12h} \tag{2}$$

where t is a time point and h is the time difference between each time point. Using Eq. (1) and Eq. (2) we estimate the maximum value of the induced field E_i. After that, we can calculate the maximum value of the induced current density J_i as provided in Eq. (3), where σ is the conductivity of the respective tissue:

$$J_\mathrm{i} = \sigma E_\mathrm{i} \, . \tag{3}$$

4 Results and discussion

In this section we provide the simulation results for electric and magnetic field for the different OTL configurations described in Table 1 and Fig. 1, and we compare the results with the reference levels for human exposure to electromagnetic fields provided by ICNIRP [6]. The reference levels for general public exposure to electric field at 50 Hz are set to 5 kV/m and for the magnetic field at the same frequency are set to 200 µT. For ground clearance of the transmission lines equal to $h_g = 30$ m, the results are represented by dashed lines, and for $h_g = 15$ m the results are represented by solid lines.

In Fig. 4 the results of the electric and magnetic fields for the single-circuit OTL are shown. It is observed that the maximum value of the electric field for the 400 kV OTL is 1.68 times lower than the reference levels and for the 110 kV OTL it is 12.2 times lower for the $h_g = 15$ m case. In comparison, the values are further lowered by a factor of 3.54 for the $h_g = 30$ m case. We can conclude that the maximum values of electric field appear close to the origin at $x = 0$ m, that is directly below the central axis of the OTL. The 400 kV tower is an exception to this where at $x = 0$ a sharp drop of the RMS electric field is observed mostly due to the annulment of the fields of each phase in one period. However, the range between 10 m and 20 m distance on the x-axis is of concern where the highest values of the electric field appear. Considering the geometry of the system described in Table 1, this is close to the shortest distance between the ground level and nearest phase conductor. In reality the height of the conductors may be lower along the power line. If we consider a lower value for h_g which is not constant along the length of the OTL, the 400 kV OTL can represent a potential risk to human health.

The maximum value of the magnetic field for the 400 kV OTL is 9.4 times lower and for the 110 kV OTL it is 68 times lower than the reference levels for the $h_g = 15$ m case. For the $h_g = 30$ m case, there is a further decrease by a factor of 3.6. Although the magnetic field for the single-circuit OTL is many times lower than the reference levels, these values will be considered for further estimation of the maximum induced currents in human tissues.

In Fig. 5 the results of the electric and magnetic fields for the double-circuit towers are provided. The maximum values for both the electric and magnetic fields appear when the phases are untransposed. It is observed that the maximum value of the electric field for the untransposed case is 7.5 times lower, and for the transposed case is 21.2 times lower than the reference levels for $h_g = 15$ m. The maximum value of the magnetic field for the untransposed case is 40 times lower, and for the transposed case is 72.9 times lower than the reference levels for $h_g = 15$ m. For $h_g = 30$ m, more than 3 times lower values are observed.

When comparing the magnetic fields from Fig. 4 and Fig. 5 for 110 kV OTL, a noticeable difference can be seen that impacts the estimation of the induced currents. Table 2 shows the estimated maximum values of the induced current densities in human tissue as described in Section 3. For this calculation, only the $h_g = 15$ m case was considered. The results show that the induced currents by the magnetic fields from the analyzed OTL's should not have any impact on the heart and brain, as the values are more than 188 times lower than the heart's endogenous currents and more than 22.5 times lower than the brain's endogenous currents. It should be noted that the estimated maximum values were obtained by using the highest value of the time derivative of the magnetic field $^{\partial B}/_{\partial t}$ in one full period. When multiple phase conductors are considered, the changes in the values of the magnetic field in one period are less drastic, which in turn will reduce the magnitude of the induced currents.

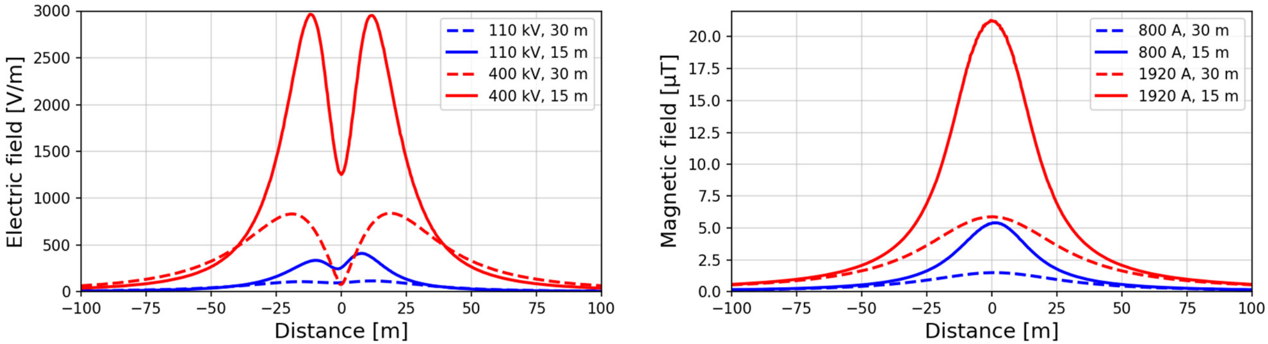

a) b)

Fig. 4 RMS electric field a) and RMS magnetic field b) for single-circuit towers.

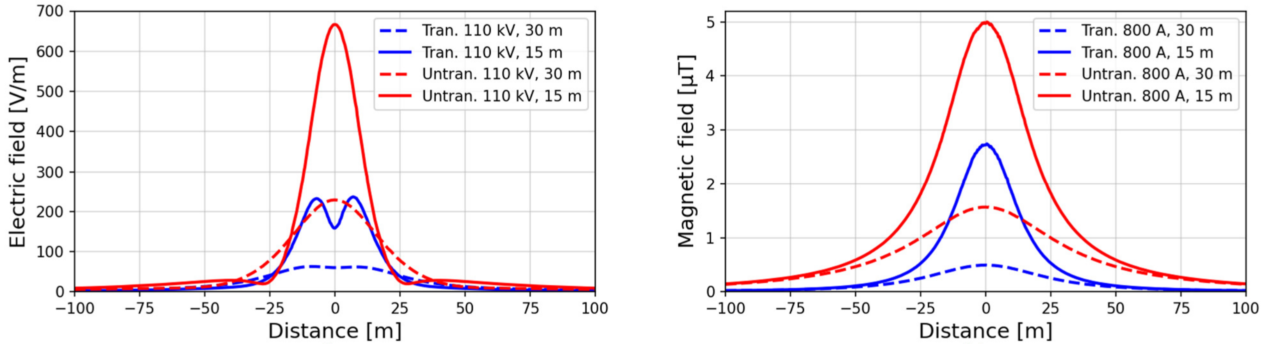

a) b)

Fig. 5 RMS electric field a) and RMS magnetic field b) for double-circuit towers.

Table 2 Estimated maximum values for the induced current densities in tissues [$\mu A/m^2$].

Tissue type	110 kV single-circuit	110 kV double circuit		400 kV single-circuit
		Untransposed	Transposed	
Heart	13.641	13.246	7.179	52.99
Brain	11.367	11.038	5.9825	44.158

5 Conclusion

In this paper we have numerically computed the RMS values of ELF electric and magnetic fields near 110 kV and 400 kV overhead transmission lines. Simulations were performed using the open source software FEMM 4.2, using an automated procedure that has been briefly described and verified. The electric and magnetic field levels for different OTL configurations were compared with the reference levels for human exposure to electromagnetic fields established by the ICNIRP, and possible exceeding of these levels in particular situations have been identified. Furthermore, using the obtained values for the magnetic field, we have calculated the maximum estimated values for the induced current densities in simplified models of human organs. By comparing the estimated values of estimated induced currents and the endogenous currents, we have concluded that the magnetic field would have a negligible effect on said organs.

Acknowledgements

This work was supported by the Ss. Cyril and Methodius University in Skopje, Project NIP.UKIM.20-21.10.

References

[1] A.W. Wood, K. Karipidis (Eds.), Non-Ionizing Radiation Protection - Summary of Research and Policy Options. Part V: Extremely Low-Frequency (ELF) Electric and Magnetic Fields, John Wiley & Sons, Hoboken, pp. 257-338, (2017).

[2] IEC TR 61000-5-1, Electromagnetic compatibility (EMC) - Part 5-1: Installation and mitigation guidelines - General considerations, (1996).

[3] IEC 62110, Electric and magnetic field levels generated by AC power systems - Measurement procedures with regard to public exposure, (2009).

[4] EN 50443, Effects of electromagnetic interference on pipelines caused by high voltage a.c. electric traction systems and/or high voltage a.c. power supply systems, (2011)

[5] Directives concerning the protection of telecommunication lines against harmful effects from electric power and electrified railway systems. CCITT Directives, Vol. II, Geneva, (1989).

[6] International Commission on Non Ionizing Radiation Protection (ICNIRP), (2010), “Guidelines for Limiting Exposure to Time-Varying Electric and Magnetic Fields (1 Hz - 100 kHz)”, *Health Physics*, Vol. 99, No. 6, pp. 818-836.

[7] E. Lunca, S. Vornicu, A. Salceanu, O. Bejenaru, (2018), “2D Finite Element Model for computing the electric field strength-rms generated by overhead power lines”, *Journal of Physics:Conference Series*, Vol. 1065, No. 5, pp. 1-4.

[8] B. Markovski, L. Grcev, V. Arnautovski-Toseva, (2021), “Fast and Accurate Transient Analysis of Large Grounding Systems in Multilayer Soil”, *IEEE Transactions on Power Delivery*, Vol. 36, No. 2, pp. 598-606.

[9] National Research Council, Possible Health Effects of Exposure to Residential Electric and Magnetic Fields, The National Academies Press, Washington, DC, pp. 46-48, (1997).

[10] P. Gajsek, A. Kuhar, V. Rakovic, C. Tomaz and B. Valic, The impact of radiation from telecommunication devices and technologies on human health and the environment which surrounds us (4G, 5G, etc.), Agency for Electronic Communications, Skopje, Institute of Non-Ionizing Radiation (INIS), Ljubljana, pp. 21-22, (2021).

Characteristics of the dynamic battery model for different loads

Venco Ćorluka[1], Željko Hederić[2], Miralem Hadžiselimović [3]
[1] Faculty of Electrical Engineering, Computer Science and Information Technology
Osijek, Croatia, venco.corluka@ferit.hr

[2] Faculty of Electrical Engineering, Computer Science and Information Technology
Osijek, Croatia, zeljko.hederic@ferit.hr

[3] University of Maribor, Faculty of Energy Technology Krško, Slovenia,
miralem.h@uni-mb.si

***Abstract* – A good analysis of the dynamic parameters of the battery requires a correct model in order to obtain the characteristics of the simulation test on the basis of which to assess the correctness and life of the battery. Key factors such as charging, discharging and capacity depend on battery modeling. The paper will present different types of batteries and determine the parameters for various loads in the Matlab / Simulink software package based on the model.**

1 Introduction

A battery is an electrochemical device that converts chemical energy into direct current electricity and serves to store electricity. When we talk about batteries, we are talking about one cell or more connected cells that are connected in series or in parallel. The main challenges of the electric vehicle industry are in the development of batteries for the accumulation of electricity (as much capacity as possible, longer service life and less mass of rechargeable batteries). Electric vehicles currently have a shorter range than traditional vehicles, but this problem is being solved by intensive research and development. Starting batteries have a larger number of thinner plates. This is especially useful in engine start-up situations. In order to accurately determine the state of charge of the battery (SOC) in all operating conditions, it is important to set up a good mathematical model that describes the behavior of the battery [4].

The most important characteristics of the battery are: V_{bat} - Battery output voltage [V], OCV - Battery open circuit voltage [V], Z_{eq} - Internal battery impedance [Ω], I_{bat} - Battery current [A], ΔE (T) - Temperature correction of potential [V], SOC - State of charge of the battery, SOC_{init} - Initial battery capacity status, C_{usable} - Battery capacity [Ah], C_{init} - Initial battery capacity [Ah], T - Temperature [oC-oK], t - Storage time (self-discharge) [months], Q_n - Battery negative electrode charge state change, N - Number of cycles, CCF - Capacity correction factor.V_{bat} [V] is the DC voltage measured by a voltmeter on the battery terminals, and is important information for working with batteries [3].

Battery capacity is the battery charge and is expressed in [Ah]. Battery discharge rate is the speed at which the battery discharges under certain conditions. A battery is considered empty when the battery voltage falls below a voltage called the cut-off voltage. Energy density is a term that tells us how much electricity we can store in a battery relative to its mass Charging time is an important feature that tells you how long the battery takes to charge to maximum capacity. Potential difference between anode and cathode battery – OCV. The main types of batteries used for electric cars are: lithium-ion (LI-Ion), nickel-metal hydride (NiMH), zebra (Na-NiCl2), lithium-sulfur (Li-S) battery [5].

2 Battery model

The most commonly used battery equivalent circuit model (Figure 1) consists of the open connector voltage U_0 and two parallel combinations of resistors and capacitors R_1C_1 and R_2C_2 representing the effects between capacitor layers. The internal resistance R_0 can be calculated based on the instantaneous change in battery voltage before and after the load. Determining the parameters R_1C_1 and R_2C_2 is a complex procedure due to the two time constants included in the model [2,10].

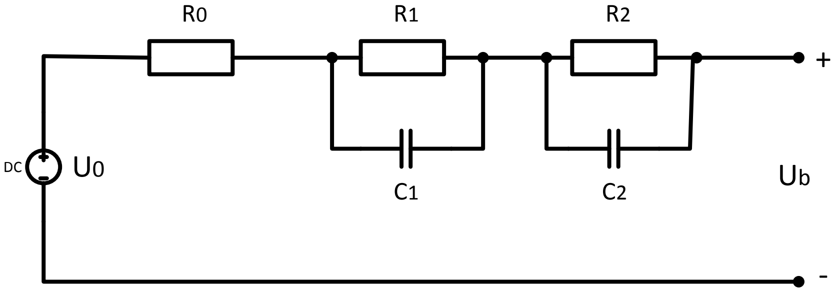

Fig. 1 Equivalent circuit of a battery

From the picture of the equivalent circuit it follows:

$$U_0 - U_{R0} - U_{RC1} - U_{RC2} - U_b = 0 \tag{1}$$

The internal resistance of the battery is calculated according to the expression

$$R_0 = \frac{U_0}{i} \tag{2}$$

The following equation applies during charging:

$$C_1 \frac{\mathrm{d}U_1}{\mathrm{d}t} + \frac{U_1}{R_1} = 0 \tag{3}$$

And during discharge:

$$C_2 \frac{\mathrm{d}U_2}{\mathrm{d}t} + \frac{U_2}{R_2} = 0 \tag{4}$$

3 Lithium-ion battery

Li-Ion batteries have almost completely replaced all battery technologies used in the automotive industry thanks to their high energy density and favorable mass-to-energy ratio. Li-Ion batteries have provided the same amount of energy with smaller dimensions and less weight compared to other types of batteries, and maintain an acceptable price for use in the automotive industry. The main characteristics of Li-Ion batteries are high voltage, high energy density, low self-discharge factor and reliability.
The high voltage makes them acceptable for use in almost all devices where the goal is to reduce the volume of the device. One Li-Ion battery can replace two or more conventional batteries. The weak self-discharge factor of the battery allows them to preserve their capacity for a long time without significant losses. Advanced Li-Ion batteries in ideal conditions can retain up to 90% capacity during long-term storage [2].

4 Nickel-metal-hydride battery

Nickel-meta-hydrogen batteries are used in devices that require a large amount of energy and are often used, such as digital cameras, GPS devices, MP3 players, electric scooters and bicycles. Ni-HM batteries play the role of a replacement power source in devices that work at high temperatures due to their exceptional heat resistance. Ni-HM batteries have five essential characteristics: charging, discharging, service life, storage life and safety.
Battery charging characteristics are affected by time, temperature and current. The battery voltage rises when the charging current increases or when the battery temperature drops. Batteries should be charged at

temperatures from 0°C to 40°C using constant current. The ideal temperature would be between 10°C to 30°C degrees. Constant charging at high or low temperatures, and constant overcharging negatively affects battery performance.

Battery discharge characteristics depend on current, temperature, battery discharge voltage, which is 1.2V. The charging voltage drops as the current increases and the temperature decreases. Continuous charging and discharging of these batteries below the recommended voltage (1.2V per cell) causes a permanent loss of capacity [6].

5 Nickel-cadmium battery

Nickel-cadmium batteries have a variety of applications; we use less batteries in portable electronics such as LED lighting, toys and cameras, but we find them mostly in cordless phones and security lamps. Due to the relatively low internal resistance of these batteries, we often use them in devices that require a high current supply. This makes them a good choice for powering electric models [7].

Nickel-cadmium batteries are similar in construction to nickel-metal-hydride batteries, and are composed of a positive electrode made of nickel hydroxide, which is its main active material, a cadmium negative electrode, a separator located between the positive and negative electrodes and is responsible for for their separation. The separator is made of non-woven fabric and together with the electrodes is spirally wrapped in the battery case. Due to their similar construction, Ni-Cd batteries and Ni-Mh batteries have the same five main characteristics: charging, discharging, lifetime, storage life and safety.

6 Lead-Acid battery

A storage battery is composed of individual cells connected in series, where each cell contains layers of lead alloys immersed in an electrolyte solution, which is usually made of 35% sulfuric acid (H2SO4) and 65% water. Pure lead is too soft and would not be able to maintain its texture alone, so small amounts of other metals are added to the lead alloy in order to obtain mechanical strength and improve electrical properties. Compared to other types of rechargeable batteries, rechargeable batteries have the lowest density. energy, and therefore have a significantly shorter lifespan in case of deep cycling or frequent discharge compared to, for example, nickel (Ni) or lithium (Li) batteries [1,9].

There are many variations of lead acid batteries. Each designed for its own particular application with specific discharge and charge characteristics. These battery types are specifically designed for a given intended end application. It is important to choose the right lead battery that will meet all our needs. Failure to do so can result in reduced performance and in some cases irreversible damage to the battery, resulting in a drastic reduction in its overall lifespan. Generally speaking, lead batteries are divided into two main categories:

- Flooding (or wet) cells
- Closed lead acids without maintenance (SLA)
- AGM sealed accumulator batteries
- Deep cycle rechargeable batteries
- Accumulator batteries for starting the motor
- Fan regulated battery

7 Simulation results for ohmic-inductive load

The simulation was performed using the MATLAB / simulink program. The first test shows the characteristics of batteries for one hour. The battery was discharged for the first half hour and the battery was charged for the second half hour. Figure 1 shows the block diagram used during the simulation. The characteristics of 4 batteries were measured: lead-acid, Liti-ion, Ni-Cd and Ni-MH. The block diagram shows the model of the controller that serves to provide the battery with the desired power, the RL connection shown in the diagram as a series connection of resistance and inductance.

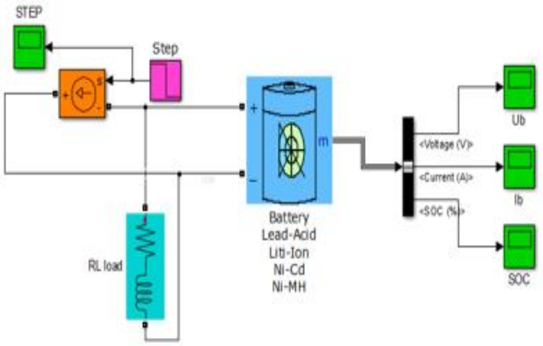

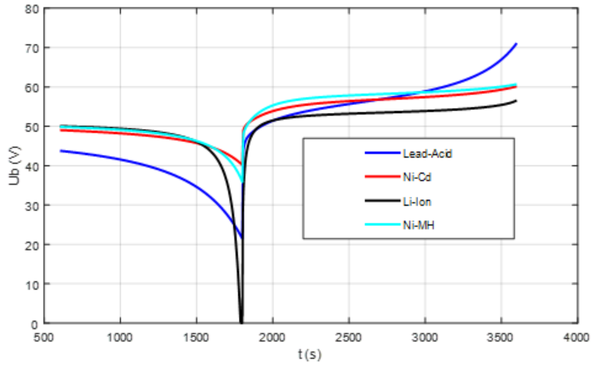

Fig. 2 Block diagram when testing batteries loaded with RL load

Fig. 3 Battery voltage Ub as a function of time

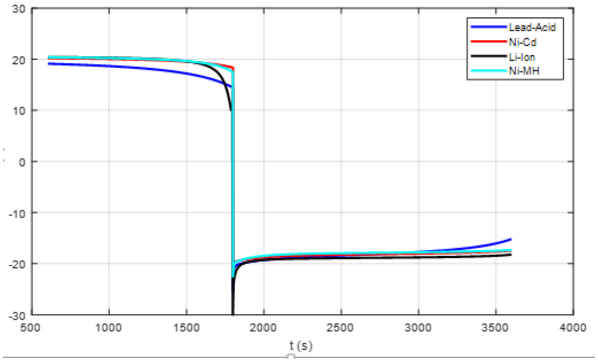

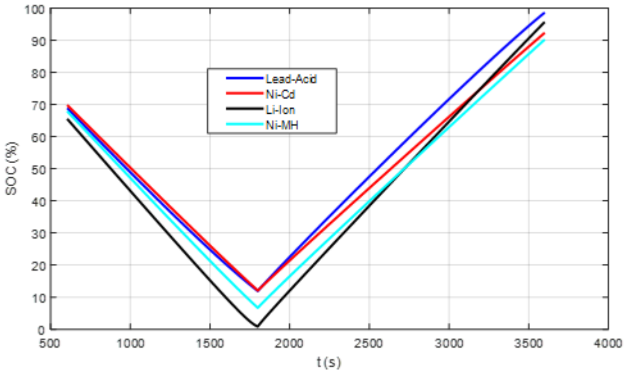

Fig. 4 Battery current Ib as a function of time

Fig. 5 SOC battery charge status

Figure 3 shows the battery voltage status during discharge and charging. The first 1800 seconds (30 minutes) the battery was discharged and the other 1800 seconds was charged. In Figure 3, the discharge current of the Ni-Cd and Ni-MH batteries remains constant, and the Li-ion battery current starts to drop earlier. Lead-acid batteries have a higher current drop during discharge. Figure 5 shows the battery charge characteristics over time. During discharge, the battery charge decreases linearly with the change of time. When discharging, Lead-acid and Ni-Cd batteries are discharged at the same speed, and their charge dropped to 15% in half an hour of discharging. The charge of the Ni-MH battery dropped to 8%, and the Li-ion battery was completely discharged, which can also be seen from the diagram.

8 Simulation results when charging the battery with a DC motor

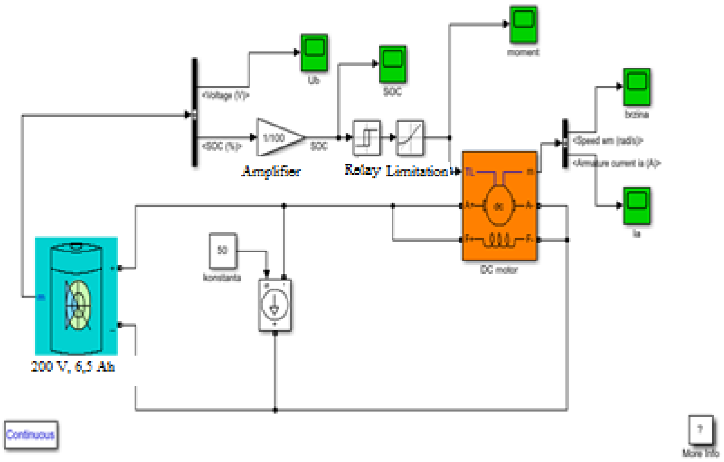

Fig. 6 Battery load with DC motor

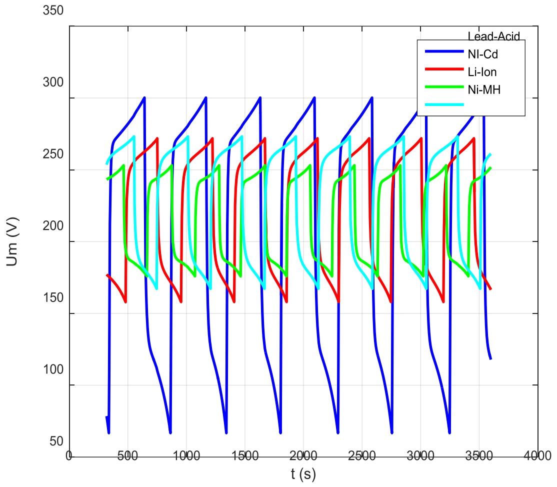

Fig. 7 Battery voltages

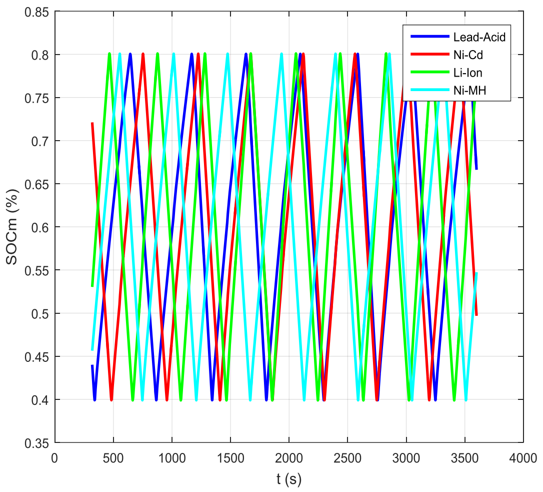

Fig. 8 Battery charge status (SOC)

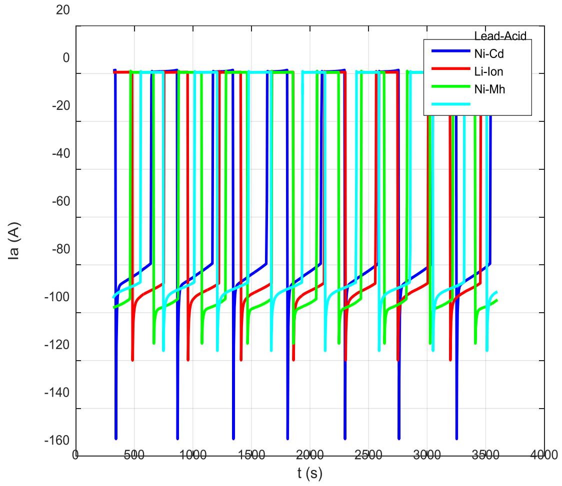

Fig. 9 Armature currents for 4 types of batteries

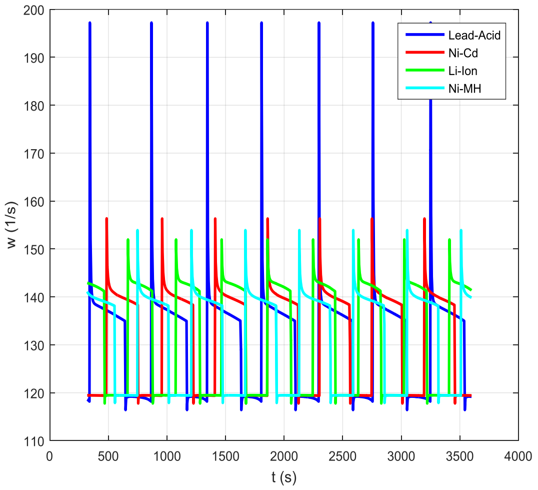

Fig. 10 Number of revolutions of the DC motor for 4 types of batteries

Figure 6 shows a block diagram for testing DC motor batteries. The diagram consists of a battery connected to a DC motor. We control the torque using a relay and limiter connection. Speed regulation was not used in the DC motor testing. During the battery test for the DC motor, the voltages, currents and charge of the batteries were measured, as well as the change in the number of revolutions during the operation of the motor.
From the pictures of battery currents and voltages, it can be seen that the values of Lead-acid batteries vary the most, which makes them less suitable compared to other types. Ni-Cd and Ni-MH have similar characteristics, while the values of Li-ion batteries vary the least, and this makes them a better choice than other batteries. During the experiment, the batteries were discharged to 40% capacity and then charged to 80% capacity. During the experiment of 1 hour, the Lead-acid battery takes the most time to discharge and charge, and the Li-ion the least. The Li-ion battery has the best characteristics because it can be charged in less time than other types of batteries. The test shows that the engine can be operated longer with a Li-ion battery than with a Lead-acid battery in a given time.
A DC motor when operating with a Lead-acid battery has the largest speed jumps at maximum capacity, and its speed decreases as the battery discharges. Li-ion has the least jumps, which makes it the best choice. Also, the speed of the motor during operation with the DC motor remains constant until the battery is completely discharged.

9 Conclusion

The simulation of electric vehicle batteries is done in order to get a representation of the characteristics and expected values without creating a model of the vehicle. Various batteries that can be used in electric vehicles, and their advantages and disadvantages, were observed. Battery simulations were performed in the MATLAB/simulink program, which graphically displayed all the important characteristics of batteries under different conditions. From the performed simulations, it can be concluded that the Li-ion battery is the most suitable for use in electric vehicles due to its charging speed, large number of work cycles and high specific power and, ultimately, reliability. Ni-Cd and Ni-HM batteries are also good choices for electric car operation, but the characteristics of these two batteries are not as suitable as those of Li-ion batteries. Lead-acid batteries have the most unfavorable characteristic, which is why they are not used in the commercial production of electric cars. The values of the MATLAB simulation would not be the same as in the real operation of the electric vehicle due to the fact that during the simulation things such as the ambient temperature and the load change during the test were ignored.

Acknowledgements

This research is supported by the European Union from the European Regional Development Fund within the Operational Program Competitiveness and Cohesion 2014-2020 under the project: “Development of zero-emission passenger sailing ship”, under the project number KK.01.2.1.02.0127.

References

[1] Z. L. Yang, G. Q. Zhang, Z. L. Wang, “The modeling method ofhigh capacity lead-acid storage battery”, *Marine Elect. Electron.*, vol. 32, pp. 35-37, Jun. 2012.
[2] Gomadam, Parthasarathy M., Weidner, John W., and Dougal, Roger A., White, Ralph E., Mathematical Modeling of Lithium-ion and Nickel Battery Systems, Journal of Power Sources 110 (2002) 267-284.
[3] Liaw, Bor Yann, Nagasubramanian, Ganesan, Jungst, Rudolph G., Doughty, Daniel H., Modeling of Lithium Ion Cells-A Simple Equivalent-Circuit Model Approach, Solid State Ionics 175 (2004) 835-839.
[4] Kroeze, Ryan C., Krein, Philip T., Electrical Battery Model for Use in Dynamic Electric Vehicle Simulations, Power Electronics Specialists Conference, 2008, IEEE.
[5] Knauff, Michael, Niebur, Dagmar and Nwankpa, Chika, A Platform for the Testing and Validation of Dynamic Battery Models, Electric Ship Technologies Symposium, 2009, IEEE.
[6] Chen, Min and Rincon-Mora, Gabriel A., Accurate Electrical Battery Model Capable of Predicting Runtime and *I-V* Performance, IEEE Transactions on Energy Conversion, Vol. 21, No. 2, June 2006, 504-511.
[7] Schweighofer, Bernhard, Raab, Klaus M., and Brasseur, Georg, Modeling of High Power Automotive Batteries by the Use of an Automated Test System, IEEE Transactions on Instrumentation and Measurement, Vol. 52, No. 4, 2003.
[8] Hu, Y., Yurkovich, S., Guezennec, Y., Yurkovich, B. J., A Technique for Dynamic Battery Model Identification in Automotive Applications Using Linear Parameter Varying Structures, Control Engineering Practice 17 (2009)
[9] Z. L. Yang, G. Q. Zhang, Z. L. Wang, “The modeling method of high capacity lead-acid storage battery”, *Marine Elect. Electron.*, vol. 32, Jun, 2012
[10] G. L. Wu, Z. Y. Zhou, D. R. Yu, “Unsteady open circuit voltage method for state of charge estimation of electric vehicle batteries”, *Elect. Mach. Cont.*, vol. 17, pp. 110-115, Apr. 2013.

The Identification of the Parameters of a Laboratory Electrohydraulic Complex in the Development of Nonlinear Processes in the Hydraulic Network

Mykhaylo Zagirnyak[1], **Viktoriya Kovalchuk**[2], **Tetyana Korenkova**[3]
Kremenchuk Mykhailo Ostrohradskyi National University, ul. Pershotravneva, 20, 39600 Kremenchuk, Ukraine,
[1]e-mail: mzagirn@gmail.com, [2]e-mail: viktoriya_kovalch@ukr.net, [3]e-mail: tanya74kor@gmail.com

Abstract ***– The possibility of applying the energy method to the problems of identifying the parameters of the laboratory electrohydraulic complex is considered. An equivalent electric circuit of the electrohydraulic complex is developed based on the principles of the electrohydraulic analogy. The experimental curves of hydraulic power changes during the development of cavitation phenomena in the pipeline network are obtained. A harmonic analysis of power curves was performed and it confirmed the possibility of their representation by trigonometric series in the development of unsteady processes. The systems of identification equations at different degrees of development of cavitation oscillations in the hydraulic network are obtained. Their solution by the matrix method allowed calculating unknown parameters. It is found that the total resistance of pumping and pipeline equipment is more affected by cavitation oscillations.***

1 Introduction

In the practice of operation of electrohydraulic complexes (EHC) it is often necessary to adjust their parameters by turning on/off pumping units (PU) or individual sections of the pipeline, closing/opening of shut-off valves with time-varying nature of water consumption [1, 2]. This is accompanied by the propagation of periodic waves of fluid, which causes changes in the main technological (head, discharge) and energy (hydraulic power) parameters of the EHC over time, deviation of the parameters of electrohydraulic equipment from the published values and reducing pump efficiency. The approximation of the parameters of pumping and pipeline equipment to the threshold values can lead to cavitation failure of the PU, clogging or rupture of the pipeline, the development of a surge, etc. [3].

In the tasks of working out the current water consumption and stabilization of the necessary technological parameter PU variable-frequency electric drive (VFED) systems are often used, which allows to save both electricity and work product [4]. It should be noted, that the question of determining the actual parameters and characteristics of the VFED taking into account the nonlinear properties and asymmetry of the stator windings of the asynchronous motor, was considered in many papers [5, 6]. However, they do not take into account the influence of technological load and operation modes of production mechanisms. Therefore, the identification of the EHC current parameters is topical task in the construction of VFED control systems for pumping equipment of various purposes.

Analysis [7, 8] revealed that the existing methods for determining the current parameters (head, discharge, efficiency, active power, hydraulic resistance of the pump and pipeline) are based either on the direct measurement of electrical and technological parameters, or the use of indirect (calculation) methods. This is due to a number of shortcomings: low accuracy of measurements caused by the use of empirical dependences; determining the parameters of only individual elements of the EHC; the impossibility of identification directly during PU operation. In such conditions, the use of the energy method [9], which is based on the equations of power balance between the source and the elements of the power channel of the technological complex, deserves consideration.

2 The method and results of the research

Fig. 1 contains the appearance of EHC physical laboratory facility, which including two pump unit (PU1, PU2) with two induction motor (IM1, IM2), two tanks (T1, T2), pressure sensors (PS1, PS2, PS3) and discharge sensor (DS). Laboratory stand conditionally divided into two sections: I – a pump with the adjacent section of the hydraulic network; II – the second section of the hydro network with the consumer at the end. The description of the electromechanical equipment and the functional possibilities of the stand are given in more detail in [10].

When identifying the parameters of the hydraulic system, it is advisable to represent the EHC by equivalent electric circuits based on the method of electrohydraulic analogy (MEHA), according to which the basic electrical equations are transformed into the appropriate hydraulic ratios [11]. In this case, it is possible to take into account the different configuration of the pipeline network, PU connecting circuits (serial or parallel), the development of nonlinear processes in the hydraulic network [12].

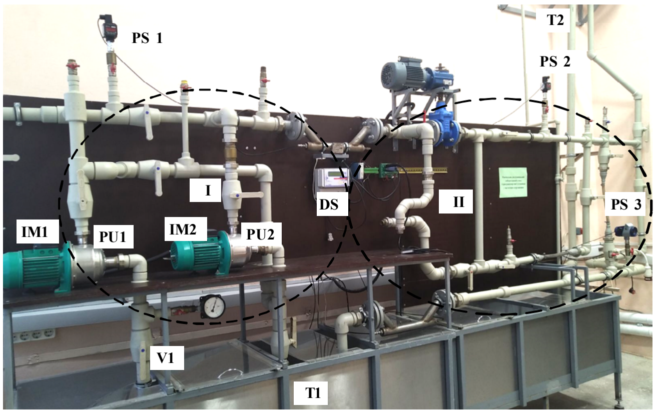

Fig. 1.

The equivalent electric circuit of the laboratory EHC (Fig. 2) contains: $H_0 \nu^2(t)$ – the hydraulic energy supply; H_0 – the head generated by the pump at zero discharge; $\nu(t)$ – relative rotation frequency; R_p , R_{con} – the hydraulic resistance of PU and the consumer, respectively; $Q_p(t)$ – pump output; $Q'_j(t)$ – discharge loss at the *j*-th section of the pipeline; $R_{net\,j}$, $L_{net\,j}$, $C_{net\,j}$ – hydraulic resistance, inductive reactance and capacitive reactance at the *j*-th section of the pipeline, respectively; H_{net1}, H_{net2} – the head at the first and second sections of the pipeline network, respectively.

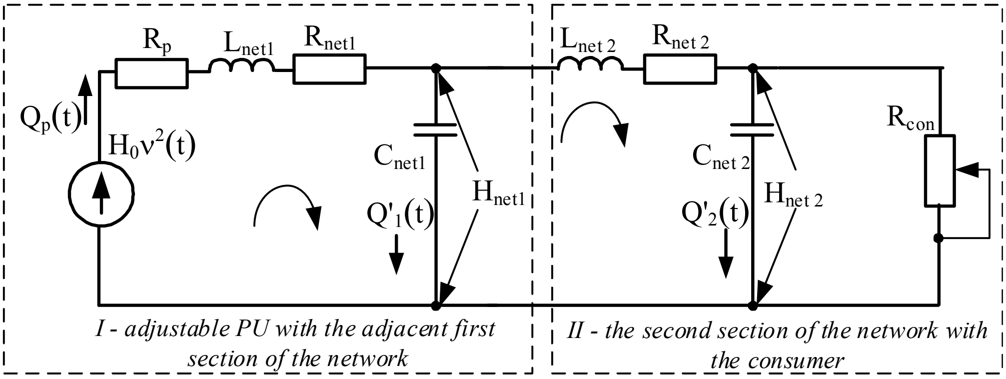

Fig. 2.

It is proved that in order to minimize dynamic loads in the hydraulic system, to compensate for the influence of non-stationary processes in the EHC, it is advisable using pumps and valves VFED [13]. The influence of nonlinear cavitation processes on the change of the parameters of EHC physical stand was analyzed with the maintenance of constant value of hydraulic power (pressure according to indications of the PS3 sensor) at the consumer by means of the variable-frequency electric drive (VFED). The development of cavitation processes in the pipeline network is caused by the growth of the vacuum zone at the input of the PU impeller, implemented by shutting stopcock S1 on the suction pipe [10]. To ensure a constant value of the head at the consumer, frequency f_{fc} of the supply voltage is regulated by means of PU VFED at the output of the frequency converter.

The development of cavitation phenomena in the pipeline network results in periodic non-sinusoidal changes in the discharge rate at PU output, which can be represented by a trigonometric Fourier series:

$$Q_p(t) = Q_{p0} + \sum_{n=1}^{N} Q_{pn} \cos(n \Omega_{kav} t) \tag{1}$$

where Q_{p0}, Q_{pn} – the amplitude values of the constant and cosine *n*-th harmonics of the discharge signal, respectively.

For the given EHC equivalent circuit the equation of energy balance is of the form:

$$p_s(t) = \Delta p_{Rp}(t) + \Delta p_{Rnet1}(t) + \Delta p_{Lnet1}(t) + \Delta p_{Cnet1}(t) + \Delta p_{Rnet2}(t) + \Delta p_{Lnet2}(t) + \Delta p_{Cnet2}(t) + p_{con}(t) \tag{2}$$

where $p_s(t)=H_0 \nu^2(t) Q_p(t)$, $p_{con}(t)=R_{con} Q_{con}^3(t)$ – the power of the hydraulic power supply and the consumer, respectively; $\Delta p_{Rp}(t)=R_p\, Q_p^3(t)$ – power loss at the pump resistance; $\Delta p_{Rnet\,j}(t)=R_{net\,j} Q_j^3(t)$, $\Delta p_{Lnet\,j}(t)=L_{net\,j} Q_j(t) \frac{d}{dt}\left(Q_j(t)\right)$, $\Delta p_{C\,net\,j}(t)=\frac{\rho g Q_j(t)}{C_{net\,j}} \int_0^T Q_j(t) dt$ – power loss at the resistance, inductive reactance and capacitive reactance of the *j*-th section of the pipeline network, respectively.

The active development of the theory of energy processes analysis led to using the instantaneous power method in electromechanical systems [14], [15], which is quite successfully used in reactive power compensation systems, reducing the higher harmonics of the current consumed by the converting equipment from the network; in the synthesis of systems for diagnosing the current state of electromechanical equipment, identifying the parameters of electric motors, etc. [16]–[18].

The use of the mathematical apparatus of Fourier series allows giving the signals of hydraulic power on the elements of EHC power channel as the sum of constant and variable (cosine and sine) components [19].

So, the hydraulic power at the output of the hydraulic power supply (pump):

$$\begin{aligned} p_s(t) &= \rho g H_0 \nu^2 Q_p(t) = \rho g H_0 \nu^2 \left(Q_0 + \sum_{l=1}^{L} Q_{la}\, cos(\Omega_l t) + \sum_{l=1}^{L} Q_{lb}\, sin(\Omega_l t) \right) = \\ &= \sum_{r=1}^{R} P_{rs0} + \sum_{r=1}^{R} P_{rsa}\, cos(\Omega_r t) + \sum_{r=1}^{R} P_{rsb}\, sin(\Omega_r t) \end{aligned} \tag{3}$$

where r, R – the number and quantity of harmonics of the hydraulic power signal, respectively; $P_{rs\,0}, P_{rsa}, P_{rsb}$ – the amplitude values of the constant and orthogonal cosine and sine components of the hydraulic power signal, respectively; Ω_r – the angular frequency of the pump hydraulic power signal.

The signals of hydraulic power on EHC elements, included in the general equation of energy balance, are presented similarly (2). This representation of hydraulic power signals allowed making a system of identification equations based on the energy balance equations for each component of hydraulic power between the hydraulic power supply and EHC elements [10], [11]:

$$\left. \begin{array}{l} P_{s0} = P_{st0} + P_{R\Sigma 0} + P_{Lnet\,j0} + P_{Cnet\,j0} + P_{Rcon0}; \\ P_{s1a} = P_{st1a} + P_{R\Sigma 1a} + P_{Lnet\,j1a} + P_{Cnet\,j1a} + P_{Rcon1a}; \\ P_{s1b} = P_{st1b} + P_{R\Sigma 1b} + P_{Lnet\,j1b} + P_{Cnet\,j1b} + P_{Rcon1b}; \\ \cdots\cdots\cdots\cdots\cdots\cdots\cdots\cdots\cdots\cdots\cdots\cdots \\ P_{ska} = P_{stka} + P_{R\Sigma ka} + P_{Lnet\,jka} + P_{Cnet\,jka} + P_{Rcon\,ka}; \\ P_{skb} = P_{st\,kb} + P_{R\Sigma\,kb} + P_{Lnet\,j\,kb} + P_{Cnet\,jkb} + P_{Rcon\,kb} \end{array} \right\} \tag{4}$$

where the constant power components correspond to the components with the index "0"; with indices "a", "b" – cosine and sine components, respectively; k – power signal harmonic number; P_{st} – the amplitude value of the loss of hydraulic power to overcome the back pressure in the network; $P_{R\Sigma}$ – the amplitude value of hydraulic power losses at the total hydraulic resistance $R_\Sigma = R_p + \sum_{j=1}^{J} R_{net\,j}$; $P_{Lnet\,j}$, $P_{Cnet\,j}$ – the amplitude values of hydraulic power losses at the inductive and capacitive reactance of the *j*-th section of the pipeline, respectively; P_{con} – the amplitude value of hydraulic power at the consumer.

The obtained system of identification linear equations (4) is solved in matrix form:

$$AX=B \tag{5}$$

where $A = \begin{vmatrix} P_{Rp0} & P_{Rnet\Sigma 0} & P_{Lnet\Sigma 0} & P_{Cnet\Sigma 0} & P_{st0} & P_{Rcon0} \\ P_{Rp1a} & P_{Rnet\Sigma 1a} & P_{Lnet\Sigma 1a} & P_{Cnet\Sigma 1a} & P_{st1a} & P_{Rcon1a} \\ P_{Rp1b} & P_{Rnet\Sigma 1b} & P_{Lnet\Sigma 1b} & P_{Cnet\Sigma 1b} & P_{st1b} & P_{Rcon1b} \\ \vdots & \vdots & \vdots & \vdots & \vdots & \vdots \\ P_{Rpka} & P_{Rnet\Sigma ka} & P_{Lnet\Sigma ka} & P_{Cnet\Sigma ka} & P_{stka} & P_{Rconka} \\ P_{Rpkb} & P_{Rnet\Sigma kb} & P_{Lnet\Sigma kb} & P_{Cnet\Sigma kb} & P_{stkb} & P_{Rconkb} \end{vmatrix}$ – the coefficients matrix formed by the amplitude values of the constant and variable cosine and sine components by individual harmonics of hydraulic power losses at the resistance of the pump, at the resistance, inductive and capacitive reactance of the *j*-th section of the pipeline network, hydraulic power losses at the resistance of the consumer; $B = \begin{vmatrix} P_{s0} \\ P_{s1a} \\ P_{s1b} \\ \vdots \\ P_{ska} \\ P_{skb} \end{vmatrix}$ – the matrix of free members formed by the amplitude values of the constant and variable cosine and sine components by individual power harmonics at the output of the hydraulic power supply; $X = \begin{vmatrix} H_{st} \\ R_{p\Sigma} \\ L_{net\,j} \\ C_{net\,j} \\ \vdots \\ R_{con} \end{vmatrix}$ –the matrix of unknowns formed by the unknown parameters of the equivalent electrical circuit of the hydraulic system.

Using the inversion of matrix A^{-1}, we obtain the equation: $X = A^{-1}B$. Its solution allows to determine the unknown parameters: total resistance of the pump R_p, pipeline $R_{net\,j}$ and consumer R_{con}, inductive $L_{net\,j}$ and capacitive $C_{net\,j}$ reactance of the hydraulic network sections.

For laboratory EHC with the following parameters of the motor: power P_n = 830 W; rotation frequency ω_n = 303.7 s^{-1}; current I_n = 1.7 A; pump: discharge Q_{pn} = 0.00138 m^3/s; maximum head H_0 = 20.8 m; nominal head H_{pn} = 18 m; pipeline: diameter d = 0.04 m; length l = 6 m, obtained the hydraulic power curves at the pump output $p_p(t)$, in the pipeline network $p_{net}(t)$ and at the consumer $p_{con}(t)$ for different degree of cavitation development: at $n_{kav1} = 3.7$ (Fig. 3, a); at $n_{kav5} = 31.3$ (Fig. 3, b).

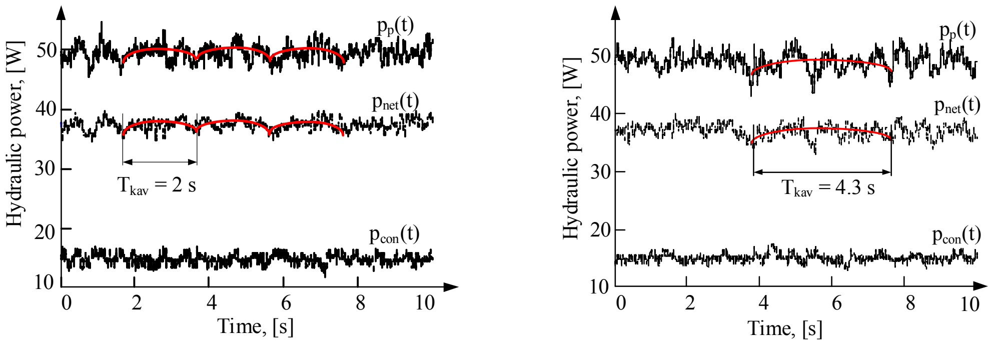

a) **b)**

Fig. 3.

The analysis in Fig. 3 confirmed that the appearance of cavitation processes in the hydraulic network leads to the development of oscillations in the signals of hydraulic power with the corresponding period T_{kav}. It is obtained that at n_{kav5} the oscillations in power signals have the most pronounced character.

The frequency spectra of the hydraulic power signals in the pipeline network at $n_{kav1} = 3.7$ (Fig. 4, a) and at $n_{kav5} = 31.3$ (Fig. 4, b) confirm the appearance of low-frequency components in the development of cavitation processes, which makes it possible to present the signals by trigonometric series.

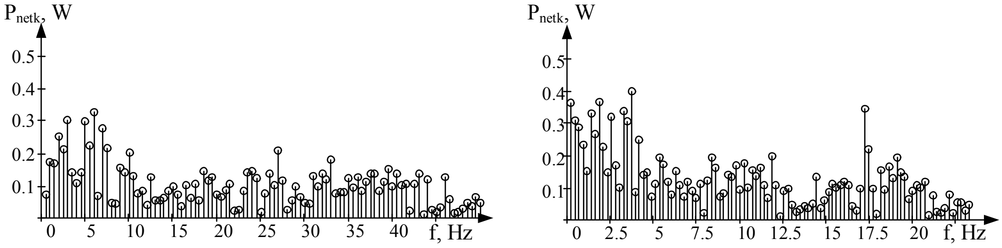

a) **b)**

Fig. 4.

In this case, the unknown parameters of the equivalent electrical circuit of EHC physical stand include: total resistance $R_{\Sigma} = R_p + R_{net1} + R_{net2} + R_{con}$, total inductive $L_{net\Sigma}$ and capacitive reactance $C_{net\Sigma}$ of the hydraulic network. Therefore, the first three equations of the system are used for their calculation (4):

$$\left.\begin{aligned} P_{s0} &= P_{\Sigma 0} + P_{Lnet\Sigma 0} + P_{Cnet\Sigma 0}; \\ P_{s1a} &= P_{\Sigma 1a} + P_{Lnet\Sigma 1a} + P_{Cnet\Sigma 1a}; \\ P_{s1b} &= P_{\Sigma 1b} + P_{Lnet\Sigma 1b} + P_{Cnet\Sigma 1b}. \end{aligned}\right\} \tag{6}$$

The representation of system (6) in a matrix form (Table 1) made it possible to calculate the unknown parameters of the experimental EHC (Table 2) in the case of the development of cavitation oscillations of varying degrees n_{kav} in the hydraulic network.

Table 1. Coefficients matrix

Cavitation degree	Main matrix, A	Absolute term matrix, B	Decision matrix X
3.7	$\begin{vmatrix} 1.664\cdot10^5 & 9.218\cdot10^3 & 1.723\cdot10^4 \\ -2.827\cdot10^5 & 8.978\cdot10^5 & -9.496\cdot10^5 \\ 5.998\cdot10^4 & 6.875\cdot10^4 & 8.238\cdot10^4 \end{vmatrix}$	$\begin{vmatrix} 1.558\cdot10^8 \\ 3.554\cdot10^{12} \\ 5.617\cdot10^{11} \end{vmatrix}$	$\begin{vmatrix} R_{\Sigma} \\ L_{\Sigma} \\ C_{\Sigma} \end{vmatrix}$
31.3	$\begin{vmatrix} 1.669\cdot10^5 & 9.155\cdot10^3 & 1.67\cdot10^4 \\ -7.726\cdot10^4 & 8.824\cdot10^4 & 2.393\cdot10^5 \\ 1.856\cdot10^5 & -7.772\cdot10^4 & 6.232\cdot10^4 \end{vmatrix}$	$\begin{vmatrix} 1.547\cdot10^8 \\ 3.596\cdot10^{11} \\ -1.377\cdot10^{11} \end{vmatrix}$	

Table 2. Results of identification

Cavitation degree, n_{kav}	R_{Σ}, kg/m⁴s	L_{net}, kg/m⁴	C_{net}, m⁻¹
$n_{kav} \approx 1.0$ (without cavitation)	$1.698\cdot10^7$	$1.14\cdot10^3$	$1.429\cdot10^{-4}$
$n_{kav1} = 3.7$	$1.7\cdot10^7$	$1.244\cdot10^3$	$1.42\cdot10^{-4}$
$n_{kav2} = 7$	$1.73\cdot10^7$	$1.317\cdot10^3$	$1.45\cdot10^{-4}$
$n_{kav3} = 19.7$	$2.21\cdot10^7$	$1.474\cdot10^3$	$1.413\cdot10^{-4}$
$n_{kav4} = 26$	$3.597\cdot10^7$	$1.512\cdot10^3$	$1.376\cdot10^{-4}$
$n_{kav5} = 31.3$	$4.585\cdot10^7$	$1.547\cdot10^3$	$1.43\cdot10^{-4}$

The results obtained in the development of cavitation oscillations in the pipeline network confirmed the possibility of using the energy method to identify EHC parameters [10]. Thus, a comparative analysis of the mathematical model parameters (Fig. 5, dotted line) and experimental EHC (Fig. 5, solid line) calculated by the energy method, showed a fairly high convergence of results: determination coefficient R^2 is within the limits (0.9..0.98).

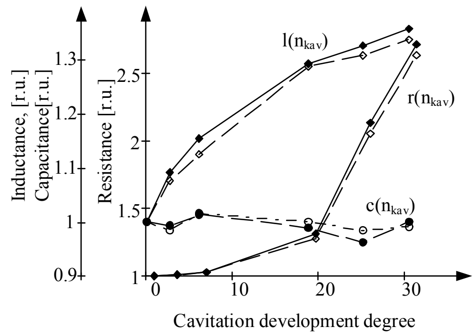

Fig.5.

In this case, the analysis of the curves of changes in EHC parameters from the degree of development of cavitation (Fig. 5) showed that the total resistance of electrohydraulic equipment is more influenced by cavitation oscillations. The said is confirmed by the relative hydraulic resistance change curve $r = R_{\Sigma r}/R_{\Sigma i}$ from degree n_{kav} of cavitation development, where $R_{\Sigma r}$, $R_{\Sigma i}$ – the value of hydraulic resistance in the system with cavitation and in its absence, respectively. It is obtained that at low n_{kav} the change in relative hydraulic resistance is insignificant; at the developed cavitation there is a sharp increase of r [14]. It is obvious that when the threshold value of hydraulic resistance is reached, the pipeline may become clogged. This causes the necessity of measures for cavitation protection of hydraulic equipment: the opening of aeration valves for venting air, changes in the mode of PU operation to exit the cavitation zone, etc.

3 Conclusions

It is demonstrated that the operation of electrohydraulic complexes is often accompanied by the development of unsteady hydrodynamic processes, which can result in deviations of the current parameters of pumping and piping equipment from their nominal values.

The possibility of applying the energy method of identification of the parameters of the electrohydraulic complex on the basis of the equations of energy balance between the power supply and the elements of the power channel is proved. It is demonstrated that the method is grounded on the formation of identification equations based on the harmonic analysis of hydraulic power using equivalent electric circuits that take into account the configuration of the pipeline and the occurrence of unsteady processes in the hydraulic system.

The timely determination of current parameters and their comparison with the threshold values at which the development of abnormal situations is possible, enables determining the service life of pumping and piping equipment to decide on their repair or replacement.

References

[1] Pejović S., Boldy A. P., Obradović D., *Guidelines to hydraulic transient analysis*, Technical Press, 1987, 145 p.

[2] Ellis J., *Pressure transients in water engineering: A guide to analysis and interpretation of behavio*r, London, United Kingdom, Thomas Telford Publishing Ltd 2008, 540 p.

[3] Adamkowski, Adam & Lewandowski, Mariusz. "Investigation of Hydraulic Transients in a Pipeline with Column Separation". *Journal of Hydraulic Engineering*, 2012 138. 10.1061/(ASCE)HY.1943-7900.0000596.

[4] Ferreira F. J. T. E., Fong J. A. C. and de Almeida A. T., "Ecoanalysis of Variable-Speed Drives for Flow Regulation in Pumping Systems". *IEEE Transactions on Industrial Electronics*, vol. 58, no. 6, pp. 2117-2125, June 2011. doi: 10.1109/TIE.2010.2057232.

[5] Zagirnyak M., Kalinov A., Melnykov V. "Sensorless vector control systems with the correction of stator windings asymmetry in induction motor", *Przegląd elektrotechniczny*, 2013, 89, (12), pp. 340–343

[6] Zagirnyak M., Kalinov A. & Chumachova A. "Correction of operating condition of a variable-frequency electric drive with a non-linear and asymmetric induction motor", *IEEE EuroCon*, 2013, pp. 1033.

[7] Fenton J. D. "Calculating resistance to flow in open channels", *Technical report, Alternative Hydraulics*, Paper 2, 2010, pp. 1–7.

[8] Petrosov V.A. *Water supply sustainability*, Harkiv, Faktor, 2007, 355 p. [in Russian]

[9] M. Zagirnyak, D. Rodkin, I. Romashykhin, N. Rudenko and V. Chenchevoi, "Identification of nonlinearities of induction motor equivalent circuits with the use of the instantaneous power method," 2016 17th *Internati* doi: 10.1109/CPEE.2016.7738721.

[10] Zagirnyak M., Korenkova T., Serdiuk O., Kravets O. and Kovalchuk V. *The Control of the Pumping Complex Electric Drive in Non-Steady Operation States.* Monograph – New York, Nova Publisher, 2019. – 278 p. ISBN: 978-1-53615-017-9

[11] Kovalchuk V., Korenkova T. and Almashakbeh A. S. "Electrohydraulic Complex Parameters Determination Based on the Energy Balance Equations," 2020 *IEEE Problems of Automated Electrodrive. Theory and Practice* (PAEP), 2020, pp. 1-6, doi: 10.1109/PAEP49887.2020.9240819.

[12] Nicolet C., Kaelbel T., Alligne S., Ruchonnet N., Allenbach P., Bergant A., Avellan F., "Simulation of water hammer induced column separation through electrical analogy", 4-th *International Meeting on Cavitation and Dynamic Problems in Hydraulic Machinery and Systems*, October, 26-28, 2011, Belgrade, Serbia.

[13] Zagirnyak M., Kravets O., Korenkova T., "The optimal control of dynamic loads in a pump complex with adjustable pipeline valves", *Naukovyi Visnyk Natsionalnoho Hirnychoho Universytetu*, 2016, vol. 3, pp. 78-86.

[14] T. Korenkova, V. Kovalchuk and M. Z. Qawaqzeh, "The Assessment of the Electrohydraulic Complex Power Controllability in the Event of an Emergency Shutdown of the Power Supply," 2020 *IEEE Problems of Automated Electrodrive. Theory and Practice* (PAEP), 2020, pp. 1-6, doi: 10.1109/PAEP49887.2020.9240854.

[15] Zagirnyak, M.V., Rodkin, D.I. & Korenkova, T.V. 2014, "Estimation of energy conversion processes in an electromechanical complex with the use of instantaneous power method", 16th *International Power Electronics and Motion Control Conference and Exposition*, PEMC 2014, pp. 238.

[16] Zagirnyak M., Kalinov A. & Maliakova M. "An algorithm for electric circuits calculation based on instantaneous power component balance", *Przeglad Elektrotechniczny*, 2011, vol. 87, no. 12 B, pp. 212-215.

[17] Melnykov, V. & Kalinov, A. 2012, "Compensation the induction motor parametrical asymmetry", Technical Electrodynamics, , no. 3, pp. 85-86.

[18] Zagirnyak M., Kalinov A. and Melnykov V. "Decrease of the thermal overloads of a variable-frequency electric drive at damages in the electric circuit of an induction motor stator", *Przeglad Elektrotechniczny*, 2019, vol. 95, no. 5. pp. 43-46. doi:10.15199/48.2019.05.11

[19] Zagirnyak, Mykhaylo, Korenkova T., Kovalchuk V. "The automation of the procedure of the electrohydraulic complex power harmonic analysis". *Przeglad Elektrotechniczny*, 2018, vol. 94, no. 1. pp. 3-6. doi:10.15199/48.2018.01.01

The 8th International Symposium on Applied Electromagnetics – SAEM'2022

Struga, North Macedonia, 26-29 June 2022

Frequency Behavior of Specific Total Loss Model Taking into Account Anisotropy of Electrical Steel

Wojciech A. Pluta[1], Marek Patro[2], Pawel Czaja[3], Vasil Chaban[4]
[1] *Czestochowa University of Technology, Al. Armii Krajowej 17, 42-200 Czestochowa, Poland E-mail*: w.pluta@gmail.com
[2] *Czestochowa University of Technology, Al. Armii Krajowej 17, 42-200 Czestochowa, Poland E-mail*: lism@el.pcz.czest.pl
[3] *Czestochowa University of Technology, Al. Armii Krajowej 17, 42-200 Czestochowa, Poland E-mail*: *czajap@el.pcz.czest.pl*
[4] *Lviv Polytechnic National University, Ukraine, E-mail: vasyl.y.chaban@lpnu.ua*

Abstract ***Large electrical machines and transformers cores and built of electrical steel (ES). The properties of ES have a significant influence on the properties of these devices, there are built of. Improvement of ES properties was a subject of research on many years. One of the mile stone was introduction of Goss patent which cause drop of loss and increase in saturation flux density. Due to Goss texture the ES displays strong anisotropy of magnetic properties which should be taken into account by the designers of magnetic circuits as it has undesirable effect e.g. vibrations and noise. Several approaches for anisotropy of magnetic properties can be found in the literature. In this paper are presented frequency behavior of parameters of anisotropy P_S loss model based on three components specific total loss model.***

1 Introduction

Grain oriented electrical steel ES is important material for industrial applications e.g. magnetic cores of transformers. As a results of introduction of Goss patent with addition of silicon at production of ES it exhibits a strong magnetocrystalline anisotropy with a (110)[001] orientation. Grain oriented ES has a high magnetic flux saturation and magnetic permeability and low specific power loss at an easy magnetization direction. In the Goss texture, the easy magnetization direction is <001> and it is parallel to the rolling direction RD. The worst magnetic properties are determined at an angle of 55° (<111>) with RD. Intermediate magnetic properties occur at an angle 90° to RD that is transverse direction TD. Production of large transformers requires magnetocrystalline anisotropy to be taken at design process in order to minimize the core losses and the magnetizing currents. Cores of large transformers are made of tape cut along RD but at T-joints and corners the magnetic flux deviates from the easy magnetization axis [1-7]. At these places anisotropy of magnetic properties of ES adversely affects some technical parameters of the final product. The energy loss has particular significance as large transformers which convert all produced electrical energy. Hence, taking into consideration the anisotropic properties of ES at the design stage can lead to considerable energy and material savings.

The modeling of anisotropic properties of specific power loss in electrical steel ES is a topic of intensive research. Much research has been devoted to modeling the effect of anisotropy on the magnetic properties of GOES. We can distinguish, for example, models based on the Néel phase theory [8], on the reluctivity tensor [9] or based on the co-energy concept [10]. The experimental models describe the angular properties of power loss based on various functions. One of them is based on a third-order polynomial [11], and the other on the orientation distribution (ODF) function used in crystallographic studies [12] or model presented in [13]. Most often these models cannot be applied to high magnetic induction values, such as where grain oriented electrical sheets often work in transformer cores.

In this paper is presented analysis of frequency and flux density dependence of the anisotropy of specific total loss. The analysis is performed using novel model of directional properties of specific total loss based on loss separation approach [13, 14]. The investigation was preformed for grain-oriented GO electrical steel sheets. There was found that the model [15] can be used for analyzing of magnetic properties of ES as it is kept, in assumed ranges of flux density, permeability and frequency [2].

2. Measurements and specific total loss separation

For research were used conventional grain-oriented ES grades of different thickness form 0.27 mm to 0.35 mm and specific total loss anisotropy calculated from Eq. (1) in the range from about 50% to 60%. Measurements of chosen ES grades were taken under axial examination in a non-standard Single Sheet Tester (SST) on square samples of 100 mm width [2]. Measurements were performed at 10 frequencies for 2 Hz to 100 Hz at different angles to RD.

The anisotropy phenomenon play important role in construction of magnetic circuits. The magnetic anisotropy is a non-liner phenomenon in relation to magnetizing frequency as well as to flux density. Another way to describe the directional properties is the anisotropy of magnetic properties e.g. flux density or anisotropy of specific total loss. The anisotropy of specific total loss $\Delta AP_{S,1.5}^{90-0}$ is calculated for the magnetization angles $x = 90°$ and $x = 0°$ at the flux density 1.5 T from equation as below:

$$\Delta P_S^{y-0} = \frac{P_S^y - P_S^0}{P_S^y + P_S^0} \tag{1}$$

It is overall accepted that the specific total loss P_S consists of three components: hysteresis, classical and excess eddy current. The frequency dependence of the three components can be described by three component model and it can be applied at any angles x to the RD, is separated in the commonly used way as [16]:

$$P_S / f = \underbrace{C_h B_p^{\alpha}}_{P_h / f} + \underbrace{C_{ce} B_p^2 f}_{P_{ce} / f} + \underbrace{C_{ex} B_p^{3.2} f^{1/2}}_{P_{ex} / f} \tag{2}$$

where: C_h is the hysteresis loss coefficient, α is the exponent of flux density, $C_{ce} = \pi^2 d^2 (6\rho)^{-1}$ is the classical eddy current loss coefficient under sinusoidal magnetization, C_{ex} is the excess loss coefficient, ρ is the resistivity and d is the sheet thickness.

Classical eddy current specific total loss component Eq. (2) shows isotropic character. The hysteresis and excess eddy current loss components display anisotropic character. Additionally, both components show similarity due to their common origin [16, 17]. In Fig.1 are plotted experimental data and fitted using Eq. (2) energy loss versus frequency for different magnetizing directions obtained for ES steel M150-35S grade at $B_m = 1.2$ T. In this figure the non-linearity of frequency dependence of anisotropy of specific total loss is visible.

For each angle loss separation according to three component model Eq.(1) was used. The results showed high nonlinearity of magnetic anisotropy of ES. In a case of ES the formula (2) is valid for any magnetization angle x. To obtain two unknown coefficients C_h and C_{ex} for given magnetization angle x and flux density B_m, both sides of (2) are divided by frequency f. As a result specific total energy loss can be obtained. From fitting of Eq. (2) to experimental values the coefficient $C_h(B_m, x)$ was obtained by extrapolation of results to 0 Hz frequency and the coefficient $C_{ex}(B_m, x)$ could be calculated. Later, the hysteresis P_h, and excess P_{ex} components were calculated. It is worth to noting all three P_S loss components exponential function [18] for all considered magnetization angles in all ES under consideration.

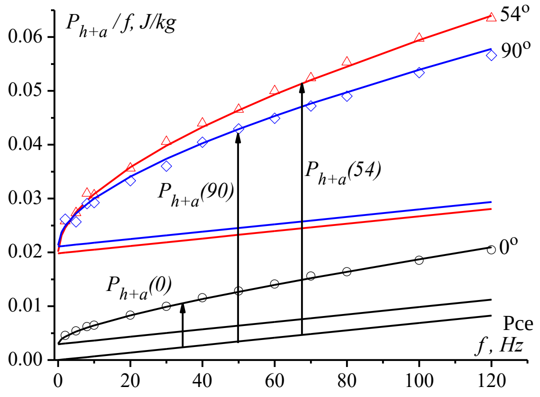

Fig. 1. Energy loss per unit mass versus frequency for different magnetizing directions obtained for steel grade M150-35S at B_m = 1.2 T

From Fig. 1 it can be seen non-linear and significant increase of the sum of hysteresis and excess eddy current specific total energy loss components for "hard" magnetization angles $x = 54°$ and $x = 90°$ over that for magnetization along RD (at angle $x = 0°$). Additionally, specific total loss increases much faster with frequency for “hard” magnetization angles $45^{o} \leq x \leq 90^{o}$ what can be attributed to “the growing number of involved Bloch walls” [19].

3 Results and discussion

The main circumstance for the new model was the interdependence of the hysteresis and eddy current excess components, showed in the works [16, 17]. This allowed proposing a model of the properties of the directional power losses $P_S(x)$ presented in [13]. This parameter can be used for description of anisotropic properties, Fig.2 a). The directional properties of ES can be described by modified exponential function with expanded exponent as Eq. (3).

$$P_{h+ex}^{x} = aB_p^{b(B_p)} \tag{3}$$

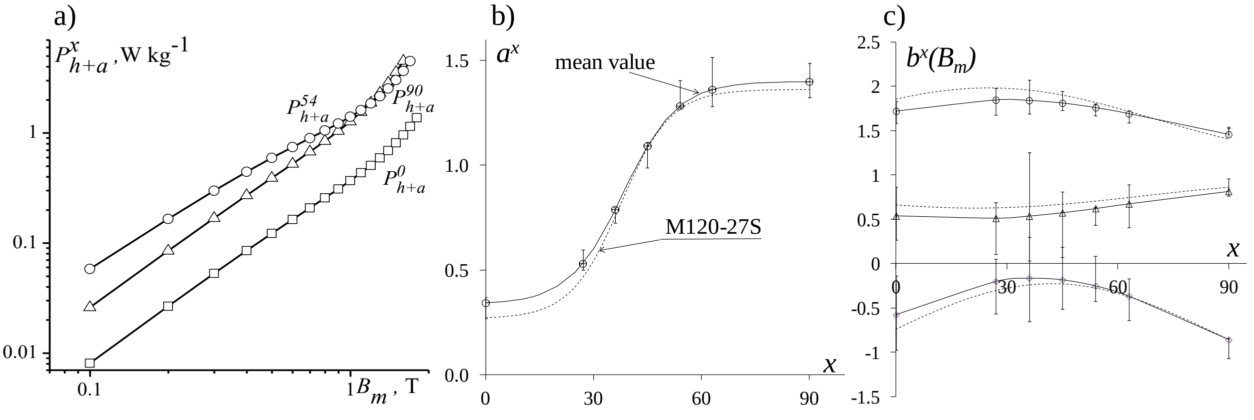

Fig. 2. Directional curves of a sum of P_h and P_{ex} components and angular parameters of exponential function used for extrapolating $P_{h+a}=aB_p^{b(Bp)}$ [13]

In Fig. 2 b) and c) are presented the angular dependence of parameter *a(x)* and polynomial coefficients *b(x)*.

Presented in Fig. 2 b) the angular dependence of parameter *a(x)* of exponential function Eq. (3) can be described by the following equation:

$$a(x) = a(0) + \left[a(90) - a(0)\right] \cdot \left[1 + \exp\left(\frac{x50 - x}{m}\right)\right]^{-1} \tag{4}$$

The parameters *a(0)* and *a(90)* determine minimum and maximum of curve *a* = f(*x*) presented in Fig.2 b). In Fig. 3 are presented behavior of parameters *a(0)* and *a(90)* of Eq. (4)

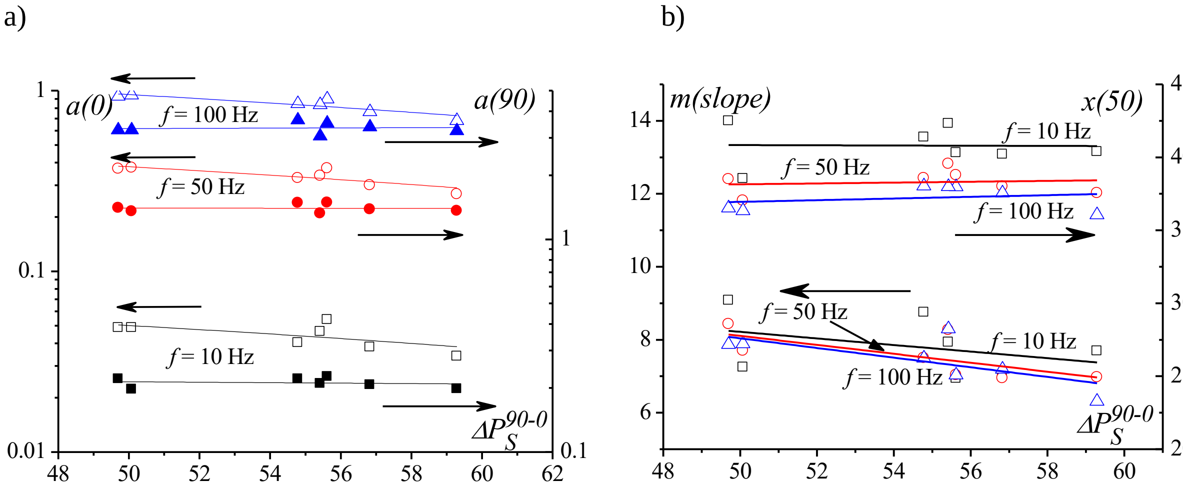

Fig. 3. Parameters of Eq. (4) as a function of anisotropy $\Delta P_S^{90\text{-}0}$ and frequency a) parameters *a(0)* and *a(90)*, b) parameters *m* and *x(50)*

As can be seen in Fig. 3 a) the parameter *a(90)* concerning transverse direction weakly depends on anisotropy $\Delta P_S^{90\text{-}0}$ in opposite to the parameter *a(0)*. The parameter *a(90)* depends on frequency but for given frequency is independent on P_S loss anisotropy. This can be due to different magnetization process at RD and TD.

The parameter *x(50)*, Fig. 3 b), dependents on frequency and nearly does not depend on anisotropy $\Delta P_S^{90\text{-}0}$. The parameter *x(50)* can be easily calculated as angle at an average between *x* = 0° and 90°. The parameter *m*, Fig. 3 b) describing the slope of curve *a(x)* weakly depends on frequency. Its dependence on anisotropy $\Delta P_S^{90\text{-}0}$ shows stronger dependence. The dependence of mentioned above parameters on frequency can be skipped by means of three component model (2). Once coefficients C_h and C_{ex} for 50 Hz were calculated for 0 and 90, P_S loss can be counted for different frequency. $C_{ex} = (P_S - P_{ce} - C_h B_p f)/f^{3/2}$ This is due to linearity of parameters of Eq. (4).

Coefficients of exponent $b(B_p)$ of peak flux density (Eq. (3)) can be described by Eq. (5). The dependence of the three coefficients of Eq. (5) on anisotropy $\Delta P_S^{90\text{-}0}$ for frequencies 10 Hz, 50 Hz and 100 Hz are presented in Fiq. 4.

$$b_i = z_0 + z_1 \sin\left[2\left(x\frac{\pi}{180} - z_2\frac{\pi}{180}\right)\right] \tag{5}$$

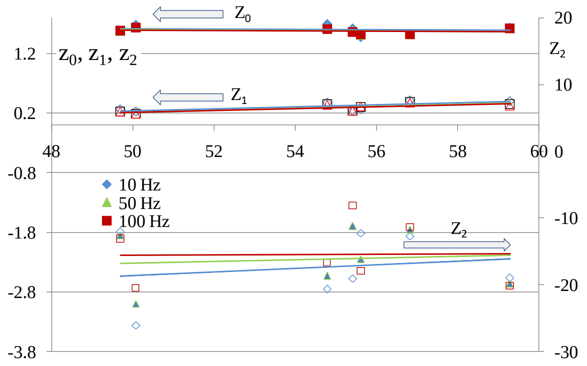

Fig. 4. Parameters z_0, z_1 and z_2 of (5) as a function of anisotropy ΔP_S^{90-0} and frequency

Parameters z_0, z_1, z_2, differently depend on frequency and anisotropy ΔP_S^{90-0}. The parameter z_0 does not depend on anisotropy and frequency. The parameter z_1 does not depend on frequency but weakly depends on anisotropy. The parameter z_2 is characterized by larger dispersion associated with anisotropy and frequency. The dispersion with frequency decreases with anisotropy ΔP_S^{90-0} showing lower changes in grades with larger orientation. This can be associated with the effect of micro and classical eddy currents increasing significantly with frequency and flux density.

4. Summary

The anisotropy of specific total loss components is a very non-linear phenomenon. As was mention the modeling of GOES anisotropic properties of specific total loss can be realized in different ways. In the paper were evaluated parameters of model of directional properties of specific total loss in Goss textured electrical steel. The advantage of this model is the possibility to modeling anisotropy of P_S los even at high flux density. It was observed larger influence of frequency on anisotropy of specific total loss in electrical steel grades with smaller grain orientation. The influence of frequency and associated with it eddy currents is observed for parameter related to sum P_h and P_a components at rolling direction. Weak influence of frequency on anisotropy shows constant parameter of exponent of flux density of the sum P_h and P_a components. The main influence of frequency was observed in rest parameters responsible for curvature of directional P_{h+a} curves.

References

[1] F. Fiorillo, “Measurements of magnetic materials,” Metrologia, vol. 47, pp. S114 – S142, 2010.

[2] W.A. Pluta, “Some properties of factors of specific total loss components in electrical steel,” IEEE Trans. Magn., vol. 46, 2, pp. 323-325, 2010.

[3] H. Pfuetzner, “Rotational magnetization and rotational losses of grain oriented silicon steel sheets-fundamental aspects and theory,” IEEE Trans. Magn., vol. 30, 5, pp. 2802-2807.

[4] J. Sievert, H. Ahlers, H. Birkfeld, B. Cornut, F. Fiorillo, K.A. Hempel, T. Kochmann, A. Kedoues-Lebouc, T. Meydan, A.J. Moses, and A.M. Rietto, “European intercomparison of measurements of rotational power loss in electrical sheet steel,” J. Magn. Magn. Mater., vol. 160, pp. 115-118, 1996.

[5] N. Stranges and R.D. Findlay, “Measurement of rotational losses in electrical steel,” IEEE Trans. Magn., vol. 36, 5, pp. 3457-3459.

[6] V. Gorican, A. Hamler, M. Jesenik, B. Stumberger and M. Trlep, “Unreliable determination of vector B in 2-D SST,” J. Magn. Magn. Mater., vol. 254-255, pp. 130-132, 2003.

[7] B. Stumberger, V. Gorican, G. Stumberger, A. Hamler, M. Trlep, and M. Jesenik, “Accuracy of iron loss calculation in electrical machines by using different iron loss models,” J. Magn. Magn. Mater., vol. 254-255, pp. 269-271, 2003.

[8] Fiorillo F., Dupre L.R., Appino C., Rietto A.M., "Comprehensive model of magnetization curve, hysteresis loops, and losses in any direction in grain -oriented Fe-Si*,” IEEE Trans. Magnetics* 38(3) (2002), s.1467-1476

[9] Sande H. V., Boonen T., Podoleanu I., Henrotte F., and Hameyer K., "Simulation of a Three-Phase Transformer Using an Improved Anisotropy Model," *IEEE Trans. on Magn.* Vol. 40 (2) (2004), pp. 850-855

[10] Cornut B., Kedous-Lebouc A., Waeckerlé T., "From metallurgy to modeling of electrical steels: A multiple approach to their behavior and use based on physics and experimental investigations," *J. Magn. Magn. Mater.*, Vol. 160 (1996), s. 102–108

[11] Soinski M., Moses A.J., Handbook of Magnetic Materials, Chapter 4, Vol. 8, Elsevier Science B.V., 1994

[12] de Campos M. F., "Anisotropy of steel sheets and consequence for Epstein test: I theory", *XVIII IMEKO WORLD CONGRES Metrology for a Sustainable Development* September, 17 – 22, 2006, Rio de Janeiro, Brazil.

[13] W.Pluta, A.J. Moses: Prediction of angular variation of specific total loss of Goss oriented electrical steel, Physica B: Condensed Matter, Vol. 544 (2018), s.28-33

[14] Pluta W.A., Calculating power loss in electrical steel taking into account magnetic anisotropy, Przegląd Elektrotechniczny, nr 2 (2018), s. 100-103.

[15] G. Bertotti, General properties of power losses in soft ferromagnetic materials, *IEEE Trans. Magn.* , vol. 24, no. 1 (1988), 621 – 630

[16] Bertotti G., "Hysteresis in magnetism", Academic Press (1998)

[17] Pluta W.A., Angular properties of specific total loss components under axial magnetization in grain-oriented electrical steel. IEEE Trans. on Magnetics, Vol. 52, nr 4 (2016), 12 stron, s. 6300912.

[18] L.R. Dupre, F. Fiorillo, J. Melkebeek, A.M. Rietto, C. Appino, "Loss versus cutting angle in grain-oriented Fe-Si lamination", *J. Magn. Magn. Mater.*, vol. 215-216 (2000) pp. 112–114.

[19] H. Pfutzner, P. Schonhuber, B. Erbil, G. Harasko and T. Klinger, "Problems of loss separation for crystalline and consolidated amorphous soft magnetic materials", *IEEE Trans. on Magn*., vol. 27, no 3, (1991), pp. 3426-3432.

Measuring the Impact of High Order Harmonics on the Transformer No-Load Losses

Mihail Digalovski, Goga Cvetkovski, Krste Najdenkoski, Goran Rafajlovski

Ss. Cyril & Methodius University, Faculty of Electrical Engineering & Information Technologies,
Rugjer Bošković 18, P.O.Box 574, 1000 Skopje, North Macedonia
E-mail: mihaild@feit.ukim.edu.mk, gogacvet@feit.ukim.edu.mk, krste@feit.ukim.edu.mk, goran@feit.ukim.edu.mk

Abstract ***– Transformers are normally designed and built for use at rated frequency, sinusoidal voltages and load current. A non-sinusoidal sources and non-linear load on a transformer leads to harmonic power losses which cause increased operational costs and additional heating in certain transformer parts. It leads to higher losses, early fatigue of insulation, premature failure and reduction of the useful life of the transformer. In this work a dry type 500 VA three phase transformer is powered, once directly by to the grid and then through voltage inverter. The no-load losses and high order harmonics are measured using power analyzer. The power losses are also determined analytically obtained by deriving equations for the no-load power losses depending on the harmonics order, its frequency and the amplitude of the magnetic flux density, and compared with the measured ones.***

1 Introduction

In the past years, there has been an increased concern about the effects of nonlinear loads on the power system. Nonlinear loads are such a type of loads that draws current with non-sinusoidal shape. In practice those loads are: fluorescent lamp, gas discharge lighting, solid state motor drives, power converters, static converters, rectifiers, arc furnaces, electronic phase control, cycloconvertors, switch mode power supplies, pulse width modulated drives and the increasingly common electronic power supplies. Harmonics are voltages and currents that appear in the electric power system at frequencies that are integer multiples of the generated frequency. The presence of nonlinear loads results to a significant increase of the level of harmonics and distortion in power system electrical quantities. Transformers are one of the components in the power system that are usually the interface between the supply and most non-linear loads. They are usually manufactured for operating with linear load under rated frequency. Nowadays the presence of nonlinear load results in production of current harmonics. The increased presence of harmonic currents causes extra power losses in the transformer winding and thus, leads to increase in temperature, reduction in insulation life, increase of the power losses and finally reduction of the useful life of transformer [1]. Voltage harmonics increase the power losses in its magnetic core (iron power losses) while current harmonic increase the power losses in its winding and structure. From the above information it is evident that there is a need for detailed analysis of the impact of higher order harmonics on power losses in transformers [2] especially of no-load power losses.

2 No-Load power losses

2.1 Hysteresis power losses

One part of no-load power losses belongs to the hysteresis power losses. Hysteresis power losses originate from the molecular magnetic domains in the core laminations, resisting being magnetized and demagnetized by the alternating magnetic field. Each time the magnetising force produced by the primary of a transformer changes because of the applied ac voltage, the domains realign them in the direction of the force. The energy to accomplish this realignment of the magnetic domains comes from the input power and is not transferred to the secondary winding. It is therefore a loss. This depends upon the area of the magnetizing B-H loop and frequency. Typically, this accounts for 50% of the constant core losses for CRGO (Cold Rolled Grain Oriented) sheet steel with normal design practice. Hysteresis power losses can be determined using the following equation:

$$P_h = K_h \cdot f \cdot B_m^{1,6} \text{ (W/kg)} \tag{1}$$

where:
K_h - the hysteresis constant
f - frequency (Hz)
B_m - maximum flux density (T)

- **Eddy current power losses in the magnetic core**

The alternating flux induces an EMF in the bulk of the iron core that is proportional to flux density and frequency. The resulting circulating current is inversely dependent upon the resistivity of the material and directly proportional to the thickness of the core. The power losses per unit mass of core material, thus vary with square of the flux density, frequency and thickness of the core laminations. Eddy current power losses contribute to about 50% of the no-load power losses [1]. Eddy current power losses are defined with following equation:

$$P_e = K_e \cdot B_m^2 \cdot f^2 \cdot t^2 \text{ (W/kg)} \tag{2}$$

where:
K_e - the eddy current constant
f - frequency in Hertz
B_m - maximum flux density (T)
t - thickness of lamination strips

- **Harmonics effect of no-load power losses**

Transformer manufacturers usually try to design transformers in a way that their minimum losses occur at rated voltage, rated frequency and sinusoidal current. However, by increasing the number of non-linear loads in recent years, the voltages and currents is no longer sinusoidal. Transformer power losses are divided into two major groups, no load and load power losses as shown as:

$$P_{TL} = P_{NL} + P_{LL} \tag{3}$$

where:

P_{NL} - no-load power losses (core losses)
P_{LL} – load power losses
P_{TL} - total power losses.

The no-load power losses are given with following equation [4]:

$$P_{NL} = P_{NLn} \cdot \sum_{i=1}^{n} \frac{K_{fi} \cdot K_{Bi}^{1,6} + K_{fi}^2 \cdot K_{Bi}^2}{2} = P_{NLn} \cdot K' \tag{4}$$

where:

i - high order harmonic

K' - coefficient

$K_{fi} = \frac{f_i}{f_1}$ - high order harmonic frequency ratio

$K_{Bi} = \frac{B_{mi}}{B_{m1}}$ - high order harmonic magnetic flux density ratio

3 Measured results

The power losses calculation and measurements are performed on a three phase dry transformer with rated power of 500 VA and rated voltage of 380/42 V. The primary and secondary windings are realized in star connection. The measurement of the power losses and the harmonics spectrum is realized with power analyzer named Haag omni-quant mobil.

The following values are obtained from the measurements for no-load losses in both cases:

- P_{NL}=13.9 (W) – when transformer is supplied from the grid
- P_{NL}=17.7 (W) - when transformer is supplied from the power inverter

In Figures 1 and 2 the measuring equipment is presented. The calculated no-load power losses at an ideal sinusoidal voltage signal from Table 1 are taken as referent, i.e. P_{NLn} according to Eq. 4.

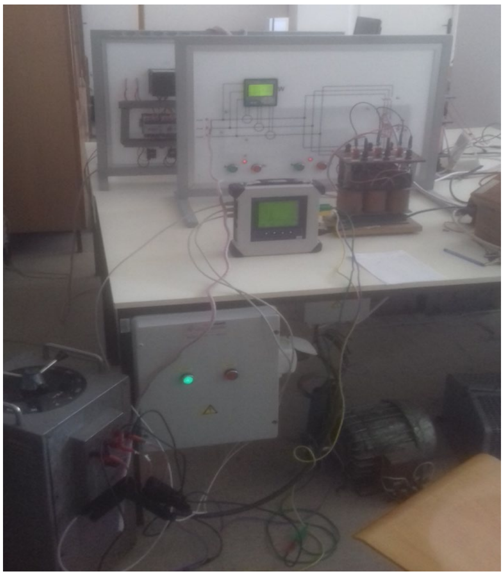

Fig. 1 Supplied from the grid

Fig. 2 Supplied from the power inverter

The analytically determined results are presented below in Table 1.

Table 1 Results from analytical calculations

Supplied from grid						**Supplied from power inverter**					
Harmonic order (/) (measured)	Amplitude of B_m (%) (measured)			Average value for K' (/) (calculated)	Value for P_{NLn} (W)-at an ideal sinusoidal voltage signal (calculated)	Harmonic order (/) (measured)	Amplitude of B_m (%) (measured)			Average value for K' (/) (calculated)	Value for P_{NLn} (W) (calculated)
	L1	L2	L3				L1	L2	L3		
3	0.35	0.40	0.20	**1.0193**	**13.63**	3	19	19	19.50	**1.3161**	**17.95**
5	1.70	1.85	1.75			4	3.50	3.80	3.50		
7	1.30	1.25	1.10			5	0.50	0.40	0.30		
9	0.30	0.40	0.30			9	1.50	1.70	1.65		
11	0.35	0.30	0.35			11	0.50	0.60	0.40		
13	0.20	0.15	0.15			12	0.20	0.15	0.20		
15	0.20	0.15	0.10			15	0.45	0.35	0.40		
17	0.20	0.20	0.20								
19	0.10	0.15	0.10								

4 Conclusion

The results show that harmonics have a great impact on the no-load power losses. The increase of power losses in the case of inverter power supply in relation to the case, for the given harmonic spectrum, is 27.34 %. Based on the presented results it can be concluded that the analytical model has quite good accuracy for determining the increase of no-load power losses from a known harmonic voltage spectrum. The measured value for the no-load losses is 17.7 W, while the calculated one is 17.95, which is a deviation of only 1.4%.

From the presented data it can be concluded that the nonlinear loads in the power system can produce additional power losses in the tower devices in the system especially the power transformers, due to the presence of current and voltage harmonics. Therefore, special attention should be given the design of power transformers especially in the application of novel magnetic materials with better characteristics and lower specific losses.

References

[1] Bureau of Energy Efficiency & Indian Renewable Energy Development Agency, (2006), "Transformer – Best Practice Manual*",* New Delhi, India.

[2] Amit Gupta, Ranjana Singh, (2011), "Computation of Transformer Losses Under the Effects of Non-Sinusoidal Currents*", Advanced Computing: An International Journal (ACIJ),* **Vol**. 2, No. 6, pp. 91 – 104.

[3] Mihail Digalovski, Krste Najdenkoski, Goran Rafajlovski, (2013), *"*Impact of current high order harmonic to core losses of three-phase distribution transformer*"*, *Proceedings of EUROCON 2013 (IEEE, Region 8),* Zagreb, Croatia, pp. 1531-1535.

The 8th International Symposium on Applied Electromagnetics – SAEM'2022

Struga, North Macedonia, 26-29 June 2022

Design and fabrication of a three-phase full-wave diode rectifier with DC voltage stabilization

Iztok Brinovar[1], Benjamin Božič[1], Gregor Srpčič[1], Klemen Sredenšek[1], Bojan Štumberger[1,2], Sebastijan Seme[1,2], Miralem Hadžiselimović[1,2]
[1] University of Maribor, Faculty of Energy Technology, Hočevarjev trg 1, Slovenia, iztok.brinovar@um.si,
[2] University of Maribor, Faculty of Electrical Engineering and Computer Science, Smetanova ulica 17, Slovenia

Abstract ***–This paper deals with the design and fabrication of a three-phase full-wave diode rectifier, which is based on an industrial modular bridge circuit consisting of six semiconductor diodes. Special attention is given to the design of DC voltage stabilization with film capacitors, which have extremely low series resistances and inductances. Thus, within the framework of this paper, a stabilized rectifier with a nominal power of 270 kW and a maximum current of 300 A was made. The manufactured stabilized rectifier is also experimentally evaluated by various tests, confirming its applicability in practice.***

1 Introduction

Three-phase power electronic conversion systems are widely utilized in motor drives, renewable energy systems, etc. systems for conditioning of the electric power. Power electronic conversion systems are used to control and convert one form of electrical power to another form, such as converting between AC and DC or changing the output magnitude, phase or frequency according to application requirements. Various applications, such as battery fed systems, applications utilizing PWM operated three-phase voltage source inverters (VSI), motor drives, etc., involve multistage power conversion with two or more converters connected in series/parallel or in cascade fashion. General example of such power conversion system structure is presented in Fig. 1. The converter on the source side may be of various structures such as diode/thyristor/transistor rectifiers, DC-DC converters, or passive filters, while the inverter on the load side is typically a three-phase VSI [1,2].

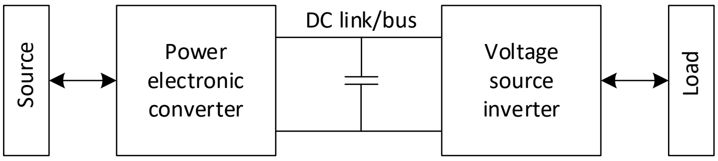

Fig. 1 General example of power conversion system structure employing VSI inverter.

On the source side, if AC-DC conversion stage is used, input current ripple is injected to the DC link. Diode or thyristor rectifiers cause low frequency current ripple, whereas PWM operated transistor rectifiers and inverters impose high frequency current ripple to the DC link. Thus, the DC link capacitor receives harmonic current from both the rectifier and inverter sides, therefore the type and size of the capacitor must be selected accordingly in order to minimize the current and voltage ripple. Generally electrolytic and film capacitors are used in the DC link. Electrolytic capacitors have very high capacitance to volume ratio, thus making them ideal to decrease the DC link ripple, but they have considerably high equivalent series resistance (ESR) and as a result, low current rating. The ESR increases with voltage which limits their operating voltage - usually less than 500V [2]. On the other hand film capacitors can operate under higher voltage levels and they suit well in circuits with high currents and voltages at the DC link.

This paper deals with the design and fabrication of a three-phase full-wave diode rectifier with a nominal power of 270 kW, nominal voltage of 900V and a maximum current of 300 A. Special attention is given to the design of DC voltage stabilization with film capacitors, which have extremely low series resistances and inductances and can operate at higher voltage levels than electrolytic capacitors. The rectifier is designed to operate at different supply voltage frequencies and for application employing three-phase voltage source inverter with PWM switching frequencies of 10-20 kHz. As mentioned in [2], the topology of an application dictates the type and size of the appropriate capacitor, since it determines the ripple current frequency spectrum characteristics. Some DC-link capacitor selection recommendations and design methods for various inverter applications can also be found in [2,3,4,5].

2 Design and fabrication of a stabilized rectifier

The designed rectifier consists of commercially available components and purpose-designed and manufactured elements. The electrical connections and insulating elements are constructed using appropriate software tools. Thus, CAD/CAM tools such as Altium Designer and Solidworks were used in the design process. The schematic presentation of the stabilized rectifier is shown in Fig 2a, while the actual prototype of stabilized rectifier is shown in Fig 2b.

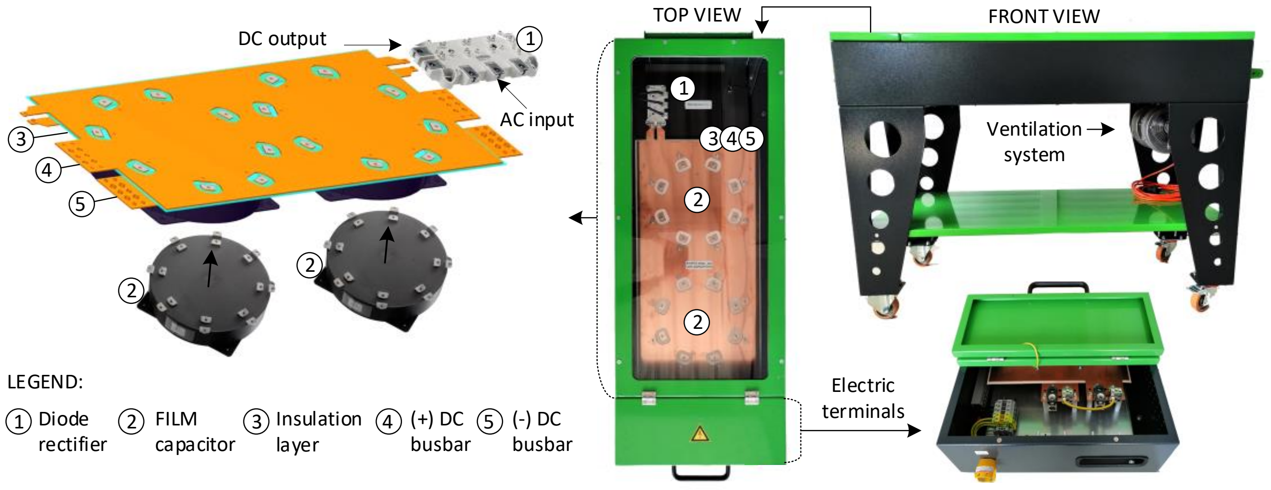

a) b)

Fig. 2 a) Schematic presentation of the stabilized rectifier, b) Stabilized rectifier prototype.

The rectifier is based on an industrial modular bridge circuit (1) mounted on a heat sink, consisting of six semiconductor diodes with a built-in temperature sensor. In order to maintain a DC voltage with small ripples at the output of the rectifier, two film capacitors (2) are connected in parallel to the output terminals of the bridge diode circuit. This type of capacitor is optimized for extremely low self inductance when connected to a suitable bus structure, and has the ability to handle higher ripple currents with less capacitance, weight and volume [6]. The capacitor requires a special arrangement of connection terminals and mounting points, therefore the laminated bus structure (4,5) and insulation layer (3) were constructed accordingly. Laminated bus structures consist of 0,5 mm thick electrically conductive metal, where copper Cu-ETP material was used, separated by a three-layer insulating material. All components are installed in a special robust housing with electric terminals and adequate ventilation system as shown in Fig 2b.

The prototype of stabilized rectifier is also experimentally evaluated by various tests, such as:

- no-load test,
- short-circuit test,
- load test and
- temperature rise test.

3 Results

This section covers the measurement results of stabilized rectifier. The schematic presentation of the measurement system is shown in Fig 1 and it consists of: electrical grid (1), converter (2), asynchronous motor (3), synchronous generator (4), excitation system (5), three phase switch (6), three phase diode rectifier (7), DC link (8), single phase switch (9) and load (10). Readings of electrical quantities such as current, voltage, power, and frequency were obtained with a high precision power analyzer-Yokogawa WT1800.

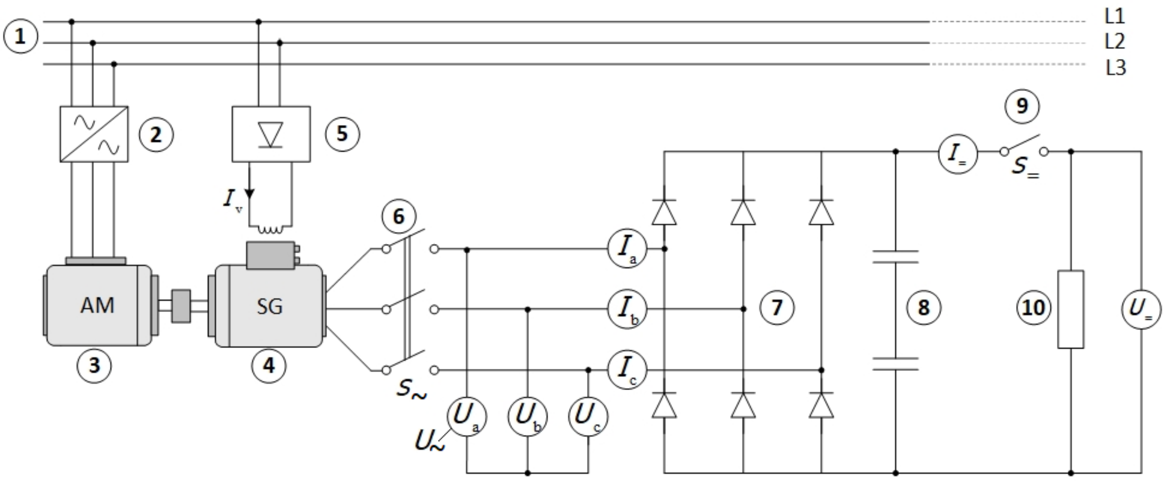

Fig. 3 Schematic presentation of the measurement system.

A synchronous generator driven by a converter fed asynchronous motor is used as a power supply for the stabilized rectifier under test. In this way, it is possible to supply the stabilized rectifier with a variable voltage and frequency via three-pole power switch. Furthermore, the stabilized rectifier can be connected to a load via single-pole power switch. All tests were carried out in the following order: no-load test, short-circuit test, load test and temperature rise test. Hereinafter, all the measured AC electrical quantities are marked with (≈) and DC electrical quantities with (=). The no-load test results at supply voltage frequency of 50Hz are shown in Fig. 4a, while the short-circuit test results are shown in Fig. 4b. The no-load test, or open-circuit test, is performed by increasing the input voltage ($U_{\approx}$) in steps over the entire operating range and measuring the output voltage ($U_{=}$) of the stabilized rectifier. The short-circuit test is performed with short-circuited terminals at the output of the stabilized rectifier and by increasing the input voltage ($U_{\approx}$) in steps, which means indirectly increasing the short-circuit current on the DC side of the rectifier up to nominal value ($I_{=(n)}$), as indicated in Fig. 4b.

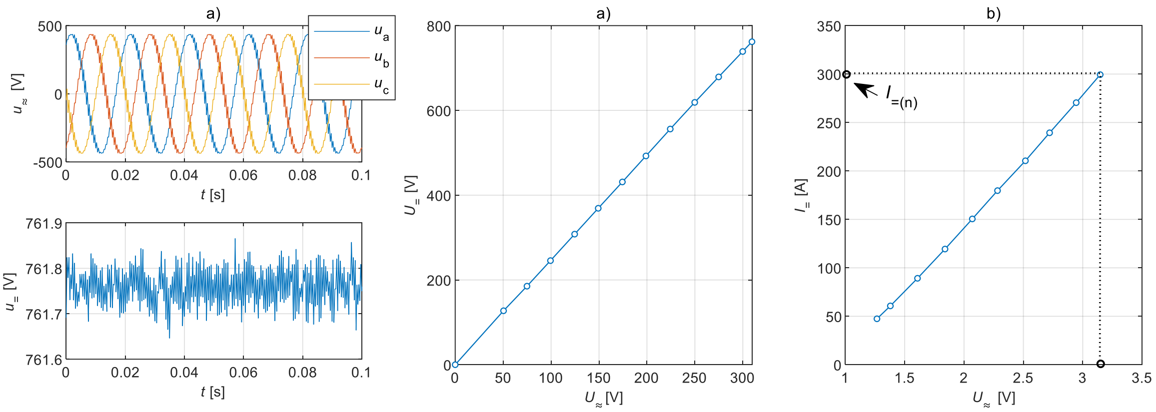

Fig. 4 a) No-load test results, b) Short-circuit test results.

For load test and temperature rise test a constant inductive resistive load was used. The load test was performed at different supply voltage frequencies, from 10 Hz to 70 Hz, in steps of 10 Hz. The load test is performed by increasing the load current ($I_{=}$) and measuring the AC ($P_{\approx}$) and DC power ($P_{=}$). Based on performed load tests, the efficiency of a stabilized rectifier was determined. The load test results are shown in Fig.5, where plot of power versus load current measured at 50Hz is shown in Fig.5a. The efficiency surface plot as a function of load current at different supply voltage frequencies is shown in Fig.5b. Power losses ($P_{=}$) determine the efficiency of the system as well as the amount of cooling required. As it can be noticed the efficiency of the stabilized rectifier increases with the load. The efficiency is relatively low compared to a typical rectifier, the reason being that an inadequate load was used for load tests. As a result, the voltage drop across semiconductor diodes was relatively large compared to the voltage drop across the load, which is reflected in lower efficiency. With an adequate load, a much higher efficiency can be expected.

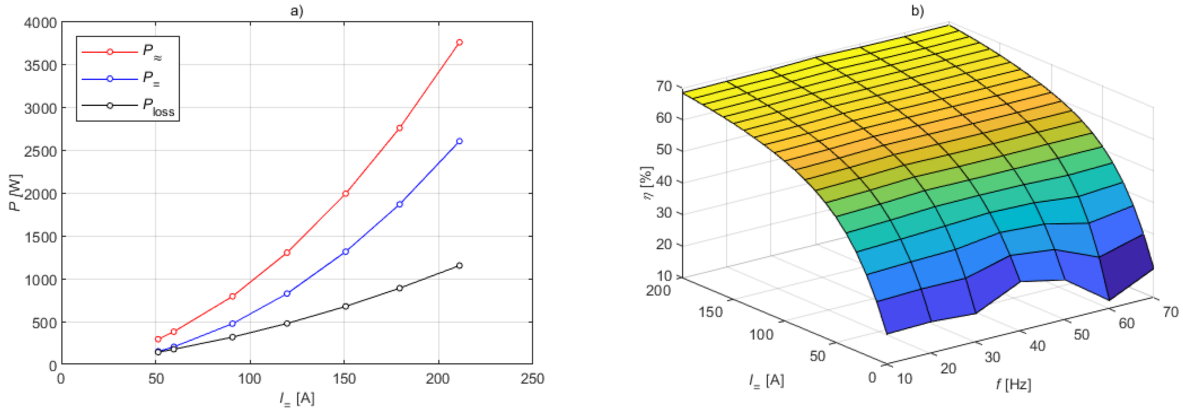

Fig. 5 a) Load test results at supply frequency of 50Hz, b) Surface plot of efficiency.

Following the load test the temperature rise test was performed. The temperature rise test results under load conditions ($I_=$=37A) are shown in Fig. 6a. The test was performed with the purpose of checking if there are any overheating issues of the components. The temperature rise test is completed after thermal equilibrium is reached and the measured temperatures begin to stabilize. As it is evident from Fig. 6 there were no overheating problems. Fig. 6a shows surface temperatures of main components during the temperature rise test, such as diode, capacitor and heat sink temperatures. A thermal image of diode bridge module mounted on a heat sink during the temperature rise test is presented in Fig. 6b.

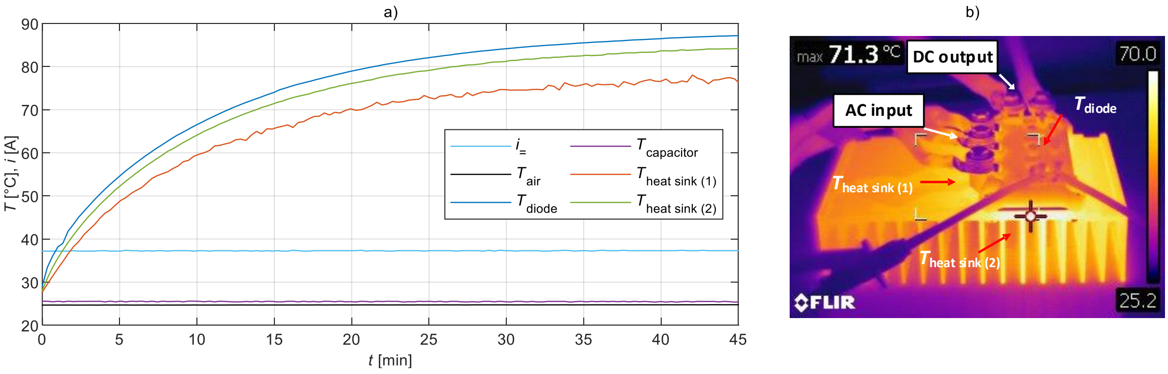

Fig. 6 a) Temperature-rise test results b) Thermal image of diode bridge module mounted on a heat sink.

4 Conclusion

This paper covers design and fabrication process of a stabilized rectifier with a nominal power of 270 kW and a maximum current of 300 A. The prototype of stabilized rectifier is also experimentally evaluated by various tests, confirming its applicability in practice. The prototype serves as a good basis for further research work and development. Additional measurement with appropriate load (VSI) are required and a detailed voltage and current spectrum analysis should be done. All measurements were carried out at the Institute of energy technology in the Electric machines and drives laboratory and Applied electrical engineering laboratory.

References

[1] S. Jain, Modeling and Control of Power Electronics Converter System for Power Quality Improvements, Academic Press, pp. 31-84, (2018).

[2] A. M. Hava, U. Ayhan, (2012), "A DC bus capacitor design method for various inverter applications", IEEE Energy Conversion Congress and Exposition (ECCE), pp. 4592-4599.

[3] R. Grinberg, P.R. Palmer, (2005), "Advanced DC link capacitor technology application for a stiff voltage-source inverter", IEEE Vehicle Power and Propulsion Conference, pp. 205-210.

[4] U. Ayhan, A. M. Hava (2011), "Analysis and characterization of DC Bus ripple current of two-level inverters using the equivalent centered harmonic approach", IEEE Energy Conversion Congress and Exposition, pp. 3830-3837.

[5] A. Safayet, M. Islam, T. Sebastian (2020), "Sizing of DC-link capacitor considering voltage and current ripple requirements", IEEE Energy Conversion Congress and Exposition, pp. 1512-1518.

[6] SBE Power ring film capacitor datasheet: https://ppmpower.co.uk/wp-content/uploads/SBE-700D590.pdf.

Index of Authors

8th Symposium on

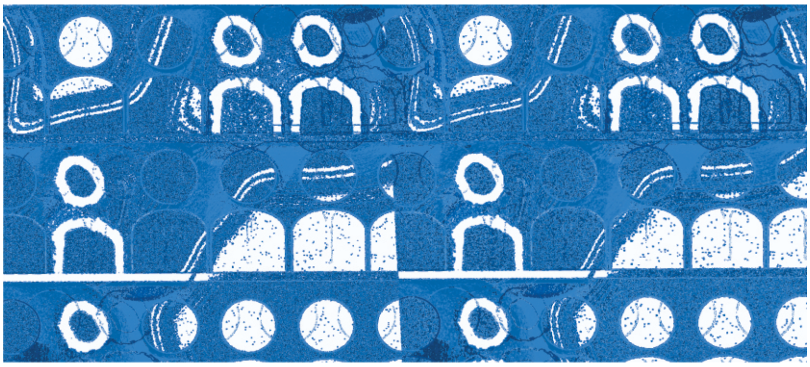

APPLIED ELECTROMAGNETICS **SAEM'2022**

ISBN 978-608-4999-01-0

SAVE
PAPER
save
TREES
SAVE
EARTH